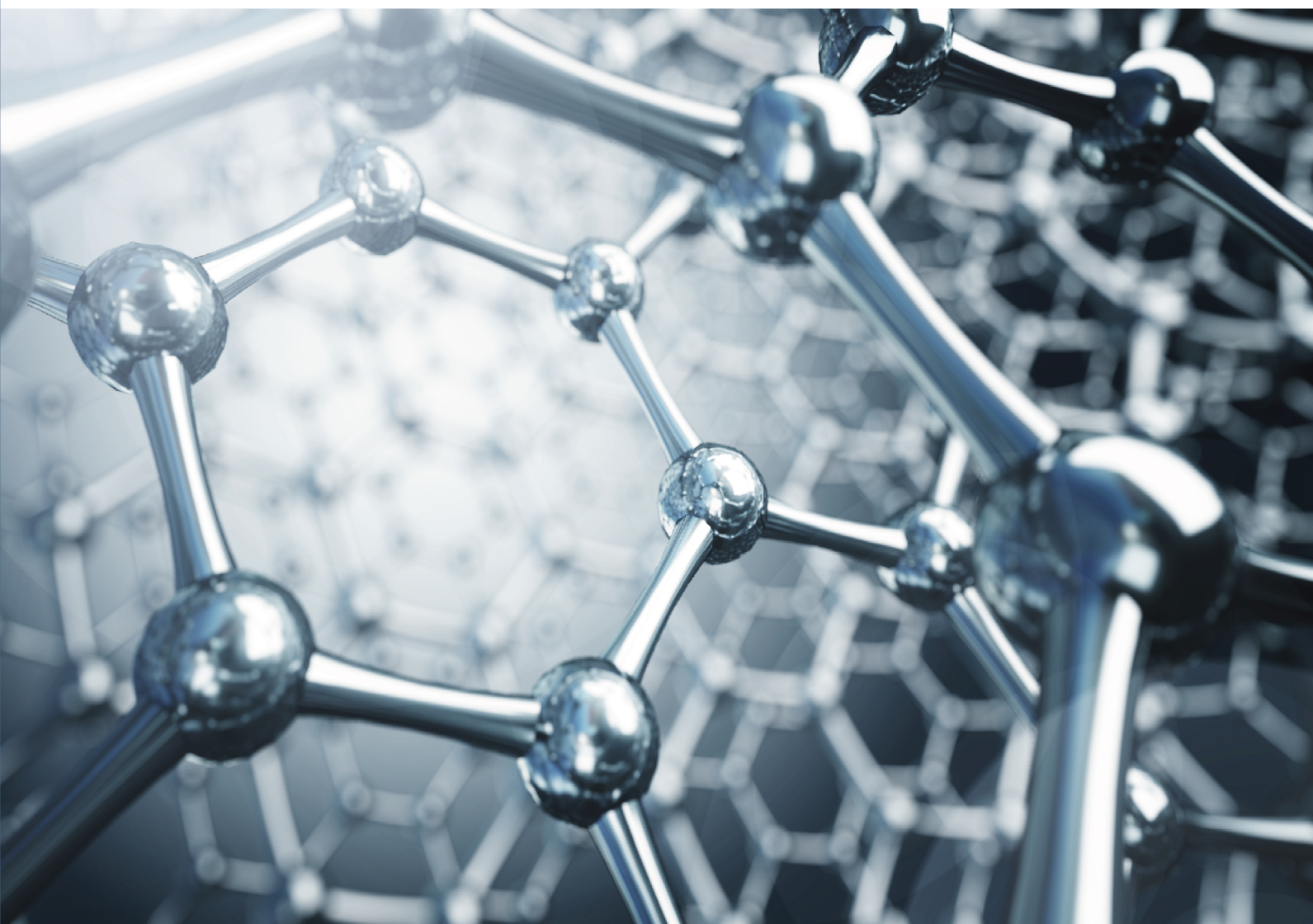


2021
Volume 4
Issue 1
ISSN: 2578-1995

CHARACTERIZATION AND APPLICATION OF NANOMATERIALS

Volume 4 Issue 1

<https://systems.enpress-publisher.com/index.php/CAN>



ISSN 2578-1995



9 772578 199042

CAN



Editorial Board

Editor-in-Chief

Prof. Sergey Victor Bulyarskiy

Institute of Nanotechnologies of Microelectronics
Russian Federation

Dr. Mohsen Sheikholeslami

Department of Mechanical Engineering, Babol Noshirvani University of Technology
Islamic Republic of Iran

Editorial Board Member

Dr. Nikolai Inokent'evich Plusnin

Institute of Automation and Control Processes
Russian Federation

Prof. Umapada Pal

Autonomous University of Puebla
Mexico

Prof. Levan Sandro Chkhartishvili

Georgian Technical University
Georgia

Prof. Haiping Xu

Shanghai Polytechnic University
China

Prof. Mostafa Ibrahim Abd-Elrahman

Assiut University
Egypt

Dr. Amir Sadeghi

Institute of Material Science and Engineering
Germany

Dr. Simge Gencalp Irizalp

Manisa Celal Bayar University
Turkey

Dr. Munshi Mahbubul Basit

Georgia Southern University
United States

Dr. Marcio Fernandes Leão

Federal University of Rio de Janeiro
Brazil

Dr. Hari Prasad Reddy Kannapu

Hanyang University
Republic of Korea

Prof. Serap Derman

Yildiz Technical University
Turkey

Dr. Sivasankaran Harish

Kyushu University
Japan

Dr. Muhammad Saeed

Government College University Faisalabad
Pakistan

Dr. Soheil Gohari

The University of Melbourne
Australia

Prof. Mumin Sahin

Trakya University
Turkey

Dr. Maryam Zohri

Tehran University of Medical Science
Islamic Republic of Iran

Characterization and Application of Nanomaterials

Editor-in-Chief

Prof. Sergey Victor Bulyarskiy

*Institute of Nanotechnologies of Microelectronics
Russian Federation*

Dr. Mohsen Sheikholeslami

*Department of Mechanical Engineering
Babol Noshirvani University of Technology
Islamic Republic of Iran*

Characterization and Application of Nanomaterials

<https://systems.enpress-publisher.com/index.php/CAN>

Contents

Original Research Articles

- 1 Nano CoO-Cu-MgO catalyst for vapor phase simultaneous synthesis of *ortho*-chloroaniline and γ -butyrolactone from *ortho*-chloronitrobenzene and 1,4-butanediol**
Hari Prasad Reddy Kannapu, Young-Woong Suh, Veeralakshmi Vaddeboina, Anand Narani, David Raju Burri, Seetha Rama Rao Kamaraju
- 11 Spin thermoelectric effects of new-style one-dimensional carbon-based nanomaterials**
Yushen Liu, Jinfu Feng, Xuefeng Wang
- 18 Study on the synthesis and adsorption properties of porous carbon/Ni nanoparticle composites**
Sailu Xu, Yuxin Du, Meiqi Hui, Zichen Wang, Junfeng Zhao, Gang Yang
- 25 A study of electrocatalytic ethanol oxidation of nanoporous PtSi alloy**
Nali Lu, Yao Li, Lei Zhang, Yong Fang, Bin Qian, Zhida Han, Xuefan Jiang
- 31 A theoretical study of (9, 0) Singlewalled Carbon Nanotubes using quantum mechanical techniques**
Deepa Sharma, Neena Jaggi
- 47 Synthesis of ZnO nanometer powders doped with Ce⁴⁺ ions and the photocatalytic degradation of dyeing wastewater**
Guishan Gu, Yuanyuan Zhang, Chi Huang, Li Sun, Xueying Wang

55 Influence of flow rate on the transport of nTiO₂ and phosphate and its modeling

Gang Feng, Nan Xu, Zuling Li, Yuhe Cao, Keqing Sun

63 Preparation and characterization of magnetic graphene oxide nanocomposite (GO-Fe₃O₄) for removal of strontium and cesium from aqueous solutions

Sule Aytas, Sabriye Yusan, Senol Sert, Cem Gok

77 Mesoscale computational prediction of lightweight, thermally conductive polymer nanocomposites containing graphene-wrapped hollow particle fillers

Jian-Jun Wang, Zhong-Hui Shen, Wen-Ying Zhou, Yang Shen, Ce-Wen Nan, Qing Wang, Long-Qing Chen

87 Liquid deposition modification of nano-ZSM-5 zeolite and catalytic performance in aromatization of Hexene-1

Yujun Fang, Xiaofang Su, Wei Wang, Wei Wu

94 Synthesis of titania fibers by electrospinning and its photocatalytic degradation properties

Yan Lv, Feng Chen, Yuanzheng Tang, Zhigang Chen

ORIGINAL RESEARCH ARTICLE

Nano CoO-Cu-MgO catalyst for vapor phase simultaneous synthesis of *ortho*-chloroaniline and γ -butyrolactone from *ortho*-chloronitrobenzene and 1,4-butanediol

Hari Prasad Reddy Kannapu^{1,2,3*}, Young-Woong Suh^{2,3*}, Veeralakshmi Vaddeboina¹, Anand Narani¹, David Raju Burri¹, Seetha Rama Rao Kamaraju¹

¹ Catalysis, Indian Institute of Chemical Technology, Hyderabad 500007, India. E-mail: kannapuhari@gmail.com/hari83@hanyang.ac.kr

² Department of Chemical Engineering, Hanyang University, Seoul 133-791, Republic of Korea. E-mail: ywsuh@hanyang.ac.kr

³ Research Institute of Industrial Science, Hanyang University, Seoul 133-791, Republic of Korea

ABSTRACT

The article aims at developing an efficient and stable catalysts for simultaneous hydrogenation of *o*-chloronitrobenzene to *o*-chloroaniline and 1,4-butanediol dehydrogenation to γ -butyrolactone. A series of CoO-Cu-MgO catalysts, composed of 10 wt% of copper, various amount of cobalt loadings (1, 5 and 10 wt%) and remaining of MgO were developed by co-precipitation followed by thermal treatment. *o*-Chloroaniline and γ -butyrolactone were the main products with high yield of 85% and 90%, respectively. The advantage of the coupling process is that the hydrogenation reaction was conducted without external hydrogen, demonstrating minimize the hydrogen consumption known as hydrogen economy route. From N₂O characterization results, the high activity of 5CoO-10Cu-MgO was found that it has high amount of Cu species (Cu⁰/Cu⁺) which govern the stable activity and selectivity on time on stream study in presence of cobalt in Cu-MgO.

Keywords: Transfer Hydrogenation; *Ortho*-chloro Aniline; γ -Butyrolactone; Atomic H₂; Basic Sites; Nano CoO-Cu-MgO

ARTICLE INFO

Received: 13 November 2020
Accepted: 4 January 2021
Available online: 11 January 2021

COPYRIGHT

Copyright © 2021 Hari Prasad Reddy Kannapu, et al.
EnPress Publisher LLC. This work is licensed under the Creative Commons Attribution-NonCommercial 4.0 International License (CC BY-NC 4.0).
<https://creativecommons.org/licenses/by-nc/4.0/>

1. Introduction

Owing to an enormous importance of aromatic halo amines in the chemical industry, specifically for synthesis of herbicides, dyes, drugs, and pesticides, synthesis of aromatic halo amines from halo nitrobenzene research has been gained a great attention in academia and industry point of view^[1-9]. Despite high demanding of this reaction, the hydrogenation of *ortho*-chloronitrobenzene (*o*-CNB) to *ortho*-chloroaniline (*o*-CAN) has been studied extensively over precious metals e.g., platinum, palladium, nickel, rhodium, ruthenium and iridium^[1-9]. Moreover, it has been mostly carried out under external hydrogen at an elevated temperatures and pressures which makes this process more complex and cost-ineffective in the industry point of view. Further, dehalogenation and ring hydrogenation are common side reactions that lead to formation of common side reactions that lead to formation of aniline and cyclohexylamine particularly over Pt, Pd and Ni catalysts. In this scenario, developing a highly selective and cost-effective cat-

alytic system still remains a challenge. Generally, alcohols are highly active for dehydrogenation over supported copper catalysts^[10-18]. 1,4-butanediol (BDO) is one of the alcohols that can make γ -butyrolactone (GBL) and two moles of hydrogen in its cyclodehydrogenation over copper-based catalysts. Another important point is noticed that the GBL has been demonstrated to be involved in the synthesis of N-vinylpyrrolidone, N-methylpyrrolidone, herbicides, and rubber additives and more over it is a green solvent. Commercially, the major production route for GBL is gas-phase dehydrogenation of BDO over supported copper metal catalysts, especially copper chromite catalysts, which are environmentally unacceptable.

As described above, owing to the high commercial value of these products, these two reactions would have great impression. Currently, coupling of hydrogenation and dehydrogenation^[10-17] is a promising and an alternative method to the conventional hydrogenation. In this method, the above mentioned two reactions can be carried out simultaneously at a time over a same catalyst bed. Copper-based catalysts were found to be outstanding for the coupling of hydrogenation and dehydrogenation reaction^[10-16]. However, the activity and stability of catalysts mainly depends on the preparation of the catalysts. A numerous results documented in the literature have found that the addition of second metal oxide to base catalyst will result in the local composition, the size and structure of active species significantly affecting the catalytic activity and selectivity of supported metal catalysts^[19]. It is generally agreed that for supported metal catalysts, highly dispersed active species can provide more active sites and thus confer the resulting catalysts with higher catalytic activity^[20]. To best of our knowledge, selective *o*-CNB hydrogenation to *o*-CAN has not been reported using 1,4-butanediol (BDO) dehydrogenation over nano CoO-Cu-MgO.

Herein, we have investigated the vapor phase selective hydrogenation of *o*-CNB to *o*-CAN with dehydrogenation of BDO to γ -butyrolactone (GBL) over CoO-Cu-MgO catalysts. All the catalysts were developed by co-precipitation followed by thermal treatment. Catalysts preparation, characterization us-

ing different analytical techniques such as BET surface area, N₂O pulse chemisorption, XRD, TPR-H₂, and TEM analysis and activity in hydrogenation and dehydrogenation have been delineated.

2. Experimental

2.1 Preparation of catalysts

An aqueous homogeneous mixed metal nitrate solution containing Cu(NO₃)₂•3H₂O and Mg(NO₃)₂•6H₂O was prepared followed immediate precipitation by drop-wise addition of 10% aqueous K₂CO₃ solution at a pH of 9.0 under constant stirring at room temperature. The resultant mixed Cu-Mg precipitate (precipitate of 10 wt% Cu-MgO catalyst, ppt1) has been separated under reduced pressure and washed thoroughly with hot distilled H₂O until the complete removal of potassium ion. In a separate experiment, requisite amount of Co(NO₃)₂•6H₂O aqueous solution has been precipitated at a pH of 9 with K₂CO₃ solution under vigorous stirring. The obtained cobalt precipitate (ppt2) was filtered and washed thoroughly with hot distilled water. Cu-Mg precipitate (ppt1) and Co precipitate (ppt2) were mixed in water under neutral condition and the resultant slurry was subjected to hydrothermal treatment at 373 K for 12 h followed by filtration with repeated washings. The precipitate was dried in oven at 393 K for 12 h followed by calcination at 723 K for 5 h. Similar procedure has been adopted for the preparation of other CoO promoted Cu-MgO catalysts. The prepared catalysts were labeled as 1CoO-10Cu-MgO, 5CoO-10Cu-MgO, and 10CoO-10Cu-MgO, here the numerical value represents the loadings of Co and Cu by weight percentage. For example, 1CoO-10Cu-MgO represents a catalyst containing 1 wt% Co, 10 wt% Cu and the remaining balance MgO.

2.2 Characterization techniques

All the CoO-Cu-MgO catalysts were thoroughly characterized by using the following analytical techniques. The Brunauer, Emmett and Teller (BET) surface area of all catalysts was measured by N₂ physisorption after degasification at 473 K for 4 h, under liquid nitrogen adsorption at 77 K using

Quadratorb-SI surface area analyzer (M/s. Quantachrome instruments, USA). The surface properties of all CoO-Cu-MgO catalysts such as Cu metal surface area (MSA), Cu dispersion (D_{Cu}), particle size (P_{Cu}) and surface coverage of Cu atoms (S_{Cu}) were estimated by N_2O pulse chemisorption on pre-reduced (553 K for 3 h) catalyst under dynamic conditions. The detailed procedure was described elsewhere^[10-13]. The X-ray diffraction (XRD) patterns of both calcined and reduced catalysts were recorded on a Miniflex diffractometer (M/s. Rigaku Instruments, Japan) using Ni filtered Cu K_α radiation in the 2θ range of 10° – 80° at a scan rate of 2° min^{-1} . The average crystallite size of copper was calculated using Debye-Scherrer principle. Transmission electron microscopy (TEM) was recorded using a Phillips Tecnai G2 FEI F12 electron microscope. The reduction behavior of the catalysts was determined by temperature programmed reduction (TPR) studies on a home-made system as per the procedure described elsewhere^[10]. The CHNS elemental analysis was carried out on Elementar, Model: VarioMicrocube to estimate the carbon content in the catalyst before and after the reaction.

2.3 Activity studies

A down flow fixed-bed reactor was used to investigate the activity of the CoO-Cu-MgO catalysts for the individual hydrogenation of *o*-CNB (dissolved in ethanol) to *o*-CAN and dehydrogenation of BDO to GBL as well as coupling of both reactions. For separate experiments, first tests were carried out on

o-CNB hydrogenation. Approximately, 500 mg of the catalyst powder (sieved to $< 200 \mu\text{m}$) diluted with an equal amount of quartz beads was charged to the reactor and supported on a quartz wool bed. The catalyst was reduced at 553 K for 3 h under hydrogen. Then, the reactor was fed with *o*-CNB under H_2 ($18 \text{ ml}\cdot\text{min}^{-1}$), using as a reducing gas. Similarly, the dehydrogenation of BDO was conducted under N_2 atmosphere. Finally, the coupling of *o*-CNB hydrogenation and BDO dehydrogenation was performed at the molar ratio of 2:3 under nitrogen atmosphere. The liquid products, such as *o*-CAN and GBL were analyzed by using GC-17A (M/s. Shimadzu, Japan) with ZB-wax capillary column equipped FID detector. The products were identified and analyzed by using GCMS-QP5050 (M/s. Shimadzu instruments, Japan) equipped with ZB-5 capillary column ($25 \text{ m} \times 0.32 \text{ mm}$) supplied by M/s. J&W Scientific, USA.

3. Results and discussion

3.1 Catalyst characterization

3.1.1 BET Surface area studies

Table 1 presents BET surface area, crystalline phases of various cobalt loadings of Cu-MgO catalysts both in calcined and reduced form. The surface area of the CoO-Cu-MgO catalysts is higher compared to MgO ($42 \text{ m}^2\cdot\text{g}^{-1}$) alone. This indicates that addition of cobalt to Cu-MgO increases the surface areas of Cu-MgO.

The BET surface area of catalysts increases with

Table 1. BET surface area and XRD results of CoO-Cu-MgO catalysts

Catalyst	BET surface area ($\text{m}^2\cdot\text{g}^{-1}$)	XRD phases		Cu^0 (nm) reduced	Cu^0 (nm) spent
		Calcined	Reduced		
1CoO-10Cu-MgO	78	CuO, MgO	Cu^0 , Cu_2O , MgO	20	30.48
5Co-10Cu-MgO	88	CuO, MgO	Cu^0 , Cu_2O , MgO	15	20.30
10CoO-10Cu-MgO	50	CuO, MgO	Cu^0 , Cu_2O , MgO	13	26.48

increasing in CoO loading and displayed maximum surface area ($88 \text{ m}^2\cdot\text{g}^{-1}$) at 5 wt% CoO loading and thereafter decreases with further increasing in the Co content. It was found that hydrothermal treatments of Fe/MgO catalysts transformed into lamella-like Fe/Mg(OH)₂ catalysts, resulted in increasing the specific surface areas^[21]. Since, in the present study, due to hydrothermal treatment, CoO-CuO-MgO interacted

species in large number is responsible for high surface area of 5CoO-10Cu-MgO catalyst. Formation of an interacted phase (CuCo_3O_4) between Cu and Co was reported to be appeared at a temperature of 573 K which was stable up to 1073 K^[22]. Such interacted phase might be accountable for the increasing trend of surface area and pore volume with the increase in Co content up to 5 wt%. Contrarily, beyond 5 wt%

Co loading, a reverse trend was observed due to surface coverage by cobalt oxide. The crystallite size of copper in reduced and spent catalysts is calculated and depicted in **Table 1**. It is obvious that the development of copper size influenced by the cobalt addition is inevitable. In the case of reduced catalysts copper crystallite size linearly minimized whereas in spent catalysts, only 5CoO-10Cu-MgO has stability and maintain lower crystallite size among other two catalysts.

3.1.2 X-Ray diffraction studies (XRD)

The XRD patterns of calcined catalysts are shown in **Figure 1**. A low intense diffractions of CuO phase (d values of 2.52 at $2\theta = 35.6^\circ$, 2.32 at $2\theta = 38.78^\circ$ and 2.53 at $2\theta = 35.45^\circ$, ICDD Card No. 5-661) and high intensity of MgO (d values of 2.11 at $2\theta = 42.82^\circ$, 1.49 at $2\theta = 62.25^\circ$ and 1.22 at $2\theta = 78.30^\circ$, ASTM Card No. 4-829) are observed in all cobalt loading catalysts. Interestingly, no diffractions were noticed for CoO oxide phase at all loadings which indicates amorphous form of cobalt species. It was reported that in 11% Co-MgO catalyst, MgO is in amorphous form when it is calcined at 673 K and it is in crystalline phase above 973 K^[23]. In addition, CoO is formed after calcination at 773 K through the decomposition of $\text{Co}(\text{NO}_3)_2$ and might have diffused into the matrix of MgO or form a solid solution or oxidized to Co_2O_3 , which on reaction either with CoO or with MgO to yield Co_3O_4 or MgCo_2O_4 ^[24].

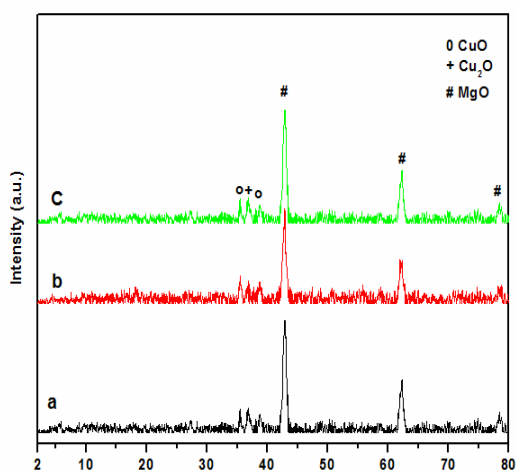


Figure 1. XRD patterns of calcined CoO-Cu-MgO catalysts. (a) 1CoO-10Cu-MgO; (b) 5CoO-10Cu-MgO; (c) 10CoO-10Cu-MgO.

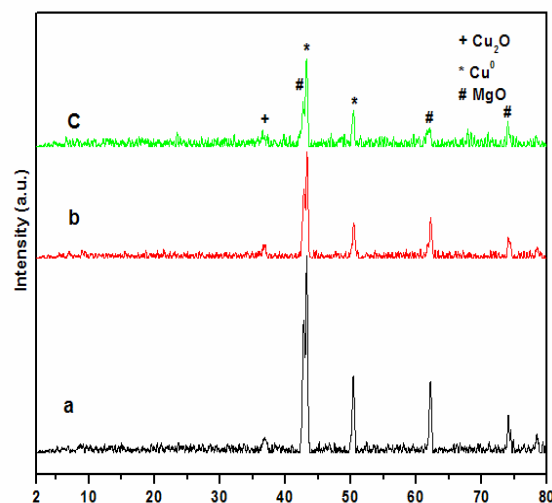


Figure 2. XRD patterns of reduced CoO-Cu-MgO catalysts. (a) 1CoO-10Cu-MgO; (b) 5CoO-10Cu-MgO; (c) 10CoO-10Cu-MgO.

XRD patterns of reduced (at 523 K in H_2 flow) CoO-Cu-MgO catalysts are shown in **Figure 2**. The Cu^0 phase with corresponding d values of 2.09 at $2\theta = 43.25^\circ$, 1.81 at $2\theta = 50.37^\circ$ and 1.28 at $2\theta = 73.99^\circ$, ICDD Card No. 4-836 is observed for all catalysts. But, the d values of Cu^0 and MgO are closer; therefore, the diffraction lines are not separated properly. As evidenced from the XRD results almost all CuO phases are reduced to Cu^0 or Cu_2O . It can also be seen that MgO phase decreased with addition of cobalt oxide representing the formation of amorphous MgCo_2O_4 species particularly at 10 wt% CoO. XRD pattern of 10CoO-10Cu-MgO catalyst revealed that Cu^0 , Cu_2O and MgO crystallites were lower than other two catalysts.

3.1.3 N_2O pulse chemisorption

The estimated surface properties of Cu-MgO with cobalt catalysts such as (i) number of surface copper sites, (ii) dispersion, (iii) metal surface area, and (iv) particle size are shown in **Table 2**. N_2O pulse chemisorption is a facile and proven technique for the estimation of metal area and allied surface properties of supported copper catalysts.

Even though Co oxides are hard to get reduced at 523 K (the temperature at which the catalysts of the present investigation are reduced prior to N_2O pulse chemisorption), small amount of lower oxidation states of Co species might have resulted to participate in the decomposition of N_2O thus giving

Table 2. N₂O pulse chemisorption results for different CoO-10Cu-MgO catalysts

Catalyst	S _{Cu} atoms × 10 ⁻¹⁹ (atoms g ⁻¹)	D _{Cu} (%)	Metal surface area (m ² ·g ⁻¹)	Particle size (nm)	Surface density S _{Cu} /BET S.A
1CoO-10Cu-MgO	10	19	07	13	10/78
5CoO-10Cu-MgO	18	21	13	06	18/88
10CoO-10Cu-MgO	12	14	11	10	12/50

Note: S_{metal} = Number of surface metal sites (Cu); D_{metal} = Dispersion of metal (Cu); SA_{metal} = Surface area of metal (Cu); P_{metal} = Particle size of metal (Cu)

a chance to over estimation of Cu dispersion^[12]. As shown in **Table 2**, the number active surface sites of copper catalysts are higher in 5CoO-10Cu-MgO. Similarly, dispersion of active metal (copper plus cobalt) and active metal surface area (copper plus cobalt) are higher in all the cobalt promoted catalysts. Contrarily, the particle size (copper plus cobalt) of metal is lower in all cobalt promoted catalysts. 5CoO-10Cu-MgO catalyst possesses a little higher surface density (copper plus cobalt) compared to other Co promoted catalysts. The surface density of 5CoO-10Cu-MgO catalyst is nearly double than that of 1CoO-10Cu-MgO catalyst.

3.1.4 TEM analysis

Figures 3a, b and **c** are copper particles with an appearance of dark contrasts as well as copper-free MgO particles with an appearance of light contrasts. At lower cobalt loadings the morphology of catalysts seems to be rod type structure, whereas at 10CoO-10Cu-MgO, catalyst regains its particle type structure. Such a gathering of copper species in CoO-Cu-MgO catalysts has also been reported in the literature^[21–25]. However, no obvious copper particles can be found in the hydrothermal-treated catalyst (**Figure 4**).

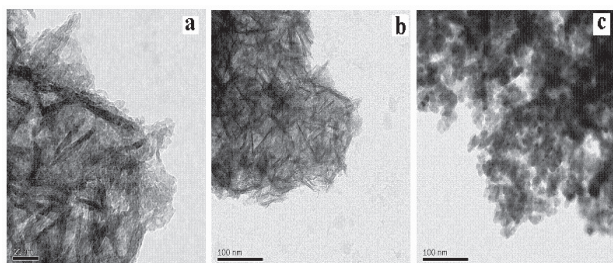


Figure 3. TEM images of CoO-Cu-MgO. (a) 1CoO-10Cu-MgO; (b) 5CoO-10Cu-MgO; (c) 10CoO-10Cu-MgO.

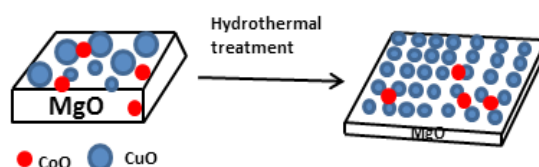


Figure 4. Suggested mechanism of hydrothermal treatment and nanoparticle growth.

3.1.5 Temperature programmed reduction (TPR) studies

The reducibility of the catalysts can be determined by temperature programmed reduction with H₂/Ar mixture and results are depicted in **Figure 5**. According to the TPR results of 10Cu-MgO catalyst, the catalyst characterized by a single symmetric peak centered at a temperature maximum (T_m) of 710 K^[16]. The present results showed that the 1CoO-10Cu-MgO catalyst exhibits a single reduction, indicating the 1 wt% CoO did not affect Cu-MgO interactions. However, presence of a shoulder on an asymmetric peak is the indication of two-stage reduction: (i) CuO to Cu⁰ and (ii) partial reduction of CuCO₂O₄/MgCO₂O₄. In the case of 5CoO-10Cu-MgO catalyst, the high temperature signal corresponds to the reduction of interacted species formed between CoO precursor and CuO. It is noteworthy to mention that the amount of cobalt oxide species are less at 5 wt% cobalt oxide compared with that of 10 wt% CoO. The reaction between CuO and CoO can make more CuCO₂O₄ species in 5CoO-10Cu-MgO. Whereas, the high cobalt oxide content in 10CoO-10Cu-MgO might have resulted to have less CuCO₂O₄ and more MgCO₂O₄ which are reduced at 850 K. The three-stage reduction including copper oxide, cobalt oxides and spinals (CuCO₂O₄ and MgCO₂O₄) providing high acidity for 10CoO-10Cu-MgO.

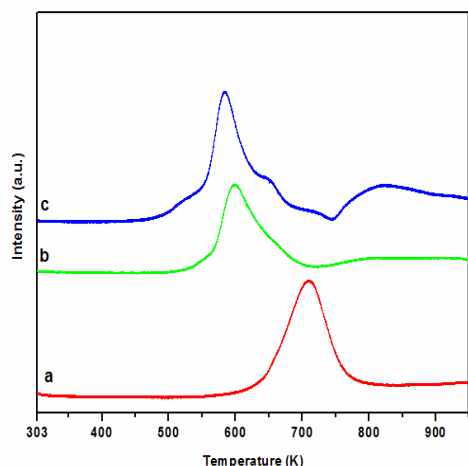


Figure 5. TPR patterns of CoO-Cu-MgO. (a) 1CoO-10Cu-MgO; (b) 5CoO-10Cu-MgO; (c) 10CoO-10Cu-MgO.

Due to high cobalt oxide content in 10CoO-10Cu-MgO, the reduction behavior is unlike to other two catalysts. It was reported that the peaks at 650 and 730 K were assigned to reduction of large crystalline Co_3O_4 to CoO and CoO to Co metal, respectively, but a shoulder peak at 850 K was attributed to the reduction of MgCo_2O_4 ^[26]. As reported by Wang and Ruckenstein^[24], Co_3O_4 is getting reduced below 773 K while MgCo_2O_4 below 973 K and the solid solution of Co-MgO at higher than 1273 K temperature. The TPR results of this study are well collaborated with those reported in the literature^[12]. The shifting of T_{max} to lower temperature in 5 wt% and 10 wt% Co catalysts is an indication of interaction between Co and Cu species. It was reported that when a mixture of Cu and Co oxides were supported on Al_2O_3 , cobalt oxide reacts during calcination not only with CuO but also with Al_2O_3 , which leads to formation of the spinel CoAl_2O_4 ^[27]. When the same oxides were supported on non-interacted supports like silica, they interact to form the spinel CuCo_2O_4 ^[28]. Thus, the TPR patterns clearly indicate the presence of Co oxide interacted species with both Cu and Mg-oxides.

3.2 Activity studies

3.2.1 Hydrogenation of *ortho*-chloronitrobenzene (*o*-CNB)

The catalytic activity of CoO-Cu-MgO catalysts evaluated for the vapor phase selective hydrogenation of *o*-CNB to *o*-CAN at atmospheric pressure

with H_2 /*o*-CNB required mole ratio at a reaction temperature in the range of 548 K–723 K and results are shown in **Figure 6**. The conversion of *o*-CNB to *o*-CAN increases significantly with the increasing of temperature from 540 K to 680 K. Thereafter conversion is nearly about 95% and 90% for 5CoO-10Cu-MgO and 1CoO-10Cu-MgO, respectively. Precisely, 5CoO-10Cu-MgO has shown highest conversion about 98% at 720 K. But, the conversion of *o*-CNB to *o*-CAN is maximum of 63% at 673 K and reached to 50% at final temperatures over 10CoO-10Cu-MgO. These results demonstrated the effect of cobalt loadings on hydrogenation of *o*-CNB to *o*-CAN over CoO-Cu-MgO. The high activity of 5CoO-10Cu-MgO is associated to the presence of more number of surface active Cu^0 particles as observed from N_2O pulse chemisorption.

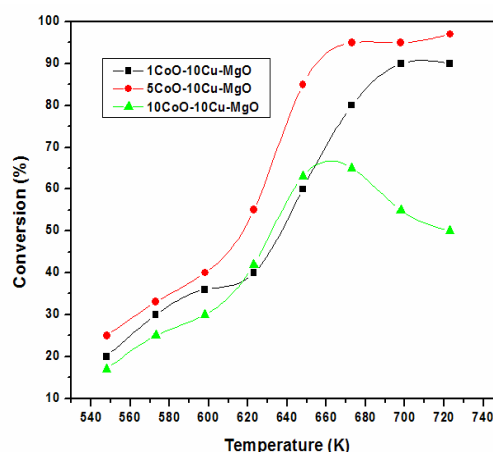


Figure 6. Effect of temperature on hydrogenation of *ortho*-chloronitrobenzene over CoO-Cu-MgO catalysts.

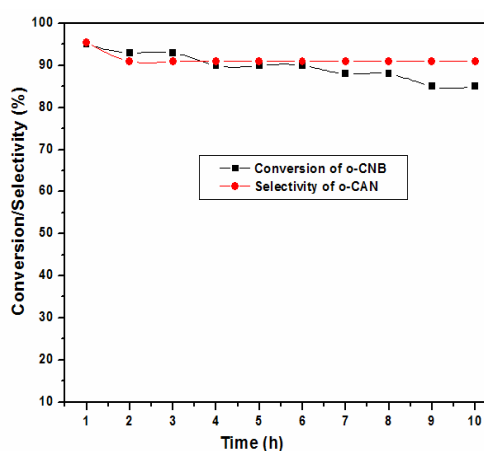


Figure 7. Time on studies over 5CoO-10Cu-MgO at 623 K for 10 h.

Figure 7 shows the conversion of *o*-CNB to *o*-CAN at 623 K over a period of 10 h reaction. It is found that the activity of the catalyst is stable with 90% conversion up to 6 h and then reached to 85% at final hours. It is concluded that agglomeration of copper might be responsible for loss of the activity. These results are in good agreement with that the crystallite size of copper after reaction is bigger than reduced copper as shown in **Table 1**.

3.2.2 Dehydrogenation of 1,4-butanediol (BDO)

Figure 8 illustrates BDO conversion as a function of temperature. The dehydrogenation of BDO is an endothermic reaction; hence the conversion of BDO to GBL increases with the rise of temperature over CoO-Cu-MgO catalysts. The result shows that the maximum catalytic activity of CoO-Cu-MgO catalysts is noticed at 523 K, which is the best temperature to obtain the GBL with high yields. In contrast, conversion of BDO is falling gradually for all catalysts except over 5CoO-Cu-MgO. The highest BDO conversion (> 97%) and GBL selectivity (99%) can be seen at 5 wt% CoO loading Cu-MgO. Importantly, the selectivity towards GBL is almost the same for all the catalysts.

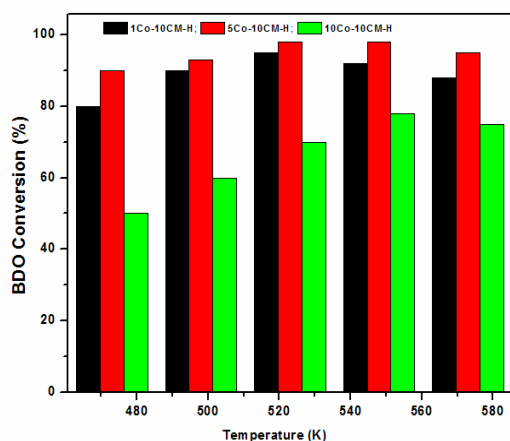


Figure 8. Effect of temperature on BDO dehydrogenation over CoO-Cu-MgO catalysts.

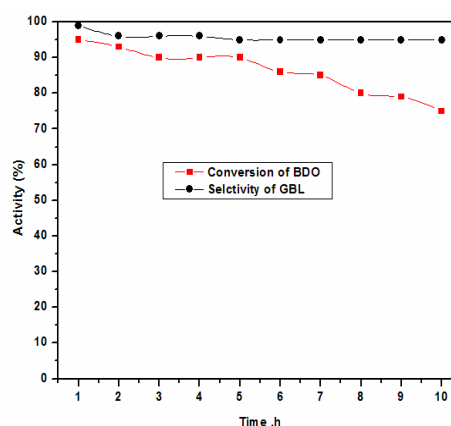


Figure 9. Time on stream study of BDO dehydrogenation over 5Co-10CM-H catalyst.

Based on above results, the stability of 5CoO-10Cu-MgO for BDO to GBL was evaluated for 10 h at 523 K. The conversion of BDO is above 95% at beginning of the reaction whereas with increasing in the time the conversion declines slowly from 95% to 75%. Interestingly, selectivity to GBL remains constant up to 10 h (**Figure 9**). The deactivation of the catalyst is mainly due to agglomeration of copper particles during course of the reaction.

3.2.3 Coupling of *o*-chloronitrobenzene hydrogenation and 1,4-butanediol dehydrogenation

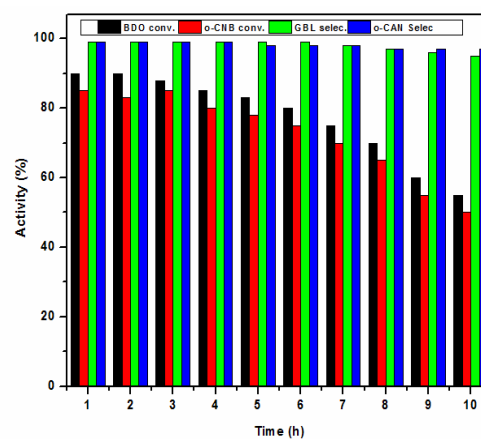


Figure 10. Time on stream study coupling of BDO dehydrogenation and *o*-CNB hydrogenation over 5Co-10CM-H catalyst.

The independent reactions: (i) hydrogenation of *o*-CNB to *o*-CAN and (ii) dehydrogenation of BDO to GBL provide the best catalyst and temperature to conduct the titled reactions. The mole ratio of BDO

versus *o*-CNB is 1.5:1, which is an optimum for coupling process and results are shown in **Figure 10**. The reaction results clearly demonstrate that conversions of BDO and *o*-CNB are 90% and 85%, respectively, in early hours. When reaction time increases, the conversion of both reactions linearly dropped which could be attributed to the agglomeration of copper and finally reached to 54% and 50% with 99% selectivity of their corresponding products. Surprisingly, the individual hydrogenation of *o*-CNB at 523 K with 1.5 moles of external hydrogen is very low (< 5%). But, in coupling process, hydrogenation of *o*-CNB with dehydrogenation of BDO was substantially increased from 5% to 90%. This enhancement of *o*-CNB conversion in the coupling reaction is ascribed to the active role of in-situ production of hydrogen atom from BDO to GBL reaction which gets instantaneously utilized^[10–18]. The deactivation of catalysts may be due to agglomeration copper. The color of the catalyst physically changed to black, which further indicates the coke deposition on the catalyst during course of the reaction.

4. Conclusions

The different amount of CoO incorporated 10Cu-MgO prepared by co-precipitation followed by hydrothermal treatment has shown excellent catalytic activity compared to unpromoted Cu-MgO catalyst. The best catalytic activity of 5Co-10Cu-MgO is due to the addition of cobalt increased number of surface copper atoms and decreased the reduction ability of copper as observed from TPR results. Contrarily, in 10CoO-10Cu-MgO the high amount of cobalt oxide covered active copper sites. Deactivation of catalyst in coupling reaction is mainly due to agglomeration as well the coke formation during the course of reaction. In summary, two industrially important reactions can be carried out over CoO-Cu-MgO catalyst simultaneously.

Conflict of interest

The authors declare that they have no conflict of interest.

Acknowledgements

Authors gratefully thank CSIR-UGC (INDIA) for the financial support. This research was also financially supported by Basic Science Research Program through the National Research Foundation of Korea (NRF) funded by the Ministry of Education (NRF-2016R1A6A1A03013422) and New & Renewable Energy Core Technology Program of the Korea Institute of Energy Technology Evaluation and Planning (KETEP), granted financial resource from the Ministry of Trade, Industry & Energy, Republic of Korea (No. 20163010092210).

References

1. Yang X, Deng Z, Liu H. Modification of metal complex on hydrogenation of *ortho*-chloronitrobenzene over polymer-stabilized platinum colloidal clusters. *Journal of Molecular Catalysis A: Chemical* 1999; 144: 123.
2. Khilnani VL, Chandalia SB. Selective hydrogenation. I. para-chloronitrobenzene to para-chloroaniline platinum on carbon as catalyst. *Organic Process Research and Development* 2001; 5: 257.
3. Liang M, Wang X, Liu H, *et al.* Excellent catalytic properties over nanocomposite catalysts for selective hydrogenation of halonitrobenzenes. *Journal of Catalysis* 2008; 255: 335.
4. Motoyama Y, Kamo K, Nagashima H. Catalysis in polysiloxane gels: Platinum-catalyzed hydrosilylation of polymethyl hydrosiloxane leading to reusable catalysts for reduction of nitroarenes. *Organic Letter* 2009; 11: 1345.
5. Yuan X, Yan N, Xiao C, *et al.* Highly selective hydrogenation of aromatic chloronitro compounds to aromatic chloroamines with ionic-liquid-like copolymer stabilized platinum nano catalysts in ionic liquids. *Green Chemistry* 2010; 12: 228.
6. Yang X, Liu H, Zhong H. Hydrogenation of *ortho*-chloronitrobenzene over polymer-stabilized palladium–platinum bimetallic colloidal clusters. *Journal of Molecular Catalysis A: Chemical* 1999; 147: 55.
7. Sreedhar B, Reddy PS, Devi DK. Direct one-pot

- reductive amination of aldehydes with nitroarenes in a domino fashion: Catalysis by gum-acacia-stabilized palladium nanoparticles. *Journal of Organic Chemistry* 2009; 74: 8806.
8. Liu M, Yu W, Liu H. Selective hydrogenation of ortho-chloronitrobenzene over polymer-stabilized ruthenium colloidal catalysts. *Journal of Molecular Catalysis A: Chemical* 1999; 138: 295.
 9. Kratky V, Kralik M, Mecarova M, *et al.* Effect of catalyst and substituents on the hydrogenation of chloronitrobenzenes. *Applied Catalysis A* 2002; 235: 225.
 10. Nagaraja BM, Padmasri AH, Seetharamulu P, *et al.* A highly active Cu-MgO-Cr₂O₃ catalyst for simultaneous synthesis of furfuryl alcohol and cyclohexanone by a novel coupling route—Combination of furfural hydrogenation and cyclohexanol dehydrogenation. *Journal of Molecular Catalysis A: Chemical* 2007; 278: 29.
 11. Reddy KHP, Mullen CA, Elkasabi Y, *et al.* Catalytic transfer hydrogenation for stabilization of bio-oil oxygenates: Reduction of p-cresol and furfural over bimetallic Ni-Cu catalysts using isopropanol. *Fuel Processing Technology* 2015; 137: 220–228.
 12. Reddy KHP, Neeli CKP, Rao KSR, *et al.* Unusual effect of cobalt on Cu-MgO catalyst for the synthesis of γ -butyrolactone and aniline *via* coupling reaction. *Catalysis Science and Technology* 2016; 6: 5494.
 13. Reddy KHP, Rahul R, Reddy SSV, *et al.* Coupling of 1,4-butanediol dehydrogenation reaction with the hydrogenation of nitrobenzene over Cu/MgO catalysts. *Catalysis Communication* 2009; 10: 879.
 14. Reddy KHP, Anand N, Venkateswarlu V, *et al.* A selective synthesis of 1-phenylethanol and γ -butyrolactone through coupling processes over Cu/MgO catalysts. *Journal of Molecular Catalysis A: Chemical* 2012; 355: 180.
 15. Reddy KHP, Suh YW, Anand N, *et al.* Coupling of 1,4-butanediol dehydrogenation with nitrobenzene hydrogenation for simultaneous synthesis of γ -butyrolactone and aniline over promoted Cu-MgO catalysts: Effect of promoters. *Catalysis Letters* 2017; 147: 90–101.
 16. Reddy KHP, Young-Woong S, Anand N, *et al.* Coupling of *ortho*-chloronitrobenzene hydrogenation with 1,4-butanediol dehydrogenation over Cu-MgO catalysts: A hydrogen free process. *Catalysis Communications* 2017; 95: 21–25.
 17. Reddy KHP, Young-Woong S, Anand N, *et al.* One-pot synthesis of ethylbenzene/1-phenylethanol and γ -butyrolactone from simultaneous acetophenone hydrogenation and 1,4-butanediol dehydrogenation over copper based catalysts: Effect of support. *RSC Advances* 2017; 7: 35346–35356.
 18. Reddy KHP, Anand N, PSS Prasad, *et al.* Influence of method of preparation Co-Cu-MgO catalysts on dehydrogenation/dehydration reaction pathway of 1,4-butanediol. *Catalysis Communications* 2011; 12: 866–869.
 19. Daage M, Chianelli RR. Structure-function relations in molybdenum sulfide catalysts: The “rim-edge” model. *Journal of Catalysis* 1994; 149: 414.
 20. Vradman L, Landau MV, Herskowitz M, *et al.* High loading of short WS₂ slabs inside SBA-15: Promotion with nickel and performance in hydrodesulfurization and hydrogenation. *Journal of Catalysis* 2003; 213: 163.
 21. Ning G, Liu Y, Wei F, *et al.* Porous and lamella-like Fe/MgO catalysts prepared under hydrothermal conditions for high-yield synthesis of double-walled carbon nanotubes. *Journal of Physical Chemistry C* 2007; 11: 1969.
 22. Shaheen WM, Ali AA. Characterization of solid–solid interactions and physicochemical properties of copper-cobalt mixed oxides and Cu_xCo_{3-x}O₄ spinels. *Materials Research Bulletin* 2001; 36: 1703.
 23. Omata K, Nukui N, Hottai T, *et al.* Cobalt-magnesia catalyst by oxalate co-precipitation method for dry reforming of methane under pressure. *Catalysis communications* 2004; 5: 771.
 24. Wang H, Ruckenstein E. CO₂ reforming of CH₄ over Co/MgO solid solution catalysts effect of calcination temperature and Co loading. *Applied Catalysis A: General* 2001; 209: 207.
 25. Ago H, Nakamura K, Uehara N, *et al.* Roles of metal–support interaction in growth of single- and double-walled carbon nanotubes studied with diameter-controlled iron particles supported on MgO. *Journal of Physical Chemistry B* 2004; 108: 18908.
 26. Furusawa T, Tsutsumi A. Comparison of Co/MgO

- and Ni/MgO catalysts for the steam reforming of naphthalene as a model compound of tar derived from biomass gasification. *Applied Catalysis A: General* 2005; 278: 207.
27. Stoyanova D, Christova M, Dimitrova P, *et al.* Copper–cobalt oxide spinel supported on high-temperature aluminosilicate carriers as catalyst for CO–O₂ and CO–NO reactions. *Applied Catalysis B* 1998; 17: 233.
28. Cesar DV, Perez CA, Schmal M, *et al.* Quantitative XPS analysis of silica-supported Cu–Co oxides. *Applied Surface Science* 2000; 157: 159.

ORIGINAL RESEARCH ARTICLE

Spin thermoelectric effects of new-style one-dimensional carbon-based nanomaterials

Yushen Liu^{1*}, Jinfu Feng¹, Xuefeng Wang²

¹ School of Physics and Electronic Engineering, Changshu Institute of Technology, Changshu 215500, China. E-mail: yslu@csit.edu.cn

² College of Physics, Optoelectronics and Energy, Soochow University, Suzhou 215006, China

ABSTRACT

Based on first-principles methods, the authors of this paper investigate spin thermoelectric effects of one-dimensional spin-based devices consisting of zigzag-edged graphene nanoribbons (ZGNRs), carbon chains and graphene nanoflake. It is found that the spin-down transmission function is suppressed to zero, while the spin-up transmission function is about 0.25. Therefore, an ideal half-metallic property is achieved. In addition, the phonon thermal conductance is obviously smaller than the electronic thermal conductance. Meantime, the spin Seebeck effects are obviously enhanced at the low-temperature regime (about 80 K), resulting in the fact that spin thermoelectric figure of merit can reach about 40. Moreover, the spin thermoelectric figure of merit is always larger than the corresponding charge thermoelectric figure of merit. Therefore, the study shows that they can be used to prepare the ideal thermospin devices.

Keywords: Graphene Nanoribbons; Carbon Chains; Graphene Nanoflake; Spin Seebeck Coefficients; Thermoelectric Figure of Merit

ARTICLE INFO

Received: 15 November 2020
Accepted: 8 January 2021
Available online: 14 January 2021

COPYRIGHT

Copyright © 2021 Yushen Liu, *et al.*
EnPress Publisher LLC. This work is licensed under the Creative Commons Attribution-NonCommercial 4.0 International License (CC BY-NC 4.0).
<https://creativecommons.org/licenses/by-nc/4.0/>

1. Introduction

Carbon is one of the elements widely distributed in nature. As a tetravalent non-metallic element, it can form covalent bonds with metals and non-metals and combine into a variety of carbon-based nanomaterials. Graphene, as a two-dimensional allotrope of carbon, has been widely studied because of its unique electrical properties. Reviewing its development history, it is found that it has attracted early attention in theory, but the extensive research on its properties began with Geim and Novoselov, who obtained nearly perfect monolayer and free state graphene by simple mechanical method for the first time^[1]. From the atomic level, graphene is composed of sp_2 hybrid carbon atoms. It is also an aromatic compound with a large π electron conjugate system. The special energy band structure leads to a semiconductor with zero energy gap. Unlike traditional semiconductor materials, graphene follows Dirac equation rather than Schrodinger equation. The migration rate of carriers in the conjugate system is very high, even close to the speed of light, making graphene one of the materials with the lowest resistivity at present.

Although graphene has very unique electrical properties, it cannot be directly used in logic devices due to the energy band structure of zero energy gap. In order to open the energy gap, a common method is

to shear two-dimensional graphene into one-dimensional nano band structure and introduce quantum confined domain effect and boundary effect. When the width is less than 10 nm, graphene nanoribbons will open the energy gap. The preparation methods of graphene nanoribbons can be divided into two kinds: one is the top-down synthesis method. For example, carbon nanotubes can be cut by physical or chemical methods using carbon nanotubes as basic raw materials. The other is the bottom-up synthesis method, that is, the nanoribbon structure is synthesized from small molecular raw materials. According to the boundary structure characteristics of the ribbons, graphene nanoribbons can be divided into two types: armchair and zigzag. Armchair nanoribbons (AGNRs) show non-magnetic semiconductor behavior, and the band gap decreases with the gradual increase of width^[2]. Zigzag nanoribbons (ZGNRs) have spin-polarized boundary states due to the presence of non-bonding electrons in boundary carbon atoms. Theoretical study shows that the ground state of zigzag nanoribbons (ZGNRs) is that the boundary spin has antiferromagnetic order, that is, the directions of different boundary spins are opposite, but on the same side, the boundary spins show ferromagnetic arrangement. With a suitable applied magnetic field, we can realize the ferromagnetic order of different boundary spins^[3]. Regardless of whether different boundary carbon atoms show ferromagnetic order or antiferromagnetic order, the density of states at the Fermi plane is spin degenerate, which limits their application in spintronics. However, using a transverse electric field, we can make ZGNRs realize semi-metallic property^[4]. Here, the semi-metallic property refers to the fact that the Fermi surface shows an insulating state for one spin band structure and a metallic state for the other. In addition, the magnetic property and transport property of ZGNRs are also affected by chemical element doping or defect^[5-7]. Interestingly, some studies show that a single spin negative differential resistance is found in the boundary doped ZGNRs^[5].

In addition to voltage driving electrons or holes in materials to move at a certain direction, temperature difference can also drive electrons. More

electrons or holes are often accumulated at the high and low temperature ends, so the voltage caused by temperature difference will appear in this material. This phenomenon is called Seebeck effect. Recently, with the progress of spin detection technology, K. Uchida, *et al.* firstly observed spin voltage caused by temperature difference in metal magnets, which is called spin Seebeck effect^[8]. This pioneering experiment inspired people to theoretically study spin-related thermoelectric effects in various systems^[9-21]. Recently, we have obtained high spin polarizability and large single spin Seebeck effect at the Fermi plane by doping ferromagnetic ZGNRs with boundary non-magnetic elements^[16]. At present, a stable carbon atom chain (CAC) can be synthesized from graphene by electron irradiation technology using high-resolution transmission electron microscope^[22]. Shen, *et al.* found that the channel transport property of CACs does not depend on structural deformation, structural defects and hydrogen adsorption^[23]. Carbon-based nanostructures exhibit perfect spin filtering effect and giant magnetoresistance under near zero bias. Recently, Dong, *et al.* have studied the transport property of zigzag graphene nanoribbons connected with CACs^[24]. It is found that the electron transport near the Fermi level can be changed by adjusting the position and the number of atoms in CACs. Fano resonance effect is an interference effect existing between the local state and the extended state. It was first found in the inelastic scattering of electrons in helium. In 2002, Kobayashi, *et al.* found that the adjustable Fano effect was observed in the Aharonov-Bohm ring embedded in quantum dots^[25]. Two quantum dots can be coupled into an artificial molecule, and then the electrons will be shared by the two quantum dots. When the electron energy is close to Fano linear system, the Seebeck effect is significantly strengthened^[26].

In this paper, the spin thermoelectric property of one-dimensional spin quantum devices composed of graphene nanoribbons, carbon chains and graphene nanosheets was studied. The first principle calculation shows that the spin-down transfer function at the Fermi face is suppressed to almost zero, however, the spin-up transfer function is close to 0.25.

Therefore, we got distinct semimetal property. In addition, the phonon partial thermal conductivity in the low-temperature region is significantly smaller than the corresponding electron partial conductance. However, in the low temperature region (near 80 K), the spin Seebeck coefficient is significantly strengthened, resulting in the charge and spin thermoelectric quality factor close to 40. Moreover, in the whole temperature range ($0 < T \leq 400$ K), the spin thermoelectric quality factor is always greater than the corresponding charge thermoelectric quality factor, and becomes more obvious in the room temperature region. Therefore, this one-dimensional carbon-based nanoribbon can be designed as an ideal spin thermoelectric device.

2. Model establishment

In this paper, a one-dimensional nano double probe system as shown in **Figure 1(a)** was designed. The left electrode and the right electrode are composed of serrated graphene nanoribbons, and the boundary carbon atoms are saturated with hydrogen atoms. The central scattering region is connected by a graphene nano sheet to a zigzag graphene nanoribbon through two carbon atom chains. The width of the graphene nanoribbon is represented by the number of carbon atoms perpendicular to the transport direction. In this paper, the width is 6.

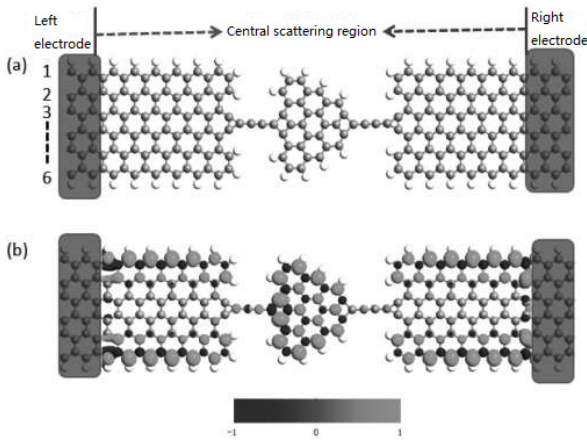


Figure 1. Thermal spin quantum double probe model and corresponding spin density.

All numerical calculations are completed based on the software package Atomistix Toolkit (ATK) of non-equilibrium Green's function and density func-

tional theory^[27-28]. The system optimization adopts Newton optimization method; the exchange correlation function adopts generalized gradient approximation (GGA), and the basis vector adopts DZP (Double-Zeta-Polarized). The size of the reduced Brillouin zone is set to (1, 1, 100). In order to avoid the interaction between images, the vacuum layer is taken as 15 Å and the truncation energy is taken as 150 Ry.

Using ATK software, the transmission coefficient of spin resolvable electrons with energy of E is:

$$\tau_{\sigma}(E) = T_r[\Gamma_{L\sigma}(E)G_{\sigma}^R(E)\Gamma_{R\sigma}(E)G_{\sigma}^A(E)] \quad (1)$$

Here, $\Gamma_{L/R\sigma}(E)$ is the linewidth function of the coupling between the central scattering region and the left/right electrode; σ is the spin index and E is the energy. $G_{\sigma}^{R(A)}(E)$ is the delayed and advanced Green's functions of the center scattering region. It can be determined by the equations

$$G_{\sigma}^r = [EI - H + i(\Gamma_{L\sigma} + \Gamma_{R\sigma})/2]^{-1} \text{ and } G_{\sigma}^A = [Gr_{\sigma}^R].$$

I is the identity matrix. H is the Hamiltonian of the central scattering region.

The spin polarizability at the Fermi plane is defined as:

$$\zeta = \frac{\tau_{\uparrow}(E) - \tau_{\downarrow}(E)}{\tau_{\uparrow}(E) + \tau_{\downarrow}(E)} \Big|_{E=E_f} \quad (2)$$

In order to study the spin thermoelectric effect, we give the expression of spin-dependent Seebeck coefficient in the linear region:

$$S_{\sigma} = -\frac{L_{1\sigma}(\mu, T)}{|e|TL_{0\sigma}(\mu, T)} \quad (3)$$

The thermal conductivity of the electronic part can be written as:

$$k_{el} = \sum_{\sigma} \left[K_{1\sigma} e S_{\sigma} + \frac{L_{2\sigma}}{T} \right]$$

Here, $L_n = \sum_{\sigma} L_{n\sigma}$, $L_{n\sigma} = -\frac{1}{h} \int dE T_{\sigma}(E) (E - \mu)^n \frac{\partial f}{\partial E}$, $n = 0, 1, 2$. $f_{L(R)}$ is the Fermi Dirac distribution function. Spin Seebeck coefficient is expressed as $S_s = (S_{\uparrow} - S_{\downarrow})/2$, and the corresponding charge Seebeck coefficient is $S_c = (S_{\uparrow} + S_{\downarrow})/2$ ^[14].

Charge (spin) thermoelectric quality factors are obtained from the following equation:

$$Z_{c(s)} T = \frac{S_{c(s)}^2 G_{e(s)} T}{\kappa_{el} + \kappa_{ph}} \quad (4)$$

$G_{e(s)}$ is the corresponding charge and spin con-

ductance, which can be obtained by the following equation:

$$G_{e(S)} = \frac{e^2}{h} (L_{0\uparrow} + (-)L_{0\downarrow}) \quad (5)$$

The phonon partial heat guide in formula (4) is available in the ATK2013 beta.

3. Results and discussion

Figure 1(b) shows that ZGNR still has boundary spin state in the buffer region, and the ferromagnetic order is maintained at the three boundaries of graphene nanosheets, that is, the spins of boundary carbon atoms are arranged in parallel. In **Figure 2(b)**, we draw the variation trend of spin resolvable transfer function with electron energy, and find a wide energy region near the Fermi plane (for example: $-0.25 \text{ eV} < E < 0.1 \text{ eV}$). The spin-up transfer function remains limited, while the spin-down transfer function is suppressed to zero. Therefore, this device shows obvious semi-metallic behavior, and the spin polarizability satisfies $\zeta = 1$. In order to reveal the physical reason behind it, we draw the spatial distribution of spin dependent local density of states at the Fermi surface in **Figures 2(c)** and **(d)**. Obviously, the spin-up local density of states is distributed in the whole central scattering region domain, including ZGNR, graphene nanosheets and carbon chains. However, the spin-down local density of states is only distributed in the ZGNR in the middle scattering region, and does not appear on carbon chains and graphene nanosheets. This result further confirmed the semi-metallic property at the Fermi plane. We also found that the spin-up Fano type tunneling spectrum appears in the -0.2 eV region below the Fermi plane, but the spin-down Fano type tunneling spectrum appears at 0.1 eV on the Fermi plane. The corresponding trend of density of state with energy shows that these Fano type tunneling spectra come from the local state in the energy region (**Figure 2(a)**). Fano resonance is formed when these local states and surrounding electronic states undergo quantum interference effect.

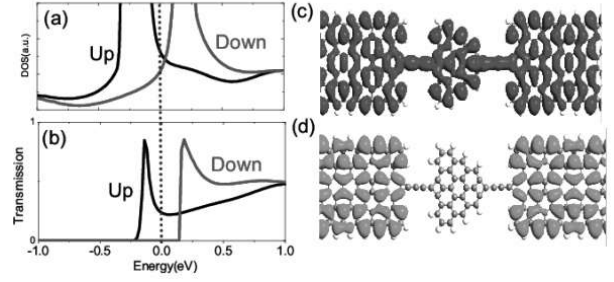


Figure 2. The spin-dependent transport property. **(a)** and **(b)** represent the variation trend of state density and transport function with the electron energy respectively, and the dashed line represents the position of the Fermi plane, letting the energy of the Fermi surface be zero. **(c)** and **(d)** indicate the local spin-up and spin-down density of states at the Fermi surface, respectively.

Fano resonance causes the transfer function to change dramatically with the electron energy, which is bound to strengthen the thermoelectric effect. Compared with other energy points, the thermoelectric performance at the Fermi surface will attract more attention of researchers. In **Figure 3(a)**, we give the change of spin-dependent Seebeck coefficient with temperature at the Fermi surface. It is found that the spin-up Seebeck coefficient is positive while the spin-down Seebeck coefficient is negative. This result can be well explained by the following equation. At low temperature, equation (3) can be simplified as:

$$S_{\sigma}(E_F) \simeq -\frac{\pi^2 k_B^2 T}{3e} [\ln \tau_{\sigma}(E)]|_{E=E_F} \quad (6)$$

This equation shows that S_{σ} at the Fermi surface is directly proportional to the negative value of the slope of the transmission probability τ_{σ} and inversely proportional to its size. At the same time, we also note that it is directly proportional to the temperature T . This equation can well explain the behavior of S_{σ} in the low temperature region ($0 < T \leq 50 \text{ K}$). However, when the temperature further increases, we find that the spin-down Seebeck coefficient is significantly strengthened, and equation (6) becomes no longer applicable. It is mainly because more nonlinearity participates in the contribution to the spin Seebeck coefficient at high temperature^[29]. In order to calculate the charge and spin thermoelectric quality factors, in **Figure 3(b)**, we give the contribution of the

electron and phonon part to the thermal conductivity. The thermal conductivity contributed by the phonon part κ_{ph} and the thermal conductivity contributed by the electron part κ_{el} increase monotonically with the increase of temperature.

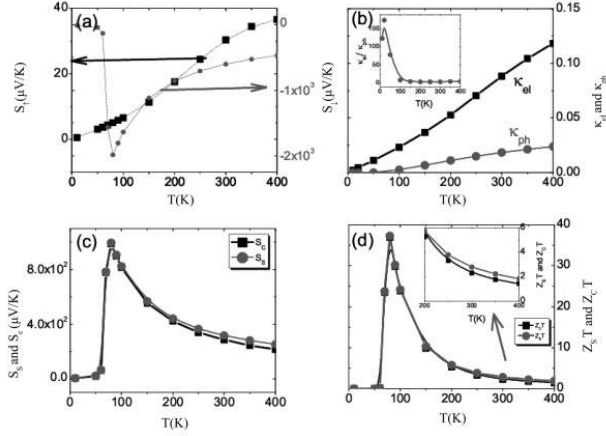


Figure 3. Spin-dependent thermoelectric property. (a) Spin-dependent Seebeck coefficients; (b) Electron and phonon partial thermal conductivity; (c) Charge and spin Seebeck coefficients; (d) Trend of spin and charge thermoelectric quality factors with temperature.

Moreover, it is important that the thermal conductivity of the phonon part is significantly lower than that of the electronic part, especially in the low temperature region ($T < 100$ K), and the thermal conductivity of the phonon part is one percent of the electronic part (See the embedded diagram in **Figure 3(b)**). Interestingly, the spin-down Seebeck coefficient is significantly strengthened near the temperature of 80 K, and the maximum value even reaches 2000 $\mu\text{V/K}$. The charge Seebeck coefficient S_c and spin Seebeck coefficient S_s are also significantly strengthened near the temperature of 80 K. In the high temperature region (near room temperature), we find that the value S_s is significantly larger than S_c , which indicates that the spin thermoelectric effect is significantly stronger than the corresponding charge thermoelectric effect. In **Figure 3(d)**, we show the variation trend of spin thermoelectric quality factor $Z_s T$ and charge thermoelectric quality factor $Z_c T$ with temperature T . The results show that their maximum value is close to 40, and the sizes of $Z_s T$ and $Z_c T$ are the same in the whole temperature region. Generally speaking, if the thermoelectric quality factor is great-

er than 3, it is considered that the material has high thermoelectric efficiency. It can be used as an ideal thermoelectric material. More interestingly, in the high temperature region (room temperature region), $Z_s T$ is significantly larger than $Z_c T$, and $Z_s T$ is close to 3. This shows that this double probe model with carbon atoms can be used as an ideal thermoelectric device at room temperature.

4. Conclusion

We designed a one-dimensional spin quantum device composed of graphene nanoribbons, carbon chains and graphene nanosheets. It is found that the spin-down transfer function at the Fermi surface is almost suppressed to zero, while the spin-up transfer function is close to 0.25, so it has obvious semi-metallic property. In addition, we also found that in this device, the thermal conductivity of the phonon part is significantly smaller than the corresponding electronic partial conductance. In the low temperature region, the phonon partial thermal conductance is only one percent of the electronic partial thermal conductance. However, in the low temperature region (near 80 K), the spin Seebeck coefficient is significantly strengthened, resulting in the charge or spin quality factor close to 40. Moreover, in the whole temperature range ($0 < T \leq 400$ K), the spin thermoelectric quality factor is always greater than the corresponding charge thermoelectric quality factor, and this effect becomes more obvious at room temperature. Therefore, this one-dimensional carbon-based nanoribbon can be used to design ideal spin thermoelectric devices at room temperature.

Conflict of interest

The authors declare that they have no conflict of interest.

Acknowledgements

National Natural Science Foundation of China “Research on theory and application of molecular thermoelectric devices” (11247028).

References

1. Novoselov KS, Geim AK, Morozov SV. Electric field effect in atomically thin carbon films. *Science* 2004; 306: 666–669.
2. Son Y, Cohen ML, Louie SG. Energy gaps in graphene nanoribbons. *Physical Review Letters* 2007; 98(8).
3. Xu C, Luo G, Liu Q, *et al.* Giant magnetoresistance in silicene nanoribbons. *Nanoscale* 2012; 4: 3111–3117.
4. Son Y, Cohen ML, Louie SG. Half-metallic graphene nanoribbons. *Nature* 2006; 444: 347.
5. Wu T, Wang X, Zhai M, *et al.* Negative differential spin conductance in doped zigzag graphene nanoribbons. *Applied Physical Letters* 2012; 100(5): 2112.
6. Maunárriz J, Gaul C, Malyshev AV, *et al.* Strong spin-dependent negative differential resistance in composite graphene superlattices. *Physical Review B Condensed Matter* 2012; 88(15): 5423.
7. Jiang C, Wang X, Zhai M. Spin negative differential resistance in edge doped zigzag graphene nanoribbons. *Carbon an International Journal Sponsored by the American Carbon Society* 2014; 68: 406.
8. Uchida K, Takahashi S, Harii K, *et al.* Observation of the spin Seebeck effect. *Nature* 2008; 455: 778.
9. Dubi Y, Di Ventra M. Thermo-spin effects in a quantum dot connected to ferromagnetic leads. *Physical Review B Condensed Matter* 2009; 79(8): 1302(R).
10. Jaworski CM, Yang J, Mack S, *et al.* Observation of spin-Seebeck effect in a ferromagnetic semiconductor. *Nature Mater* 2010; 9: 898.
11. Uchida K, Adachi H, *et al.* Long-range spin Seebeck effect and acoustic spin pumping. *Nature Mater* 2011; 10: 737.
12. Adachi H, Ohe J, Takahashi S, *et al.* Linear-response theory of spin Seebeck effect in ferromagnetic insulators. *Physical Review B* 2011; 83(9): 4410.
13. Dubi Y, Di Ventra M. Colloquium: Heat flow and thermoelectricity in atomic and molecular junctions. *Review of Modern Physics* 2011; 83: 131.
14. Liu Y, Chi F, Yang X, *et al.* Pure spin thermoelectric generator based on a rashba quantum dot molecule. *Journal of Applied Physics* 2011; 109(5): 3712.
15. Liu Y, Yang X, Chi F, *et al.* A proposal for time-dependent pure-spin-current generators. *Applied Physics Letters* 2012; 101(21): 3109.
16. Liu Y, Wang X, Chi F. Non-magnetic doping induced a high spin-filter efficiency and large spin Seebeck effect in zigzag graphene nanoribbons. *Journal of Materials Chemistry C* 2013; 2013(1): 3756–3776.
17. Yang X, Liu Y, Zhang X, *et al.* Perfect spin filtering and large spin thermoelectric effects in organic transition-metal molecular junctions. *Physical Chemistry Chemical Physics Cambridge Royal Society of Chemistry* 2014; 16: 11349–11357.
18. Liu Y, Zhang X, Wang X, *et al.* Spin-resolved Fano resonances induced large spin Seebeck effects in grapheme carbon-chain junctions. *Applied Physics Letters* 2014; 104(24): 2412.
19. Yang X, Liu Y, Wang X, *et al.* Large spin Seebeck effects in zigzag-edge silicene nanoribbons. *Aip Advances* 2014; 4(8): 7116.
20. Yang X, Zhang X, Hong X, *et al.* Temperature-controlled giant thermal magnetoresistance behaviors in doped zigzag edged silicene nanoribbons. *Rsc Advances* 2014; 4: 48539–48546.
21. Yang X, Zhou W, Hong X, *et al.* Half-metallic properties, single-spin negative differential resistance, and large single spin Seebeck effects induced by chemical doping in zigzag-edged graphene nanoribbons. *The Journal of Chemical Physics* 2015; 142(2): 4706.
22. Jin C, Lan H, Peng L, *et al.* Deriving carbon atomic chains from graphene. *Physical Review Letters* 2009; 102(20): 5501.
23. Shen L, Zeng M, Yang S, *et al.* Electron transport properties of atomic carbon nanowires between graphene electrodes. *Journal of the American Chemical Society* 2010; 132: 11481–11486.
24. Dong Y, Wang X, Zhai M, *et al.* Half-metallicity in aluminum-doped zigzag silicene nanoribbons. *The Journal of Physical Chemistry C* 2013; 117(37): 18845–18850.
25. Kobayashi K, Aikawa H, Katsumoto S, *et al.* Tuning of the Fano effect through a quantum dot in an Aharonov-bohm Interferometer. *Physics Review Letters* 2002; 88: 256806.
26. Liu Y, Yang X. Enhancement of thermoelectric efficiency in a double-quantum-dot molecular junction.

- Journal of Applied Physics 2010; 108(2): 3710.
27. Taylor T, Guo H, Wang J. Ab initio modeling of quantum transport properties of molecular electronic devices. *Physical Review B* 2001; 63(24): 5407.
 28. Brandbyge M, Mozos JL, Ordejon P, *et al.* Density-functional method for non-equilibrium electron transport. *Physical Review B, Condensed Matter* 2002; 65(16): 5401.
 29. Yang X, Liu Y. Pure spin current in a double quantum dot device generated by thermal. *Journal of Applied Physics* 2013; 113(16): 4310.

ORIGINAL RESEARCH ARTICLE

Study on synthesis and adsorption property of porous carbon/Ni nanoparticle composites

Sailu Xu¹, Yuxin Du¹, Meiqi Hui¹, Zichen Wang¹, Junfeng Zhao^{1,2*}, Gang Yang^{1,2}

¹ School of Materials Engineering, Changshu Institute of Technology, Changshu 215500, Jiangsu Province, China.

E-mail: jfzhao@cslg.edu.cn

² Suzhou Key Laboratory of Functional Ceramic Materials, Changshu 215500, Jiangsu Province, China

Abstract

The porous carbon/Ni nanoparticle composite was prepared by a freeze-drying method using NaCl as the template. It was applied in the effect of the concentration, adsorption time, and temperature of adsorption on the adsorption behavior. The kinetic model and the adsorption isothermic fitting results show that the adsorption behavior fits with the pseudo-secondary dynamics and the Langmuir isothermal model, indicating that the adsorption process is monolayer adsorption. Thermodynamic results indicate that the adsorption process is spontaneous physicochemical adsorption. The fitting showed that the porous carbon/Ni nanoparticle composites reach 217.17 mg·g⁻¹, at 313 K indicates good adsorption for Congo red.

Keywords: Porous Carbon; Magnetic; Congored; Adsorption Performance

ARTICLE INFO

Received: 3 December 2020

Accepted: 23 January 2021

Available online: 30 January 2021

COPYRIGHT

Copyright © 2021 Sailu Xu, et al.

EnPress Publisher LLC. This work is licensed under the Creative Commons Attribution-NonCommercial 4.0 International License (CC BY-NC 4.0).

<https://creativecommons.org/licenses/by-nc/4.0/>

1. Introduction

With the steady development of the economy and the deepening of industrialization, dye wastewater has become an urgent pollution problem^[1]. The adsorption method is simple and highly efficient. Porous carbon material (porous carbon material) is a porous material with carbon as the main body, which has the advantages of large than surface area, developed pores, good chemical stability, and a wide source of raw materials, rich resources, low price, and simple production process, which can carry out large-scale production. Therefore, it is widely used in energy storage and conversion, catalytic and macromolecular adsorption, and is favored by researchers at home and abroad^[2,3]. According to the internationally recognized definition, porous carbon can be divided into three types: microporous carbon material (< 2 nm), iterporous carbon material (between 2–50 nm), porous carbon material (> 50 nm). In recent years, research has found that a single type of hole structure material cannot meet the market demand of high performance and high efficiency. Therefore, artificial transformation and design of porous carbon according to performance and application requirements has become a hot research topic, and the development and application of multiporous carbon materials have emerged^[4,5]. In terms of sewage treatment, although porous carbon has the advantages of large than surface area and good adsorption performance when porous carbon is added to sewage for adsorption, it will be dispersed in water and cannot be

recycled, which leads to waste of resources and cost increase.

In this paper, porous carbon/Ni nanoparticle complexes were prepared by the freeze-drying method, using water-soluble inorganic salt NaCl as a template. The effect of adsorbent dosage, adsorption time, and temperature on the adsorption properties of porous carbon/Ni nanoparticle composites was investigated respectively, and the adsorption behavior of porous carbon/Ni nanoparticle composite is analyzed using kinetic and isothermic models.

2. Experiment

2.1 Preparation of porous carbon/Ni nanoparticle composites

0.003 mol $\text{Ni}(\text{NO}_3)_2 \cdot 6\text{H}_2\text{O}$ and 4 g NaCl, were dissolved in 20 mL deionized water, quantity 10 mL egg white was added to the above solution, stirred with a magnetic mixer for 30 min, and mixing evenly for standby. The mixture liquid is frozen in liquid nitrogen for 10 min to completely frozen, and the vacuum sublimation treatment for 48 h is removed to completely sublimate the water. Frozen dried samples were removed and placed into the crucible. The heat-treated samples were removed at 650 °C for 3 h. In N_2 atmosphere, ground dispersed in a certain amount of deionized water, the NaCl template was sonicated, and the samples were then extracted and separated, repeated to fully remove inorganic salt 3 times. The aspirated/Ni nanoparticle-washed samples were prepared by drying in a 60 °C vacuum drying tank for 8 h, to obtain a porous carbon/Ni nanoparticle composite.

2.2 Characterization of the material topography and structure

The structure was analyzed by the X-ray diffraction instrument (XRD), the scanning electron microscopy (SEM, SIGMA, 20 kV) and high-resolution transmission electron microscopy (HRTEM, JEOL-2000 CX, 200 kV), and the specific surface area and aperture size analyzer (BET) were used to analyze the specific surface area and pore structure.

2.2 Characterization of the adsorption properties

The sorbent properties of porous carbon/Ni nanoparticle composites were determined using a TU-1901 UV spectrophotometer. The adsorption properties of the adsorbent were studied, using Congo Red (CR) as a pollutant model, at 20, 40, 60, 80, 100 mg/L concentrations. A solution of CR at 40 mg/L and investigated the effects of different temperatures (298, 303, 308, 313 K) on the adsorption properties. All the above experiments were performed at $200 \text{ r} \cdot \text{min}^{-1}$ oscillations, with 5 mL mixed solution at 15 min, 30 min, 1 h, 2 h, 3 h, placed into a centrifuge tube, centrifugation for 5 min, and the remaining CR concentration was tested using a UV spectrophotometer.

3. Results and discussions

Figure 1 shows the XRD map of the prepared porous carbon/Ni nanoparticle composite, showing three sharp diffraction peaks at 2θ at 42.2°, at 51.9° and 76.2°, corresponding to (111), (200), (220) crystal surface diffraction of Ni (PDF#65-0380), respectively. Furthermore, a bulging, relatively weak diffraction peak was observed at 2θ of 25.6°, analyzed corresponding to the characteristic diffraction peak of amorphous carbon. No other miscellaneous peaks were observed, indicating that there was no impurity phase in the composite product. XRD results show that the products prepared by freeze drying-carbonization are C/Ni composite, the carbon component in protein converted to carbon material by high temperature thermolysis; nickel nitrate generates nickel oxide by high temperature, the temperature increases further, nickel oxide by carbon reduction generates magnetic nanoparticle, and eventually form porous carbon/magnetic Ni nanoparticle composite material.

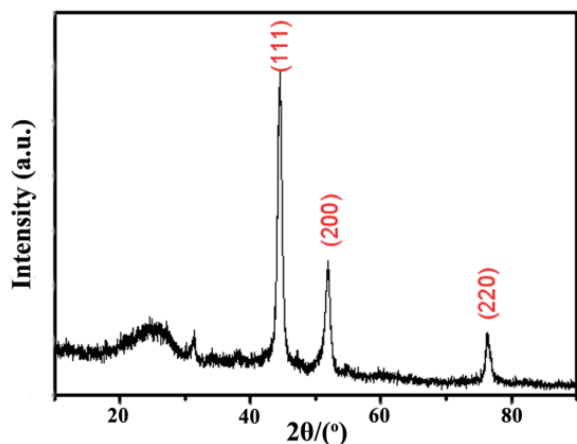


Figure 1. XRD plot of the porous carbon/Ni nanoparticle composites.

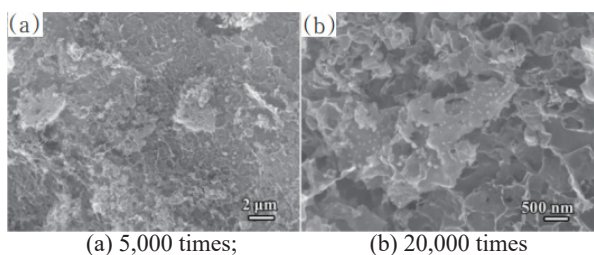


Figure 2. XRD diagram of porous carbon /Ni nanoparticle composites.

As can be seen from **Figure 2**, the material prepared by freeze-drying-carbonization presents a 3D structure similar to the block material of “frozen tofu”. Further observation found that the surface of 3D carbon material presents irregular sheet structure, in layer by layer pit gully successively filled with holes from large to small. It is believed that during the reaction precursor of liquid nitrogen freezing, NaCl cubic crystal and nickel nitrate crystal precipitate out rapidly with the sharp drop of temperature, and a large number of NaCl cubic crystal particles are self-stacked to form a 3D structure. Nickel nitrate crystals are distributed in the 3D structure, and the proteins in the precursor are also precipitated with decreasing temperature and coated in the surface of the NaCl cubic crystals. Further vacuum sublimation drying completely removes the water from the system, thus forming a protein/nickel nitrate/NaCl composite powder product. Complex powder at high temperature in an inert atmosphere, NaCl structure remains stable at high temperature, the protein carbonization on the surface is transformed into carbon material, and nickel nitrate forms nanoparticles by

decomposition and reduction reaction and nanoparticles. The product, removed from the NaCl template with simple washing, forming a honeycomb porous carbon structure with more evenly distributed dimensions, interconnected and interconnected.

Figure 3(a)–Figure 3(c) is a TEM plot of porous carbon/Ni nanoparticle complexes. It can be seen that the sample has a 3D structure of which the matrix is the porous carbon. The porous carbon structure is filled with high-density, ultra-fine nickel nanoparticles with a size of approximately 30 nm. The HRTEM plot of **Figure 3(d)** shows a distinct crystal surface orientation in the local region, corresponding to the crystal surface spacing of Ni in the composite, covered with helminth-like disordered ripples of the nickel, corresponding to the amorphous carbon layer. This result is consistent with the XRD results, indicating that nanoparticles distributed in graded porous carbon form a composite structure.

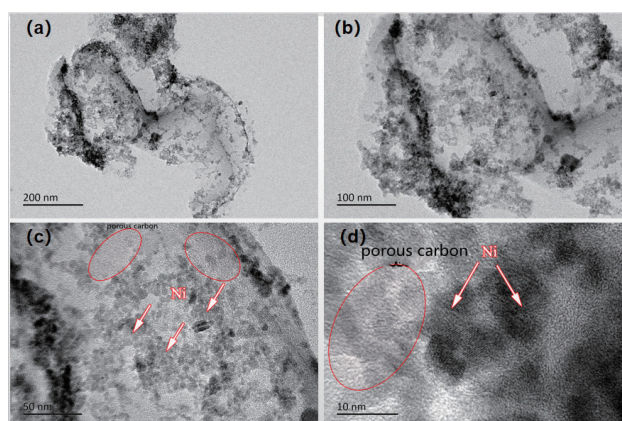


Figure 3. (a) (b) (c) TEM figures of multiwell carbon/Ni nanoparticle composites and (d) HRTEM figure.

According to the BET adsorption/desorption of **Figure 4(a)** porous carbon/Ni nanoparticle composite, the sample presents a I/IV mixed adsorption model indicating the presence of a hierarchical porous structure of the material. First, the significant uptrend at $P/P_0 < 0.01$ was attributed to type I isotherms, indicating the presence of a micropore structure in the structure. At $P/P_0 = 0.4–0.9$, there is a distinct suction attachment hysteresis loop in the relative pressure range, in line with the IV isothermic model, showing a large number of interpore structures in the structure. Besides, when $P/P_0 > 0.9$, the adsorption/desorption is further increased,

indicating that large pore structures still exist in the structure^[6-7]. Therefore, the material prepared in this experiment is a graded porous structure. The analysis of Brunauer-Emmett-Teller (BET) showed that the specific surface area of porous carbon/Ni nanoparticle composites is up to $511.532 \text{ m}^2 \cdot \text{g}^{-1}$. The aperture distribution curves of the sample are further given in **Figures 4(b)** and **4(c)**, and Barrett-Joyner-Halenda (BJH) and Dubinin Radushkevich (DR) analysis showed that the sample showed a distinct aperture distribution in both the 2–30 nm and the micropore region of 0–2 nm. By the observation, we know that the distribution of pore diameter is relatively concentrated, and the mesopore mostly concentrated around 5 nm and the micropore around 0.3 nm, further proving that the sample has a better graded porous structure. Among them, the total adsorption pore volume was $0.938 \text{ cm}^3 \cdot \text{g}^{-1}$, BJH adsorption cumulative interpore and total pore volume were $0.859 \text{ cm}^3 \cdot \text{g}^{-1}$,

DR method micropore ($< 2 \text{ nm}$) volume was $0.236 \text{ cm}^3 \cdot \text{g}^{-1}$.

Figure 5 shows plots of the adsorption properties of Congo red dye in porous carbon/Ni nanoparticle composites at 298, 303, 308, 313 K. As can be seen from the figure, the adsorption curve rises sharply when the adsorption time is within 60 min, and then tends to be flat. It shows that the adsorption tends to achieve saturation at 60 min. The intercepted 60 min time point and the adsorption concentration are $40 \text{ mg} \cdot \text{L}^{-1}$ (in the order of temperature rise), respectively, are 105.37, 124.37, 158.52, $163.87 \text{ mg} \cdot \text{g}^{-1}$, indicating that the adsorption amount will increase as the temperature increases (the increase rate is gradually slowed and reaches saturation at a temperature). It shows that as the temperature increases, the concentration of the adsorption matter will also affect the size of the adsorption quantity.

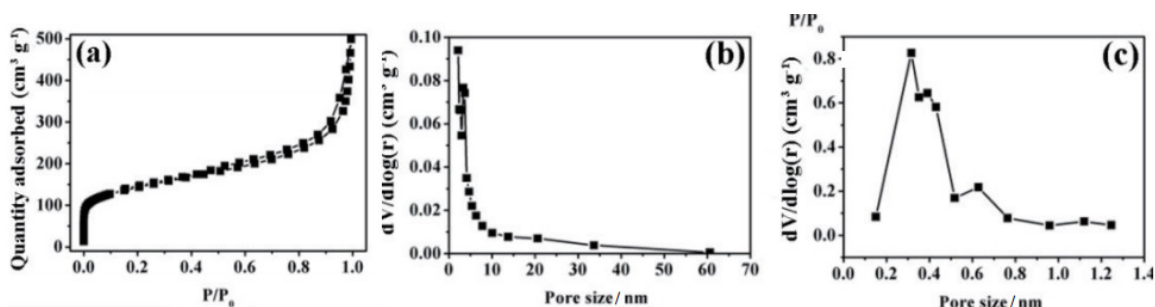


Figure 4. Diagram of BET and aperture distribution of Porous carbon/Ni nanoparticle composites. (a) BET adsorption/detachment map; (b) distribution map of interpore aperture map; (c) micropore aperture distribution map.

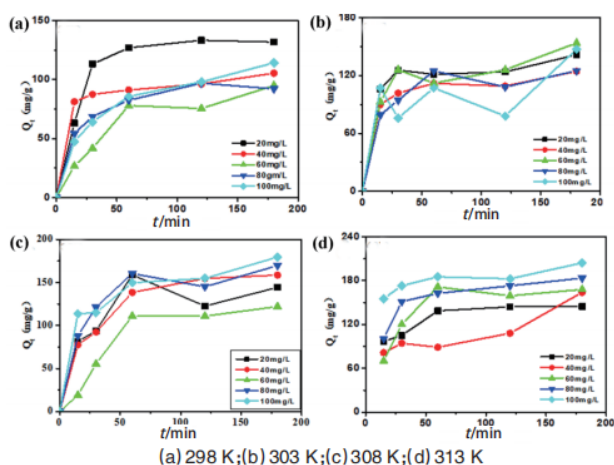


Figure 5. Effects of different temperatures on the adsorption properties.

To further explore the adsorption behavior of

porous carbon/Ni nanoparticle composites on the organic dye Congo red, a pseudo-second-order kinetic model was used to fit the adsorption data at different temperatures, with the exact formula shown in equation (1)^[8].

$$\frac{t}{q_t} = \frac{1}{k_2 q_e^2} + \frac{t}{q_e} \quad (1)$$

The q_e , q_t ($\text{mg} \cdot \text{g}^{-1}$) represent the adsorption capacity of t (min) at equilibrium and at some time, respectively; k_2 represents the pseudo-second-order rate constant ($\text{g} \cdot \text{mg}^{-1} \cdot \text{min}^{-1}$).

Figures 6(a)–Figure 6(d) shows a pseudo-fitting second-order nonlinear fitting curve for the adsorption behavior of porous carbon/Ni nanoparticle

Table 1. The fitting parameters of pseudo-second order dynamics of porous carbon/Ni nanoparticle composites to Congo red adsorption

Temperature /K	C ₀ / (mg · L ⁻¹)	Parameters of Pseudo-kinetic model		
		k ₂ / (g · mg ⁻¹ · min ⁻¹)	q _{e, cal} / (mg · g ⁻¹)	R ²
298	20	0.080 6	104.65	0.992 6
	40	0.074 3	107.41	0.994 7
	60	0.414 7	117.10	0.950 1
	80	0.122 2	117.70	0.994 2
	100	0.231 6	119.53	0.991 1
303	20	0.086 2	147.06	0.986 1
	40	0.064 9	125.79	0.989 6
	60	0.096 7	159.74	0.965 5
	80	0.071 4	127.23	0.982 7
	100	0.153 4	150.60	0.901 3
308	20	0.079 9	149.48	0.964 5
	40	0.121 6	179.53	0.994 9
	60	0.010 0	176.06	0.997 7
	80	0.079 4	177.30	0.988 0
	100	0.085 9	189.04	0.985 9
313	20	0.063 2	153.85	0.997 6
	40	0.203 3	170.94	0.824 7
	60	0.089 6	184.84	0.984 9
	80	0.060 7	193.80	0.998 2
	100	0.033 4	206.19	0.992 3

complexes at 298, 303, 308, 313 K temperatures. The kinetic parameters (k_2 and q_e) and regression coefficients (R^2) of the fitted model are shown in **Table 1**. For all four adsorption temperatures, the experimental data agree with the regression coefficients (R^2 substantially above 0.99) at all initial concentrations. From these R^2 values, the model of quasi-second order is suitable to describe the adsorption kinetic behavior. The pseudo-second-order model calculations agree well with the experimental observations. These results confirm that chemical adsorption is a rate control step and depends on the concentration of contaminants exposed to the surface of the porous carbon/Ni nanoparticle composite materials^[9]. Furthermore, the maximum adsorption of the Congo red dye at 100 mg · L⁻¹ by the porous carbon/Ni nanoparticle composite at 298, 303, 308, 313 K was 119.53, 150.60, 189.04, and 206.19 mg · g⁻¹, respectively.

The interaction of adsorbent with adsorbate describes as adsorption isotherms. The well-known model Langmuir isotherm describes the adsorption process.

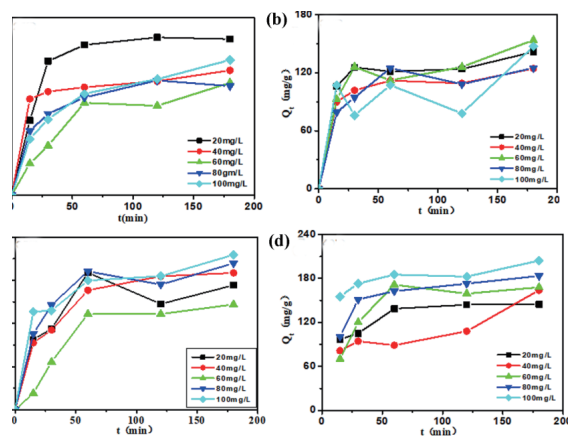


Figure 6. Fof pseudo-second-order dynamics of the adsorption process.

Langmuir isotherms are based on single-molecule adsorption processes, commonly used to describe equilibrium adsorption isotherms on homogeneous surfaces. The isothermal model can represent as Equation (2)^[10,11].

$$q_e = \frac{q_m K_L C_e}{1 + K_L C_e} \quad (2)$$

C_e is the equilibrium concentration of the solute (mg · L⁻¹); q_e indicates the adsorption amount

($\text{mg}\cdot\text{g}^{-1}$) at equilibrium; q_m is the maximum adsorption amount ($\text{mg}\cdot\text{g}^{-1}$); and K_L indicates the Langmuir adsorption constant (g^{-1}). **Figure 7** shows the fit diagram of the Langmuir isothermal model. The relevant parameters obtained from the isothermal model fitting listed in **Table 2** show that the regression coefficient R^2 is above 0.9 at different adsorption temperatures, saying that the bright Muir model can well describe the adsorption behavior of porous carbon/Ni nanoparticle composite adsorption agent. The isothermal fitting showed that the porous carbon/Ni nanoparticle composite is monolayer adsorption, and the adsorption is in a monolayer. Once the adsorption cannot be further at that position once the dye molecule occupies the active site on the magnetic porous carbon surface^[12]. By the fitting calculation, we can get that the maximum adsorption of Congo red by the porous carbon/Ni nanoparticle composite was 123.10, 144.95, 197.53, and 217.17 $\text{mg}\cdot\text{g}^{-1}$ at 298, 303, 308, 313 K, respectively.

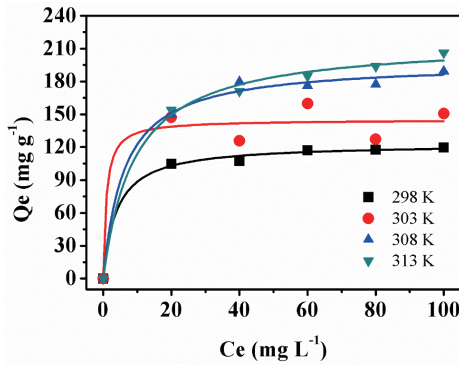


Figure 7. A fitting of the Langmuir isothermic model for the adsorption process.

Table 2. Langmuir fitting parameters for the isotherm model

T/K	Langmuir		
	$q_m/(\text{mg}\cdot\text{g}^{-1})$	$K_L/(\text{L}\cdot\text{mg}^{-1}) \times 10^3$	R^2
298	123.10	0.254 9	0.996 7
303	144.95	0.111 1	0.948 1
308	197.53	0.163 1	0.995 1
313	217.17	0.110 4	0.994 7

To further evaluate the effect of temperature on the adsorption properties of porous carbon/Ni nanoparticles composites, thermodynamic parameters, including enthalpy (ΔH°), Gibbs free energy (ΔG°), and entropy (ΔS°) were calculated, with the

specific equations of:

$$\Delta G^\circ = -RT \ln K \quad (3)$$

$$\ln K = \frac{-\Delta H^\circ}{RT} + \frac{\Delta S^\circ}{R} \quad (4)$$

R is the gas constant ($8.314 \text{ J}\cdot\text{mol}^{-1}\cdot\text{K}^{-1}$), T indicates the temperature (K), and K is the adsorption equilibrium constant. **Figure 8** shows a linear plot of $\ln K$ and $1/T$. The specific values of the thermodynamic parameter enthalpy (ΔH°), Gibbs free energy (ΔG°), and entropy (ΔS°) are calculated by fitting shown in **Table 3**.

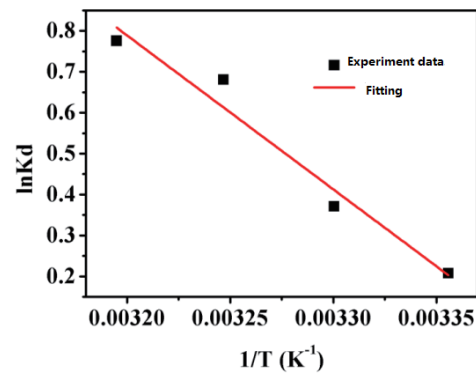


Figure 8. Linear plot between $\ln K$ and $1/T$.

Table 3. Specific values for the enthalpy of thermodynamic parameters (ΔH°), Gibbs free energy (ΔG°), and entropy (ΔS°)

T/K	$\Delta G^\circ/(\text{kJ}\cdot\text{mol}^{-1})$	$\Delta H^\circ/(\text{kJ}\cdot\text{mol}^{-1})$	$\Delta S^\circ/(\text{kJ}\cdot\text{mol}^{-1}\cdot\text{K}^{-1})$
298	-0.51		
303	-0.94		
308	-1.74	31.25	0.11
313	-2.02		

From **Table 3**, all of the ΔG° value is negative, indicating that the Congo red adsorption of the porous carbon/Ni nanoparticle composite is a spontaneous process. The ΔG° tends to decrease with the increasing temperature, which indicates that the increased temperature is favorable for adsorption. ΔH° and ΔS° are all positive, which indicates that the adsorption of porous carbon/Ni nanoparticle composite to Congo red has exothermic properties^[13]. ΔH° is $31.25 \text{ kJ}\cdot\text{mol}^{-1}$, higher than physical adsorption heat ($2.1\text{--}20.9 \text{ kJ}\cdot\text{mol}^{-1}$) and less than chemical adsorption heat ($80\text{--}200 \text{ kJ}\cdot\text{mol}^{-1}$), indicating that the adsorption of porous carbon/Ni nanoparticle composite belongs to a physicochemical adsorption process^[14].

4. Conclusion

The porous carbon/Ni nanoparticle composites synthesized by a freeze-drying method by NaCl as a template. SEM and TEM showed that Ni nanoparticles equably distributed on porous carbon carriers, which constructed into a 3D-graded porous structure. The BET and pore size distribution results show that the porous carbon/Ni nanoparticle composite is a graded porous structure composed of large holes, meshholes and micropores, with $511.532 \text{ m}^2 \cdot \text{g}^{-1}$ and $0.938 \text{ cm}^3 \cdot \text{g}^{-1}$. Compared to the surface area and the total adsorption pore volume, respectively, making the porous carbon/Ni nanoparticle composite has excellent adsorption properties. The kinetic and thermodynamic results show that the adsorption behavior, which is the composite materials to the organic pollutant Congo red, accords with the pseudo-secondary dynamics and Langmuir isothermal model. And it is with a maximum adsorption amount of $217.17 \text{ mg} \cdot \text{g}^{-1}$ at 313 K.

Conflict of interest

The authors declare that they have no conflict of interest.

References

1. Lu Y, Song S, Wang R, *et al.* Impacts of soil and water pollution on food safety and health risks in China. *Environment International* 2015; 77: 5–15.
2. Chen B, Ma Q, Tan C, *et al.* Carbon-based sorbents with three-dimensional architectures for water remediation. *Small* 2015; 11(27): 3319–3316.
3. De S, Balu AM, Van Der Wall JC, *et al.* Biomass-derived porous carbon materials: synthesis and catalytic applications. *ChemcatChem* 2015; 7(11): 1608–1629.
4. Sevilla M, Ferrero GA, Fuertes AB. One-pot synthesis of biomass-based hierarchical porous carbons with a large porosity development. *Chemistry of Materials* 2017; 29(16): 6900–6907.
5. Liu R, Liu Y, Zhou X, *et al.* Biomass-derived highly porous functional carbon fabricated by using a free-standing template for efficient removal of methylene blue. *Bioresource Technology* 2014; 154: 138–147.
6. Gupta K, Gupta D, Khatri OP. Graphene-like porous carbon nanostructure from Bengal gram bean husk and its application for fast and efficient adsorption of organic dyes. *Applied Surface Science* 2019; 476: 647–657.
7. Song Y, Wei G, Kopec M, *et al.* Copolymer-templated synthesis of nitrogen-doped mesoporous carbons for enhanced adsorption of hexavalent chromium and uranium. *ACS Applied Nano Materials* 2018; 6(1): 2536–2543.
8. Ho YS, McKay G. Pseudo-second order model for sorption processes. *Process Biochemistry* 1999; 34(5): 451–465.
9. Pour ZS, Ghaemy M. Removal of dyes and heavy metal ions from water by magnetic hydrogel beads based on poly (vinyl alcohol)/ carboxymethyl starch-g-poly (vinyl imidazole). *RSC Advance* 2015; 5: 64106–64118.
10. Hemmati F, Norouzbeigi R, Sarbisheh F, *et al.* Malachite green removal using modified sphagnum peat moss as a low-cost biosorbent: kinetic, equilibrium and thermodynamic studies. *Journal Taiwan Institute of Chemical Engineers* 2016; 58: 482–489.
11. Liu Y, Xu H. Equilibrium, thermodynamics and mechanisms of Ni^{2+} biosorption by aerobic granules. *Biochemistry Engineering Journal* 2007; (35): 174–182.
12. Cheng B, Le Y, Cai W, *et al.* Synthesis of hierarchical $\text{Ni}(\text{OH})_2$ and NiO nanosheets and their adsorption kinetics and isotherms to Congo red in water. *Journal of Hazardous Materials* 2011; 185(2-3): 889–897.
13. Zhao J, Zha J, Yang C, *et al.* Cauliflower-like Ni/NiO and NiO architectures transformed from nickel alkoxide and their excellent removal of Congo red and Cr(VI) ions from water. *RSC Advance* 2016; 6: 103585–103593.
14. Liu S, Ding Y, Li P, *et al.* Adsorption of the anionic dye Congo red from aqueous solution onto natural zeolites modified with N, N-dimethyl dehydroabietylamine oxide. *Chemical Engineering Journal* 2014; 248: 135–144.

ORIGINAL RESEARCH ARTICLE

A study of electrocatalytic ethanol oxidation of nanoporous PtSi alloy

Nali Lu^{1,3}, Yao Li^{2,3}, Lei Zhang^{3,4}, Yong Fang^{3,4}, Bin Qian^{3,4}, Zhida Han^{3,4*}, Xuefan Jiang^{3,4}

¹ School of Materials Science and Engineering, China University of Mining and Technology, Xuzhou 221116, China

² College of Chemistry, Chemical Engineering and Materials Science, Soochow University, Suzhou 215123, China

³ School of Physics and Electronic Engineering, Changshu Institute of Technology, Changshu 215500, China. E-mail: han@cslg.edu.cn

⁴ Jiangsu Key Laboratory of Advanced Functional Materials, Changshu 215500, China

ABSTRACT

In recent years, nanoporous alloys have presented the advantages of a large specific surface area, low density, and simple operation, and they have been widely used in the fields of catalysis, magnetism, and medicine. Nanoporous Pt-Si alloy was prepared by melt-spun and chemical dealloying, and was characterized by X-ray diffraction, X-ray photoelectron spectroscopy, scanning electron microscope, and transmission electron microscopy. Pt-Si alloys possess a three-dimensional bicontinuous structure and an average size of 5 nanometers. Compared with commercial Pt/C catalysts, nanoporous Pt-Si alloys exhibit excellent electrocatalytic activity and stability in ethanol-catalyzed oxidation reactions. It is taken into consideration to be a promising catalyst in direct ethanol fuel cells.

Keywords: Dealloying; Nanoporous; Electrocatalysis; Ethanol Oxidation Reaction

ARTICLE INFO

Received: 14 December 2020

Accepted: 3 February 2021

Available online: 10 February 2021

COPYRIGHT

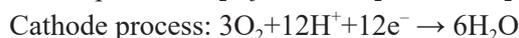
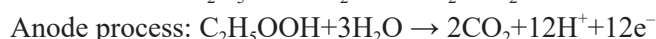
Copyright © 2021 Nali Lu, *et al.*

EnPress Publisher LLC. This work is licensed under the Creative Commons Attribution-NonCommercial 4.0 International License (CC BY-NC 4.0).

<https://creativecommons.org/licenses/by-nc/4.0/>

1. Introduction

The fuel cell is an energy conversion device, which can directly convert the energy generated by fuel through chemical reactions into electric energy, and only water is generated in the entire process^[1]. A fuel cell combines the best characteristics of an internal combustion engine and battery, like an internal combustion engine that can run only with fuel without any mechanical conversion process. Fuel cells are similar to those under load conditions^[2]. Direct ethanol fuel cell (DEFC) uses ethanol as fuel, which has attracted more and more attention. Ethanol, as a small alcohol organic molecule, converts the chemical energy into electrical energy, has higher capacity density, low toxicity, and is convenient for storage and transportation, as well as the advantages of large-scale preparation of biomass products, it is widely used in mobile devices such as automobiles, mobile phones and computers^[3-5]. The research of Wang *et al.*^[6] shows that the permeability of ethanol through the electrolytic membrane is lower than that of methanol. Under acidic conditions, the reaction process of ethanol is as follows:



The reaction mechanism of ethanol is very complex, involving 12 e transfers, accompanied by the fracture of the C-C bond, the interme-

diated products dominated by COads are generated, which gather on the surface of the catalyst and produce poisoning phenomenon that reduces the activity of the catalyst. In practical application, the catalytic oxidation of ethanol requires a high overpotential. Therefore, developing new anode catalysts with high activity and high stability has become a research hotspot. The existing research shows that the improvement of the performance of Pt-based catalysts is due to the shortening of Pt metal bonds, the enhancement of bond energy, and the easier adsorption of oxygen after alloying; the microstructure between materials is changed, the alloying effect of different elements, the specific surface area increases, and the active sites increase. To mix Pt with other non-noble metals^[7-9], and the microstructure of Pt is optimized to prepare nano Pt catalyst with controllable morphology^[10], which can prevent the aggregation of Pt particles due to the synergistic effect between bimetallic metals and is helpful to improve the stability of the catalyst^[11,12].

Based on the different properties of different elements, the dealloying method uses chemical or electrochemical methods^[13] to remove the more active components in the alloy. Then the remaining components finally obtain more stable elements through diffusion and aggregation to form the framework of nanometal materials^[13-15]. In recent years, Chen *et al.*^[16] proposed a reverse dealloying method to prepare nanosilver. To selectively remove the inert component Au in Au-Ag alloy. Meanwhile, thiourea plays a role in promoting gold dissolution and passivating silver in the process of forming the porous silver framework^[16]. According to Liu *et al.*^[17], by changing the time sequence of dealloying, a series of nanoporous metal compound products with bimodal porous metals and single peak pores can be synthesized^[17]. At present, Pt and 3d transition metals M (such as Ti, Cr, V, Mn, Fe, Co, Ni, Cu^[18-20]) form alloys and are loaded on carbon carrier, which can effectively improve the stability of catalysts. Relevant literature reports Pt-Sn^[21], Pt-W^[22], and other alloy catalysts also show CO tolerance and are excellent catalysts^[21,22]. Considering the small radius of the Si atom, the introduction of the Si atom reduces the

distance between Pt-Pt and enhances the catalytic activity. In addition, Si is relatively stable under acidic conditions and can obtain better stability. Therefore, that alloying Pt and Si expects to improve the electrocatalytic performance of the material. Although studies have shown that bulk Pt-Si alloy^[23] has great electrocatalytic oxidation activity for methanol and carbon monoxide, nano-scale Pt-Si alloy and its catalytic performance have not been reported^[23].

In this study, we successfully prepared a 3D framework nanoporous PtSi (NP PtSi) binary alloy through the combination of melt rapid quenching technology and dealloying. Meanwhile, it also studied its electrocatalytic oxidation activity and stability for ethanol.

2. Experiment

2.1 Sample preparation

The purity of metal materials Pt, Si and Al is more than 99.99%, and the corresponding stoichiometric ratio is 9:3:88. Then calculate their respective elemental mass. Put the prepared materials into a water-cooled copper crucible electric arc furnace, and inject Ar gas to melt repeatedly 3–4 times to obtain Pt₉Si₃Al₈₈ alloy ingot. Cut the melted Pt₉Si₃Al₈₈ alloy ingot into small pieces, put it into the fired quartz glass tube and melt the material slowly to obtain the alloy strip with basically the same thickness. Weigh about 50 mg of the strip and put it in 5 wt% HCl solution to produce lots of bubbles at the beginning. When the reaction is slow, put it into a constant temperature water bath at 50 °C Celsius for 48 h, take out the sample, centrifuge and wash it repeatedly 5–6 times. Finally, it obtains the NP-PtSi by drying in a vacuum drying oven for 24 h.

2.2 Characterization of materials

We used the SA-HF3 X-ray powder diffractometer (XRD) of Rigaku Company from Japan to analyze the crystal structure of the materials. Detecting the chemical composition and surface atomic state of the material by the X-ray photoelectron spectroscopy (XPS) of Axis Ultra, which is a wholly-owned subsidiary of Shimadzu group in Japan. The Sigma

scanning electron microscope (SEM) of ZEISS Company in Germany was used to observe the micromorphology of the material, the accelerating voltage is 20 kV. TecnaiG220S-TWIN transmission electron microscope (TEM) and high-resolution transmission electron microscope (HRTEM) of American FEI Company are used, which not only could detect the microstructure of materials but also obtain the crystal plane spacing of atoms. The electrochemical properties of materials are measured by the electrochemical workstation of model 760E of Shanghai Chenhua Instrument Co., Ltd.

2.3 Electrode preparation and electrochemical test

Weigh 1 mg of NP-PtSi and 1.5 mg of carbon black with an electronic balance into a 2 ml centrifuge tube, and put 980 μL absolute ethanol and 20 μL 5 wt% Nafion with a pipette gun respectively into a centrifuge tube. Then put into an ultrasonic cleaner for about 1h to obtain the catalyst suspension. Commercial Pt/C catalyst with the same concentration was prepared by the same method.

Firstly, the glassy carbon electrode (GCE, diameter 3 mm) was applied on the foot skin with 0.05 μm polishing powder shall be polished and cleaned with ultrapure water, and then placed in the mixed solution of 0.1 mol/L KCl + 1 mol/L potassium ferricyanide to measure the redox potential difference. When the value is less than 70 mV, it shall be washed with ultrapure water and dry naturally for standby.

All electrochemical tests were carried out in a three-electrode system. Before the reaction, introducing saturated N_2 , removing O_2 from the solution, and the reaction temperature was 25 degrees Celsius.

3. Results and discussion

3.1 Characterization of NP-PtSi

3.1.1 XRD characterization of NP-PtSi

Figure 1 is the XRD diagram of $\text{Pt}_9\text{Si}_3\text{Al}_{88}$ alloy before and after dealloying. It shows from the diagram that the diffraction peak of PtSiAl alloy is

very complex, and it is difficult to distinguish the alloy phase of PtSiAl, and there is no diffraction peak corresponding to pure Pt, Al, and Si, indicating the formation of Pt-Si alloy. NP-PtSi sample has three diffraction peaks, i.e. $2\theta = 40.140^\circ$, 46.599° , and 68.317° , corresponding to (111), (200), (220) crystal planes of face-centered cubic PtSi. Compared with the standard pure Pt card (JCPDS 04-0802), it finds that the diffraction peak of each crystal plane deviates slightly to a high angle, which may be because Si atoms with small atomic radius are added into the alloy to replace some Pt atoms, which reduces the distance between Pt-Pt and finally forms Pt-Si alloy.

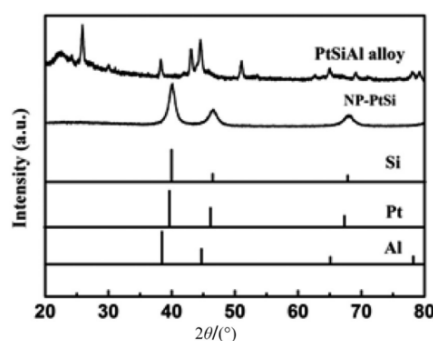


Figure 1. XRD spectra of $\text{Pt}_9\text{Si}_3\text{Al}_{88}$ alloy before and after dealloying. Standard spectra: Pt (JCPDS04-0802), Si (JCPDS35-1158), Al (JCPDS 04-0787).

3.1.2 XPS characterization of NP-PtSi

Figure 2(a) is the full spectrum of NP-PtSi. By that, we can see the peaks of Pt 4f, Si 2f, O 1s, C 1s, and other elements, in which O 1s and C 1s belong to water or carbon dioxide physically or chemically adsorbed on the material surface, which fits with XPS Peak Fit^[13]. **Figure 2(b)** is the peak diagram of Pt 4f. There are two peaks at 71.2 eV and 74.6 eV, corresponding to Pt and Pt^{2+} in the metal state. The results show that some Pt is oxidized to Pt^{2+} , but it mainly exists in the form of Pt in a metal state, which is consistent with the internal XRD test results of the material. **Figure 2(c)** is the sub-peak diagram of Si 2p. Both Si^0 and Si^{4+} can be detected, and the binding energy belongs to Si^0 at 99.5 eV; the binding energy belongs to Si^{4+} at 103.2 eV. On the surface, Si mainly exists in the form of Si^{4+} . It also can observe some metallic Si.

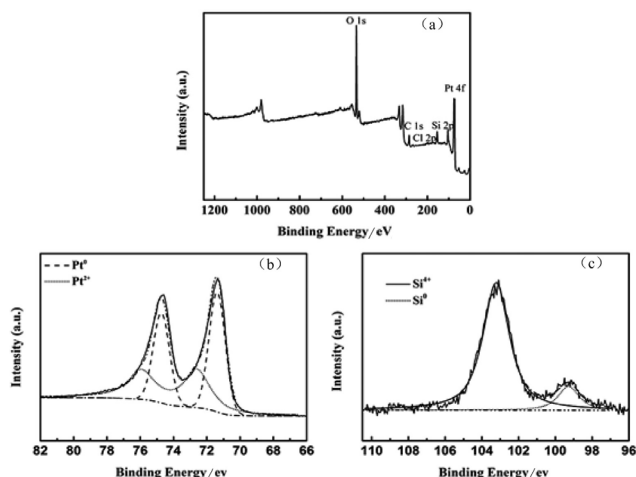


Figure 2. (a) XPS full spectrum of NP-PtSi; (b) Pt 4f peak diagram; (c) Si 2p peak diagram.

3.1.3 SEM, TEM and HRTEM characterization of NP PtSi

Figure 3(a) is the SEM diagram of $\text{Pt}_9\text{Si}_3\text{Al}_{88}$ strip after dealloying, which shows that it forms a uniform nanoporous structure composed of nanopores and ligaments. The pore size is 5–20 nm, the specific surface area increases, and the active sites of an electrochemical reaction in the material increase. **Figure 3(b)** is the cross-sectional view of NP-PtSi, from which the uniform pores can be seen. This confirms that the fine nanoporous structure is obtained in the whole sample. The TEM diagram can observe the microstructure of the sample from the nano size, as shown in **Figure 3(c)**. The uniformly distributed bright white areas can be seen more clearly from the TEM diagram. Compared with the SEM diagram, the structure with pores in the multi-level pores is more significant. It is conducive to improving the kinetics of oxygen diffusion. **Figure 3(d)** is the HRTEM diagram of NP-PtSi, and it is clear that

the continuous lattice diffraction fringes.

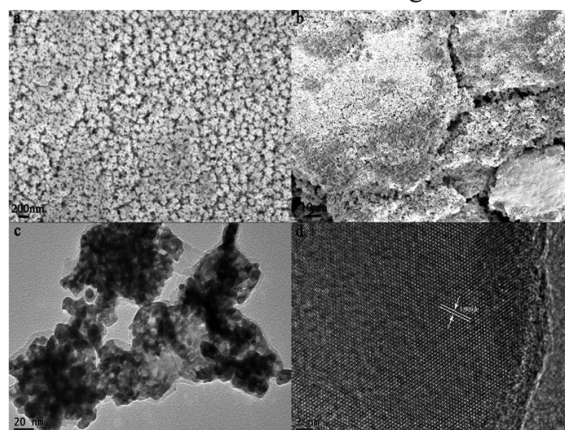


Figure 3. Characterization diagram of NP-PtSi alloy. (a) SEM diagram; (b) SEM diagram; (c) TEM diagram; (d) HRTEM diagram.

3.2 Electrochemical performance test of NP-PtSi

In 0.5 mol/L H_2SO_4 deoxidized solution, the stable CV curve of NP-PtSi alloy is shown in **Figure 4 (a)**, and commercial Pt/C catalysts can be compared. In the whole potential scanning range, NP-PtSi and commercial Pt/C catalysts show the same CV curve characteristics, including hydrogen adsorption and desorption zone: $-0.25\text{--}0.1$ V vs. SCE; electric double layer area: $0.1\text{--}0.35$ V vs. SCE; high potential region: $0.35\text{--}1.2$ V vs. SCE. In the hydrogen adsorption and desorption region, the peak of NP-PtSi alloy becomes wider and shifts to high potential compared with commercial Pt/C, which is due to the increase of hydrogen adsorption strength on Pt due to the interaction between Pt and Si. Compared with commercial Pt/C catalyst, NP-PtSi shows a significant current peak at about 0.45 V vs. SCE, which shows that lots of OH species adsorb on the surface of the catalyst.

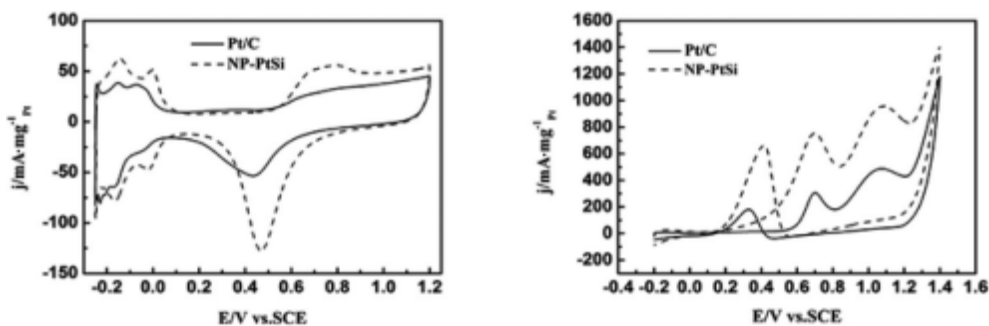


Figure 4. Cyclic voltammetric curves of Pt/C and NP PtSi catalysts in deaeration solution. (a) 0.5 mol/L H_2SO_4 solution; (b) 0.5 mol/L H_2SO_4 + 1 mol/L $\text{CH}_3\text{CH}_2\text{OH}$ mixed solution.

It believes that the activity of the catalyst is related to the electrochemical activity area (ECSA). We use Origin software to calculate the desorption peak area of H, and the formula is $ECSA = QH/(m \times c)$. In the formula, Q is the Coulomb charge $mC \cdot cm^{-2}$ in the H region, m is the Pt load, $mg \cdot cm^{-2}$, and c is the charge density adsorbed by the monolayer of H of Pt, which is $0.210 mC \cdot cm^{-2}$. It shows in **Figure 4(a)** that the electrochemically active area of NP-PtSi is much larger than that of commercial Pt/C, indicating that the number of active sites of NP-PtSi catalyst after dealloying is increased, which is conducive to the catalytic oxidation of ethanol.

Figure 4(b) shows the CV curve of NP-PtSi and commercial Pt/C catalyst in the mixed solution of $0.5 mol/L H_2SO_4 + 1 mol/L CH_3CH_2OH$. During the potential positive scanning, there are two oxidation peaks. During the negative scanning, there is a reduction peak. The Pt-based catalyst surface will adsorb -OH and be oxidized to PtO. During the negative scanning, PtO is restored. The oxidation peak (I) is about $0.7 V$, which is usually taken into consideration as the characteristic peak of ethanol oxidation to CO_2 . It is one of the basis for judging the performance of the catalyst. The oxidation peak (II) is about $1.1 V$, which is related to the secondary oxidation of intermediate products. The peak onset potential is also a key index for evaluating the activity of the catalyst. The peak onset potential of NP-PtSi alloy is negative compared with that of commercial Pt/C catalyst, which shows that the catalyst can improve the catalytic oxidation kinetics of ethanol and has good application value.

We further explored the stability of NP-PtSi alloy and commercial Pt/C catalyst by the potentiostat method. **Figure 5** is the I-t curve with a constant potential of $0.7 V$. It shows from the figure that at the beginning, the current density of NP-PtSi and Pt/C catalyst decreased sharply due to the formation of electric double-layer capacitance. The subsequent decrease in current is due to the loss of surface activity sites caused by the adsorption of oxygen-containing intermediate species on the catalyst surface. After $500 s$, the current density tends to be stable, which attributes to the continuous reduction of cat-

alyst concentration during the reaction. Although the current density of both decreased to varying degrees within the entire $3,000 s$, the current density of NP-PtSi is always higher than that of commercial Pt/C catalyst, indicating that the addition of Si makes NP-PtSi alloy show better stability than commercial Pt/C catalyst.

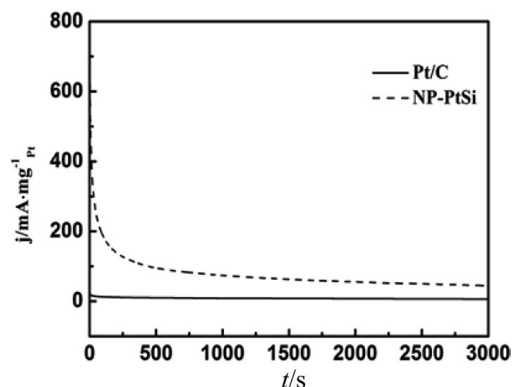


Figure 5. Potentiostatic I-t curve of Pt/C and NP-PtSi catalysts in mixed solution of $0.5 mol/L H_2SO_4 + 1 mol/L CH_3CH_2OH$ (constant potential is $0.7 V$).

4. Conclusion

Nanoporous Pt-Si alloy was prepared by the combination of melt rapid quenching technology and dealloying. NP-PtSi alloy has a three-dimensional bi-continuous structure, with an average pore size of $5 nm$ and a large specific surface area. Compared with commercial Pt/C catalyst, NP-PtSi alloy has excellent ethanol electrocatalytic activity and stability under acidic conditions, and the operation is simple, the conditions are easy to control, the cost is low, and it can produce on a large scale, which makes NP-PtSi alloy have more application potential in the field of electrocatalysis.

Conflict of interest

The authors declare that they have no conflict of interest.

Acknowledgements

Project: the National Natural Science Foundation of China Project “Research on low temperature phase effect of phase separation and exchange biasing of alloy of Ni-Mn based magnetic shape memory alloy” (51371004).

References

1. Hou M, Yi B. Development status of fuel cell technology (in Chinese). *Chinese Journal of Power Sources* 2008; (10): 649–654.
2. Cook B. Introduction to fuel cells and hydrogen technology. *Engineering Science and Education Journal* 2002; 11(6): 205–216.
3. Qu Y, Wang L, Li C, *et al.* Quantitative pinhole online electrochemical mass spectrometry study on ethanol electro-oxidation at carbon-supported Pt and Ir-containing catalysts. *International Journal of Hydrogen Energy* 2017; 42(1): 228–235.
4. Yang W, Lu M, He Y. Performance study of an alkaline direct ethanol fuel cell with a reduced two-dimensional mass transport model. *International Journal of Hydrogen Energy* 2016; 41(45): 20693–20708.
5. Abrego-Martinez JC, Wang Y, Mendoza-Huizar LH, *et al.* Mixed-reactant ethanol fuel cell using an electrochemically deposited Ag@Pt tolerant cathode. *International Journal of Hydrogen Energy* 2016; 41(48): 23417–23424.
6. Wang J, Wasmus S, Savinell RF. Evaluation of ethanol, 1-propanol, and 2-propanol in a direct oxidation polymer-electrolyte fuel cell. *Journal of the Electrochemical Society* 1995; 142: 4218–4224.
7. Koh S, Strasser P. Electrocatalysis on bimetallic surfaces: Modifying catalytic reactivity for oxygen reduction by voltammetric surface dealloying. *Journal of the American Chemical Society* 2007; 129(42): 12624–12625.
8. Kattel S, Wang G, Duan Z. Density functional theory study of oxygen reduction reaction mechanism on Pt alloy catalysts. *Journal of Physical Chemistry C* 2014; 1: 911.
9. Wang C, Vliet DVD, More K, *et al.* Multimetallic Au/FePt₃ nanoparticles as highly durable electrocatalyst. *Nano Letters* 2010; 11(3): 919–926.
10. Jiang L, Sun G, Sun S, *et al.* Structure and chemical composition of supported Pt-Sn electrocatalysts for ethanol oxidation. *Electrochimica Acta* 2005; 50(27): 5384–5389.
11. Yu X, Ye S. Recent advances in activity and durability enhancement of Pt/C catalytic cathode in PEMFC. *Journal of Power Sources* 2007; 172(1): 145–154.
12. Luo Y, Liang Z, Liao S. Recent development of anode electrocatalysts for direct methanol fuel cells. *Chinese Journal of Catalysis* 2010; 31(2): 141–149.
13. Senior NA, Newman R. Synthesis of tough nanoporous metals by controlled electrolytic dealloying. *Nanotechnology* 2006; 17(9): 2311–2316.
14. Stratmann M, Rohwerder M. A pore view of corrosion. *Nature* 2001; 410: 421–423.
15. Erlebacher J. An atomistic description of dealloying-porosity evolution, the critical potential, and rate-limiting behavior. *Journal of the Electrochemical Society* 2004; 151(10): C614–C626.
16. Chen T, Liu Z, Lu W, *et al.* Fabrication of free-standing nanoporous silver by selectively dissolving gold from gold-silver alloys via a novel inverse dealloying method. *Electrochemistry Communications* 2011; 13(10): 1086–1089.
17. Liu W, Zhang S, Li N, *et al.* A general dealloying strategy to nanoporous intermetallics, nanoporous metals with bimodal, and unimodal pore size distributions. *Corrosion Science* 2012; 58(5): 133–138.
18. Kattel S, Duan Z, Wang G. Density functional theory study of an oxygen reduction reaction on a Pt₃Ti alloy electrocatalyst. *Journal of Physical Chemistry C* 2013; 117(14): 7107–7113.
19. Ohyagi S, Sasaki T. Durability of a PEMFC Pt-Co cathode catalyst layer during voltage cycling tests under supersaturated humidity conditions. *Electrochimica Acta* 2013; 102(15): 336–341.
20. Hoffmannová H, Okube M, Petrykin V, *et al.* Surface stability of Pt₃Ni nanoparticulate alloy electrocatalysts in hydrogen adsorption. *Langmuir* 2013; 29(29): 9046–9050.
21. Liu Z, Jackson GS, Eichhorn BW. PtSn intermetallic, core-shell, and alloy nanoparticles as co-tolerant electrocatalysts for H₂ oxidation. *Angewandte Chemie International Edition* 2010; 49(18): 3173–3176.
22. Pereira LGS, Paganin VA, Ticianelli EA. Investigation of the CO tolerance mechanism at several Pt-based bimetallic anode electrocatalysts in a PEM fuel cell. *Electrochim Acta* 2009; 54(7): 1992–1998.
23. Rohner A, Han B, Jensen JO, *et al.* Pt-Si bifunctional surfaces for CO and methanol electro-oxidation. *Journal of Physical Chemistry C* 2015; 119(15): 8023–8031.

ORIGINAL RESEARCH ARTICLE

A theoretical study of (9, 0) Singlewalled Carbon Nanotubes using quantum mechanical techniques

Deepa Sharma^{1*}, Neena Jaggi²

¹ SUS Govt. College, Matak-Majri (Indri), Haryana-India. E-mail: bhargava.dp@gmail.com

² National Institute of Technology, Kurukshetra-(Haryana)-India

ABSTRACT

First principles simulation studies using the density functional theory have been performed on (9, 0) Zigzag Singlewalled Carbon Nanotube (SWCNT) to investigate its electronic, optical and thermodynamic properties using CASTEP (Cambridge Sequential Total Energy Package) and DFTB (Density Functional based Tight Binding) modules of the Material Studio Software version 7.0. Various functionals and sub-functionals available in the CASTEP Module (using Pulay Density Mixing treatment of electrons) and various eigen-solvers and smearing schemes available in the DFTB module (using smart algorithm) have been tried out to chalk out the electronic structure. The analytically deduced values of the band gap obtained were compared with the experimentally determined value reported in the literature. By comparison, combination of Anderson smearing scheme and standard diagonalizer produced best results in DFTB module while in the CASTEP module, GGA (General Gradient approximation) functional with RPBE (Revised-perdew-Burke-Ernzerh) as Sub-functional was found to be the most consistent. These optimized parameters were then used to determine various electronic, optical and thermodynamic properties of (9, 0) Singlewalled Nanotube. (9, 0) Singlewalled Nanotube, which is extensively being used for sensing NH₃, CH₄ & NO₂, has been picked up in particular as it is reported to exhibit a finite energy band gap in contrast to its expected metallic nature. The study is of utmost significance as it not only probes and validates the simulation route for predicting suitable properties of nanomaterials but also throws light on the comparative efficacy of the different approximation and rationalization quantum mechanical techniques used in simulation studies.

Keywords: Simulation; Density Functional Theory; Molecular Modeling; CASTEP; DFTB; SWCNT

ARTICLE INFO

Received: 26 December 2020

Accepted: 12 February 2021

Available online: 21 February 2021

COPYRIGHT

Copyright © 2021 Deepa Sharma, et al.
EnPress Publisher LLC. This work is licensed
under the Creative Commons Attribution-
NonCommercial 4.0 International License
(CC BY-NC 4.0).

<https://creativecommons.org/licenses/by-nc/4.0/>

1. Introduction

Since the advent of Carbon Nanotubes by Iijima in 1991^[1] and subsequent synthesis of Singlewalled Carbon Nanotubes (SWCNTs) by Iijima^[2] & Bethune^[3], Singlewalled Carbon Nanotubes have grabbed utmost attention because of their mesmerizing electrical^[4,5], mechanical^[6,7] and optical properties^[8,9]. This multifaceted seamless one-dimensional roll of a single layer of graphite (graphene) has revealed highly promising applications in future molecular electronics^[10,11] over the last few decades. The remarkable electronic properties of these 1-D structures make them suitable for various applications in nanotechnology, optics, electronics, and other fields of materials science as chemical sensors^[12-19], actuators^[20], nano biomaterial^[21,22], conductive heating film^[23,24], conductive transparent electrode^[25,26], conductive nanoink^[27], nano device^[28-32], and display (backlight, flat lamp and field emitter)^[32,33] etc. This has invoked interest in the experimentalists as well as theoreticians.

ticians. Experimentalists are trying to develop new methods of synthesizing, purifying and functionalizing SWCNTs and exploring possibilities of their use into new devices and applications. On the other hand, theoreticians are implying theory and computational modeling to determine the structural, mechanical, thermal and electronic behaviour with accuracy by using computational nanotechnology. The simulation techniques are being used for predictions. Various concepts and designs have been theoretically evolved through modeling and simulation and then realized or verified experimentally^[34].

In this paper, the electronic structure of a (9, 0) SWCNT has been investigated using DFTB & CASTEP modules of the Material Studio Software version 7.0, and relative efficacy of various functionals and subfunctionals has been compared and electronic, optical and thermodynamic properties have been studied using the optimum combination of the functional & sub-functional and diagonalization technique & density mixing scheme. The motive behind choosing (9, 0) SWCNT as the target material has on the one hand been its current extensive application as a gas sensor for the poisonous gases like NH₃^[12], CH₄^[13] and NO₂^[14]. On the other hand, the reported finite band gap in contrast to the expected metallic nature also served as a driving force for this study.

2. Theory

Beginning with the bottom-up, a few tens to hundreds of atoms can be simulated using quantum mechanics based first principle methods, which involve the solution of the complex quantum of many body by Schrödinger equation of the atomic system using different computational algorithms^[35]. The atoms are treated as a group of quantum mechanical particles governed by the Schrödinger equation:

$$\hat{H}\psi = E\psi$$

Where, \hat{H} is the many-body Hamiltonian operator. However, with Born-Oppenheimer approximation, a many body problem is reduced to a many electron problem. Current first principle methods are based on the density functional theory (DFT)

^[36,37]. DFT is based on the concept that the ground state total electronic energy is a unique functional of the density of the system. Kohn and Sham^[36,37] have shown that the DFT can be reduced to a single electron problem with self-consistent effective potential, which takes into consideration the exchange correlation effects of the interactions of the electrons. This reformulation of Schrödinger equation into a single electron problem is known as Kohn-Sham equation. Many approximations like local density approximation (LDA), general gradient approximation (GGA), Hartree Fock approximation (HF), Hartree Fock-local density approximation (HF-LDA), etc^[34-47]. were proposed to approximate the effective exchange-correlation potential^[36,40]. To be more specific, certain sub-functional are associated with the approximation functional like LDA, CA-PZ, GGA-PBE, GGA-RPBE, GGA-PW91, GGA-WC, GGA-PBESOL, etc^[34-47]. These approximation based first principles methods have been successful in various modeling and simulation tasks planned for structural, chemical & electronic characterization of nanomaterials. For practical applications, these simulation methods are implemented with a pseudo-potential approximation (ultrasoft, normconserving or on the fly) and a plane wave basis expansion of single electron wavefunctions^[47]. These approximations convert the electronic structure problem into a self-consistent matrix diagonalization problem^[34,45,46]. When the iterative matrix diagonalization procedure completes, the eigen values obtained correspond to energy states of the system. The eigen functions provide information about the electronic density distribution. CASTEP (Cambridge Sequential Total Energy Package) and DFTB (Density Functional Tight Binding) are immensely effective DFT simulation programs available through Accelrys Material Studio Software as user-friendly modules through a license agreement^[47].

3. Computational details

This paper elaborates first principles investigations on a zigzag Singlewalled Carbon Nanotube with chirality (9, 0) using the software Material Studio version 7.0 installed on an 8 core Intel(R) Core(TM) i7-3770 CPU @ 3.40 GHz with Windows

operating system. To start with, structural unit was simulated via molecular modelling, which comprised of 144 electrons in the 36 carbon atoms of the specific nanotube giving rise to 87 energy bands in its electronic band structure. The band gap studies were performed using CASTEP as well as DFTB Modules.

Initially the task was set up using DFTB module. Static calculations were performed with self-consistent charges using the smart algorithm. Different combinations of diagonalization techniques (standard/divide & conquer) and smearing schemes (Anderson/Broyden/DIIS/linear) were tried. Suitable choice of various tolerance parameters is very crucial for geometry optimization. The same task was then set up using CASTEP Module. The structure of the CNT was first electronically minimized through pseudo-atomic calculations using LDA(CA-PZ) , GGA(RPBE), GGA(WC), GGA(PW91), GGA(P-BESOL) functionals with Pulay density mixing treatment of the electrons, choosing a suitable cut-off energy & tolerance values for various parameters like energy, maximum force, maximum stress, maximum displacement, charge spilling parameter etc. Ultrasoft pseudo-potential was used in the reciprocal lattice with fixed basis set quality using Gaussian smearing scheme with suitably chosen smearing width without any periodic dipole correction. BFGS algorithm which implements variable cell method with geometry line minimiser was initiated to calculate the ground state eigen values, eigen functions and density. Continuing with the ground state wavefunction thus determined and ground state density thus calculated, general k-point calculations for band structure and density of states were performed.

In comparison with the experimental results, the calculation performed in CASTEP module with GGA (RPBE) and the calculation performed in DFTB module with standard diagonalizer & Anderson smearing scheme were found to deliver the best match. Hence thereafter, electronic, optical and thermodynamic studies were performed using the same combination of functional & sub-functional.

4. Results and discussions

4.1 Geometry optimization

4.1.1 DFTB module

While performing static calculations with self-consistent charges for geometry optimization using the smart eigen-solver in the DFTB module, different combinations of diagonalization techniques (standard, divide & conquer) and mixing schemes (Anderson, Broyden, DIIS & linear) were tried keeping SCC tolerance value at 0.1×10^4 , energy tolerance value at 0.05 kcal/mol, force tolerance value at 0.05 kcal/mol/Å and Ewald alpha parameter ≈ 0.22 (Figure 1).

The optimization process was carried out with respect to the parameters like energy change, force constant and normal stress component (Figure 2a) and converged at different energies for different mixing schemes & diagonalization techniques, finally leading to an optimized hexagonal geometry (Figures 2b & 2c).

In all the tasks set up using DFTB, thermal smearing with smearing parameter 0.005 Hartree was used without any dipole correction. The results obtained may be summarized as follows:

Table 1. DFTB Geometry optimization: (9, 0) Singlewalled Carbon Nanotube

Mixing Scheme Parameter	Standard diagonalization				Divide & conquer diagonalization			
	Anderson	Broyden	Diis	Linear	Anderson	Broyden	Diis	Linear
Total energy (Hartree)	-61.84978	-61.57981	-61.57979	-61.57985	-61.57981	-61.57981	-61.57979	-61.57985
Total enthalpy (kcal/mol)	-38777.3	-38598.7	-38598.7	-38598.7	-38598.7	-38598.7	-38598.7	-38598.7
Free energy (Hartree)	-61.85235	-61.58217	-61.58217	-61.58215	-61.58216	-61.58217	-61.58217	-61.58215
Volume (Å ³)	0.288×10^4	0.269×10^4	0.269×10^4	0.269×10^4	0.269×10^4	0.269×10^4	0.269×10^4	0.269×10^4
Pressure (-Pa)	0.260×10^8	0.139×10^8	0.054×10^8	0.511×10^8	0.082×10^8	0.139×10^8	0.054×10^8	0.511×10^8
rms force (kcal/mol/Å ⁰)	7.479	8.573	8.573	8.573	8.573	8.573	8.573	8.573
Max. force (kcal/mol/Å ⁰)	12.90	14.69	14.69	14.69	14.69	14.69	14.69	14.69
rms stress (GPa)	88.59	95.10	95.10	95.10	95.10	95.10	95.10	95.10
Max. stress (GPa)	167.6	184.3	184.3	184.3	184.3	184.3	184.3	184.3

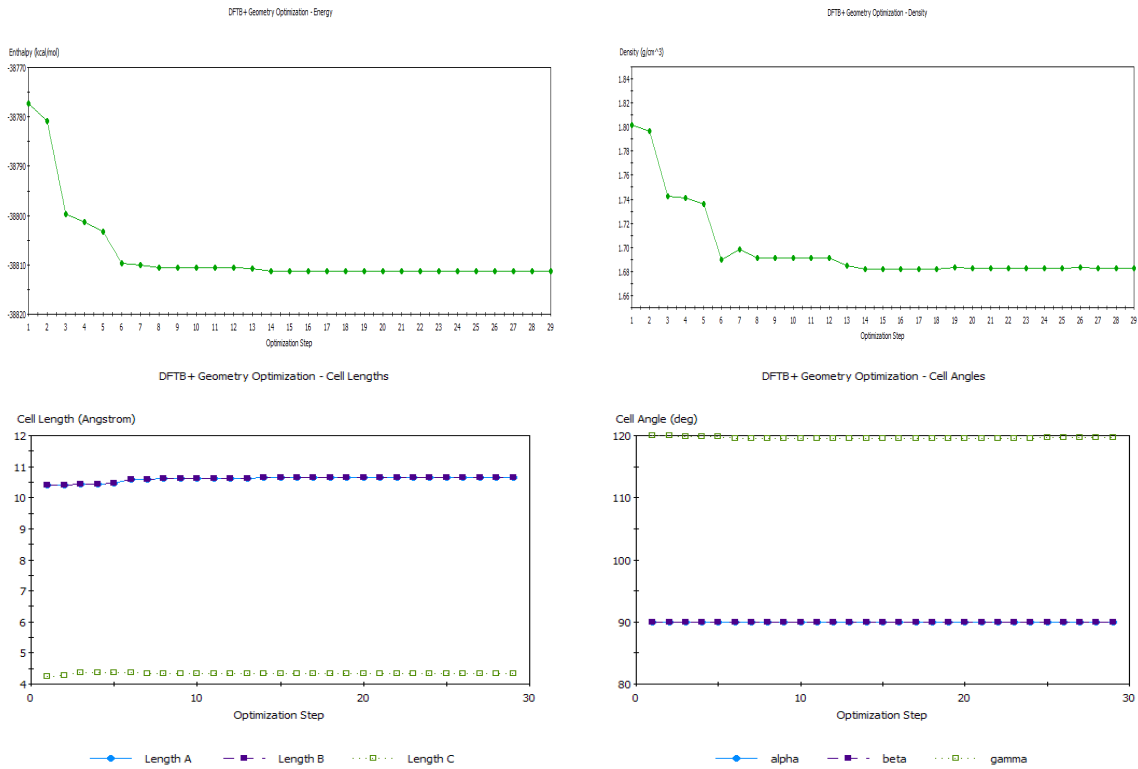


Figure 1. DFTB Geometry optimization w.r.t. a) energy b) density c) cell lengths & d) cell angles.

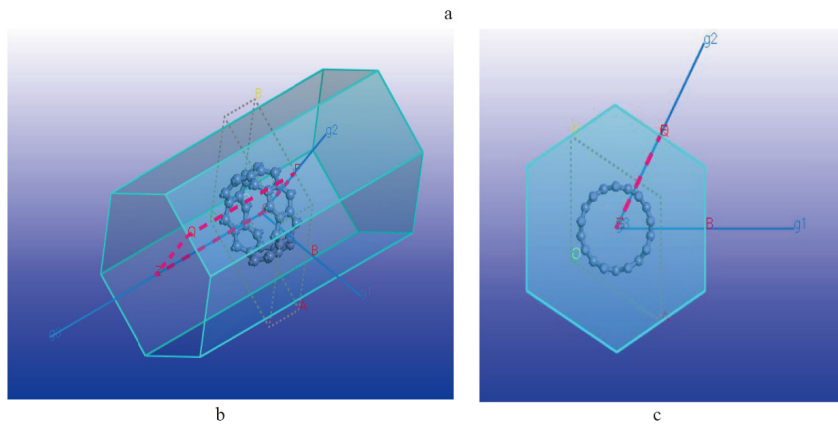
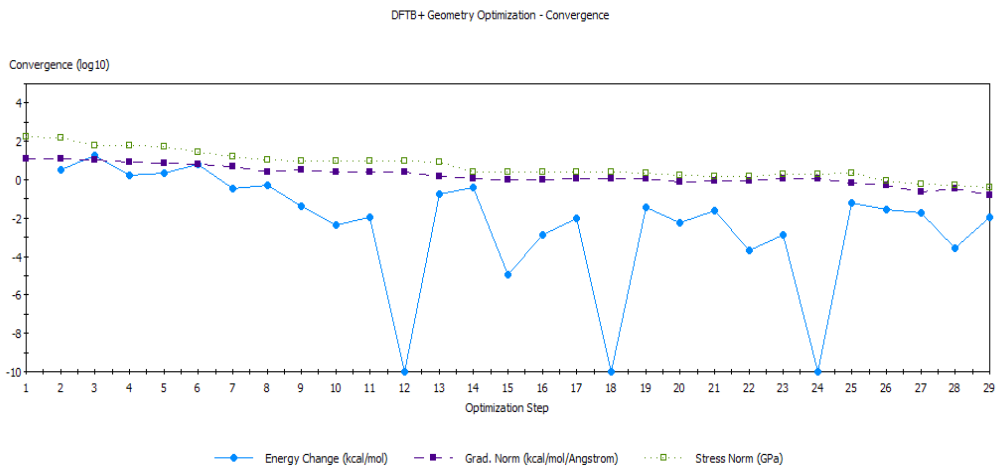


Figure 2. a) Geometry optimization convergence curve. b) Optimized geometry- 3D view c) optimized geometry- cross-sectionalview.

It can be seen that the structure is the most stable and relaxed when treated with Anderson mixing scheme under standard diagonalization (minimum energy, minimum force and minimum stress) and hence may be expected to produce the best results. Hence, Anderson smearing scheme in combination with standard diagonalization implemented using smart algorithm is strongly recommended for studying Singlewalled Nanotubes.

4.1.2 CASTEP module

In the CASTEP module, electronic minimization of the system was performed using Pulay density mixing treatment of the electrons. Cut-off energy for density mixing was chosen to be 240.0 eV with a charge density mixing g-vector of $1.5/\text{\AA}^0$. Pseudo-atomic calculations using LDA (CA-PZ), GGA (RPBE), GGA (WC), GGA (PW91) & GGA (PBE-SOL) functionals with an energy tolerance value of 2×10^{-5} eV/atom and maximum force tolerance value of 0.05 eV/ \AA^0 were performed with a charge spilling parameter for spin component 1 equal to 1.06%. Geometry of the system was optimized with respect to energy change, max. displacement, max. force and max. stress (Figure 3).

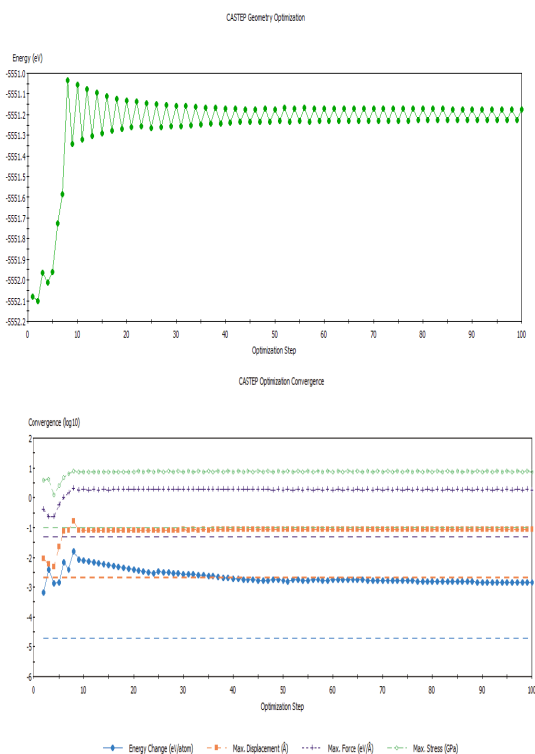


Figure 3. CASTEP geometry optimization a) energy evolution b)

optimization convergence w.r.t. i) energy ii) max. displacement iii) max. force & iv) max. stress.

Ultrasoft pseudo-potential was used in the reciprocal lattice with fixed basis set quality using Gaussian smearing scheme with smearing width of 0.1 eV without any periodic dipole correction. Geometry of the system was optimized using BFGS algorithm implementing variable cell method with geometry line minimiser of tolerance 0.4. Lattice parameters obtained after geometry optimization were $a = 10.392983 \text{ \AA}$, $b = 10.392983 \text{ \AA}$ & $c = 4.260000 \text{ \AA}$ (Cell Volume = $398.492992 (\text{\AA}^0)^3$) with cell angles 90° , 90° & 120° confirming the suggested hexagonal geometry (Figure 4).

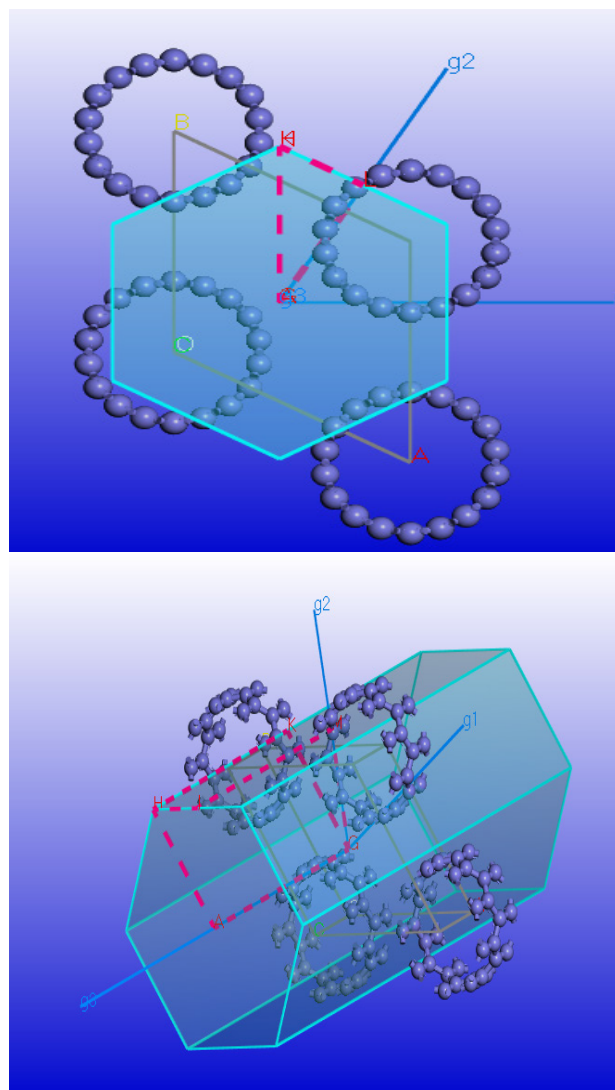


Figure 4. Optimized geometry obtained by supercell approach using CASTEP a) lateral view b) 3-D view.

The unit chosen comprised of 36 units. As ex-

pected, the first Brillion zone obtained was also hexagonal. Supercell approach was adopted. 6 k-points were chosen for BZ sampling.

4.2 Electronic properties

Continuing with the ground state wavefunctions during the geometry optimization task and the ground state density thus calculated, general k-point calculations for band structure were performed using complex wavefunction with 84 bands per k-point and a band convergence tolerance of 0.1×10^{-4} eV. Fermi energy for the spin-degenerate system with electrical quadrupole moment 0.0332700 Barn was calculated keeping 23 basis set k-points under consideration. General k-point calculations for density of states were also performed treating the system as non-spin-polarized with total energy/atom con-

vergence tolerance value equal to 0.2×10^{-5} eV, all bands spilling parameter for spin component 1 & eigen energy convergence tolerance value equal to 0.8276×10^{-6} eV.

4.2.1 DFTB module

Band Structure and density of states of the optimized structural unit were determined and investigated using smart algorithm without any dispersion correction using various combinations of diagonalization techniques (standard/divide & conquer) and mixing schemes (anderson/broyden/diis/linear) (**Figure 5**). Thermal smearing with smearing parameter equal to 0.005 Hartree was used during all these band structure calculations.

The values of band gap of (9, 0) SWCNT calculated using DFTB Module can be summarized as below:

Table 2. Band gap evaluation using DFTB: (9, 0) Singlewalled Carbon Nanotube

Standard diagonalization				Divide & conquer diagonalization			
Anderson	Broyden	Diis	Linear	Anderson	Broyden	Diis	Linear
0.063 eV	0.003 eV	0.005 eV	0.004 eV	0.003 eV	0.003 eV	0.005eV	0.004eV

On the basis of the measurements made by Leiber *et al.* under ultrahigh vacuum conditions at 5 K on a Au (111) substrate, the experimental value of the band gap of (9, 0) SWCNT has been found to be 0.080 eV^[48]. By comparing the simulation results with this experimental value, it can be inferred that DFTB module tends to drastically underestimate the

band gap value. However, the results obtained with standard diagonalizer and Anderson mixing scheme with mixing parameter 0.05 are comparatively close enough.

4.2.2 CASTEP module

Band Structure and density of states were also

Band structure and density of states of (9,0) SWCNT calculated using density functional tight binding module

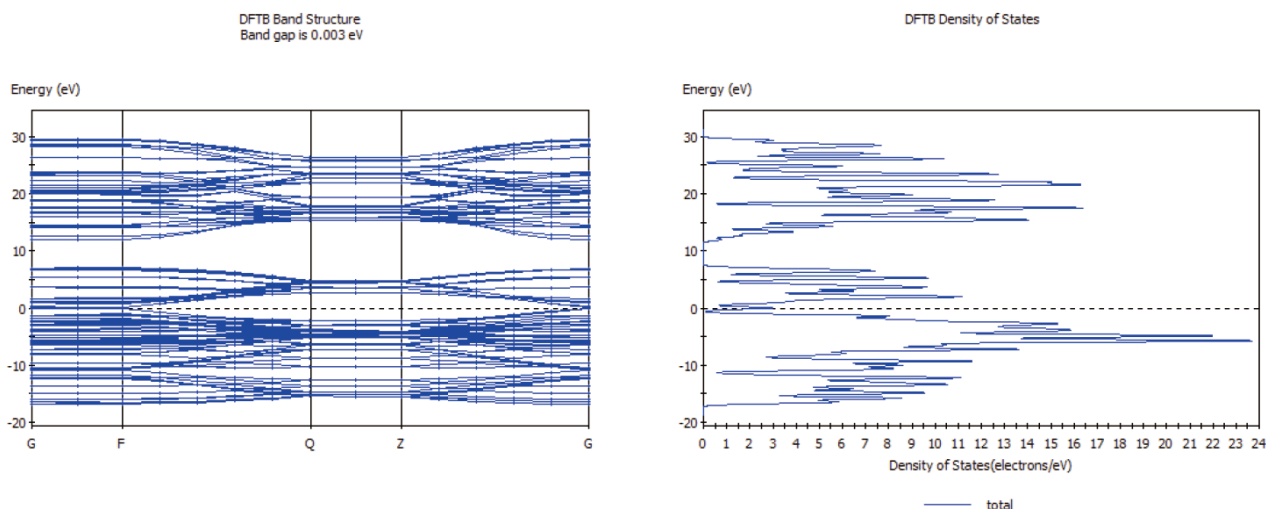


Figure 5a). Band structure deduced with eigen-solver “divide & conquer”, mixing scheme—Anderson.

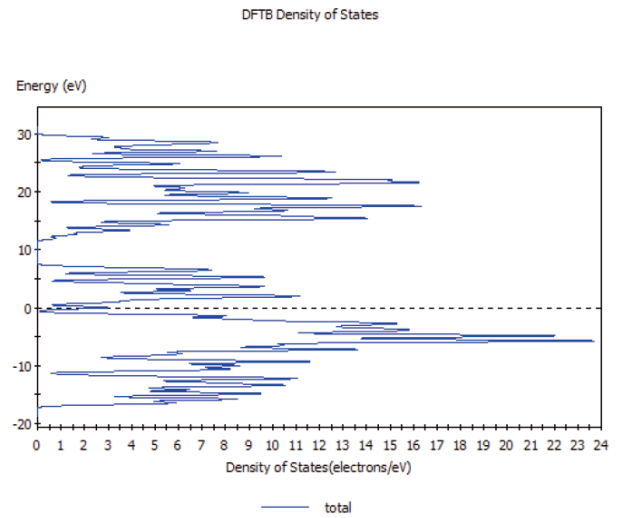
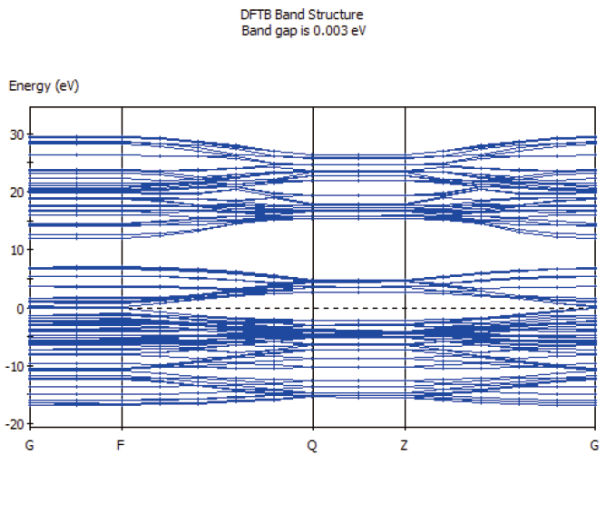


Figure 5b). Band structure deduced with eigen-solver “divide & conquer”, mixing scheme—Broyden.

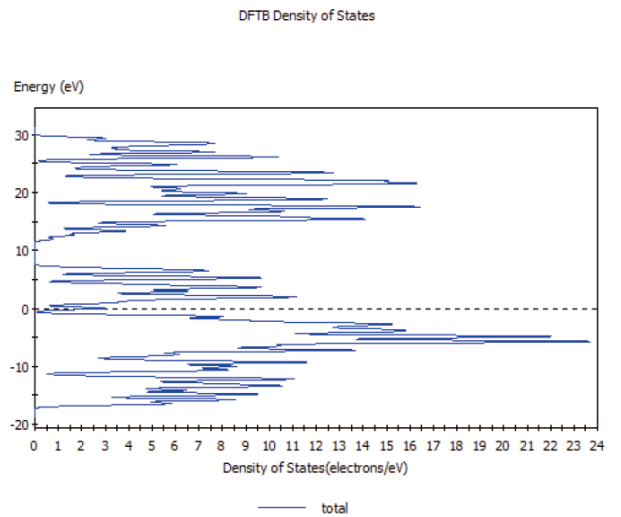
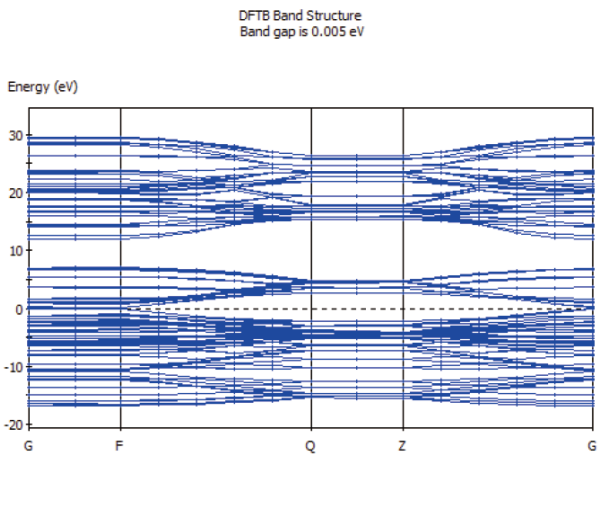


Figure 5c). Band structure deduced with eigen-solver “divide & conquer”, mixing scheme—Diis.

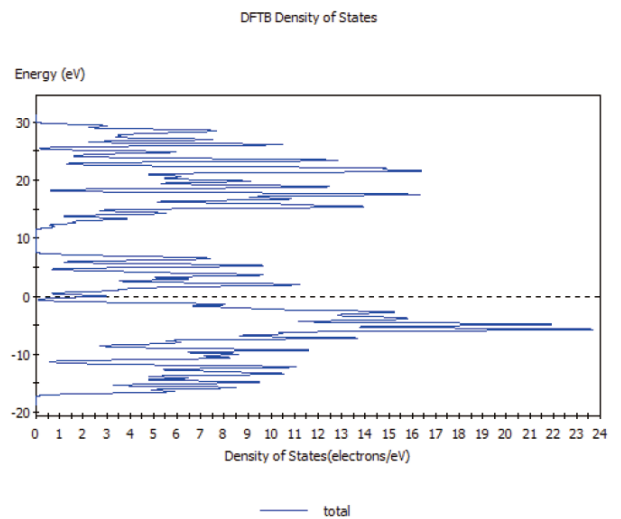
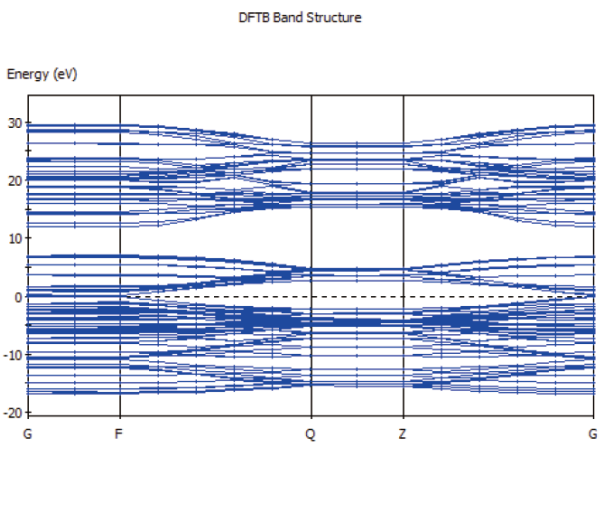


Figure 5d). Band structure deduced with eigen-solver “divide & conquer”, mixing scheme—Linear.

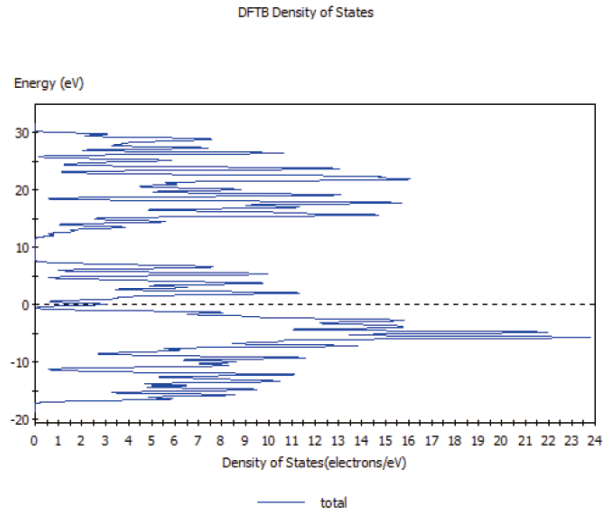
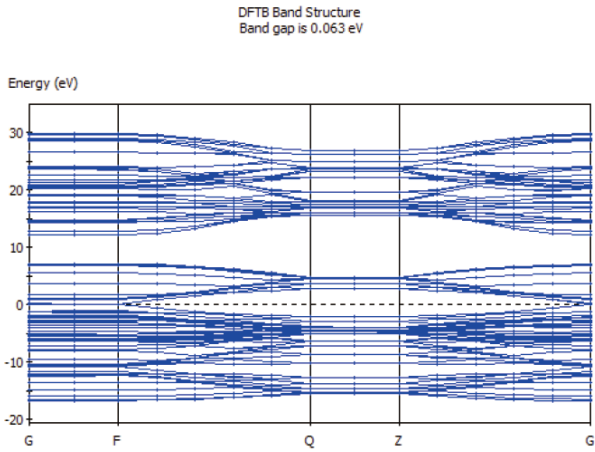


Figure 5e). Band structure deduced with eigen-solver “standard”, mixing scheme—Anderson.

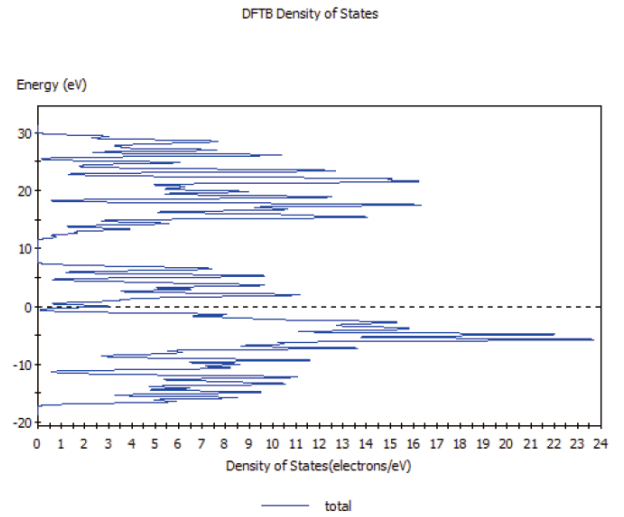
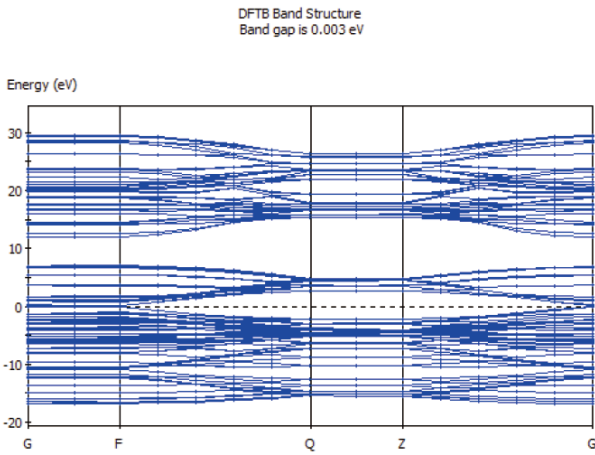


Figure 5f). Band structure deduced with eigen-solver “Standard”, mixing scheme—Broyden.

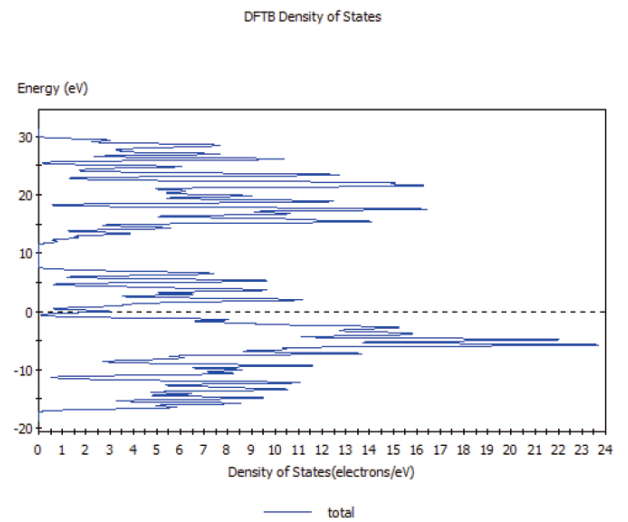
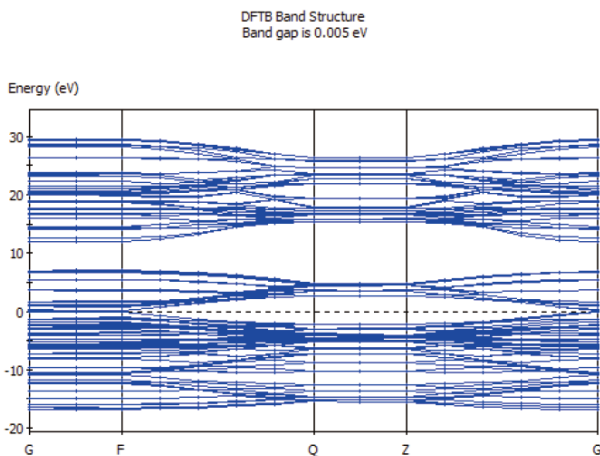


Figure 5g). Band structure deduced with eigen-solver ‘Standard’, mixing scheme—Diis.

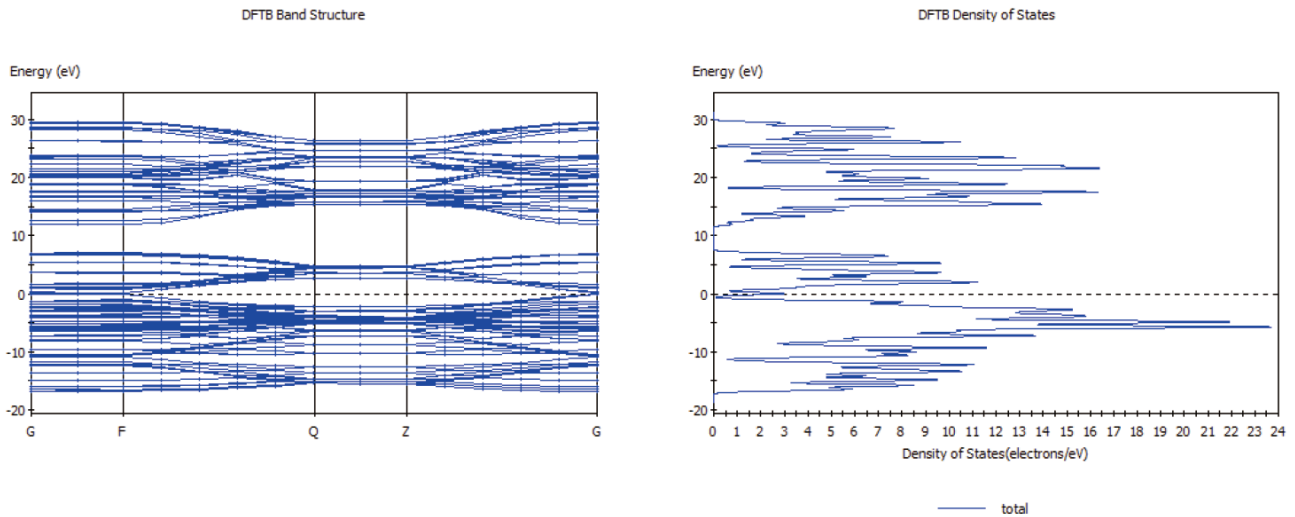


Figure 5h). Band structure deduced with eigen-solver “standard”, mixing scheme—Linear.

determined and investigated with the help of the CASTEP module of the software using various available functionals and subfunctionals (**Figure 6**). Fermi energy for the spin-degenerate system with electrical quadrupole moment 0.0332700 Barn was calculated keeping 23 basis set k-points under consideration.

The values of band gap of (9, 0) SWCNT calculated using CASTEP Module can be summarized as below:

Table 3. Band gap evaluation using CASTEP: (9,0) Single-walled Carbon Nanotube

LDA		GGA		
CA-PZ	RPBE	PBESOL	WC	PW91
0.190 eV	0.097 eV	0.161 Ev	0.063 eV	0.003 Ev

Comparing these results with the measurements made by Leiber *et al.* ($E_g = 0.080$ eV), it can be seen that some of the functional-subfunctional combinations in the CASTEP module tend to overestimate the value of the bond gap while others underestimate the value. However, the value of the band gap obtained with GGA functional and RPBE subfunctional is very close to the experimentally observed value. Hence, it can be concluded that GGA-RPBE exchange correlation approximation is the most effective theoretical tool for predicting band gaps in SWCNTs.

As (3 m, 0) SWCNTs are supposed to be of metallic nature, the finite band gap determined theo-

Band structure and density of states of (9,0) SWCNT calculated using CASTEP module

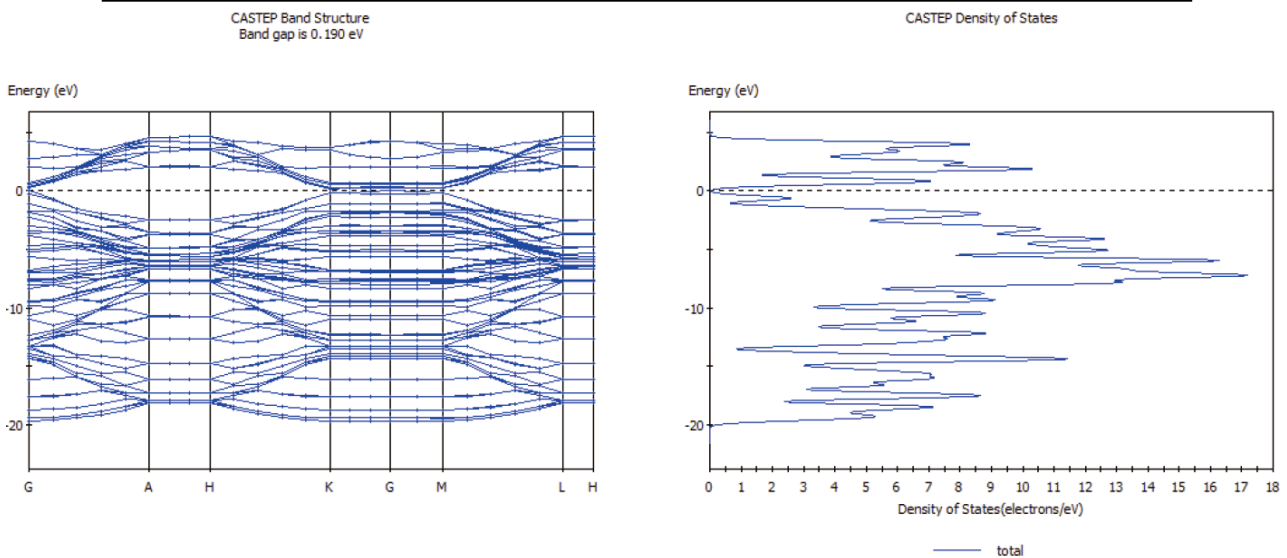


Figure 6a). Band structure deduced with functional—“LDA” and subfunctional—“CA-PZ”.

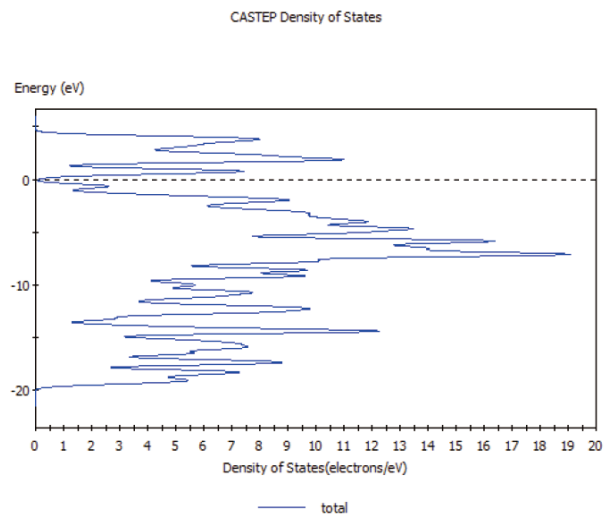
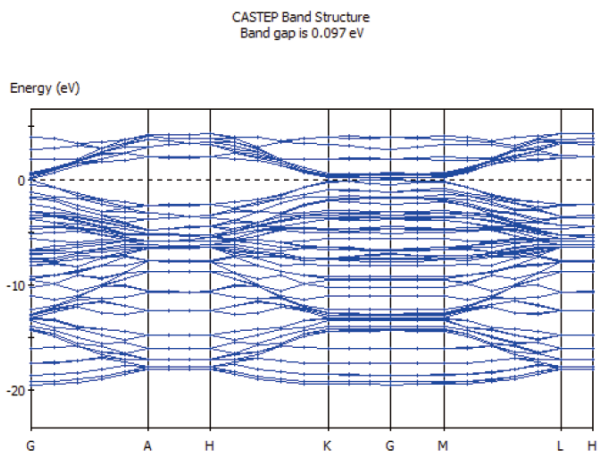


Figure 6b). Band structure deduced with functional—“GGA” and subfunctional—“RPBE”.

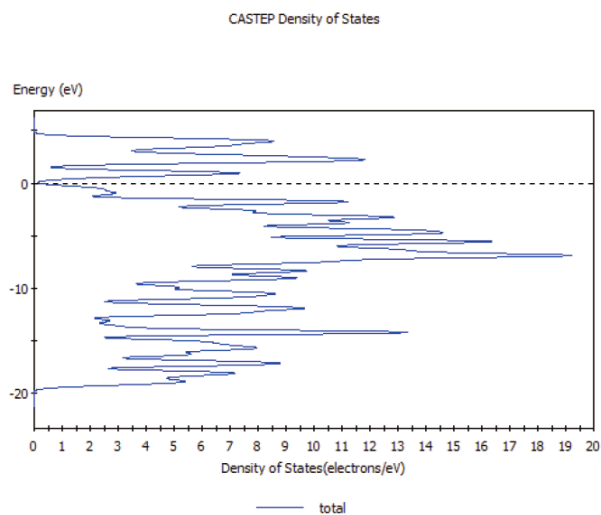
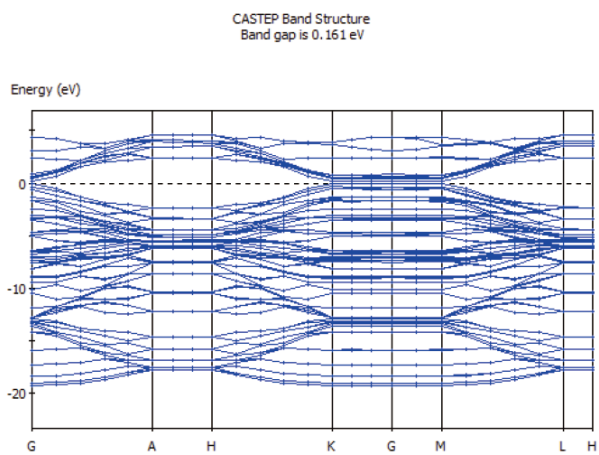


Figure 6c). Band structure deduced with functional—“GGA” and subfunctional—“PBESOL”.

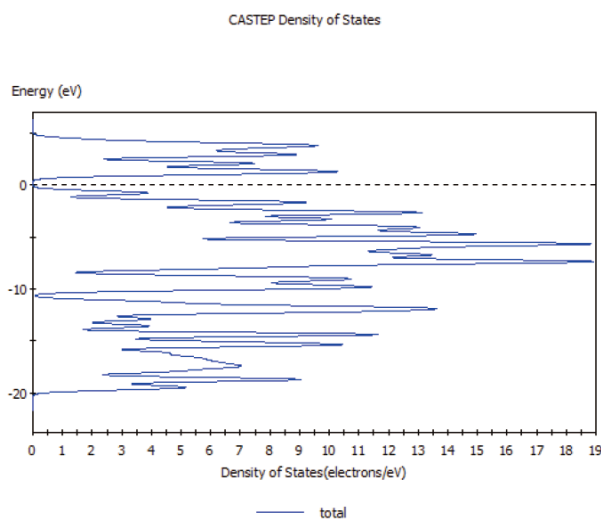
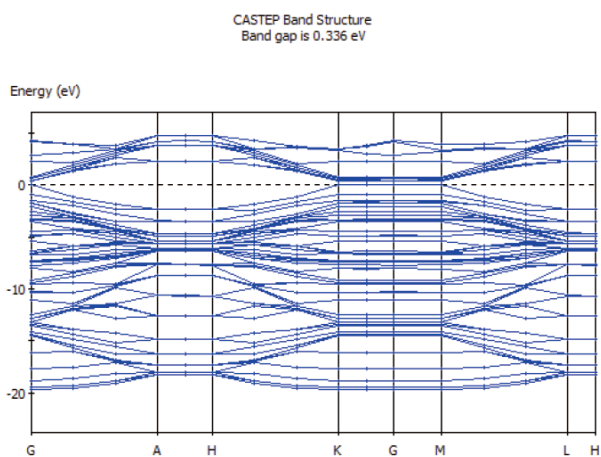


Figure 6d). Band structure deduced with functional—“GGA” and subfunctional—“WC”.

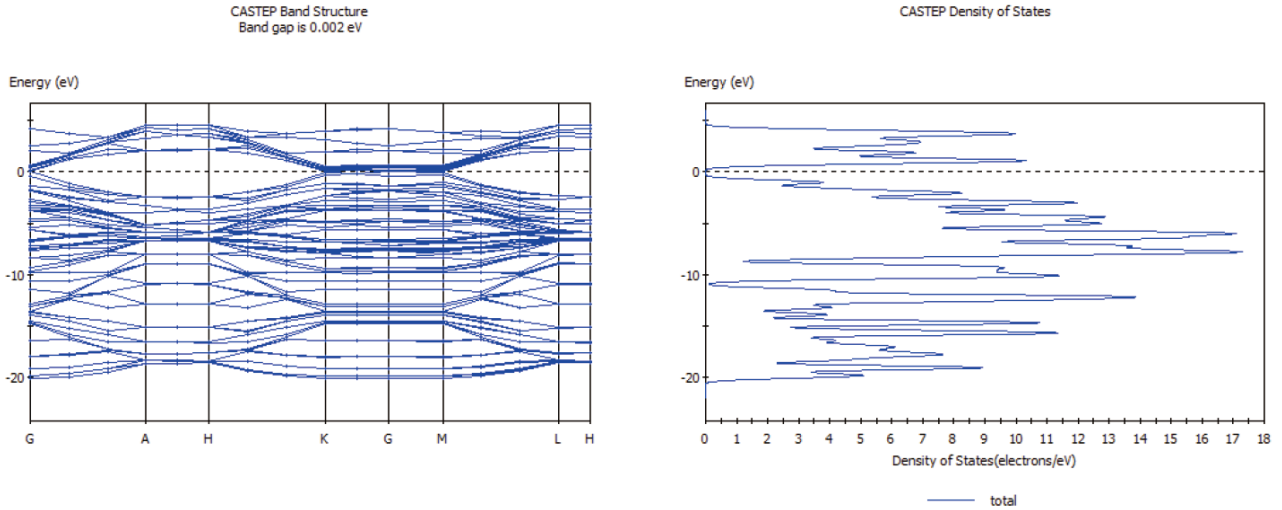


Figure 6e). Band structure deduced with functional—“GGA” and subfunctional—“PW91”.

retically (as well as experimentally by Leiber *et al.*) is somewhat unusual. This can however be explained on the basis of σ^* - π^* hybridization effects caused by the curvature of small-diameter CNTs. In these small CNTs, the π^* and σ^* states mix and repel each other, leading to lower pure π^* states.

4.3 Optical properties

Pseudo atomic calculations performed on C ($2s^2 2p^2$) converged in 17 iterations to a total energy of -145.6516 eV. Pulay density mixing treatment with Gaussian smearing was used with finite basis set correction. Partial and full phonon density of states and phonon dispersion curves were determined using linear response phonon calculation (**Figure 7**).

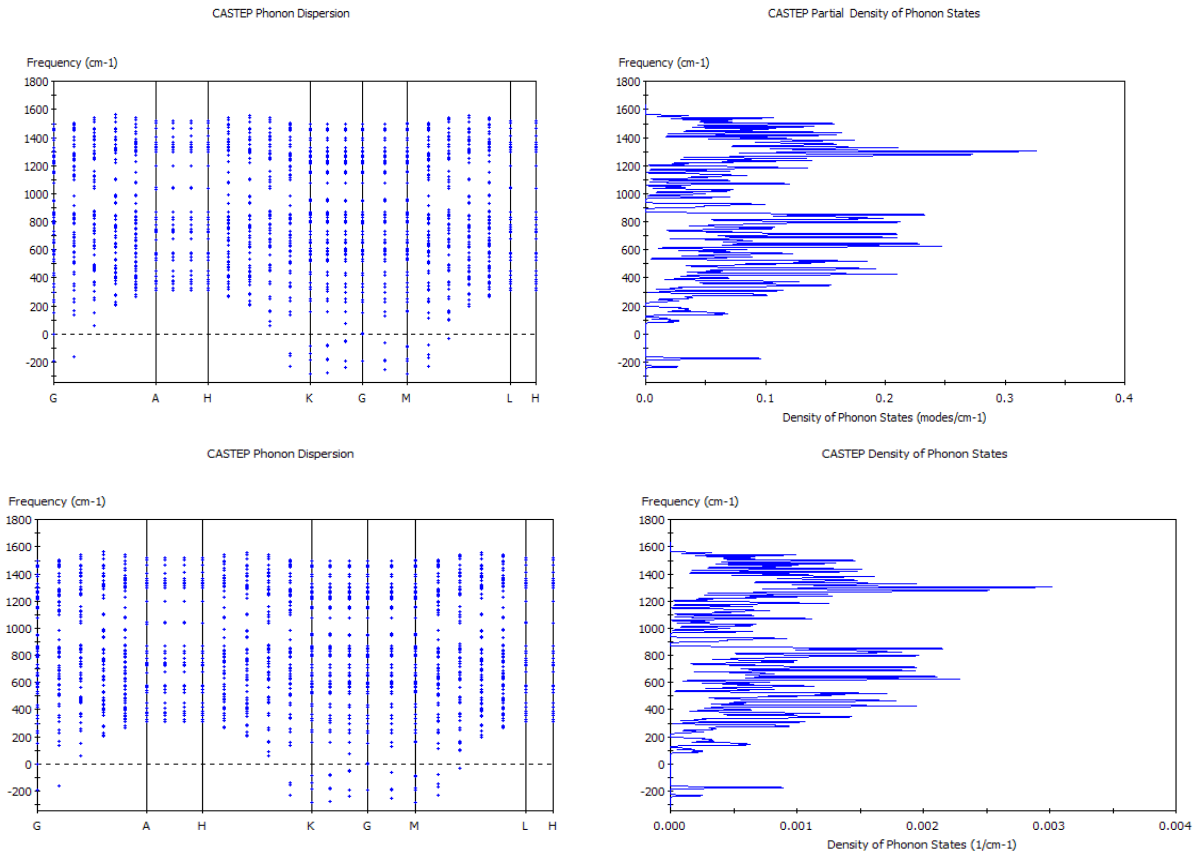


Figure 7. Phonon dispersion w.r.t. **a)** partial phonon density of states **b)** full phonon density of states.

Group theory analysis of eigenvectors reveals that the simulated structure displays Point Group 27: D6h, 6/mmm, 6/m 2/m 2/m symmetries and allows scope for 24 symmetry operations. Frequency calculation at 23 wavevectors was performed using Gonze variational method with TPA preconditioning

scheme. The optimized structure was found to belong to the point group 27: D6h, 6/mmm, 6/m 2/m 2/m. with 24 symmetry operations.

Various optical properties of the optimized geometry were investigated using 6 k-point BZ sampling over 84 bands (**Figure 8**).

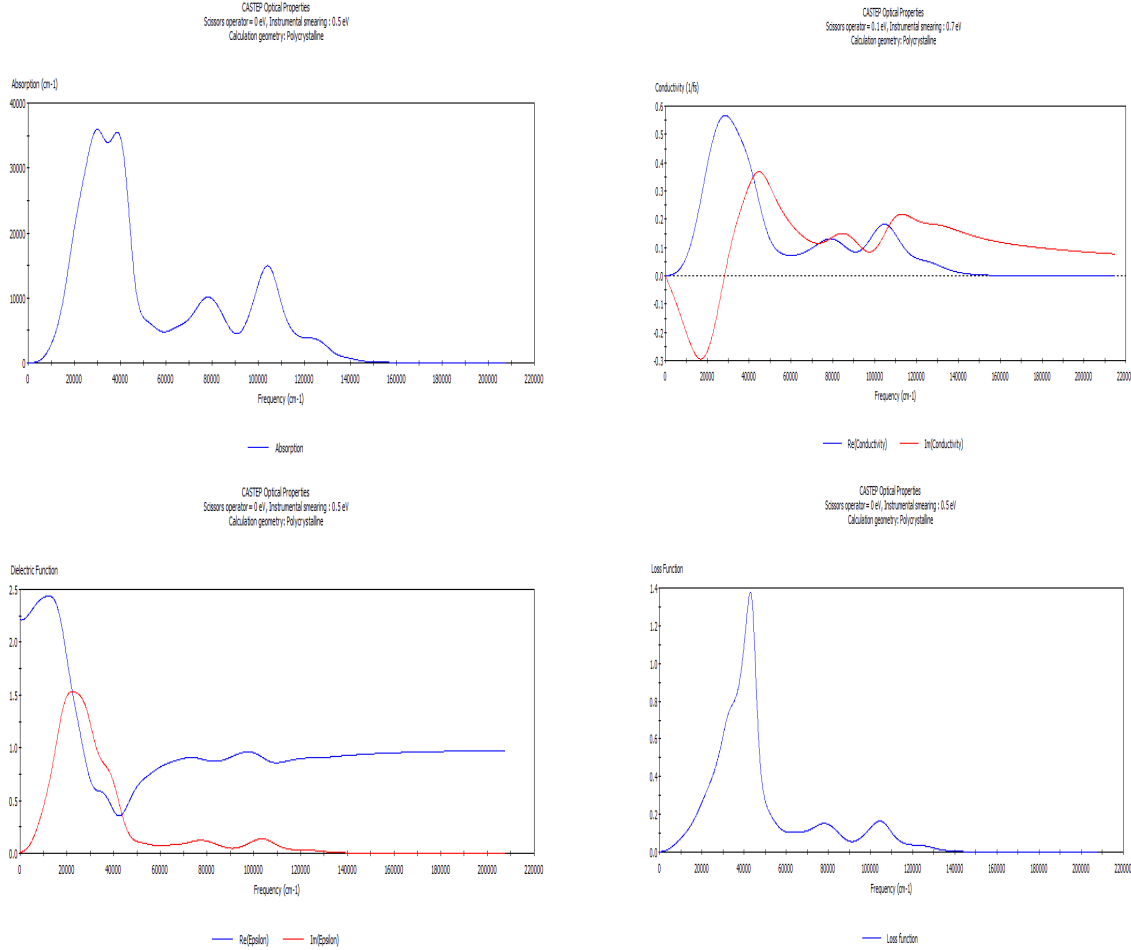


Figure 8. (9, 0) SWCNT: Optical properties **a)** absorption **b)** real & imaginary part of photoconductivity **c)** real & imaginary part of dielectric function **d)** loss function.

From the above curves, the refractive index n and the extinction coefficient k can be easily calculated for any frequency as from the Maxwell's relation:

$$n^* = \epsilon^{1/2}$$

Here n^* is a complex number. Its real part gives the refractive index n and the imaginary part gives the extinction coefficient k . i.e.

$$\text{Refractive index } n = \text{Re}(n^*)$$

$$\& \text{ Extinction coefficient } k = \text{Im}(n^*)$$

Further, the absorption coefficient α and reflection coefficient R for normally incident radiation of any frequency may also be calculated as:

$$\alpha = 2\omega\kappa/c$$

$$R = |(n^* - 1)/(n^* + 1)|^2$$

where c is the velocity of light. It is clearly evident from the definition that the reflectivity is always positive in the scheduled range of the frequency and is dimensionless. R is sometimes regarded as the index of refraction as a function of the wavelength of light used.

The conductivity $\sigma(\omega)$ is related to the dielectric constant via the relation

$$\sigma(\omega) = \sigma_1 + i\sigma_2 = -i\omega 4\pi(\epsilon - 1)$$

The loss function, which is a direct measure of the collective excitations of the systems may be calculated as $Im[-1/\epsilon]$. Some straightforward algebra may easily reveal that

$$Im[-1/\epsilon] = \epsilon_2 / \epsilon_1^2 + \epsilon_2^2$$

At the plasma frequency, the above expression attains the higher value when $\epsilon_1 \rightarrow 0$ and $\epsilon_2 < 1$.

4.4 Thermodynamic properties

Various thermodynamic properties calculated using first principles method through DFTB and CASTEP module of the software have already been discussed in **Table 1**. Also, the variation of Debye temperature with respect to the ambient temperature was determined (**Figure 9a**) for the simulated super-cell structure (**Figure 9b**).

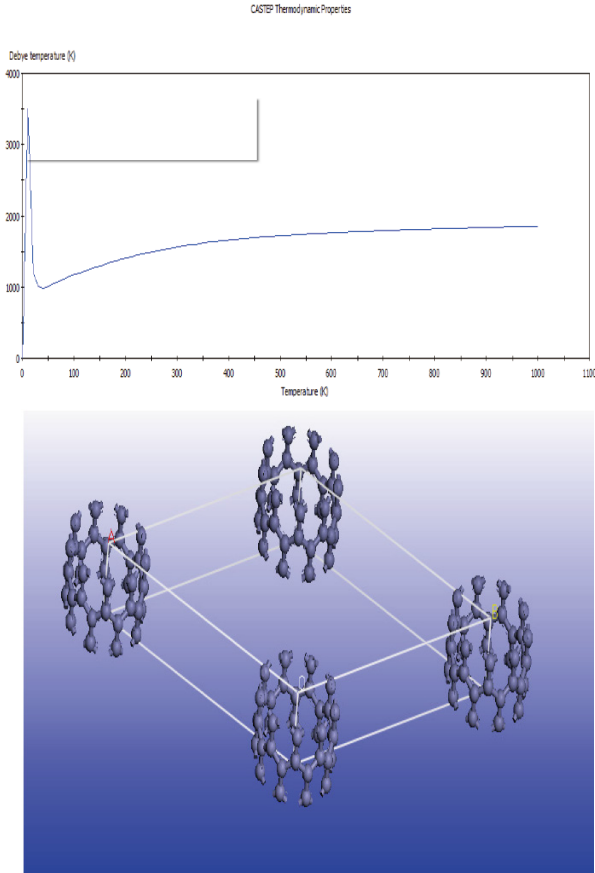


Figure 9. a). Debye temperature Vs Ambient temperature **b)** supercell approach.

It can be seen that the Debye temperature shows striking variations at extremely low temperatures. However, the general formula for the Debye temperature derived from fundamental quantum and thermodynamic assumptions has been very well known as:

$$T_D = \hbar\omega_D / 2\pi k_B$$

where ω_D is the Debye frequency and k_B is the Boltzmann constant. Having a casual look at the relation may make one wonder whether temperature dependence of the Debye temperature makes any sense. As per the relation, Debye temperature should rather be independent of the ambient temperature. At this instance, it may be emphasized that the relation arrived at involves various approximations and the Debye temperature has very important physical meaning associated to it, which must be clearly understood.

The maximum energy which can be reached by acoustic thermal vibration of a crystalline solid may be expressed as:

$$U_{acoustic}^{max} = \sum \sum \sum n N_A E_{acoustic}^{max}$$

where $E_{acoustic}^{max}$ is the maximum acoustic thermal vibration energy of an atom. Beyond this energy, interacting or organized lattice vibration does not exist and the thermodynamic behavior of the system is described by independent lattice vibration. The temperature where the collective or acoustic vibration shifts to an independent thermal vibration is the Debye temperature, which can be defined as:

$$T = T_D \text{ when } U_{acoustic}^{max} = U_{thermal}$$

In other words, Debye temperature is the temperature needed to activate all the phonon modes in a crystal. Thus, higher value of Debye temperature may be associated with stiffness of the material. The strikingly high value of the Debye temperature at extremely low ambient temperature thus points towards exceptional stiffness of the SWCNT under extreme cold conditions. At average room temperature and higher temperatures, it is more or less constant as expected.

5. Conclusions

This first principles study has been performed on (9, 0) Singlewalled Carbon Nanotube and an effort has been made to determine their electronic, optical and thermodynamic properties using CASTEP (Cambridge Sequential Total Energy Package) and DFTB (Density Functional based Tight Binding) modules of the Material Studio Software version 7.0. Various available algorithms, eigen-solvers, diagonalization techniques, density mixing methods, smearing schemes, functionals, subfunctionals have been tried out and their relative efficacy has been adjudged by comparing with the available experimental data. Combination of standard diagonalizer, smart algorithm and Anderson mixing scheme in the DFTB module and the combination of GGA functional and RPBE sub-functional in the CASTEP module have provided fairly good results. These optimized quantum-mechanical calculations not only provide an insight into the structural behaviour of nanomaterials but also present themselves as an effective, convenient and timesaving tool for predicting their physical properties. It may further be mentioned that the unit simulated was a periodic nanostructure (specific tasks on non-periodic structures not covered under the license agreement) and the length of the nanotube simulated was therefore taken at default. Variations in the length may or may not affect the results and need to be further investigated.

Compliance with ethical standards

The authors declare that the integrity of the research has been maintained and the rules of good scientific practice have been duly followed and all the ethical standards of research have been maintained.

Conflict of interest

The authors declare that they have no conflict of interest.

References

1. Iijima S. Helical microtubules of graphitic carbon. *Nature* 1991; 354: 56–58.
2. Iijima S, Ichihashi T. Single-shell carbon nanotubes of 1-nm diameter. *Nature* 1993; 363: 603–605.
3. Bethune DS, Johnson RD, Salem JR, *et al.* Atoms in carbon cages: The structure and properties of endohedral fullerenes. *Nature* 1993; 366: 123–128.
4. Wilson WL, Seabron E, Maclaren S, *et al.* (Invited) Scan-probe microwave reflectance of horizontally aligned arrays of Single-Walled Carbon Nanotubes: Nanoscale imaging of SWNT electrical properties in the Quantum Regime. *ECS Meeting Abstracts* 2015; 6: 769–769.
5. Park S, Nam JH, Koo JH, *et al.* Enhancement of ambipolar characteristics in single-walled carbon nanotubes using C 60 and fabrication of logic gates. *Applied Physics Letters* 2015; 106: 103501.
6. Verma P, Saini P, Malik RS, *et al.* Excellent electromagnetic interference shielding and mechanical properties of high loading carbon-nanotubes/polymer composites designed using melt recirculation equipped twin-screw extruder. *Carbon* 2015; 89: 308–317.
7. Hartmann S, Sturm H, Blaudeck T, *et al.* Experimental and computational studies on the role of surface functional groups in the mechanical behavior of interfaces between single-walled carbon nanotubes and metals. *Journal of Materials Science* 2015; 50: 1–17.
8. Titova LV, Pint CL, Zhang Q, *et al.* Generation of terahertz radiation by optical excitation of aligned carbon nanotubes. *Nano letters* 2015; 15: 3267–3272.
9. Battie Y, Broch L, Naciri AE, *et al.* Diameter dependence of the optoelectronic properties of single walled carbon nanotubes determined by ellipsometry. *Carbon* 2015; 83: 32–39.
10. Sharkey JJ, Stranks SD, Huang J, *et al.* Engineering nanostructures by binding single molecules to single-walled carbon nanotubes. *ACS nano* 2014; 8: 12748–12754.
11. Vosgueritchian M, Fang Y, Park S, *et al.* High-yield sorting of small-diameter carbon nanotubes for solar cells and transistors. *ACS Nano* 2014; 8(3): 2609–2617.
12. Bauschlicher Jr CW, Ricca A. Binding of NH₃ to graphite and to a (9, 0) carbon nanotube. *Physical Review B* 2004; 70(11): 115409.
13. Ricca A, Bauschlicher CW. The physisorption of CH₄

- on graphite and on a (9, 0) carbon nanotube. *Chemical Physics* 2006; 324(2): 455–458.
14. Ricca A, Bauschlicher CW. The adsorption of NO₂ on (9, 0) and (10, 0) carbon nanotubes. *Chemical Physics* 2006; 323(2): 511–518.
 15. Zhang X, Zhao J, Tange M, *et al.* Sorting semiconducting single walled carbon nanotubes by poly (9, 9-dioctylfluorene) derivatives and application for ammonia gas sensing. *Carbon* 2015; 94: 903–910.
 16. Tamburri E, Angjellari M, Tomellini M, *et al.* Electrochemical growth of nickel nanoparticles on carbon nanotubes fibers: Kinetic modeling and implications for an easy to handle platform for gas sensing device. *Electrochimica Acta* 2015; 157: 115–124.
 17. Olney D, Fuller L, Santhanam KSV. Addendum to “A greenhouse gas silicon microchip sensor using a conducting composite with single walled carbon nanotubes”. *Sensors & Actuators B: Chemical* 2014; 203: 942.
 18. Dhall S, Jaggi N, Nathawat R. Functionalized multi-walled carbon nanotubes based hydrogen gas sensor. *Sensors and Actuators A: Physical* 2013; 201: 321–327.
 19. Dhall S, Sood K, Jaggi N. A hydrogen gas sensor using a Pt-sputtered MWCNTs/ZnO nanostructure. *Measurement Science and Technology* 2014; 25: 085103.
 20. Cakmak E, Fang X, Yildiz O, *et al.* Carbon nanotube sheet electrodes for anisotropic actuation of dielectric elastomers. *Carbon* 2015; 89: 113–120.
 21. Park S, Park J, Jo I, *et al.* In situ hybridization of carbon nanotubes with bacterial cellulose for three-dimensional hybrid bioscaffolds. *Biomaterials* 2015; 58: 93–102.
 22. Mao H, Kawazoe N, Chen G. Cell response to single-walled carbon nanotubes in hybrid porous collagen sponges. *Colloids and Surfaces B: Biointerfaces* 2015; 126: 63–69.
 23. Sung SJ, Kim T, Yang SJ, *et al.* New insights into the oxidation of single-walled carbon nanotubes for the fabrication of transparent conductive films. *Carbon* 2015; 81: 525–534.
 24. Zhang Z, Geng H, Wang Y, *et al.* Temperature and voltage dependent current–voltage behavior of single-walled carbon nanotube transparent conducting films. *Applied Surface Science* 2015; 355: 1201–1205.
 25. Raïssi M, Vignau L, Cloutet E, *et al.* Soluble carbon nanotubes/phthalocyanines transparent electrode and interconnection layers for flexible inverted polymer tandem solar cells. *Organic Electronics* 2015; 21: 86–91.
 26. Rowell MW, Topinka MA, McGehee MD, *et al.* Organic solar cells with carbon nanotube network electrodes. *Applied Physics Letters* 2006; 88: 233506.
 27. Kahn BE. Patterning Processes for Flexible Electronics. *Proceedings of the IEEE* 2015; 103: 497–517.
 28. Engel M, Steiner M, Seo JWT, *et al.* Hot spot dynamics in carbon nanotube array devices. *Nano letters* 2015; 15(3): 2127–2131.
 29. Bottacchi F, Petti L, Späth F, *et al.* Polymer-sorted (6, 5) single-walled carbon nanotubes for solution-processed low-voltage flexible microelectronics. *Applied Physics Letters* 2015; 106(19): 193302.
 30. Javey A, Guo J, Wang Q, *et al.* Ballistic carbon nanotube field-effect transistors. *Nature* 2003; 424(6949): 654–657.
 31. Sazonova V, Yaish Y, Üstünel H, *et al.* A tunable carbon nanotube electromechanical oscillator. *Nature* 2004; 431(7006): 284–287.
 32. Xu X, Zhai J, Chen Y, *et al.* Well-aligned single-walled carbon nanotubes for optical pulse generation and laser operation states manipulation. *Carbon* 2015; 95: 84–90.
 33. Irita M, Homma Y. Field emission from diameter-defined single-walled carbon nanotubes. *Surface and Interface Analysis* 2014; 46(12-13): 1282–1285.
 34. Payne MC, Teter MP, Allan DC, *et al.* Iterative minimization techniques for ab initio total-energy calculations: Molecular-dynamics and conjugate gradients. *Reviews of Modern Physics* 1992; 64: 1045–1097.
 35. Hohenberg P, Kohn W. Inhomogeneous electron gas. *Physics Review* 1964; 136: B864–B871.
 36. Kohn W, Sham LJ. Self-consistent equations including exchange and correlation effects. *Physical Review Journals archive* 1965; 140, A1133–A1138.
 37. Perdew JP, Zunger A. Self-interaction correction to density-functional approximations for many-electron systems. *Physics Review B* 1981; 23: 5048–5079.
 38. Ceperley DM, Alder BJ. Ground state of the electron

- gas by a stochastic method. *Physical Review Letters* 1980; 45: 566–569.
39. Gunnarsson O, Lundqvist BI. Exchange and correlation in atoms, molecules, and solids by the spin-density-functional formalism. *Physics Review B* 1976; 13: 4274–4298.
 40. Perdew JP, Wang Y. Accurate and simple analytic representation of the electron-gas correlation energy. *Physics Review B* 1992; 45: 13244–13249.
 41. Perdew JP, Burke K, Ernzerhof M. Generalized gradient approximation made simple. *Physical Review Letters* 1995; 77: 3865–3868.
 42. Tao J, Perdew JP, Staroverov VN, *et al.* Climbing the density functional ladder: Non-empirical meta-generalized gradient approximation designed for molecules and solids. *Physical Review Letters* 2003; 91: 146401.
 43. Martin R. *Electronic structure: Basic theory and practical methods*. Cambridge, UK: Cambridge University Press; 2004.
 44. Clark SJ, Segall MD, Pickard CJ, *et al.* First principles methods using CASTEP. *Zeitschrift für Kristallographie—Crystalline Materials* 2005; 220(5-6): 567–570.
 45. Blum V, Gehrke R, Hanke F, *et al.* Ab initio molecular simulations with numeric atom-centered orbitals. *Computer Physics Communications* 2009; 180: 2175–2196.
 46. Kresse G, Furthmüller J. Efficient iterative schemes for ab initio total-energy calculations using a plane-wave basis set. *Physics Review B* 1996; 54: 11169–11186.
 47. Segall M, Linda P, Probert M, *et al.* *Materials studio CASTEP, version 2.2*. Accelrys: San Diego, CA; 2002.
 48. Matsuda Y, Tahir-Kheli J, Goddard III WA. Definitive band gaps for single-wall carbon nanotubes. *The Journal of Physical Chemistry Letters* 2010; 1(19): 2946–2950.

ORIGINAL RESEARCH ARTICLE

Synthesis of ZnO nanometer powders doped with Ce⁴⁺ ions and the photocatalytic degradation of dying wastewater

Guishan Gu, Yuanyuan Zhang, Chi Huang, Li Sun, Xueying Wang*

School of Chemistry and Material Engineering, Changshu Institute of Technology, Changshu 215500, China. E-mail: wxy62@cslg.edu.cn

Abstract

Ce⁴⁺-doped nanometer ZnO powder was synthesized by sol-gel method. The microstructures and properties of the samples were characterized through XRD, UV-Vis and FTIR. The results indicated that the Ce⁴⁺ was successfully incorporated into ZnO, and the diameter of the nanometer was about 10.7 nm. It induced the redshifting in the UV-Vis spectra. The photocatalytic activity of the samples was investigated using methylene blue (MB) as the model reaction under irradiation with ultraviolet light. The results showed that the doping of Ce⁴⁺ could increase the photocatalytic activities of ZnO nanopowders and that the best molar ratio of Ce⁴⁺ was $n(\text{Ce})/n(\text{Zn}) = 0.05$, that the surfactant was sodium dodecyl sulfate, and that the nanometer ZnO was calcinated at 550 °C for 3 hours. Meanwhile, it inspected the effect of photocatalytic efficiency through the pH of MB, the amount of catalyst, and illumination time. The experimental results revealed that the initial mass concentration of MB was 10 mg/L, that the pH value was 7–8, that the dosage of Ce⁴⁺/ZnO photo-catalyst was 5 g/L, that the UV-irradiation time was 2 h, and that the removal rate of MB reached above 85%. Under the optimized conditions, the degradation rate of real dye wastewater was up to 87.67% and the removal efficiency of COD was 63.5%.

Keywords: Ce⁴⁺-doped Nanometer ZnO Powder; Photocatalytic Degradation; Methylene Blue

ARTICLE INFO

Received: 28 December 2020
Accepted: 14 February 2021
Available online: 23 February 2021

COPYRIGHT

Copyright © 2021 Guishan Gu, *et al.*
EnPress Publisher LLC. This work is licensed under the Creative Commons Attribution-NonCommercial 4.0 International License (CC BY-NC 4.0).
<https://creativecommons.org/licenses/by-nc/4.0/>

1. Introduction

In recent years, with the increasing abundance of textile products, the substances that are difficult to biodegrade in printing and dyeing wastewater are increasing, resulting in the poor treatment effect of the simple biochemical process on printing and dyeing wastewater, which has become one of the important factors threatening the safety of water environment in China. Azo compounds and organic compounds in printing and dyeing wastewater, the discharge of phenols and amines in wastewater seriously pollute the water environment and endanger human health^[1-4]. At present, the treatment methods of dyeing wastewater mainly include adsorption, coagulation, oxidation, reduction, electrolysis, biodegradation, etc.^[5] However, above methods have the disadvantages of secondary pollution and high cost. Photocatalytic oxidation of organic pollutants is a new technology developed in recent years. Nano ZnO has become the most active research direction for the elimination and degradation of organic contaminants due to many outstanding characters, such as high catalytic activity, complete degradation, carried out at room temperature and pressure, wide application range, and other advantages^[6,7]. Nano ZnO is one of the highly active photocatalysts with great application prospects because of its high effi-

ciency and non-toxic characteristics. In recent years, its preparation and performance studies have become a hot topic in the field of catalysis research^[8-10]. It can be of extensive application.

In this paper, Zinc acetate is the raw material, ammonium ceric nitrate is dopant. Then, hydrolytic and condensation reaction in organic medium so that the solution is soldered and gelatinized, and the gel is dried and burned into powder. The samples were characterized through X-ray diffraction (XRD), ultraviolet-visible spectroscopy (UV-Vis), and FT-IR (IR). The decolorization and degradation of MB were for the model reaction. It investigated the effects of cerium doping amount, calcination temperature, and calcination time on catalytic performance. At the same time, it also studied the influence of the initial pH value of the solution, reaction time, and catalyst addition on the catalytic effect. The results show that the synthesized cerium doped nano Zinc oxide powder could effectively under UV light. This experiment has the advantages of low raw material cost, easy synthesis of catalytic materials, simple operation, low requirements for equipment, and environmental protection.

2. Experimental section

2.1 Main reagents and instruments

Main instrument: TU-1901 dual-beam UV-visible spectrophotometer (Beijing General Instrument Co., Ltd.); X-ray powder diffractor (D/max-2200/PC, Rigaku Corporation, Japan); UV-Visible spectrophotometer (Shimin Manufacturing Institute); the Fourier Infrared Spectral Analyzer (NICO-LET380, Shimjin Manufacturing Institute); Nano Ce/ZnO GGZ-125 UV HP mercury lamp (200–670 nm, 125 W, Shanghai Yaming Co., Ltd.); LG10-2.4 A high-speed centrifuge (Beijing Leibel Centrifuge Co., Ltd.).

The reagents used were analyzed pure, cerium ammonium nitrate, Zinc acetate, triethanolamine, sodium dodecyl phenyl sulfonate (SDS), polyethylene glycol-400, sodium dodecyl sulfate (SDBS), sodium stearate, oxalic acid (AR, Jiangsu Strong Chemical Co., Ltd.); methylene blue (AR, Shanghai Maikun

Chemical Co., Ltd.).

2.2 Preparation of nano Ce/ZnO

Dissolve 11.34 g of oxalic acid into 100 ml of absolute ethanol, then it obtains solution A. Dissolve 7.859 g of Zinc acetate ($\text{Zn}(\text{AC})_2 \cdot 2\text{H}_2\text{O}$) into 50 ml of distilled water, then add an appropriate amount of surfactant and ceric ammonium nitrate solution to obtain solution B. Then, slowly drop solution B into an under vigorous stirring, react for about 1.5 h, and keep it in a constant temperature (80 °C) water bath for 0.5 h. It obtains the sol. The sol was washed twice with distilled water and ethanol, dried in an 80 °C drying oven for 2 h, calcined in a muffle furnace for a certain time, cooled and ground, and finally prepared the sample. Except that ceric ammonium nitrate solution should not be added, the nano ZnO was prepared according to the above steps.

2.3 Characterization of nano Ce/ZnO

The crystal phase of the product was analyzed by XRD and Scherrer formula [$D(hkl) = K\lambda/\beta\cos\theta$]. The average grain size of the sample was calculated, the UV absorption spectrum of nanomaterials was measured by UV-Vis spectrophotometer, and the infrared spectrum of Ce/ZnO crystal was measured by Fourier infrared spectrum analysis.

2.4 Determination of the photocatalytic degradation efficiency of 1.4 nano Ce/ZnO

Weigh some amount of photocatalyst, add it to MB solution of 20 mL 10 mg/L, stir and degrade it for some time under UV irradiation, take a certain volume of solution and centrifuge it in a centrifuge tube at high speed for 5 min, take the supernatant, analyze and measure it with UV-1901 UV-V is spectrophotometer. During measurement, take distilled water as blank and measure the absorbance at 665 nm, that is, the absorbance of the liquid sample A at this time. Set the absorbance of MB solution without catalyst at 665 nm as A_0 , and calculate the degradation rate according to the following formula.

$$D\% = (A_0 - A) / A_0 \times 100\%$$

3. Experimental results and discussion

3.1 Characterization of nano Ce/ZnO

3.1.1 XRD analyses

Figure 1 shows the XRD spectra of pure nanoscale ZnO prepared with doped cerium nanosize ZnO(n(Ce): n(Zn) = 0.05 under optimal conditions. As shown from Figure 1, all diffraction peaks are sharp, indicating that the well crystalline generated under this condition^[11]. Compared to the standard map, it should be hexagonal, and the peaks became slightly wider after doping, but no cerium oxide peak was observed, indicating the incorporation of Ce into ZnO. The particle size of Ce/ZnO was approximately 10.7 nm, while undoped nano ZnO was about 17 nm.

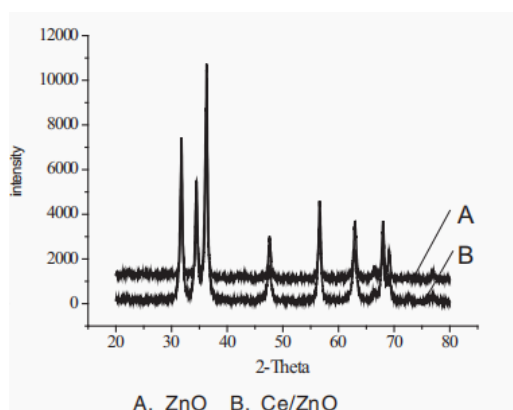


Figure 1. XRD patterns of nano ZnO and CE/ZnO.

3.1.2 Ultraviolet analysis

Figure 2 shows the UV absorption spectra of pure ZnO and cerium-doped zinc oxide prepared under optimal conditions. As shown from Figure 2, the absorption intensity of the nano zinc oxide doped UV region is much higher than the undoped nano zinc oxide with a small redshift in the UV peak, indicating successful incorporation of rare earth Ce ions into the ZnO lattice and a better crystal mass^[12,13].

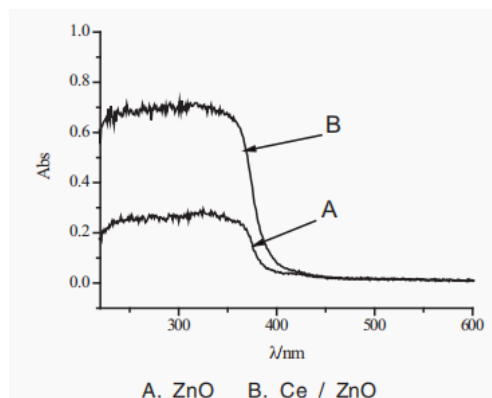


Figure 2. UV spectra of Ce⁴⁺/ZnO and ZnO.

3.1.3 Infrared spectrum analysis

It can be seen from the infrared spectrum of Figure 3 that there is a strong absorption peak around 430 cm⁻¹, which is the skeleton peak of ZnO, indicating that it got ZnO after calcination^[14]. There is a wide absorption peak at 3380–3600 cm⁻¹, and it is caused by the stretching vibration of -OH group that forms intermolecular hydrogen bond, indicating that there is strong adsorbed water on the surface of small-size Ce/ZnO nanoparticles. The adsorption activity is high, which is conducive to improving the photocatalytic properties of Ce/ZnO.

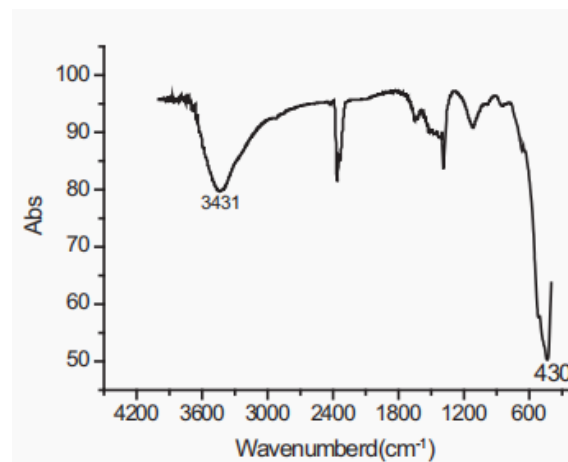


Figure 3. Infrared Spectro Spectra (FT-IR) plots of nano zinc oxide doped with cerium.

3.2 Optimization of the preparation conditions for the nanoscale Ce/ZnO

3.2.1 Effect of the different doping ratios on the photocatalytic properties

Weigh 0.1000 g of ZnO (n(Ce):n(Zn) = 0, 0.01,

0.05, 0.10, 0.20) respectively, use sodium dodecyl sulfonate as surfactant, add the catalyst with calcination temperature of 550 °C and calcination time of 3 h to 20 ml of 10 mg/L MB solution, and irradiate it under UV lamp for 2 h. Then centrifuge the reaction solution at high speed and take the supernatant. The absorption spectrum and absorbance were measured with an ultraviolet spectrometer. The absorbance at 665 nm was measured with distilled water as blank. The experimental results are shown in **Figure 4**.

As can be seen from **Figure 4**, when $n(\text{Ce}):n(\text{Zn}) = 0.05$, the effect of nano Zinc oxide on MB reached the maximum degradation, and the degradation rate of MB was about 26.27%, higher than that of pure zinc oxide. The possible reason is that some Ce^{4+} ions enter the ZnO lattice during heat treatment, which result in local lattice defects and charges imbalance. To achieve charge balance, some OH^- will be adsorbed on the surface of the catalyst, which can combine with holes generated under UV irradiation to form $\bullet\text{OH}$, which can react with the adsorbed substances on the surface. In addition, some Ce^{4+} ions cover the surface of ZnO grains in the form of small clusters of CeO_2 , while Ce^{4+} ions can generate electron-hole pairs under UV excitation, which may play the synergism with the generation of electron-hole pairs by photocatalysts^[16]. The doped photocatalyst also has a strong adsorption capacity for photons, promotes the migration of photons to the catalyst surface, prevents the simple recombination of electron-hole pairs, and improves photocatalytic efficiency. However, when the content of Ce^{4+} further increases, CeO_2 covers part of the surface of zinc oxide nanoparticles, affecting the light absorption of zinc oxide^[17]. Therefore, the optimal doping degree of cerium is $n(\text{Ce}):n(\text{Zn}) = 0.05$.

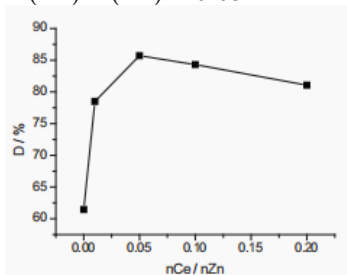


Figure 4. Effect of cerium doping on the catalytic properties of zinc oxide nanomaterials.

3.2.2 Effect of different calcination temperatures on the photocatalytic degradation effects

Figure 5 shows the photocatalytic activity of cerium doped zinc oxide nanoparticles obtained at different calcination temperatures (450–650 °C) under ultraviolet light. It can be seen from the figure that the catalytic activity of cerium doped zinc oxide nanoparticles obtained at 550 °C under ultraviolet light is the highest, and the degradation rate of MB is the highest at 2 h. The calcination temperature affects the photocatalytic performance of nano zinc oxide. In the temperature range of 500–600 °C, the catalyst has a good degradation effect on MB, but 550 °C is the highest, and the degradation rate decreases rapidly when it exceeds 600 °C. It may be that the nano zinc oxide crystal obtained at 550 °C develops best, and with the further increase of temperature, the growth rate of the ZnO crystal nucleus is accelerated, resulting in the bigger particle size and agglomeration in some parts^[15]. The particle increases while the specific surface area decreases, resulting in the decline of photocatalytic performance. Therefore, the calcination temperature is 550 °C.

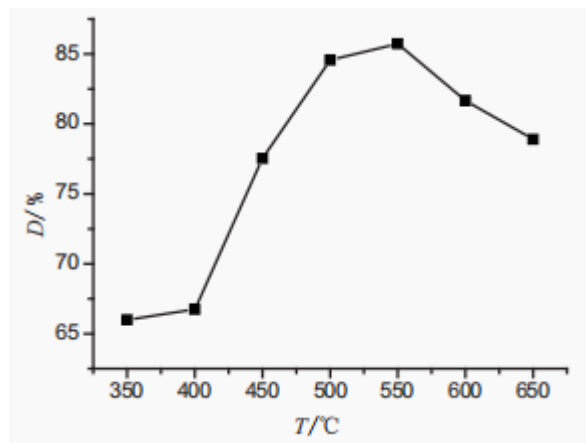


Figure 5. Effect of the calcination temperature on the photocatalytic activity of the cerium-doped nanoscale ZnO.

3.2.3 Effect of different calcination times on the photocatalytic properties

Figure 6 shows the photocatalytic activity of cerium doped zinc oxide nanoparticles under ultraviolet light when $n(\text{Ce}):n(\text{Zn}) = 0.05$, the surfactant is SDS, the calcination temperature is 550 °C, and

calcination time is different. It shows from the figure that the calcination time is in the range of 3–3.5 h, and the degradation rate of MB reaches about 85%. Because the longer the calcination time, the more small grains will be formed by the precursor. If burning time is too short, the precursor can not sufficiently decompose. Thus, the particle size of the product is coarse. Therefore, when the time is 3.0 h, the precursor can sufficiently decompose, and there are not too large grains, so the photocatalytic degradation efficiency is the highest.

3.2.4 The effect of different surfactants

Taking $n(\text{Ce}) : n(\text{Zn}) = 0.05$, calcination temperature 550 °C, calcination time 3.0 h, adding a small amount of different surfactants, the prepared catalyst is 0.1 g, and adding 20 ml 10 mg/L MB for catalytic degradation for 2 h. The experimental results show that the catalyst prepared by adding a small amount of triethanolamine and sodium dodecyl sulfonate has a good effect on the degradation of MB. It can effectively reduce the agglomeration of nano zinc oxide, but considering the impact on the environment, the selected surfactant is sodium dodecyl sulfonate^[18].

In summary, the doping degree of CE is $n(\text{Ce}) : n(\text{Zn}) = 0.05$, the burning temperature is 550 °C, the burning time is 3.0 h, and the surfactant is sodium dodecyl sulfonate, is the optimum conditions for the synthesis of the photocatalyst.

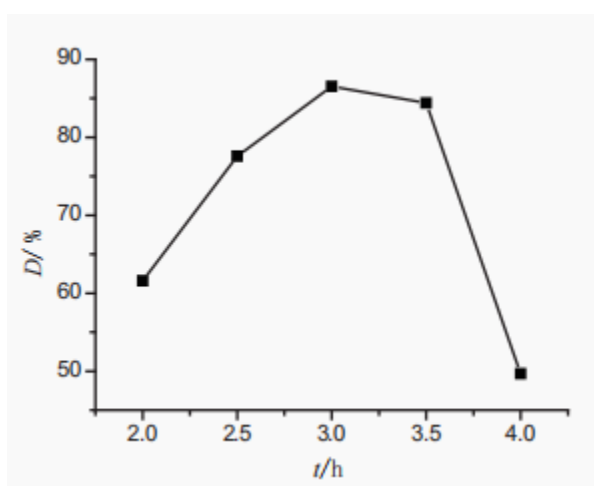


Figure 6. Effect of burning time on the photocatalytic properties of nano Ce/ZnO.

3.3 Optimization of MB degradation conditions

3.3.1 Effect of the initial pH values of the dye solution on the catalytic degradation

Take 8 parts of 20 ml and 10 mg/L MB solution, adjust the pH values of the solution to 3, 4, 5, 6, 7, 8, 9 and 10 with 1 mol/L HCl and NaOH individually, add 0.1000 g catalyst, and carry out photocatalytic degradation for 2 h. The experimental results are as in **Figure 7**. It shows from **Figure 7** that cerium doped ZnO has a high degradation rate of MB under neutral and alkaline conditions, but a low degradation rate under acidic conditions. However, when pH = 4, the degradation rate suddenly increases and then decreases. It may be due to that the change of catalyst surface charge caused by the change of pH value and affecting the adsorption behavior on the catalyst surface^[19,20]. MB ($\text{C}_{16}\text{H}_{18}\text{N}_3\text{S}^+$) is a cationic dye. Under acidic conditions, MB molecules cannot be effectively adsorbed on the catalyst surface, resulting in low photocatalytic capacity. Under alkaline conditions, OH^- can trap holes, and the generated $\bullet\text{OH}$ harms photocatalytic degradation. Solution plays a vital role. With the increase of pH value, the OH^- content in the solution increases, and the adsorption ability of MB enhances. The combined action of the two makes MB have a high photocatalytic degradation rate under alkaline conditions^[21]. Excessive acidity and alkalinity may cause changes in the structure of nano ZnO, which is not conducive to photocatalytic degradation. Therefore, the pH value of photocatalytic degradation of MB is 7.

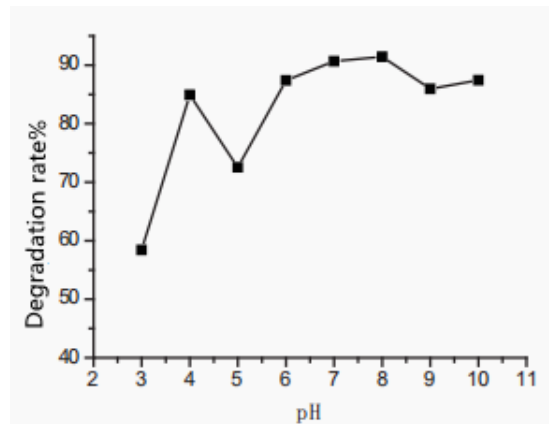


Figure 7. Effect of initial pH on MB degradation rate.

3.3.2 Effect of the catalyst dosage on the photocatalytic degradation of MB

Under the conditions of MB solution concentration of 10 mg/L, pH = 7 and photocatalyst dosage of 1 g/L, 2 g/L, 3 g/L, 5 g/L, 7 g/L and 10 g/L individually, it studied the effect of catalyst dosage on the degradation rate of MB solution. It shows from Figure 8 that the photocatalytic degradation efficiency of MB increased rapidly with the increase of catalyst dosage in the range of 1–5 g/L. When the dosage exceeds 5 g/L, the increase decreases. If the dosage of nanocatalyst continues to increase, the photocatalytic degradation efficiency of MB decreases. The reason is that when the dose of catalyst is small, it cannot utilize the light energy adequately, and the carrier produces less. With the increase of the dose of catalyst, it means more electron-hole pairs form, which accelerates the photocatalytic reaction when the amount of catalyst reaches. At 7 g/L, the degradation rate reaches the maximum. However, when the number of catalyzers increases to a certain extent, the excessive catalyzers will cause light scattering, coupled with the shielding effect between catalyst particles, so that photons cannot be used effectively, resulting in the decline of photocatalytic degradation rate^[22]. Considering the cost and environmental effects, the amount of catalyst is 5 g/L.

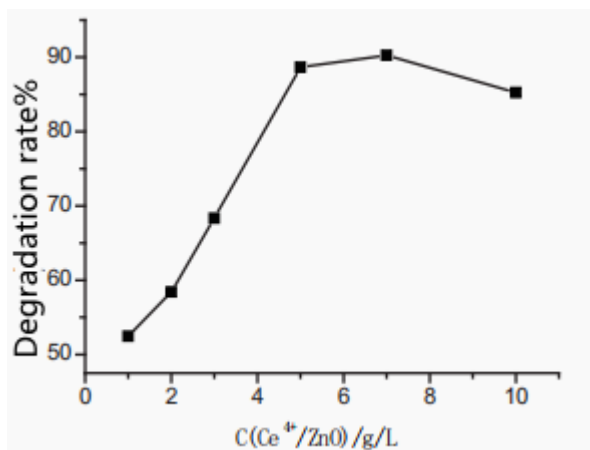


Figure 8. Effect of the catalyst dosage on the photocatalytic degradation of methylene blue.

3.3.3 Effect of light time on the photocatalytic degradation of MB

Weigh 6 parts of 0.1000 g catalyst, add 20 ml of

10 mg/L MB solution with a pH value of 7 respectively, and stir with the magnetic force for 20 min, 40 min, 60 min, 90 min, 120 min, and 150 min under the irradiation of UV light to investigate the influence of illumination time on the catalytic effect. The results show in Figure 9. It shows that in the initial stage of photocatalysis, the catalyst degradation rate of MB increases rapidly. When the photocatalytic time exceeds 60 min, the increased degradation rate slows down. It is mainly due to the strong adsorption capacity of nano materials for MB in the initial stage and more active sites on the catalyst surface, so the photocatalytic efficiency increases rapidly. With the extension of photocatalytic time, the oxygen molecules in water constantly capture electrons, and the final generation with the amount of highly active superoxide anion (O^{2-}) and hydroxyl radical (OH) also increased. Therefore, the degradation rate increased with the extension of illumination time, but the adsorption of nanomaterials gradually became saturated during the reaction. Some intermediates accumulated in nanomaterials and occupied some active sites, resulting in the reduction of photocatalytic efficiency of photocatalysts. Therefore, the increase of degradation rate slows down, that is the cause the degradation time is 2 h.

In conclusion, the optimum conditions for photocatalytic degradation are as follows: pH is neutral or weakly alkaline, catalyst mass is 5 g/L, and illumination time is about 2 h.

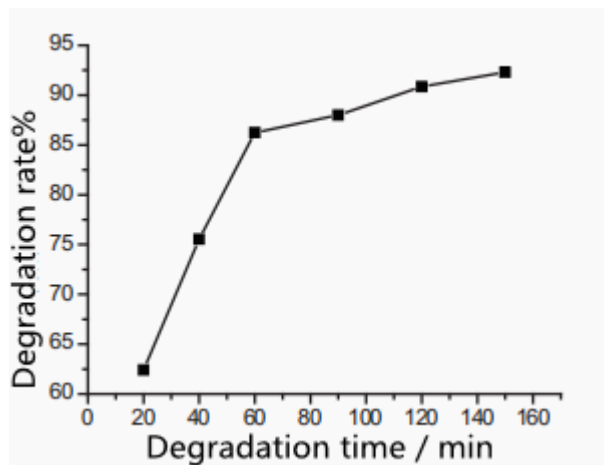


Figure 9. Effect of light time on Ce/ZnO photocatalytic methylene blue.

3.4 Practical application of the photocatalyst

It measured the actual dye wastewater in the experiment. The dye wastewater from a printing and dyeing enterprise was taken, and the decolorization rate and COD_{cr} removal rate were measured by photocatalytic degradation method and national standard method separately. Put 100 ml of the diluted wastewater into a beaker, add 0.5000 g of self-made Ce/ZnO catalyst, adjust the pH value to 7, and stir the reaction under UV light for 2 hours. Measure the decolorization rate and COD_{cr} removal rate separately. The decolorization rate was 87.67%, the COD_{cr} removal rate was 63.5%.

After 2 hours of light degradation, the dye wastewater is almost colorless, but the COD value is still high. It speculates that the organic dye molecules may not completely convert into small molecule inorganic substances in the process of light degradation. How to improve the removal efficiency of COD by photocatalyst needs further research.

4. Conclusion

a. Characterized by XRD, UV-vis and FTIR, the particle size of Ce/ZnO nanopowder prepared in this experiment is smaller than that of pure nano ZnO. The absorption ability in the UV-vis region is stronger and moves to the visible region. The broad absorption peak at 3380–3600 cm⁻¹ shows that there is strong adsorbed water on the surface of Ce/ZnO nanoparticles and high adsorption activity. These properties will help to improve the photocatalytic ability of Ce doped nano ZnO.

b. Taking MB as the photocatalytic model, the effects of cerium doping, calcination temperature and calcination time on photocatalytic performance were studied. The results showed that the degradation of MB by nano ZnO reached the maximum when n(Ce): n(Zn) = 0.05, calcination temperature 550 °C, calcination time 3.0 h and surfactant SDS.

c. It studied the effects of pH value, photocatalyst dosage, and photocatalytic time on the photocatalytic degradation of MB by Ce/ZnO nanoparticles. The results showed that the initial pH value of MB had more influence on the degradation rate, and the

degradation efficiency was higher under neutral and weak alkaline conditions. However, the hydrolysis rate is lower in strong acids. The dosage of catalyst also affects the degradation. When the dosage of catalyzers reaches 5 g/L, the catalytic efficiency is higher. The light application time also has an impact on the degradation. The changing trend shows more growth rate in the initial stage, and the increase slows down after 1 h of reaction. The longer the time is, the higher the degradation rate is. In view of the cost, the time should be 2 h after the reaction starts.

d. The composition of the actual dye wastewater is complex. The decolorization rate is 87.67% and the COD_{cr} removal rate is 63.5% when it is catalyzed by Ce/ZnO nano photocatalyst under ultraviolet light for 2 h.

Conflict of interest

The authors declare that they have no conflict of interest.

Acknowledgements

Changshu science and Technology Bureau project “preparation of composite nano photocatalytic materials and soil remediation” (CS201110); “Synthesis of micro nano magnetic photocatalyst and its application in printing and dyeing wastewater treatment”.

References

1. Department of science and technology standards, State Environmental Protection Administration. Technical guide for pollution prevention and control of printing and dyeing wastewater. Beijing: China Environmental Science Press; 2002. p. 75.
2. Messina PV, Schulz PC. Adsorption of reactive dyes on titania-silica mesoporous materials. *Journal of Colloid and Interface Science* 2006; 299(1): 305–320.
3. Verma AK, Dash RR, Bhunia AP. A review on chemical coagulation/flocculation technologies for removal of colour from textile wastewaters. *Journal of Environmental Management* 2012; 93(1): 154–168.
4. Sun L, Yu C. Status and prospect of dyeing and print-

- ing wastewater treatment. *Textile Auxiliaries* 2009; 26(12): 1–6.
5. Zhuang Y. On the reuse of the iron-containing waste residues in the wastewater treatment. *Environmental & Pollution & Control* 1997; 19(6): 27–29.
 6. Aber S, Mehrizade H, Khataee AR. Preparation of ZnS nanocrystal and investigation of its photocatalytic activity in removal of CI acid blue 9 from contaminated water. *Desalination and Water Treatment* 2011; 28(1-3): 92–96.
 7. Sun JH, Dong SY, Wang YK, *et al.* Preparation and photocatalytic property of a novel dumbbell-shaped ZnO microcrystal photocatalyst. *Journal of Hazardous Materials* 2009; 172(2-3): 1520–1526.
 8. Lv H, Jiang P, Liu, Y, *et al.* Preparation and photocatalytic degradation properties of ZnO nanopowers with different morphologies. *Journal of Functional Materials* 2010; 41(2): 292–295.
 9. Li Q, Chen X, Jiang W. Preparation of nano zinc oxide and development of nanofunctional textiles. *Dyeing Technology* 2003; 25(5): 16–18.
 10. Li F, Yan B, Shao C, *et al.* Correlation of Nano-Ce-ZnO structure with its desulfurizing performance at ambient temperature. *Chinese Journal of Inorganic Chemistry* 2006; 22(10): 1895–1898.
 11. Liu G, Xu G, Luo Q. Preparation of surface modified nano zinc oxide by sol-gel method. *Electronic Components and Materials* 2005; 24(10): 36–38.
 12. Lang J, Li X, Liu X, *et al.* Preparation and characterization of ZnO nanorods. *Jilin Normal University Journal (Natural Science Edition)* 2009; 30(2): 35–37.
 13. Justicia P, Ordejón G, Canto G, *et al.* Designed self-doped titanium oxide thin films for efficient visible-light photocatalysis. *Advanced Materials* 2002; 14(19): 1399–1402.
 14. Abdul M, Akbar A. Red shift of near band edge emission in cerium implanted GaN. *Journal of Physics D: Applied Physics* 2009; 42(4): 45412–45415.
 15. Shang X. Preparation and photocatalytic properties of nano zinc oxide [MSc thesis]. Qufu: Qufu Normal University; 2009.
 16. Qourzal S, Barka N, Tamimi M, *et al.* Photodegradation of 2-naphthol in water by artificial light illumination using TiO₂ photocatalyst: Identification of intermediates and the reaction pathway (in Chinese). *Applied Catalysis A: General* 2008; 334(1-2): 386–393.
 17. Zhang Z. Preparation of N-Ce Codoped Nano-ZnO and the study of its capability [Master's thesis]. Suzhou: Suzhou University; 2010. p. 11–14.
 18. Zhu W. The Study on the preparation and photocatalytic capability of Nano Zinc Oxide [Master's thesis]. Shanghai: East China Normal University; 2008. p. 27.
 19. Li F, Gu, G. Photocatalytic decoloration and degradation of methylene blue in TiO₂ suspension. *Environmental Pollution & Control* 1999; 21(6): 1–4.
 20. Satoko H, Yasuaki K, Isao Y, *et al.* Development of hydrophilic outside mirror coated with titania photocatalyst. *JSAE Review* 2000; 21(1): 97–102.
 21. Shang F, Shi Z, Du H. Degradation of dye wastewater by ZnO nanorod photocatalyst. *Guangzhou Chemical Industry* 2012; 40(17): 74.
 22. Cao J, Guo JB, Li PF, *et al.* Complexation between pentaerythritol derived bis(crown ether)s and CBPQT⁴⁺ salt: ion-controlled switchable processes and changeable role of the CBPQT⁴⁺ in Host-Guest systems. *Journal of Organic Chemistry* 2011; 76(6): 1644–1652.

ORIGINAL RESEARCH ARTICLE

Influence of flow rate on the transport of nTiO₂ and phosphate and its modeling

Gang Feng^{1,2}, Nan Xu^{1,2*}, Zuling Li^{1,2}, Yuhe Cao^{1,2}, Keqing Sun^{1,2}

¹School of Chemistry, Biology and Material Engineering, Suzhou University of Science and Technology, Suzhou 215009, China. E-mail: nanxu@mail.usts.edu.cn

²Jiangsu Key Laboratory of Environmental Functional Material, Suzhou 215009, China

ABSTRACT

We studied Zeta potentials of nanoparticles titanium dioxides (nTiO₂) in different concentration of NaNO₃ and phosphate (P) solutions. In addition, the effect of flow rate on the transport of nTiO₂ in P was investigated at pH = 6.5. Experimental results show that the Zeta potential of nTiO₂ is compressed with the increasing ion concentration (IC) of NaNO₃ at pH = 6.5. The negative charge increases with the augment of P. Therefore, the high P and low NaNO₃ induce the stabilization of nTiO₂ aggregates. The transport experiments suggest that the rapid flow rate is favorable for the transportability of nTiO₂ and soluble phosphate. The breakthrough transport curves (BTCs) of nTiO₂ in sand columns can be fitted well with two-site kinetic attachment model. The modeling results suggest that the values of first-order attachment rate coefficients (k_2) and detachment rate coefficients (k_{2d}) on site 2 and first-order attachment rate coefficients (k_1) on site 1 are responsible to the attaching efficiency of nTiO₂ on sands and their transportability.

Keywords: nTiO₂; Zeta Potential; Transport; Phosphate

ARTICLE INFO

Received: 14 January 2021
Accepted: 28 February 2021
Available online: 6 March 2021

COPYRIGHT

Copyright © 2021 Gang Feng, *et al.*
EnPress Publisher LLC. This work is licensed under the Creative Commons Attribution-NonCommercial 4.0 International License (CC BY-NC 4.0).
<https://creativecommons.org/licenses/by-nc/4.0/>

Nano titanium dioxide (nTiO₂) is one of the mass-produced metal oxide nano materials. Due to the ultra-high photocatalytic ability of nano materials, it has been more and more used in various fields and commercial products^[1-5]. In mass production and wide application, some nTiO₂ cannot be avoided to be released into natural water and soil environment. A large amount of evidence shows that after artificial nTiO₂ enters the water body, it has adverse effects on aquatic organisms, including microorganisms, algae, invertebrates and fish^[6,7]. Therefore, the study of the relationship between nanoparticles attached to soil saturated particles and nanoparticles in soil particle saturated porous media has become a hot spot in the study of the environmental behavior of nanoparticles. At present, the artificial nano materials studied internationally are mainly industrial fullerene nC₆₀, carbon nanotubes and silica nanoparticles. The mobility of these nano materials in saturated porous media is different. The flow rate of solution, ion concentration and surface potential of nanoparticles will affect their migration behavior^[8,9]. Therefore, it is necessary to explore the changes of surface properties of nTiO₂ under different environmental conditions and its migration in the natural world. In agricultural production and people's life and production, a large number of phosphorus containing substances are used, which makes phosphorus containing substances enter into

soil and water. nTiO₂ particles have certain adsorption on phosphate, which changes its surface properties, and finally changes the migration properties of nTiO₂ in soil^[10,11]. Therefore, this paper will explore the changes of surface Zeta potential of nTiO₂ under different environmental conditions and the effects of different environmental water flow velocities on its migration in phosphate environment.

1. Materials and methods

1.1 Preparation of the nTiO₂ phosphate suspension

All chemicals used in the experiment are analytical pure and purchased from Sinopharmgroup. 20 nm nTiO₂ was purchased from Shanghai Gaoquan Chemical Co., Ltd., 1 g·L⁻¹ TiO₂ was weighed and dissolved in 0.1 mM phosphate solution (NaH₂PO₄) and 10 mM NaNO₃ electrolyte solution, and ultrasonic was used with an ultrasonic cleaner (KQ 2200B, ultrasonic instruments Co., Ltd., Hunshan, China) for 30 mins for migration experiment.

1.2 Test of the Zeta potential on the nTiO₂ particle surface

Accurately weigh 0.01 g of TiO₂ particles into a 100 mL beaker and prepare suspensions under different conditions. The different conditions are electrolyte NaNO₃ concentration (0.1–5 mM) and phosphate solution (0.1–5 mM), in which the pH value of all suspensions is adjusted to pH = 6.50 with diluted HCl and NaOH. Then, the suspension of nTiO₂ particles with adjusted pH value was placed on the ultrasonic instrument for 30 mins. After ultrasonic treatment, the suspension was placed on a stirrer and stirred for 30s. Finally, the Zeta potential of nTiO₂ particles was tested with Marvin Nano-ZS90. All samples were tested three times, and the average value was taken as the final Zeta potential value.

1.3 Migration experiment of quartz sand column

Referring to Fang, *et al.*, column leaching experiment was used to study the migration behavior of nTiO₂^[2]. A chromatographic column with a length

of 17.5 cm and an inner diameter of 25 mm was selected. The chromatographic column was filled with quartz sand and saturated with deionized water for 12 h. Inject 200 ml (10 mM NaNO₃) of background solution into the saturated chromatographic column with a peristaltic pump, and collect 10ml of effluent every 10 mins with an automatic sample partial collector (BS-100A, Huxi, Shanghai). Then, about 5 pore volumes (PV) of the nTiO₂ suspension were injected into the chromatographic column, and 20 tubes of effluent were collected with an automatic partial collector. After the suspension is injected, continue to inject 5 PV NaNO₃ background solution, collect the effluent and wait for test.

1.4 Analysis and determination of the titanium and phosphorus concentrations

Analysis and determination of titanium (TI): take 2 mL of nTiO₂ suspension and put it into a 25 mL beaker, add 1–2 mL of sulfuric acid ammonium sulfate digestion solution to the beaker, place it on a heating plate and heat it at 220 °C for 1–1.5 h. After digestion, transfer the solution to a 50 mL volumetric flask for constant volume, then transferring 5 mL into a 50 mL volumetric flask, and successively adding 8 mL ($V_{\text{hydrochloric acid}}:V_{\text{deionized water}} = 5:1$) dilute hydrochloric acid, 2 ml (10 g·L⁻¹) ascorbic acid and 10 mL diantipyrylmethane hydrochloride solution with constant volume. The concentration of Ti was measured with an ultraviolet spectrophotometer (TU-1901, Shimadzu, Japan) at a wavelength of 390 nm. Dilute 1000 mg·L⁻¹ titanium standard stock solution (matrix is 0.15 mol·L⁻¹ HNO₃) into a series of standard solutions (concentration gradient is 1–5 mg·L⁻¹), and then obtain the standard curve and measure the concentration of titanium.

Analysis and determination of total phosphorus: determine the phosphorus concentration by molybdenum blue chromogenic method, put the solution to be measured into a 50 mL volumetric flask to volume, and successively add a drop of phenolphthalein, a drop of 1 mol·L⁻¹ NaOH solution (shake well), a drop of 1 mol·L⁻¹ sulfuric acid solution (shake well to colorless), 1 mL (100 g·L⁻¹) anti chemical acid and 2 mL molybdate to volume^[12]. After 20 mins of

color development, the absorbance of phosphorus (P) was measured with an ultraviolet spectrophotometer at the wavelength of 700 nm. In addition, dilute the phosphorus standard stock solution into a series of standard solutions with a concentration gradient of 1–5 mg·L⁻¹, measure the absorbance at the same wavelength, then obtain the standard curve and determine the phosphorus concentration.

Analysis and determination of dissolved phosphorus: take 5 mL of nTiO₂ suspension into 7 mL high-speed centrifuge tube, place the centrifuge tube in ultra-high-speed centrifuge (GL-21M, Thermo Fisher Technology Company), and centrifuge at 4 °C and 15,000 r·min⁻¹ for 1 h. Pass the supernatant over 0.22 μM porous filter membrane, test the concentration of dissolved phosphorus according to the above method of testing total phosphorus.

1.5 A two-point kinetic model

A two-point kinetic adsorption model (TSKAM) was chosen with the equation^[13,14].

$$\frac{\partial \theta C}{\partial t} + \rho_b \frac{\partial (S_1)}{\partial t} + \rho_b \frac{\partial (S_2)}{\partial t} = \frac{\partial}{\partial x} \left(\theta D \frac{\partial C}{\partial x} \right) - \frac{\partial v C}{\partial x} \quad (1)$$

Among them, θ is the porosity of the quartz sand column, and C represents the concentration of nTiO₂ particles in the solution, ρ_b represents the unit weight of quartz sand, x represents the spatial vertical coordinate axis, and D represents the hydraulic dispersion coefficient, v represents the water flow velocity, S_1 and S_2 represent nTiO₂ sites 1 and 2, respectively. The core of TSKAM model is to divide the sites on the quartz sand surface conducive to the adsorption of TiO₂ particles into site 1 and site 2. The nTiO₂ particles retained at site 2 are controlled by convection dispersion, and the mass conservation equation is the first-order kinetic adsorption and desorption equation.

$$\rho_b \frac{\partial (S_2)}{\partial t} = \theta k_2 C - \rho_b k_{2d} S_2 \quad (2)$$

k_2 and k_{2d} are the adsorption and desorption rates at site 2, respectively, and the adsorption of the nTiO₂ particles at site 2 belongs to the reversible adsorption. The mass conservation equation on site 1

is:

$$\rho_b \frac{\partial (S_1)}{\partial t} = \theta k_1 \psi_x C \quad (3)$$

k_1 is the adsorption rate at the colloidal site 1. Adsorption at site 1 is irreversible adsorption. ψ_x is a function related to the depth of the filled column^[13].

$$\psi_x = \left(\frac{d_c + x - x_0}{d_c} \right)^{-\beta} \quad (4)$$

Where, d_c is the average particle size of quartz sand and x_0 is the distance on the coordinate axis. At this distance, the reten of nTiO₂ particles is related to the column depth. β is an empirical coefficient that controls the shape of the spatial nTiO₂ curve. The smaller the values of site 2 adsorption efficiency (k_2), analytical efficiency (k_{2d}) and site 1 adsorption efficiency (k_1) are, the less the reten nTiO₂ of particles on quartz sand and the higher their mobility will be. The penetration curve of nTiO₂ particles is simulated by HYDRUS-1d software to obtain parameters k_1 , S_1 , k_2 and k_{2d} ^[15].

1.6 Migration parameters

The nTiO₂ particle mass recovery can be obtained by performing area integration of its migration curves.

$$MR(\%) = \frac{\int_0^{\infty} Q(t)C(t)dt}{\int_0^{t_0} Q(t)C_0(t)dt} \quad (5)$$

In formula, Q is the pore flow velocity (mL·min⁻¹), C_0 and C are the inflow and outflow TiO₂ concentration (mg·L⁻¹), t is time (min) and t_0 is pulse duration (min).

The probability of nTiO₂ particles adsorbing on the quartz sand surface is called the adsorption efficiency (α).

$$\alpha = \frac{2d_c}{3(1-\theta)L\eta^0} \ln \left(\frac{C}{C_0} \right) \quad (6)$$

In formula, L is the length of the column. θ is

the porosity of the filled column. d_c is the diameter of sand and η_0 is the theoretical single medium contact efficiency.

Net bed penetration coefficient:

$$\lambda_0 = -\frac{1}{L} \ln \left(\frac{C}{C_0} \right) \quad (7)$$

Particulate deposition rate coefficient:

$$k = \lambda_0 v_p \quad (8)$$

In formula, v_p is the flow velocity and k is the

coefficient of time and distance correlation.

The maximum migration distance of the nTiO₂ particles was defined as the distance at which the nTiO₂ particles move when 99.9% of the nTiO₂ particles are trapped, that is,

$$L_{\max} = -\frac{v_p}{\kappa} \ln \left(\frac{C}{C_0} \right) \quad (9)$$

The results of the various migration parameters for the above formula are shown in **Table 1**.

Table 1. Physical and computational parameters of nTiO₂ particles and quartz sand columns in the migration experiments

Number	NaNO ₃ Concentrated/mM	P concentrated/mM	Flow speed/ml·min ⁻¹	Outflow ratio/%	Single medium contact efficiency	Adsorption efficiency	Adsorption efficiency/cm ⁻¹	Sedimentation rate coefficient/h ⁻¹	Maximum migration distance/cm
1	10	0.1	0.5	3.9	35.9	3.56×10^{-4}	0.19	2.705	37.3
2	10	0.1	1	12	35.9	2.32×10^{-4}	0.12	3.536	57
3	10	0.1	2.5	38	35.9	1.06×10^{-4}	0.06	4.034	124.9

2. Results and discussion

2.1 Effect of different concentrations of NaNO₃ electrolytes on the Zeta potential on the nTiO₂ surface

When pH = 6.5, the change of surface Zeta potential of nTiO₂ in different concentrations of NaNO₃ is shown in **Figure 1(a)**. At different electrolyte concentrations, the Zeta potential on the surface of TiO₂ particles is negative, which indicates that the surface of TiO₂ particles is negatively charged at different concentrations of NaNO₃. With the increas-

ing concentration of NaNO₃ in the solution, the Zeta potential on the surface of nTiO₂ particles decreases (the absolute value decreases, that is, the negative is getting smaller and smaller). When the NaNO₃ concentration increased from 0.1 mM to 5 mM, the corresponding Zeta potential changed from -19 mV to -6.09 mV. This is mainly because with the increasing solubility of NaNO₃ in the solution, the charge shielding effect and electrostatic double layer on the surface of nTiO₂ particles are compressed, and the net negative charge on the surface of TiO₂ particles decreases^[16,17]. As a result, the Zeta potential on the

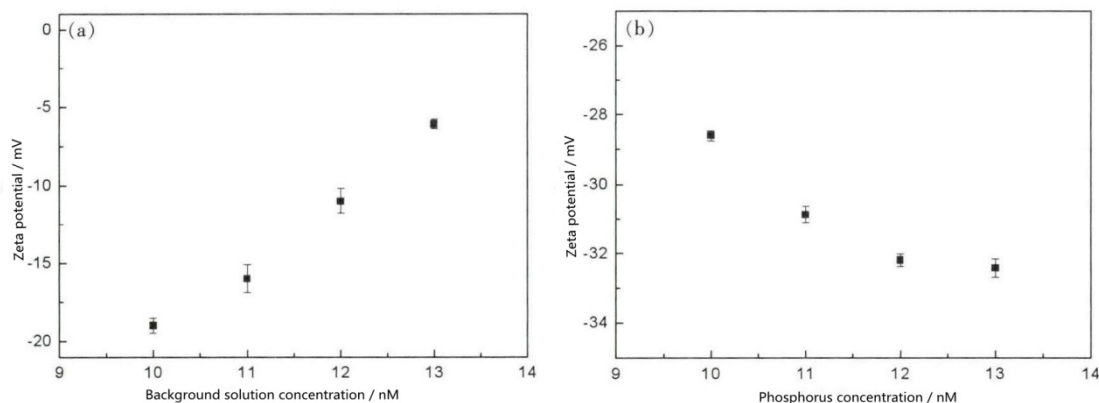


Figure 1. Zeta potentials of nTiO₂ particles with different NaNO₃ concentrations (a) and different phosphorus concentrations (b) in the 10 mM NaNO₃ background solution (pH = 6.5).

surface of nTiO₂ particles is reduced, so the dispersion stability of nTiO₂ particle suspension is also reduced.

2.2 Effect of different phosphorus concentrations on the Zeta potential on the nTiO₂ surface

As shown in **Figure 1(b)**, when pH = 6.5 and background solution NaNO₃ is 10 mM, the Zeta potential on the surface of nTiO₂ particles increases with the increase of P concentration. For example, when the P concentration is 0.1 mM, its surface Zeta potential is -28.6 mV, while when the P concentration is increased to 5 mM, its surface Zeta potential increases to -32.43 mV. The results show that because phosphate is adsorbed on the surface of nTiO₂ particles, the charge density on the surface of nTiO₂ particles is improved through the deprotonation of surface carboxyl groups^[18]. Therefore, the electrostatic repulsion between the nTiO₂ particles and the nTiO₂ particles adsorbing P is strengthened, which eventually leads to the improvement of the dispersion stability of the nTiO₂ particle suspension^[19].

2.3 Effect of water flow velocity on the migration of nTiO₂ particles suspended in a phosphate solution

The effects of different water flow velocities (0.5–2.5 mL·min⁻¹) on the migration of TiO₂ particles and P in quartz sand column were investigated when the suspension pH was 6.5, the phosphate concentration was 0.1 mM and the background solution NaNO₃ concentration was 10 mM. The flow velocity selected in this group of experiments is within the range of groundwater flow velocity. **Figure 2** shows the penetration curve of nTiO₂ particles at different water velocities. With the increase of water flow velocity, the outflow ratio (C/C_0) of nTiO₂ particles increases continuously. When the water flow velocity increases from 0.5 mL·min⁻¹ to 2.5 mL·min⁻¹, the outflow ratio of nTiO₂ particles increases from 3.9% to about 38.0%, which is similar to the migration law of nano-hydroxyapatite in quartz sand column under different water flow velocities^[21]. The above phenomenon is mainly because with the increase of wa-

ter flow velocity in the quartz sand column, the total sites on the quartz sand surface that can be adsorbed by nTiO₂ particles in the quartz sand column also decrease. When the water flow velocity is very high, the total sites on the quartz sand surface that can be adsorbed by nTiO₂ particles decrease sharply due to the action of hydraulic shear force. The retention of nTiO₂ particles in quartz sand column also decreases. In addition, when the water flow velocity is very low, it is difficult to provide enough kinetic energy for nTiO₂ particles to penetrate the quartz sand column in the quartz sand column with small porosity, and a large number of nTiO₂ particles are retained in the quartz sand column^[21–23].

In addition, it can be seen from **Table 1** that when the water flow rate increases from 0.5 mL·min⁻¹ to 2.5 mL·min⁻¹, the adsorption efficiency of nTiO₂ particles on the surface of quartz sand reduces from 3.56×10^{-4} to 1.06×10^{-4} , the retention of nTiO₂ particles in quartz sand column is reduced and the migration ability is continuously improved. Although the deposition rate coefficient increased from 2.705 h⁻¹ to 7.699 h⁻¹, due to the increase of water flow velocity, the continuous improvement of hydraulic shear force improves continuously, the active collision increases continuously during migration, the retention of nTiO₂ particles on the surface of quartz sand decreased constantly, and more nTiO₂ particles penetrated the quartz sand column. In addition, the maximum migration distance of nTiO₂ particles is also increasing with the increase of water flow velocity, and the maximum migration distance is greater than the height of the column by 17.5 cm, which shows that nTiO₂ particles can smoothly penetrate the quartz sand column under these three different water flow velocities. Therefore, the increase of water flow velocity promotes the migration of nTiO₂ particles in the quartz sand column. As for the effect of water velocity on the migration of nTiO₂ particles in saturated quartz sand column, the two-point dynamic model can well simulate the penetration curve of nTiO₂ particles in quartz sand column. As shown in Table 2, the water flow velocity is 0.5–2.5 mL·min⁻¹, and the simulated R^2 are 0.983, 0.996 and 0.990 respectively, indicating that the model has

high fitting degree. With the increase of water flow velocity, the adsorption efficiency of site 1 (k_1), site 2 (k_2) and the first-order desorption rate (k_{1d}) on site 1 decrease, which indicates that the adsorption of nTiO₂ particles on the surface of quartz sand is less, resulting in the increase of their migration, which is more conducive to their migration.

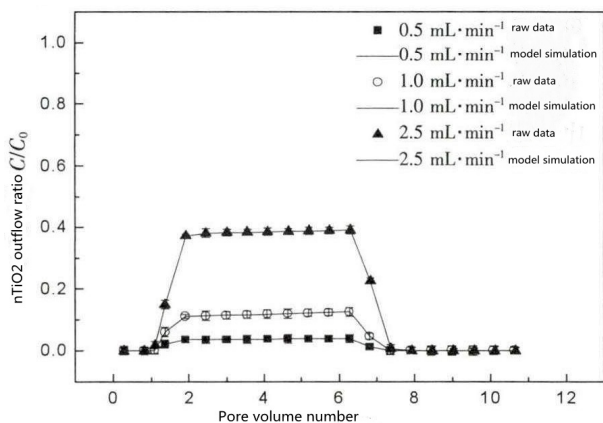


Figure 2. Penetration curve of nTiO₂ particles at different water flow speeds.

2.4 Effect of water flow velocity on phosphate migration

As shown in **Figure 3**, the outflow ratio of total P increases with the increase of water flow rate. When the water flow rate was 0.5 mL·min⁻¹, the outflow ratio of total P was 38.0%; When the flow rate increases to 1 mL·min⁻¹, the outflow ratio of total P is 50%. Continue to increase the flow rate to 2.5 mL·min⁻¹, and the outflow ratio of total P increases to 67.9%. This is mainly because with the increase of water flow velocity in the quartz sand column, the ability of nTiO₂ particles to penetrate the quartz sand column increases, so that the P adsorbed on the nTiO₂ particles also migrate out of the quartz sand

column. After digestion, the measured total P concentration also increases. However, with the increase of water flow velocity, the outflow ratio of dissolved P does not change significantly, as shown in **Figure 4**. At this time, the outflow ratio of dissolved P is basically maintained at about 21.5%. There is no obvious change in the outflow ratio of dissolved P, mainly because the change of water flow velocity will not affect the adsorption capacity of nTiO₂ particles for P. Therefore, no matter how the water flow velocity changes, the concentration of dissolved P in the solution will not change. In addition, the dissolved P is obtained by subtracting the total phosphate from the bound P of nTiO₂ particles. Therefore, when the velocity is changed and the concentration of dissolved P remains unchanged, the water flow rate is at 0.5 mL·min⁻¹, the dissolved P in the effluent is the main, and only a small part of the bound P with nTiO₂ particles exists. When the water flow rate increases, most of the P in the effluent exists in the form of bound P with nTiO₂ particles, and only a small part exists in the form of dissolved P.

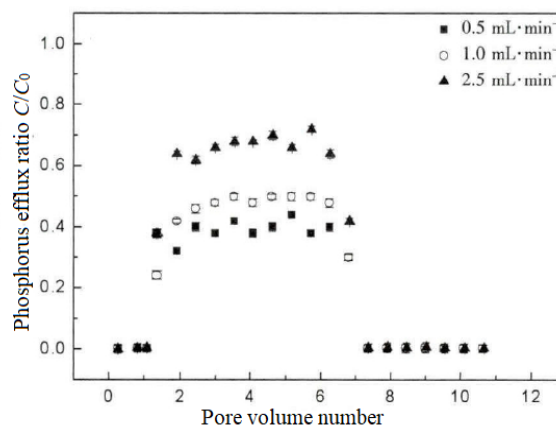


Figure 3. Penetration curves of total phosphorus suspended in (0.1 mM) phosphate solution at different flow rates.

Table 2. Simulation parameters of two-point kinetic adsorption model under different experimental conditions

Number	Site 2 adsorption efficiency	Site 2 resolution efficiency	Maximum value of retention at point 1	Site 1 adsorption efficiency	Person mean square correction factor
1	14.470	6.271	97.15	0.230	0.983
2	14.160	6.028	45.67	1.152	0.996
3	3.138	1.224	33.50	0.067	0.990

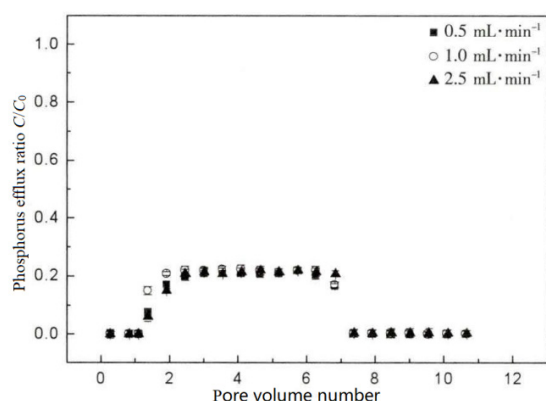


Figure 4. Penetration curves of dissolved phosphorus suspended in (0.1 mM) phosphate solution by different flow velocities.

3. Conclusion

(1) When $\text{pH} = 6.5$, with the increase of electrolyte NaNO_3 concentration, the Zeta negative potential on the surface of nTiO_2 particles decreased gradually; (2) The surface negative charge of nTiO_2 increases with the increase of P concentration, and its dispersion stability also improves constantly; (3) High flow velocity promotes the mobility of nTiO_2 , and the migration of soluble phosphate also increases continuously; (4) The two-point kinetic adsorption model can well simulate the migration and penetration curve of nano materials in quartz sand column. The model results show that with the increase of flow rate, the adsorption efficiency of site 2 (k_2), analytical efficiency (k_{2d}) and site 1 adsorption efficiency (k_1) decrease, and the adsorption efficiency of nTiO_2 particles on quartz sand decreases, so that more nTiO_2 particles penetrate the quartz sand column.

Conflict of interest

The authors declare that they have no conflict of interest.

Acknowledgements

General Research Project of National Natural Science Foundation of China, No. 21377090.

References

- Fang J, Shan X, Wen B, *et al.* Stability of titania nanoparticles in soil suspensions and transport in

- saturated homogeneous soil columns. *Environmental Pollution* 2009; 157(4): 110–109.
- Higashi MM, Jardim WF. Remediation of pesticide contaminated soil using TiO_2 , mediated by solar light. *Catalysis Today* 2002; 76(2-4): 201–207.
- Nagaveni K, Sivalingam G, Hegde MS, *et al.* Photocatalytic degradation of organic compounds over combustion-synthesized nano- TiO_2 . *Environmental Science & Technology* 2004; 38(5): 1600–1604.
- Quan X, Zhao X, Chen S, *et al.* Enhancement of p, p'-DDT photodegradation on soil surfaces using TiO_2 induced by UV-light. *Chemosphere* 2005; 60(2): 266–273.
- And TA, Madras G. Photocatalytic degradation of rhodamine dyes with nano- TiO_2 . *Industrial & Engineering Chemistry Research* 2007; 46(1): 1–7.
- Wei J, Hamid M, Baoshan X. Bacterial toxicity comparison between nano- and micro-scaled oxide particles. *Environmental Pollution* 2009; 157(5): 1619–1625.
- Hund-Rinke K, Simon M. Ecotoxic effect of photocatalytic active nanoparticles (TiO_2) on algae and daphnids. *Environmental Science & Pollution Research* 2006; 13(4): 225–232.
- Saleh N, Kim H, Phenrat T, *et al.* Ionic strength and composition affect the mobility of surface-modified FeO nanoparticles in water-saturated sand columns. *Environmental Science & Technology* 2008; 42(9): 3349–3355.
- French RA, Jacobson AR, Bojeong K, *et al.* Influence of ionic strength, pH, and cation valence on aggregation kinetics of titanium dioxide nanoparticles. *Environmental Science & Technology* 2009; 43(5): 1354–1359.
- Healy KE, Ducheyne P. Hydration and preferential molecular adsorption on titanium in vitro. *Biomaterials* 1992; 13(8): 553–561.
- Kaushik RD, Gupta VK, Singh JP. Distribution of zinc, cadmium, and copper forms in soils as influenced by phosphorus application. *Arid Soil Research & Rehabilitation* 2009; 7(2): 163–171.
- Chen J, Gao F, Sun X. Determination of phosphorus content in alcoholic by molybdenum blue extraction photometric method. *Chemical Engineer* 2005; 115(4): 29–30.

13. Schijven JF, Simunek J. Kinetic modeling of virus transport at the field scale. *Journal of Contaminant Hydrology* 2002; 55(1-2): 113–135.
14. Bradford SA, Simunek J, Bettahar M, *et al.* Modeling colloid attachment, straining, and exclusion in saturated porous media. *Environmental Science & Technology* 2003; 37(10): 2242–2250.
15. Marquardt DW. An algorithm for least-squares estimation of nonlinear parameters. *Journal of the Society for Industrial & Applied Mathematics* 2006; 11(2): 431–441.
16. Elimelech M, Gregory J, Jia X, *et al.* Particle deposition and aggregation: Measurement modeling and simulation. Woburn: BuaerworthHeinemann; 1995.
17. Hunter RJ. Foundations of colloid science. New York: Oxford University Press; 1987.
18. Solovitch N, Labille J, Rose J, *et al.* Concurrent aggregation and deposition of TiO₂ nanoparticles in a sandy porous media. *Environmental Science & Technology* 2010; 44(13): 4897–4902.
19. Pelley AJ, Tufenkji N. Effect of particle size and natural organic matter on the migration of nano- and microscale latex particles in saturated porous media. *Journal of Colloid & Interface Science* 2008; 321(1): 74–83.
20. Wang D, Bradford SA, Paradelo M, *et al.* Facilitated transport of copper with hydroxyapatite nanoparticles in saturated sand. *Soil Science Society of America Journal* 2012; 76(2): 375–388.
21. Gargiulo G, Bradford SA, Simunek J, *et al.* Transport and deposition of metabolically active and stationary phase deinococcus radiodurans in unsaturated porous media. *Environmental Science & Technology* 2007; 41(4): 1265–1271.
22. Gargiulo G, Bradford SA, Simunek J, *et al.* Bacteria transport and deposition under unsaturated flow conditions: The role of water content and bacteria surface hydrophobicity. *Vadose Zone Journal* 2008; 7(2): 406–419.
23. Bradford SA, Torkzaban S, Wiegmann A. Pore-scale simulations to determine the applied hydrodynamic torque and colloid immobilization. *Vadose Zone Journal* 2010; 10(1): 252–261.

ORIGINAL RESEARCH ARTICLE

Preparation and characterization of magnetic graphene oxide nanocomposite (GO-Fe₃O₄) for removal of strontium and cesium from aqueous solutions

Sule Aytas¹, Sabriye Yusan^{1*}, Senol Sert¹, Cem Gok²

¹ Institute of Nuclear Sciences, Ege University, 35100 Bornova, Izmir, Turkey. E-mail: sabriye.doyurum@ege.edu.tr

² Faculty of Technology, Department of Metallurgical and Materials Engineering, Pamukkale University, 20160 Kinikli Denizli, Turkey

ABSTRACT

Magnetic graphene oxide nanocomposites (M-GO) were successfully synthesized by partial reduction co-precipitation method and used for removal of Sr(II) and Cs(I) ions from aqueous solutions. The structures and properties of the M-GO was investigated by X-ray diffraction, Fourier transformed infrared spectroscopy, X-ray photoelectron spectroscopy, transmission electron microscopy, scanning electron microscopy, vibrating sample magnetometer (VSM) and N₂-BET measurements. It is found that M-GO has 2.103 mg/g and 142.070 mg/g adsorption capacities for Sr(II) and Cs(I) ions, respectively. The adsorption isotherm matches well with the Freundlich for Sr(II) and Dubinin–Radushkevich model for Cs(I) and kinetic analysis suggests that the adsorption process is pseudo-second-ordered.

Keywords: Graphene Oxide; Magnetite; Nanocomposite; Strontium; Cesium, Sorption

ARTICLE INFO

Received: 26 January 2021
Accepted: 12 March 2021
Available online: 18 March 2021

COPYRIGHT

Copyright © 2021 Sule Aytas, *et al.*
EnPress Publisher LLC. This work is licensed under the Creative Commons Attribution-NonCommercial 4.0 International License (CC BY-NC 4.0).
<https://creativecommons.org/licenses/by-nc/4.0/>

1. Introduction

Nuclear and Industrial Safety Agency (Japan) reported that the Fukushima Daiichi reactor meltdowns have thus far released 15,000 tera becquerels of radioactive cesium-137 into the environment^[1]. Also, strontium was measured in plant samples in four others villages, with values ranging from 12 to 61 Bq/kg for Sr-89 and 1.8 to 5.9 Bq/kg for Sr-90^[2]. This accident caused a great environmental disaster for living metabolisms and plants. Furthermore, diverse anthropogenic activities like nuclear research reactors, the production and use of radioisotopes and radiopharmaceuticals bring about the spread of radioactive wastes in the environment^[3].

Some radionuclides as cesium and strontium are biologically toxic and of great importance due to their long-lasting nature and high solubility in aqueous systems^[4]. For this reason, it is a significant subject to find out efficient, economic method that can be used in the removal and recovery of cesium and strontium from contaminated environments. Different types of physicochemical methods as ion exchange, chemical precipitation, membrane separation and adsorption, etc. are used for removal and recovery of radionuclides. Considering many parameters, one of these techniques comes to the forefront. Adsorption is widely-used technique that is fast and effective approach in eliminating pollutants from aqueous solutions^[5].

The most critical point in the development of new adsorption methods is developed new adsorbent materials. Among the previously developed adsorbents, nanomaterial and especially nano-composites have been received great attention owing to high adsorption capacity, selectivity, high surface area, fast kinetic performances, and reusability for several cycles use^[6,7]. Furthermore, nano-engineered magnetic adsorbents can be widely applied in contaminant removal due to the magnetism and high surface area. The magnetic particles can be quickly separated from the water after adsorption and this provides easily controlled process^[8].

In recent years, graphene oxide nanomaterials, which has a large theoretical surface area and high sorption capacity for the metallic cations, has with wide range of surface oxygen-containing functional groups such as hydroxyl, epoxy, and carboxyl^[9,10]. According to literature, graphene oxide has a notable affinity toward hard and semi-hard cations like uranium, thorium, lanthanides, and also strontium. These superior properties make graphene oxide proper for efficient adsorbent of cesium and strontium. Unfortunately, disadvantage of the graphene oxide is colloidal behavior of its dispersion, which makes separation of its reaction products with metallic cations quite unfairable^[9]. Preparation of composite is one of the possible solutions to solve this problem. In this study, magnetic-nano composites were synthesized by using graphene and also magnetite, which is economic and readily available material; on the other side it is not selective. Integration of these two materials solved agglomeration problem and chemical instability in acidic media^[11,12]. Preparation of nano-composite material with graphene and magnetite, not only brings about the chemical resistance, but also increase adsorption capacity. In recent years, combining of magnetite and graphene into nanocomposites has become an important subject of research due to their new and/or enhanced functionalities that cannot be obtained by either component alone. So, this topic holds a great promise for a wide variety of applications in removal of contaminants from wastewater, surface enhanced Raman scattering, biomedical fields, catalysis, etc.^[13,14]

In despite of various studies, there is lack of efficient, low cost, secure, high capacity, modifiable, dopeable and reusable technique about cesium and strontium removal from aqueous solution. Based on that, magnetic-nano graphene composites were synthesized and characterized to investigate the removability of radiotoxic strontium and cesium ions from aqueous solutions. Adsorption performance of prepared composite by batch experiment was studied by physicochemical parameters. The adsorption isotherm parameters were estimated by linear regression analysis, thermodynamic and kinetic parameters have been also calculated to clarify the adsorption mechanism. The interaction mechanism of cesium and strontium on the magnetic nano-composites was discussed from the experimental results.

2. Experimental procedure

2.1. Reagents and materials

The graphene oxide powder was purchased from the Sigma Aldrich. The stock standard solutions of strontium and cesium were prepared by dissolving an appropriate amount of $\text{Sr}(\text{NO}_3)_2$ (Merck) and CsNO_3 (Merck) in distilled deionized water. Considering the radioactivity of the ^{90}Sr , non-radioactive ^{88}Sr was used. All reagents used were of analytical reagent grade.

2.2. Instrumental and analytical conditions

The strontium and cesium concentration measurements were done using a Perkin-Elmer Optima 2000 DV ICP-OES. The shaking was carried out in a thermostated electronic shaker bath (GFL-1083 model).

To analyze the characteristics of the M-GO, scanning electron microscope (SEM, COXEM EM-30), transmission electron microscopy (TEM, FEI 120kV CTEM), Fourier transform infrared spectroscopy (FTIR, PERKIN ELMER SPECTRUM TWO), X-ray diffraction (XRD, Thermo Scientific ARL K-Alpha), X-ray photoelectron spectroscopy (XPS, Thermo Scientific Al K-Alpha), vibrating sample magnetometer (VSM, VSM550-100, Dexing Magnet Tech. Co) and N2-BET adsorption-desorption were

determined at 77 K using Micromeritics ASAP 2020.

2.3. Synthesis of M-GO

The M-GO nanocomposite was prepared by co-precipitation method, as reported in the literature^[15]. 0.05 g graphene oxide powder was used during the synthesis of the nanocomposite.

2.4. Batch adsorption experiments

All sorption experiments were performed by the batch technique using 0.01 g of the sorbent suspended in 10 mL of strontium/cesium solution in a polyethylene (PE) flask at selected pH (2–9) and pH (2–12) for Sr(II) and Cs(I), respectively. The effects of sorption parameters such as contact time (15–300 min), Sr(II) concentration (10–50 mg/L), Cs(I) concentration (200–500 mg/L), adsorbent dosage (m/V) ratio (1–10) and temperature (25–45 °C) on the sorption of Sr(II)/Cs(I) were determined by changing a parameter and keeping others constant. The pH was adjusted by adding 0.1 mol/L HCl and NaOH to the solutions at the each experiment. After reaction, the solid and liquid was separated by the magnetic separation method. The concentrations of total Sr and Cs were determined by using ICP-OES. Each experiment was repeated three times and average values were used for calculation. The percentage sorption of metal ions from aqueous solution was computed as follows:

$$\text{Adsorption (\%)} = \frac{(C_i - C_e)}{C_i} \times 100 \quad (1)$$

where C_i and C_e are the initial and final metal ions concentration, respectively.

2.5 Kinetic studies

Kinetic studies were carried out in a thermostated shaker with polyethylene tubes at room temperature. In each run, 0.01 g of M-GO was added to 10 mL of Sr and Cs solution (50, 100, 150 mg/L and 200, 250, 300 mg/L), respectively and adjusted to the desired pH level. The contact time varied from 5 to 180 min. Samples were filtered from each tube at specified time intervals and analyzed for the remaining Sr/Cs ion concentrations by ICP-OES.

3. Results and discussion

3.1. Characterization

The micro-structure of the Fe₃O₄-GO(M-GO) was characterized by XRD (**Figure 1**). The peaks at 2θ values of 30.42°, 35.06°, 43.48°, 53.22°, 57.78° and 63.06° are the characteristic peaks of the Fe₃O₄ crystal with the cubic spinel structure for magnetic graphene nanocomposites matching well with those from the JCPDS card (19-0629)^[16,17]. The small peak at 2θ = 26.5° corresponds to well-ordered graphene layers of GO skeleton and indicates that this way the formation of the magnetic composite as reported by other groups^[18]. Generally we can conclude from the XRD pattern, the nanocomposite contains mostly Fe₃O₄ and it was synthesized with GO.

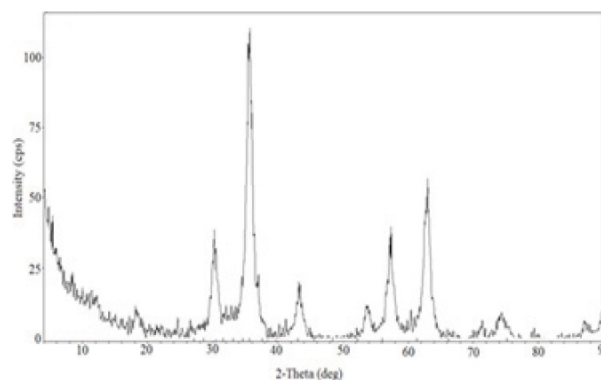


Figure 1. XRD pattern of M-GO.

SEM and TEM images of the obtained M-GO nanocomposite are showed in **Figure 2** and **Figure 3**. SEM images confirm the Fe₃O₄ nanoparticles are attached to the surface of the GO sheet in homogeneously. Nevertheless, TEM images of the M-GO shows that Fe₃O₄ nanoparticles are well decorated and clearly observed on the surface of graphene sheet.

XPS technique was used to verify the chemical state of M-GO and the results were shown in **Figure 4**. The wide scan XPS spectra of the M-GO shows the binding energy peaks about 285, 530 and 710 eV, which are attributed to C1s, O1s and Fe 2p, respectively^[19,20]. In the figure spectrum, the peaks of Fe 2p 3/2 and Fe 2p 1/2 were located at about 711.12 and 724.79 eV, confirming that Fe₃O₄ was fairly synthesized on the GO.

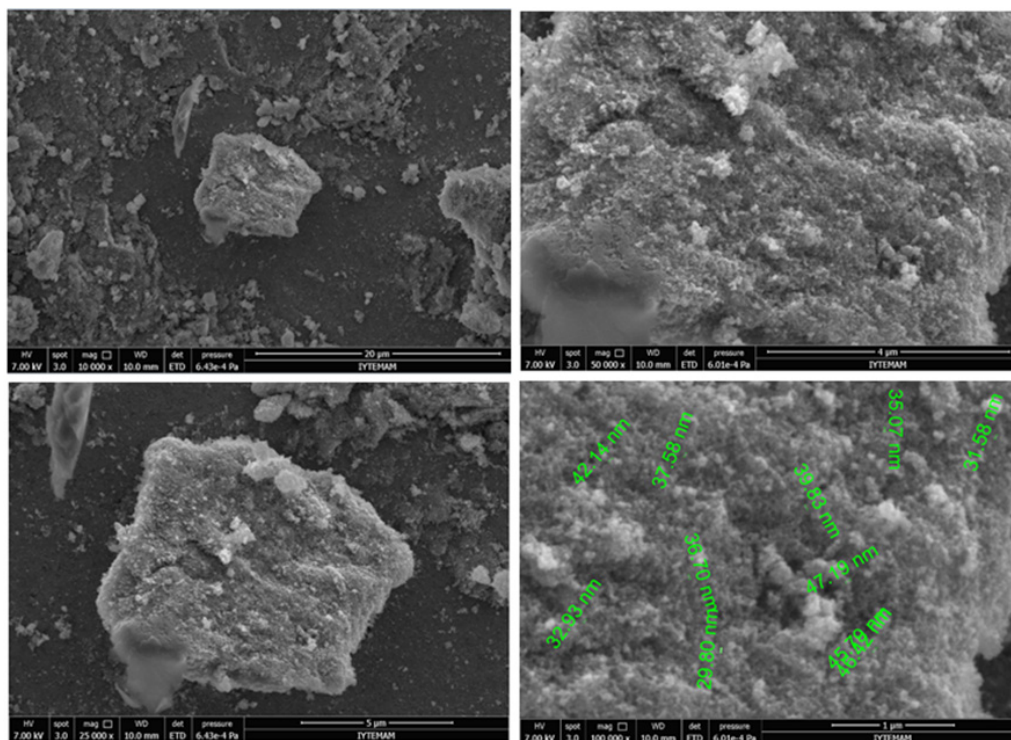


Figure 2. SEM image of M-GO.

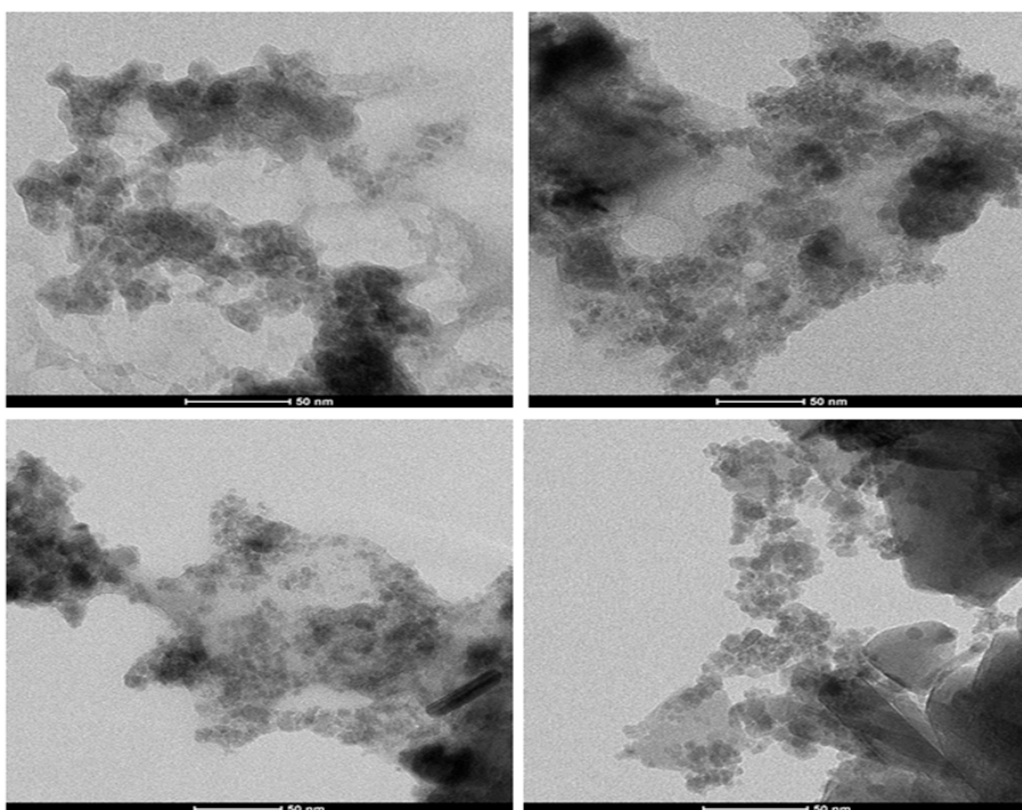


Figure 3. TEM image of M-GO.

The FT-IR spectrum of GO and M-GO is depicted in **Figure 5**. The GO sheet showed apparent adsorption bands for the carboxyl groups (stretching

vibrations from C=O; $1,716\text{ cm}^{-1}$), aromatic (C=C; $1,580\text{ cm}^{-1}$), and alkoxy (stretching vibration from C–O ($1,041\text{ cm}^{-1}$)). The intense peak at $1,415\text{ cm}^{-1}$ can

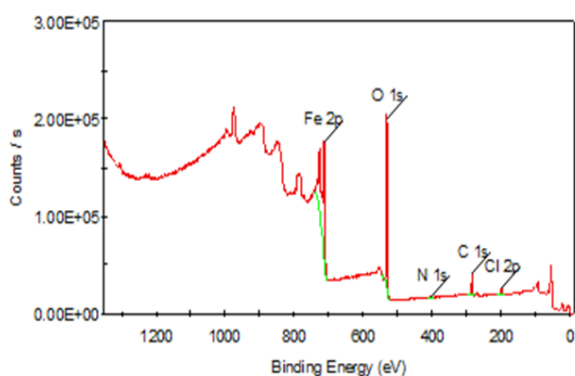


Figure 4. XPS survey scan spectrum of M-GO.

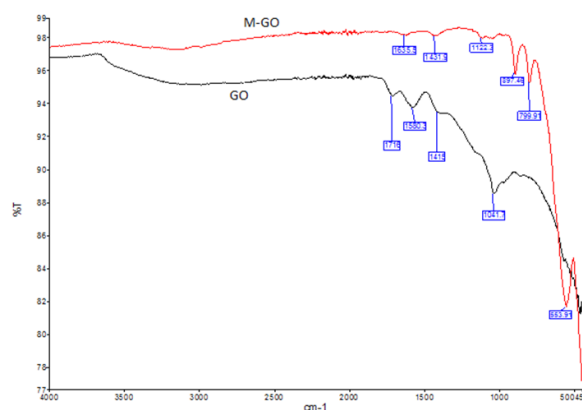


Figure 5. FT-IR spectra of M-GO.

be attributed to epoxy groups (C=C vibration) also showed at 1,122, 897 and 799 cm^{-1} in M-GO spectrum that related to symmetric stretching, asymmetric stretching, and deformation vibrations, respectively^[18].

For M-GO, band at 1,635 cm^{-1} is assigned to H-O bending vibration. The peak at 553 cm^{-1} showed Fe-O bond from Fe_3O_4 . The peak around 1,400 cm^{-1} can be explained by symmetric vibration of COO-groups which indicates the carboxylate groups of GO coordination with the iron cations^[21].

The magnetic properties of the Fe_3O_4 nanoparticles, GO and the M-GO nanocomposite were determined at room temperature. The hysteresis loop of magnetite, GO and M-GO composite are shown in Figure 6, where the magnetization hysteresis loops appear S-like, and saturation magnetization is 16.16 and 10.74 emu/g for magnetite and M-GO, respectively. Nevertheless, as shown in the figure, GO sample has no magnetic property. The reduction in the saturation magnetization could be related to existence of GO and impurities on the surface of the magnetite nanoparticles^[22]. However, M-GO still could be separated rapidly under the external magnet.

BET analysis was performed to investigate the specific surface area and pore size of the synthesized material. The BET surface area and pore size of M-GO was found as 124.37 m^2/g and 0.386 nm, respectively. In the literature, Cheng *et al.* and Hur *et al.* found the BET surface area for magnetic graphene oxide composites are 111.8 m^2/g and 49.9 m^2/g , respectively^[23,24]. The results obtained in this

study are consistent with the literature.

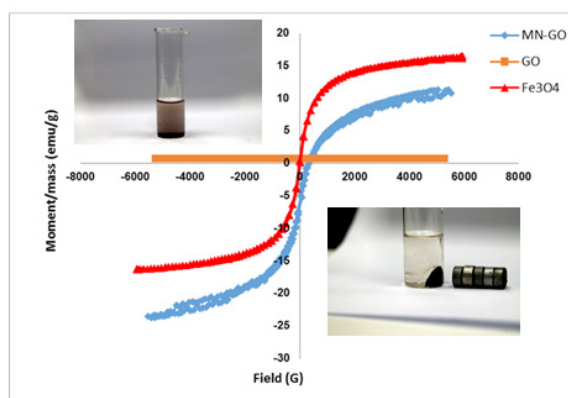


Figure 6. Magnetization versus magnetic field for magnetite, GO and M-GO.

3.2 Adsorption studies

3.2.1 pH effect

The pH value of solutions is a determining factor of the removal efficiency because it affects surface charge of the sorbent, and also the degree of ionization and speciation of the metal in solution. The effect of pH on Sr^{2+} and Cs^+ adsorption is shown in Figure 7 (a-b). As can be seen, the strontium and cesium removal on M-GO adsorbent are affected by the pH change of the solution. The maximum strontium and cesium uptake were found 40% at pH 4 and 17.92 mg $\text{Sr}(\text{II})/\text{g}$ and 59.5% at pH 10 and 148.77 mg $\text{Cs}(\text{I})/\text{g}$ as adsorbent, respectively. For this reason, pH 4 and pH 10 were used in subsequent experiments for $\text{Sr}(\text{II})$ and $\text{Cs}(\text{I})$, respectively. In addition, M-GO depicted higher adsorption capacity for Cs^+ than for Sr^{2+} under the same experimental conditions. This can be attributed to the smaller hydrated ionic

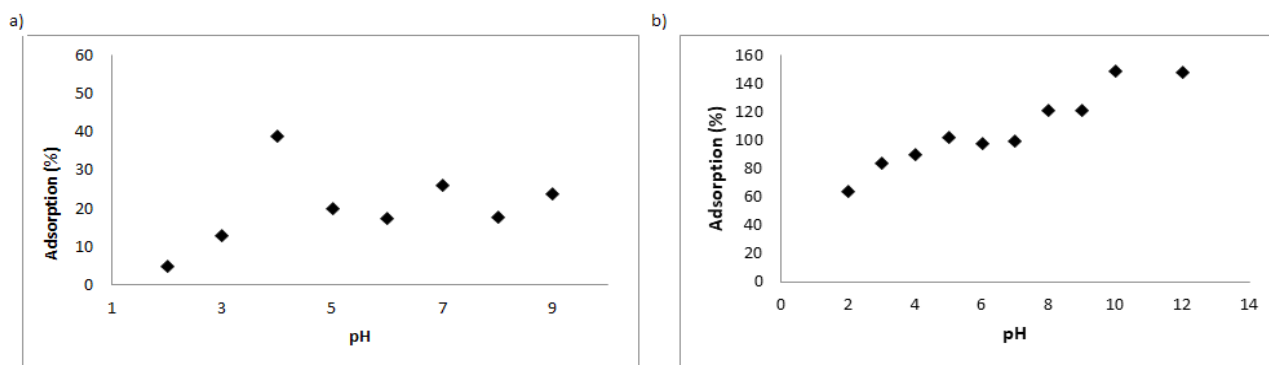


Figure 7. a) The effect of pH on the adsorption of Sr(II) ions with M-GO (c: 50 mg/L, m: 0.01 g, V: 10 mL, t: 120 min, T: 25 °C); **b)** The effect of pH on the adsorption of Cs(I) ions with M-GO (c: 250 mg/L, m: 0.01 g, V: 10 mL, t: 120 min, T: 25 °C).

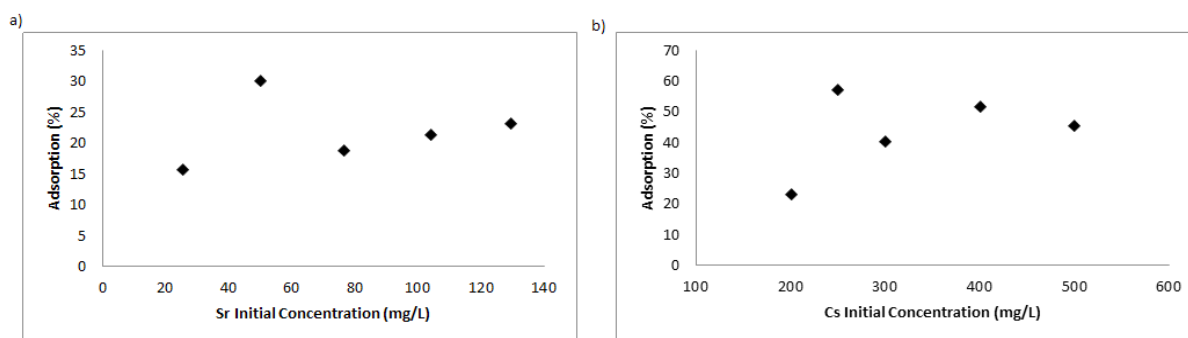


Figure 8. a) The effect of initial concentration on the adsorption of Sr(II) ions with M-GO (pH: 4, m: 0.01 g, V: 10 mL, t: 120 min, T: 25 °C); **b)** The effect of initial concentration on the adsorption of Cs(I) ions with M-GO (pH: 10, m: 0.01 g, V: 10 mL, t: 120 min, T: 25 °C).

radius of Cs^{+25} .

3.2.2 Concentration effect

The Sr(II) and Cs(I) ions adsorption capacities of the M-GO were given as a function of the initial concentrations of metal ions in **Figure 8(a-b)**. The solution concentration of Sr(II) and Cs(I) was varied in the range 25–125 mg/L and 200–500 mg/L, respectively.

As shown in **Figure 8a**, when the strontium concentration increased, % adsorption value increased but the concentration value decreased from the 50 mg/L. The highest uptake for M-GO adsorbent was calculated as 29.98% at 50 mg/L strontium concentration. This concentration was used in subsequent parameter assays.

As shown in **Figure 8b**, when the cesium concentration increased, % adsorption value increased but the concentration decreased from 250 mg/L concentration to the equilibrium. The highest uptake for M-GO adsorbent was calculated as 57.2% at a cesium concentration of 250 mg/L. In subsequent

parameter assays, this concentration has been studied at maximum adsorption.

3.2.3 Effect of dosage (m/V)

The adsorption of Sr(II) and Cs(I) ions decreases by increasing the ratio of the mass of the M-GO to volume of aqueous phase (m/V) (**Figure 9**). The highest values for the adsorption was obtained using 0.01 mL Sr/Cs solution and 0.01 g adsorbent (m/V) = 1 and it was taken as the optimum amount for other experiments for Sr and Cs adsorption. It can be concluded that low amount of nanocomposite can give higher metals adsorption. Increasing the adsorbent dose above 1 g/L have a little or no change on Cs(I) removal while it can lead to significant removal for Sr(II).

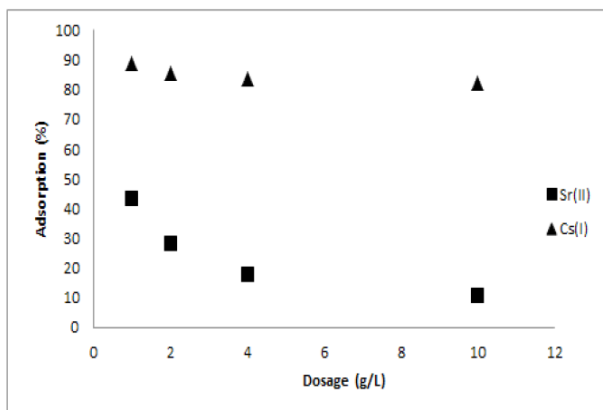


Figure 9. The effect of adsorbent dosage on the adsorption of Sr(II) and Cs(I) ions with M-GO (Sr; pH: 4, c: 50 mg/L, m: 0.01 g, V: 10 mL, t: 120 min, T: 25 °C; Cs; pH: 10, c: 250 mg/L, m: 0.01 g, V: 10 mL, t: 120 min, T: 25 °C).

3.3 Adsorption equilibrium and isotherm models

The adsorption process is a mass transfer operation that can be described mathematically by equilibrium and a rate process. The equilibrium is established between the concentration of the metal ions dissolved in aqueous phase and that bound to the adsorbent. The data obtained from experimental results is fundamental requirements for the design of adsorption systems. The data are used to develop equations and also to calculate isotherm parameters. By this way, the data, provide some insight into both the sorption mechanism and the surface properties and affinity of the sorbent can be used to compare different adsorbents under different operational conditions and to design and optimize an operating procedure^[26–28]. In order to analyze the equilibrium data of the adsorption system, experimental data were fitted to Langmuir, Freundlich, Dubinin–Radushkevich, Temkin, Flory-Huggins and Brunauer, Emmer & Teller isotherms among the varied models. The constants of isotherm models along with correlation coefficients (R^2) have been calculated from the plots for adsorption of cesium and strontium on the composite material and the results are given in **Table 1**.

Adsorption equilibrium in the concentration range of 25–125 mg/L and 200–500 mg/L was studied with 10 mg of magnetic nanocomposite at 25 °C, 120 min contact time and pH 4 and 10.0 strontium and cesium, respectively.

The Langmuir isotherm, probably the most widely used model, assumes monolayer coverage of adsorbate over a homogeneous adsorbent surface^[29]. The linear forms of this model are expressed by the following equations:

$$\frac{C_e}{q_e} = \frac{1}{Q_0 b_L} + \frac{C_e}{Q_0} \quad (2)$$

where q_e is the amount of cesium and strontium ions adsorbed onto adsorbent; C_e is the equilibrium concentration of these metals in solution, and Q_0 and b_L are Langmuir constants related to adsorption capacity and adsorption energy, respectively. Q_0 and b_L were calculated from the slope and intercept of linear plots of C_e/q_e versus C_e .

The Freundlich model has been used to describe adsorption of strontium and cesium from solution onto composite material. This model is not restricted to the formation of the monolayer coverage. It assumes an empirical expression encompassing the surface heterogeneity and the exponential distribution of the energy of active sites as well as multilayer adsorption. Linear form of Freundlich model can be represented as follows^[30]:

$$\log q_e = \log K_F + \frac{1}{n_F} \log C_e \quad (3)$$

where K_F represents the adsorption capacity (mg/g), n_F is a constant related to adsorption intensity (dimensionless). The data obtained are well described by the Freundlich isotherm equation when plotted as $\log q_e$ versus $\log C_e$ (**Figure 10**).

Dubinin–Radushkevich is the other model that used extensively to determine the type of adsorption for the removal of strontium and cesium^[31]. This model was used to calculate the apparent free energy of adsorption, proposed an equation to find out the adsorption mechanism on the basis of the potential theory assuming a porous structure of the sorbent and heterogeneous surface.

The linearized equation form of the D-R isotherm is given as:

$$\ln C_{ads} = \ln X_m - \beta \varepsilon^2 \quad (4)$$

where C_{ads} (mmol/g) is the amount of solute ad-

sorbed per unit weight of solid, X_m (mmol/g or mg/g) is the adsorption capacity, β (mol/K)² is a constant related to energy and ε is the Polanyi potential. Polanyi potential can be computed by the following equation:

$$\varepsilon = RT \ln \left(\frac{1}{1 + C_e} \right) \quad (5)$$

where R is a gas constant in kJ/mol and T is the temperature in Kelvin. If $\ln C_{ads}$ is plotted against ε^2 , β and X_m can be obtained from the slope and intercept, respectively (**Figure 11**). The adsorption mean energy (E), the free energy change when one mol of ion is transferred to the surface of the solid from infinity in the solution, is assumed by the following equation using the constant β :

$$E = \frac{1}{\sqrt{-2\beta}} \quad (6)$$

The Temkin isotherm model contains a factor that obviously assuming adsorbent–adsorbate interactions. This model takes into account that heat of adsorption of all molecules in the layer would decrease linearly rather than logarithmic with coverage by neglecting the extremely low and large value of concentrations^[32]. The Temkin isotherm has generally been applied as follow:

$$q_e = \frac{RT}{b_{Te}} \ln a_{Te} + \frac{RT}{b_{Te}} \ln C_e \quad (7)$$

Where, b_{Te} is the constant of Temkin related to adsorption heat (J/mol); a_{Te} is the Temkin isotherm constant (L/mg); R is the gas constant and T is the absolute temperature (K). b_{Te} and a_{Te} constants were calculated from the intercept and slope of straight line of the plot of the q_e versus $\ln C_e$.

The Flory–Huggins isotherm model was examined to account for the degree of surface coverage characteristics of the sorbate on the sorbent^[33,34]. The equation of the isotherm is as follows:

$$\frac{\Theta}{C_i} = K_{FH} (1 - \Theta)^{n_{FH}} \quad (8)$$

Where, Θ is the degree of surface coverage, K_{FH} is the Flory–Huggins model equilibrium constant

and n_{FH} is the Flory–Huggins model exponent. Θ is calculated using the following equation:

$$\Theta = 1 - \frac{C_e}{C_i} \quad (9)$$

The linearized equation of the model is given as:

$$\log \frac{\Theta}{C_i} = \log K_{FH} + n_{FH} \log(1 - \Theta) \quad (10)$$

The constants of isotherm were extrapolated from plots of plot of $\log(\Theta/C_i)$ versus $\log(1 - \Theta)$, and values of K_{FH} and n_{FH} calculated from the slope and intercept of the plot and are shown in **Table 1**. Equilibrium constant (K_{FH}) was used for the calculation of spontaneity of the Gibbs free energy (ΔG^0) on following equation:

$$\Delta G^0 = -RT \ln K_{FH} \quad (11)$$

The negative values of ΔG^0 confirmed the feasibility of the process and the spontaneous nature of adsorption onto adsorbent.

Brunauer–Emmett–Teller (BET) isotherm model, related to the liquid–solid interface, is a theoretical equation, most widely applied in the gas–solid equilibrium systems^[35]. This equation is presented as:

$$q_e = \frac{q_s C_{BET} C_e}{(C_s - C_e) [1 + (C_{BET} - 1)(C_e / C_s)]} \quad (12)$$

where C_{BET} , C_s , q_s and q_e are the BET adsorption isotherm constants relating to the energy of interaction with the surface (L/mg), adsorbate monolayer saturation concentration (mg/L), theoretical isotherm saturation capacity (mg/g) and equilibrium adsorption capacity (mg/g), respectively^[36]. Linearized equation of the model is as follows:

$$\frac{C_e}{q_e(C_s - C_e)} = \frac{1}{q_s C_{BET}} + \frac{(C_{BET} - 1) C_e}{q_s C_{BET} C_s} \quad (13)$$

The curve was plotted between $C_e/q_e(C_s - C_e)$ and C_e/C_s , and values of both constants q_s and C_{BET} were calculated from the intercept and slope. BET isotherm parameter for linear regression analyses and error functions are given in **Table 1**.

The high determination coefficients for linear

Table 1. Isotherm constants of models for strontium and cesium adsorption onto M-GO

Isotherm models	Parameters	Strontium	Cesium
Langmuir	Q_o (mg/g)	256.410	434.78
	b_L (L/mg)	0.004	0.035
	R^2	0.9249	0.2483
Freundlich	K_F (mg/g)	2.103	29.058
	n_F	0.772	1.973
	R^2	0.9987	0.4260
Dubinin–Radushkevich	X_m (mmol/g)	0.638	1.069
	β (mol/kJ) ²	2.10^{-4}	3.10^{-5}
	E (kJ/mol)	0.016	0.129
	R^2	0.8843	0.9611
Temkin	a_{TE} (L/g)	5.820	6.991
	b_{TE} (kJ/mol)	0.245	0.025
	R^2	0.9235	0.4867
Flory-Huggins	K_{FH}	$2.38.10^{-3}$	$3.93.10^{-5}$
	n_{FH}	1.190	1.860
	ΔG^0 (kJ/mol)	14.972	25.142
	R^2	0.1920	0.5004
Brunauer, Emmer & Teller	q_s (mg/g)	3.753	39.745
	C_{BET} (L/mg)	0.421	2.020
	R^2	0.3481	0.5785

models show applicability of the model for metals adsorption using the present adsorbent. According to the correlation coefficients, the adsorption of strontium could be well described by Freundlich equation. Freundlich’s model theory is regarded as the heterogeneous adsorption and the exponential distribution of the energy of active sites as well as multilayer adsorption. Dubinin and Radushkevich isotherm provide a particularly good model for the adsorption of cesium. This model has reported that the characteristics of sorption curve is related to the porous structure of the sorbent.

According to the results, the maximum adsorption capacities of strontium and cesium were calculated as 2.103 mg/g from Freundlich model and 142.07 mg/g from Dubinin–Radushkevich model, respectively (**Table 1**). The $1/n_F$ value between 0 and 1 indicates that the adsorption is favorable under the experimental conditions. As seen in **Table 1**, cesium adsorption on magnetic graphene composite was found high enough for separation. Moreover, the value of $1/n_F$ is known as heterogeneity factor and ranges between 0 and 1; the more heterogeneous the surface, the closer $1/n_F$ value is to 0. The numerical

value of $1/n_F$ (< 1) indicates that adsorption capacity is only slightly suppressed at lower equilibrium concentration and the isotherm does not present any saturation of the solid surface of the sorbent by the sorbate^[36].

One of the unique features of the Dubinin–Radushkevich isotherm model lies on the fact that it is temperature-dependent, which when adsorption data at different temperatures are plotted as a function of logarithm of amount adsorbed vs the square of potential energy, all suitable data will lie on the same curve, named as the characteristic curve^[36]. The calculated E value is used to estimate the reaction mechanism of adsorption process. If value of E is smaller than 8 kJ/mol, it indicates a physical adsorption. If value of E is higher than 8 kJ/mol, the adsorption process is of a chemical nature. The E values obtained were 0.016 kJ/mol and 0.129 kJ/mol for strontium and cesium, respectively. Therefore, the magnitudes of E values are in the energy range of physical adsorption for strontium and cesium^[7,8].

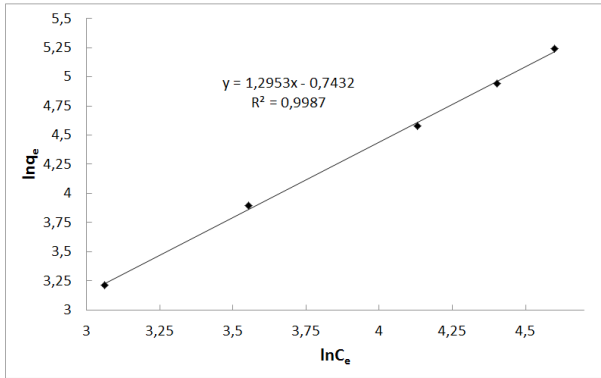


Figure 10. Linear isotherm models of Freundlich for strontium adsorption on magnetic graphene oxide composite.

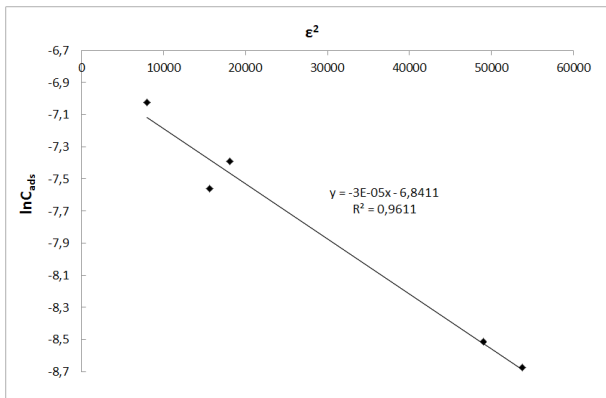


Figure 11. Linear isotherm models of Dubinin and Radushkevich for cesium adsorption on magnetic graphene oxide composite.

3.4 Kinetic parameters of adsorption

A study on the kinetics of adsorption is carrying out to obtain information about the adsorption mechanism, which is important for the efficiency of the process^[37]. Therefore, two well-known kinetic equations were adopted to model the experimental data and identify the adsorption mechanism.

In order to analyze the sorption of Sr(II)/Cs(I) onto M-GO, the pseudo first equation and pseudo second order equation was employed^[38–40]:

$$\log (q_e - q_t) = \log q_e - \frac{k_1 t}{2.303} \quad (14)$$

$$\frac{t}{q_t} = \frac{1}{k_2 q_e^2} + \frac{t}{q_e} \quad (15)$$

Where, q_e is the amount of metal ion adsorbed onto adsorbent at equilibrium (mg/g); q_t is the amount of metal ion adsorbed at various times; t (min) is the time of adsorption duration and k_1 is the first order rate constant (min^{-1}); k_2 (g/mol·min) is the

second-order rate constant.

The experiments were conducted at different concentrations 50, 100, 150 ppm for Sr(II) and 200, 250, 300 ppm for Cs(I). From the slope of each linear trace, the rate constants were calculated and the results are presented in the **Table 2** and **Table 3** (pseudo-first-order model was not shown as figure because the R^2 values of the adsorption of Sr(II) and Cs(I) are low at the studied concentrations). The data obtained separately for each of the kinetic models from the slopes of plots show a good compliance with the pseudo second order equation. High R^2 values for the linear plots showed that kinetic data fitted the pseudo second order adsorption kinetic equation for Sr(II) and Cs(I) removal (**Figure 12** and **Figure 13**).

The theoretical values of q_e for Sr(II) and Cs(I) removal also agree very well with the experimental ones. Both facts suggest that the adsorption of Sr(II) and Cs(I) onto M-GO follows the pseudo-second-order kinetic model. Therefore, the rate-limiting step may be chemical sorption or chemisorption through sharing or exchange of electrons between sorbent and adsorbate^[5].

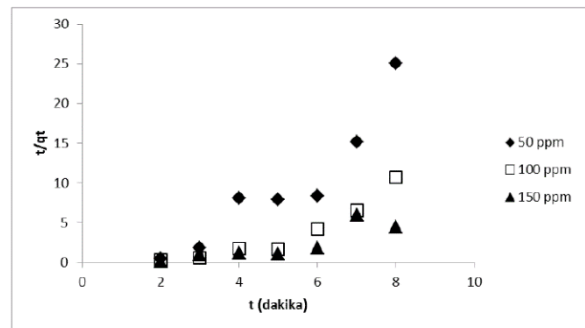


Figure 12. Pseudo-second-order plot for the adsorption of Sr(II) by M-GO.

Table 2. Rate parameters for the adsorption of Sr(II) onto M-GO at various initial concentrations

Concentration	50 ppm	100 ppm	150 ppm
Pseudo-first-order model			
q_e (mg/g)	1.8539	1.2600	4.5790
k_1 (1/min)	0.0999	0.0096	0.0145
R^2	0.0913	0.3406	0.0321
Pseudo-second-order model			
q_e^e (mg/g)	7.4404	16.7504	33.55
k_2 (g/mol·min)	1.1579	0.0627	1.1100
R^2	0.9646	0.9823	0.7632
Experimental q_e (mg/g)	7.89	18.22	32.30

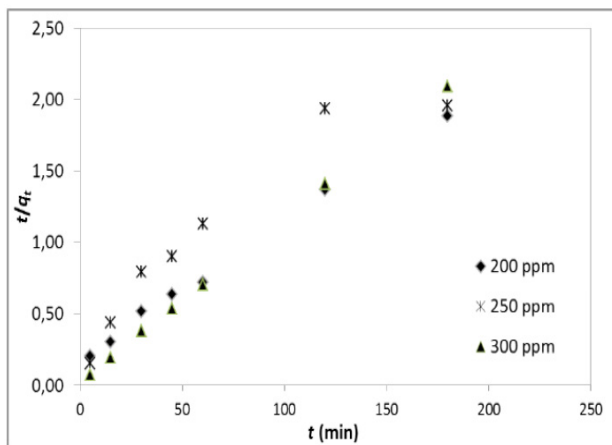


Figure 13. Pseudo-second-order plot for the adsorption of Cs(I) by M-GO.

Table 3. Rate parameters for the adsorption of Cs(I) onto M-GO at various initial concentrations

Concentration	200 ppm	250 ppm	300 ppm
Pseudo-first-order model			
q_e (mg/g)	69.47	100.74	120.46
k_1 (1/min)	0.0203	0.0205	0.0257
R^2	0.9586	0.7875	0.7567
Pseudo-second-order model			
q_e (mg/g)	104.17	96.15	86.96
k_2 (g/mol min)	0.0051	0.0003	0.0059
R^2	0.9965	0.8965	0.999
Experimental q_e (mg/g)	102.8	95.0	85.5

3.5 Thermodynamic studies

In this study, the adsorption of Sr(II) and Cs(I) onto M-GO was examined in the temperature range of 25–40 °C under optimized conditions (Sr: pH = 4, C: 50 mg/L, m/V: 1, t: 120 min; Cs: pH = 10, C: 250 mg/L, m/V: 1, t: 120 min and adsorbent amount of 0.01 g). **Figure 14 (a-b)** show the effect of tem-

perature on the adsorption of Sr(II) and Cs(I) on the nanocomposite, respectively. Thermodynamic parameters like enthalpy change (ΔH^0), entropy change (ΔS^0) and free energy change (ΔG^0) were estimated using the following equations.

$$\ln K_d = \frac{\Delta S^0}{R} - \frac{\Delta H^0}{RT} \quad (16)$$

$$\Delta G^0 = \Delta H^0 - T\Delta S^0 \quad (17)$$

The enthalpy ΔH^0 (kJ/mol) and the entropy ΔS^0 (J/molK) of adsorption can be determined from the slope and the intercept of the linear fits which are gained by drawing $\ln K_d$ against $1/T$ respectively. The negative amounts ΔG^0 show that the adsorption process is spontaneous for both of the ions. The values are well under those related to chemical bond constitution, showing the physical property of the adsorption process^[41]. Besides, the enthalpy variation ΔH^0 following adsorption is negative in all cases representing the exothermic nature of the adsorption. The results indicated that the reaction efficiency decreased as the temperature increased for Sr(II) removal but the reaction efficiency increased as the temperature increased for Cs(I) removal.

The negative value of ΔS^0 for Sr(II) shows the change in the randomness at the M-GO-solution interface during the adsorption. The entropy variations ΔS^0 of the system along with the adsorption of Cs(I) ions on the M-GO is positive in all cases, showing that more disorder is generated following adsorption. The results were calculated in **Table 4**.

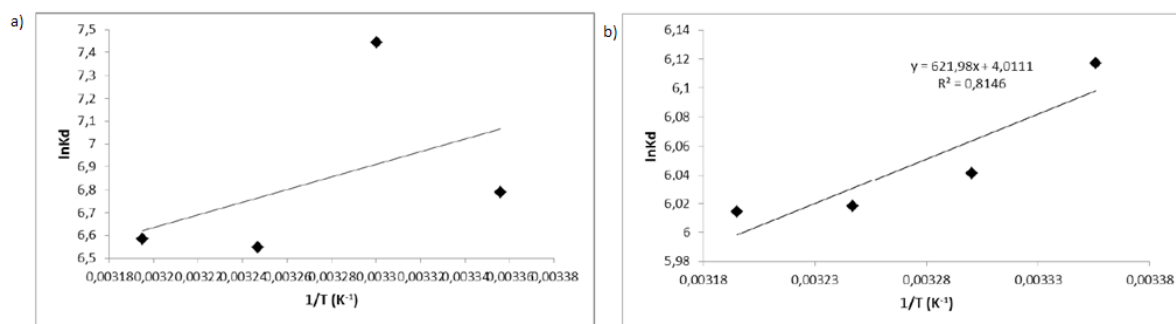


Figure 14. Plots of $\ln K_d$ versus $1/T$ for Sr (a) and Cs (b) adsorption on M-GO.

Table 4. Thermodynamic parameters for Sr(II) and Cs(I) sorption on M-GO as a function of temperature

M-GO	ΔH^0 (kJ/mol)	ΔS^0 (J/molK)	ΔG^0 (kJ/mol)			
			298 K	303 K	308 K	318 K
Sr(II)	-22.97	-18.37	-17.49	-17.42	-17.33	-17.24
Cs(I)	-5.17	33.35	-15.11	-15.28	-15.44	-15.61

4. Conclusion

M-GO nanocomposite was synthesized using partial reduction co-precipitation method, which is simple, effective, economical and environmentally friendly technique for the removal of Sr(II) and Cs(I) from aqueous solutions. Prepared nanocomposite was characterized by SEM, TEM, XRD, FTIR, XPS and VSM. According to all characterization methods and literature data, we can conclude that M-GO was successfully prepared and possessed with the desired properties. The adsorption capacity of M-GO for Sr(II) and Cs(I) were found as 2.103 mg/g and 142.070 mg/g, respectively. Kinetic results indicated that the adsorption process could be defined by the pseudo-second-order kinetic model under the selected strontium and cesium concentration range which provides the best correlation of the data in all cases and the experimental q_e values agree with the calculated ones and the adsorption isotherm was fitted well to Freundlich model and D-R model for Sr(II) and Cs(I), respectively. The thermodynamic analysis of the sorption process for both of the radionuclides indicates that the system is spontaneous and exothermic. The values of ΔG^0 for Sr(II) and Cs(I) are well under those related to chemical bond constitution, showing the physical property of the adsorption process. It could be therefore concluded that the sorption mechanism was dominated by physisorption, but the overall observations suggest that the sorption process was administrated by combination of several mechanisms, such as physical sorption, ion exchange and complexation. Based on the results, M-GO can effectively remove the strontium and cesium ions from aqueous solutions.

Author contributions

Sule Aytas, Sabriye Yusan and Senol Sert performed the experiments and analyzed the data. Sule Aytas supervised and designed data. Sabriye Yusan and Cem Gok designed and analyzed data, and prepared the manuscript. Senol Sert realized ICP-OES measurements and also designed the manuscript.

Conflict of interest

The authors declare that they have no conflict of interest.

Acknowledgements

This research project was supported by Ege University Scientific Research Project Unit Project No. 2014 NBE 005.

References

1. Japan's Challenges Towards Recovery. Ministry of Economy, Trade and Industry [Internet]. [cited March 2012]. Available from: http://www.meti.go.jp/english/earthquake/nuclear/japan-challenges/pdf/japan-challenges_full.pdf.
2. IAEA Briefing on Fukushima Nuclear Accident [cited 13 April 2011]. Available from: <https://www.iaea.org/newscenter/news/fukushima-nuclear-accident-update-log-17>.
3. Tangestani F, Mallah MH, Rashidi A, Habibzadeh R. Adsorption of Cesium, Strontium, and Rubidium radionuclides in the Magmolecular process: The influence of important factors. *Advances in Environmental Technology* 2017; 3: 139–49.
4. Anzai, K, Ban N, Ozawa T, *et al.* Fukushima Daiichi Nuclear Power Plant accident: Facts, environmental contamination, possible biological effects, and countermeasures. *Journal of Clinical Biochemistry & Nutrition* 2012; 50(1): 2–8.
5. Yusan S, Gok C, Erenturk S, *et al.* Adsorptive removal of thorium (IV) using calcined and flux calcined diatomite from Turkey: Evaluation of equilibrium, kinetic and thermodynamic data. *Applied Clay Science* 2012; 67: 106–116.
6. Yusan SD, Akyil S. Sorption of uranium (VI) from aqueous solutions by akaganeite. *Journal of Hazardous Materials* 2008; 160(2-3): 388–395.
7. Yusan S, Bampaiti A, Erenturk S, *et al.* Sorption of Th (IV) onto ZnO nanoparticles and diatomite-supported ZnO nanocomposite: Kinetics, mechanism and activation parameters. *Radiochimica Acta* 2016; 104(9): 635–647.
8. Gok C. Neodymium and samarium recovery by magnetic nano-hydroxyapatite. *Journal of Radioanalytical and Nuclear Chemistry* 2014; 301(3) :641–651.

9. Tayyebi A, Outokesh M, Moradi S, *et al.* Synthesis and characterization of ultrasound assisted “graphene oxide–magnetite” hybrid, and investigation of its adsorption properties for Sr(II) and Co(II) ions. *Applied Surface Science* 2015; 353: 350–362.
10. Yang H, Li H, Zhai J, *et al.* Magnetic prussian blue/graphene oxide nanocomposites caged in calcium alginate microbeads for elimination of cesium ions from water and soil. *Chemical Engineering Journal* 2014; 246: 10–19.
11. Jolivet J-P, Chanéac C, Tronc E. Iron oxide chemistry. From molecular clusters to extended solid networks. *Cheminform* 2004; 35(18): 481–483.
12. Chen S, Brown L, Levendorf M, *et al.* Oxidation resistance of graphene-coated Cu and Cu/Ni alloy. *ACS Nano* 2011; 5(2): 1321–1327.
13. Zhang Y, Chen B, Zhang L, *et al.* Controlled assembly of Fe₃O₄ magnetic nanoparticles on graphene oxide. *Nanoscale* 2011; 3: 1446–1450.
14. Yao Y, Miao S, Liu S, *et al.* Synthesis, characterization, and adsorption properties of magnetic Fe₃O₄ @ graphene nanocomposite. *Chemical Engineering Journal* 2012; 184: 326–332.
15. Yusan S, Korzhynbayeva K, Aytas S, *et al.* Preparation and investigation of structural properties of magnetic diatomite nanocomposites formed with different iron content. *Journal of Alloys & Compounds* 2014; 608: 8–13.
16. El-din TAS, Elzatahry AA, Aldhayan DM, *et al.* Synthesis and characterization of magnetite zeolite nano composite. *International Journal of Electrochemical Science* 2011; 6: 6177–6183.
17. Chen L, Xu J, Hu J. Removal of U(VI) from aqueous solutions by using attapulgite/iron oxide magnetic nanocomposites. *Journal of Radioanalytical & Nuclear Chemistry* 2013; 297(1): 97–105.
18. Nodeh HR, Ibrahim WAW, Ali I, *et al.* Development of magnetic graphene oxide adsorbent for the removal and preconcentration of As(III) and As(V) species from environmental water samples. *Environmental Science and Pollution Research* 2016; 23: 9759–773.
19. Guo J, Wang R, Tjiu WW, *et al.* Synthesis of Fe nanoparticles @ graphene composites for environmental applications. *Journal of Hazardous Materials* 2012; 225–226: 63–73.
20. Qin Y, Long M, Tan B, *et al.* RhB adsorption performance of magnetic adsorbent Fe₃O₄/RGO composite and its regeneration through a Fenton-like reaction. *Nano-Micro Letters* 2014; 6(2): 125–135.
21. Lujanienė G, Semcuk S, Lecinskyte A, *et al.* Magnetic graphene oxide based nano-composites for removal of radionuclides and metals from contaminated solutions. *Journal of Environmental Radioactivity* 2017; 166(1): 166–174.
22. Dorniani D, Bin Hussein MZ, Kura AU, *et al.* Preparation of Fe₃O₄ magnetic nanoparticles coated with gallic acid for drug delivery. *International Journal of Nanomedicine* 2012; 7: 5745–5756.
23. Cheng, G, Yu, X, Zhou M, *et al.* Preparation of magnetic graphene composites with hierarchical structure for selective capture of phosphopeptides. *Journal of Materials Chemistry B* 2014; 2(29): 4711–4719.
24. Hur J, Shin J, Yoo J, Seo Y-S. Competitive adsorption of metals onto magnetic graphene oxide: Comparison with other carbonaceous adsorbents. *The Scientific World Journal* 2015: 836287.
25. Kakutani Y, Weerachawanajak P, Hirata Y, *et al.* Highly effective K-Merlinoite adsorbent for removal of Cs⁺ and Sr²⁺ in aqueous solution. *RSC Advances* 2017; 7: 30919–30928.
26. Khambhaty Y, Mody K, Basha S, *et al.* Kinetics, equilibrium and thermodynamic studies on biosorption of hexavalent chromium by dead fungal biomass of marine *Aspergillus niger*. *Chemical Engineering Journal* 2009; 145: 489–495.
27. Khani MH. Statistical analysis and isotherm study of uranium biosorption by *Padina* sp. algae biomass. *Environmental Science & Pollution Research* 2011; 18: 790–799.
28. Gok C, Aytas S. Recovery of thorium by high-capacity biopolymeric sorbent. *Separation Science and Technology* 2013;48(14): 2115–2124.
29. Langmuir I. The adsorption of gases on plane surfaces of glass, mica and platinum. *Journal of Chemical Physics* 2015; 40(9): 1361–1403.
30. Freundlich H. Adsorption in solution. *Journal of Physical Chemistry* 1906; 57: 384–410.
31. Dubinin MM. The potential theory of adsorption of gases and vapors for adsorbents with energetically non-uniform surface. *Chemical Reviews* 1960; 60:

- 235–266.
32. Temkin MJ, Pyzhev V. Recent modifications to Langmuir isotherms. *Acta Physiochim* 1940; 12: 217–222.
 33. Flory PJ. Thermodynamics of high polymer solutions. *Journal of Chemical Physics* 1942; 10: 51–62.
 34. Huggins ML. Some properties of solutions of long-chain compounds. *Journal of Chemical Physics* 1942; 10: 151–158.
 35. Bruanuer S, Emmett PH, Teller E. Adsorption of gases in multimolecular layers. *Journal of the American Chemical Society* 1938; 60: 309–316.
 36. Foo KY, Hameed BH. Insights into the modeling of adsorption isotherm systems. *Chemical Engineering Journal* 2010; 156: 2–10.
 37. Jain AK, Gupta VK, Bhatnagar A, *et al.* Utilization of industrial waste products as adsorbents for the removal of dyes. *Journal of Hazardous Materials* 2003; B101: 31–42.
 38. Lagergren S. Zur theorie der sogenannten adsorption geloster stoffe. *Kungliga Svenska Vetenskapsakademiens. Handlingar* 1898; 24(4): 1–39.
 39. Ho YS, McKay G. The kinetics of sorption of basic dyes from aqueous solution by sphagnum moss peat. *The Canadian Journal of Chemical Engineering* 1998; 76: 822–827.
 40. Liang S, Guo X, Feng N, *et al.* Isotherms, kinetics and thermodynamic studies of adsorption of Cu^{2+} from aqueous solutions by $\text{Mg}^{2+}/\text{K}^{+}$ type orange peel adsorbents. *Journal of Materials Chemistry* 2010; 174: 756–762.
 41. Almeida CAP, Debacher NA, Downs AJ, *et al.* Removal of methylene blue from colored effluents by adsorption on montmorillonite clay. *Journal of Colloid and Interface Science* 2009; 332(1): 46–53.

ORIGINAL RESEARCH ARTICLE

Mesoscale computational prediction of lightweight, thermally conductive polymer nanocomposites containing graphene-wrapped hollow particle fillers

Jianjun Wang^{1,a,*}, Zhonghui Shen^{2,a}, Wenying Zhou^{3*}, Yang Shen², Cewen Nan², Qing Wang¹, Longqing Chen^{1*}

¹ Department of Materials Science and Engineering, The Pennsylvania State University, University Park, Pennsylvania 16802, United States. E-mail: wjj8384@gmail.com (J Wang); lqc3@psu.edu (L Chen)

² School of Materials Science and Engineering, State Key Lab of New Ceramics and Fine Processing, Tsinghua University, Beijing 100084, China

³ College of Chemistry and Chemical Engineering, Xi'an University of Science & Technology, Xi'an 710054, China. E-mail: wyzhou2004@163.com (W Zhou)

ABSTRACT

Heat removal has become an increasingly crucial issue for microelectronic chips due to increasingly high speed and high performance. One solution is to increase the thermal conductivity of the corresponding dielectrics. However, traditional approach to adding solid heat conductive nanoparticles to polymer dielectrics led to a significant weight increase. Here we propose a dielectric polymer filled with heat conductive hollow nanoparticles to mitigate the weight gain. Our mesoscale simulation of heat conduction through this dielectric polymer composite microstructure using the phase-field spectral iterative perturbation method demonstrates the simultaneous achievement of enhanced effective thermal conductivity and the low density. It is shown that additional heat conductivity enhancement can be achieved by wrapping the hollow nanoparticles with graphene layers. The underlying mesoscale mechanism of such a microstructure design and the quantitative effect of interfacial thermal resistance will be discussed. This work is expected to stimulate future efforts to develop light-weight thermal conductive polymer nanocomposites.

Keywords: Thermal Conductivity; Polymer Nanocomposites; Materials Design; Graphene-Wrapped Hollow Nanoparticles

ARTICLE INFO

Received: 2 February 2021
Accepted: 17 March 2021
Available online: 25 March 2021

COPYRIGHT

Copyright © 2021 Jianjun Wang, *et al.*
EnPress Publisher LLC. This work is licensed under the Creative Commons Attribution-NonCommercial 4.0 International License (CC BY-NC 4.0).
<https://creativecommons.org/licenses/by-nc/4.0/>

1. Introduction

The effective thermal management in applications, such as LED (light emitting diode) lighting, batteries, automobile cooling systems, and high-power density microelectronic devices, where heat accumulation can have deleterious effects, is critically important to ensure the device performance and reliability, and therefore to enhance the lifetime and accuracy of the system^[1-3]. With further miniaturization, integration and functionalization of microelectronics and the emerging applications, such as electronic assembly and packaging, and solar the thermal dissipation has become a challenge^[4-6]. Addressing this challenge requires the development of novel materials with enhanced thermal conductivity as well as light weight, low cost, good processability, and corrosion resistance. Polymers have many of these charac-

^a These authors contributed equally to this work.

teristics, but they generally have very low thermal conductivity ($0.1\text{--}0.4\text{ Wm}^{-1}\cdot\text{K}^{-1}$)^[7,8]. Therefore, heat conductive fillers, such as carbon nanotube^[9–13] ($> 2,000\text{ Wm}^{-1}\cdot\text{K}^{-1}$), graphene^[14–18] ($\sim 5,000\text{ Wm}^{-1}\cdot\text{K}^{-1}$), aluminum oxide^[19–21] ($> 20\text{ Wm}^{-1}\cdot\text{K}^{-1}$), boron nitride^[22–26] ($\sim 350\text{ Wm}^{-1}\cdot\text{K}^{-1}$), and metal particles^[27–31] ($> 100\text{ Wm}^{-1}\cdot\text{K}^{-1}$), etc., are traditionally added into polymers to enhance their thermal conductivity while preserving the above-mentioned advantages of polymers.

The influences of the filler type, size, shape, alignment, and loading level on the effective thermal conductivity of the resulted polymer composites have been extensively investigated, see e.g., the recent reviews^[5,12,32]. It was generally accepted that a high filler loading level ($\geq 30\%$ in volume) is necessary in order to achieve the appropriate level ($\geq 1\text{ Wm}^{-1}\cdot\text{K}^{-1}$) of thermal conductivity in a polymer nanocomposite. For example, heat sinks in micro-electronic systems require polymer nanocomposites with a thermal conductivity approximately from 1 to $30\text{ Wm}^{-1}\cdot\text{K}^{-1}$, which normally needs a filler loading level higher than 30% in volume^[7,33]. The high loading level of the filler, particularly for metallic fillers, usually significantly increases the mass density and costs, and weakens the mechanical performances, such as tensile strength and flexibility, and processibility, which prevents the polymer composites from being used commercially, in particular in aerospace where a lightweight is extremely desired^[32,34]. Therefore, it is imperative to seek for alternative approach-

es to developing novel material microstructures with enhanced thermal conductivity but low density and costs.

To effectively reduce the weight and improve the specific thermal conductivity of filled polymers, in this work, we propose to fill the polymer matrix with hollow nanoparticles to increase the thermal conductivity while preserving a low mass density of the nanocomposite. In particular, we computed the effective thermal conductivity (κ_{eff}) and the effective mass density (ρ_{eff}) of the polyethylene (PE) polymer nanocomposites filled with various hollow nanoparticles. It is predicted that by wrapping a thin graphene layer onto the hollow nanoparticles, the effective thermal conductivity can be further significantly enhanced.

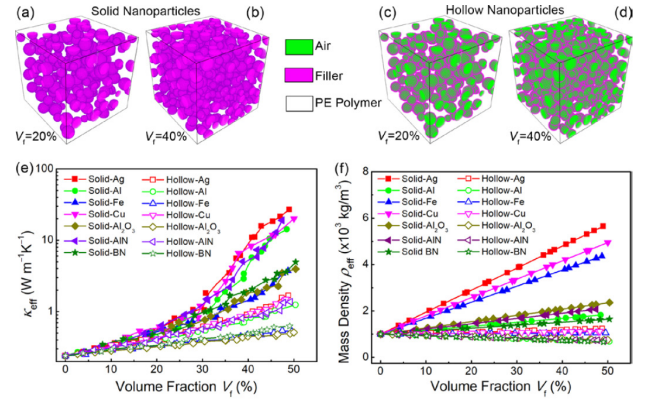


Figure 1. Computationally-generated microstructures for polymer nanocomposites filled with (a) 20 vol.% solid nanoparticles, (b) 40 vol.% solid nanoparticles, (c) 20 vol.% hollow nanoparticles, and (d) 40 vol.% hollow nanoparticles, (e) the effective thermal conductivity and (f) mass density as function of filler volume fraction for polymer nanocomposites filled with various solid and hollow nanoparticles.

Table 1. Thermal conductivities and mass density of the filler materials used in the simulation. For BN nanoparticles, the thermal conductivity used is smaller than the literature values which were reported for the in-plane thermal conductivity in BN nanosheets. For PE polymer, the thermal conductivity depends on the density

Materials	Thermal Conductivity ($\text{Wm}^{-1}\cdot\text{K}^{-1}$)	Mass Density (kg/m^3)	Literature Values ($\text{Wm}^{-1}\cdot\text{K}^{-1}$)	Refs.
Ag	417	10,490	427	31
Al	237	2,700	247	28
Fe	40	7,900	67	38
Cu	397	8,900	398	28
Al_2O_3	33	3,700	30–36	39
AlN	300	3,260	100–300	5
BN	57	2,290	185–300	5,40
Graphene	4,000	2,250	2,000–6,000	41,42
PE polymer	0.24	1,000	0.3–0.45	5
Air	0.024	1.225	0.024	5

2. Methods

The heat conduction equation in the polymer nanocomposite can be written as:

$$\frac{\partial}{\partial x_i} \left(k_{ij}(\mathbf{x}) \frac{\partial T(\mathbf{x})}{\partial x_j} \right) + q(\mathbf{x}) = \rho(\mathbf{x}) c_p(\mathbf{x}) \frac{\partial T(\mathbf{x})}{\partial t} \quad (1)$$

where $k_{ij}(\mathbf{x})$, $T(\mathbf{x})$, $\rho(\mathbf{x})$, and $c_p(\mathbf{x})$ represent the spatial-dependent thermal conductivity tensor, temperature, the mass density, and the specific heat capacity, respectively. Those spatial-dependent material properties such as $k_{ij}(\mathbf{x})$, $\rho(\mathbf{x})$, and $c_p(\mathbf{x})$ are determined by the microstructure of the polymer nanocomposite specified by a phase-field variable. The internal heat source of the material is represented by $q(\mathbf{x})$. Eq. (1) can be solved using the spectral iterative perturbation method which was developed in previous work^[35] or using the finite element method via the COMSOL software. When incorporating the interfacial thermal resistance, slit boundary conditions are applied at the heterointerfaces between phase A and phase B, i.e.,

$$-\mathbf{n}_A \cdot (-\mathbf{k}^A \nabla T_A) = \frac{T_B - T_A}{R_k}, \quad -\mathbf{n}_B \cdot (-\mathbf{k}^B \nabla T_B) = \frac{T_A - T_B}{R_k} \quad (2)$$

where n_A and n_B represent the normal directions of the interface pointing to phase A and phase B, respectively. The variable T_A and T_B represent the temperature at the two boundaries of the heterointerfaces, and k_A and k_B represent the thermal conductivity of phase A and phase B, respectively. Once the temperature distribution is solved, the heat flux density that flows through a unit area per unit time can be determined from the Fourier's law, i.e.,

$$J_i = -k_{ij}(\mathbf{x}) \partial T(\mathbf{x}) / \partial x_j \quad (3)$$

The effective thermal conductivity tensor k_{ij}^{eff} of the polymer nanocomposite can then be determined from Eq. (3) by solving

$$\langle J_i \rangle = -k_{ij}^{\text{eff}} \langle \partial T(\mathbf{x}) / \partial x_j \rangle \quad (4)$$

where $\langle \rangle$ represents the average property per volume.

2. Results and discussions

Figures 1a-d show the microstructures of PE nanocomposites filled with 20 vol.% and 40 vol.%

solid nanoparticles, 20 vol.% and 40 vol.% hollow nanoparticles, respectively, computationally generated assuming random distributions of the filler nanoparticles. For hollow nanoparticles, the thickness of the filler layer is about 4% to 7% of the radius of the nanoparticles. The effective thermal conductivity for the polymer nanocomposite is calculated by solving the steady-state heat conduction equation using the phase-field spectral iterative perturbation method^[35-37]. The intrinsic thermal conductivities and mass densities of the filler materials, polyethylene (PE) polymer, and air used in the computation are listed in **Table 1**.

Figure 1e shows the effective thermal conductivity as function of the filler volume fraction for PE nanocomposites filled with various nanoparticles. For all listed nanocomposites, the effective thermal conductivity increases with the volume fraction of the fillers for both the solid and hollow nanoparticles. For a filler material at a given V_f , the solid nanoparticles are more effective than the hollow nanoparticles in enhancing the thermal conductivity. For example, at a V_f of ~50%, the polymer nanocomposites filled with solid Ag, solid Al, solid Fe, solid Cu, solid Al_2O_3 , solid AlN, and solid BN nanoparticles have a κ_{eff} of ~28 $\text{Wm}^{-1}\cdot\text{K}^{-1}$, ~14 $\text{Wm}^{-1}\cdot\text{K}^{-1}$, ~3.6 $\text{Wm}^{-1}\cdot\text{K}^{-1}$, ~20 $\text{Wm}^{-1}\cdot\text{K}^{-1}$, ~4.1 $\text{Wm}^{-1}\cdot\text{K}^{-1}$, ~22 $\text{Wm}^{-1}\cdot\text{K}^{-1}$, and ~5.0 $\text{Wm}^{-1}\cdot\text{K}^{-1}$, while their counterparts filled with corresponding hollow nanoparticles have a κ_{eff} of ~1.9 $\text{Wm}^{-1}\cdot\text{K}^{-1}$, ~1.2 $\text{Wm}^{-1}\cdot\text{K}^{-1}$, ~0.5 $\text{Wm}^{-1}\cdot\text{K}^{-1}$, ~1.7 $\text{Wm}^{-1}\cdot\text{K}^{-1}$, ~0.5 $\text{Wm}^{-1}\cdot\text{K}^{-1}$, ~1.4 $\text{Wm}^{-1}\cdot\text{K}^{-1}$, and ~0.6 $\text{Wm}^{-1}\cdot\text{K}^{-1}$, respectively (see **Table 2**).

However, the effective mass density of the PE nanocomposite is significantly increased by the solid nanoparticles compared to the hollow nanoparticles. As shown in **Figure 1f**, at a V_f of ~50%, the nanocomposites filled with solid Ag, solid Cu, and solid Fe nanoparticles respectively have a ρ_{eff} of ~5,646 kg/m^3 , ~4,971 kg/m^3 , and ~4,374 kg/m^3 , while their counterparts filled with hollow nanoparticles have a much lower ρ_{eff} of ~1,246 kg/m^3 , ~1,135 kg/m^3 , and ~1,109 kg/m^3 , respectively (see **Table 2**). More interestingly, the effective mass density of the polymer nanocomposites filled with hollow Al, hollow Al_2O_3 , hollow AlN, and hollow BN even decreases with

the volume fraction of the nanoparticles. More specifically, the effective mass density of the polymer nanocomposites can be reduced from $\sim 1,000 \text{ kg/m}^3$ to $\sim 681 \text{ kg/m}^3$, $\sim 756 \text{ kg/m}^3$, $\sim 731 \text{ kg/m}^3$, and ~ 663

kg/m^3 when it is respectively filled with hollow Al, hollow Al_2O_3 , hollow AlN, and hollow BN nanoparticles at a V_f of 50 percent (see **Table 2**).

Table 2. Effect thermal conductivity and mass density for polymer nanocomposites filled with various solid, hollow, and graphene-wrapped hollow nanoparticles at a volume fraction of 50%.

Nanoparticle	$V_f = 50\%$	Ag	Al	Fe	Cu	Al_2O_3	AlN	BN
Solid	$\kappa_{\text{eff}} (\text{Wm}^{-1}\cdot\text{K}^{-1})$	28	14	3.6	20	4.1	22	5.0
	$\rho_{\text{eff}} (\text{kg/m}^3)$	5,646	1,849	4,374	4,971	2,380	2,097	1,663
Hollow	$\kappa_{\text{eff}} (\text{Wm}^{-1}\cdot\text{K}^{-1})$	1.9	1.2	0.5	1.7	0.5	1.4	0.6
	$\rho_{\text{eff}} (\text{kg/m}^3)$	1,246	681	1,109	1,135	756	731	663
Graphene-wrapped	$\kappa_{\text{eff}} (\text{Wm}^{-1}\cdot\text{K}^{-1})$	~ 11	~ 11	~ 5	~ 11	~ 5	~ 11	~ 5
	$\rho_{\text{eff}} (\text{kg/m}^3)$	1,290	817	1,153	1,196	877	847	789

Figure 2a shows the mapping result of the κ_{eff} as function of the thermal conductivity of the filler material (κ_{filler}) and V_f for the polymer nanocomposites filled with hollow nanoparticles. The calculations in **Figure 1e** are included in this more comprehensive mapping result. For example, for nanocomposites filled with 10 vol.% hollow AlN, 20 vol.% hollow Cu, 30 vol.% hollow Al, and 40 vol.% hollow Ag nanoparticles, which are marked on **Figure 2e**, they have a κ_{eff} of $\sim 0.31 \text{ Wm}^{-1}\cdot\text{K}^{-1}$, $\sim 0.41 \text{ Wm}^{-1}\cdot\text{K}^{-1}$, $\sim 0.54 \text{ Wm}^{-1}\cdot\text{K}^{-1}$, $\sim 0.91 \text{ Wm}^{-1}\cdot\text{K}^{-1}$, respectively, as indicated by the color bar. The κ_{eff} increases with both κ_{filler} and V_f . At $\kappa_{\text{filler}} = 2000 \text{ Wm}^{-1}\cdot\text{K}^{-1}$ and $V_f = 50\%$, the effective thermal conductivity can be increased to $\sim 4.8 \text{ Wm}^{-1}\cdot\text{K}^{-1}$. In contrast, **Figure 2b** shows the mapping result for the nanocomposite filled with solid nanoparticles. The solid nanoparticles are indeed more effective in enhancing the κ_{eff} than their hollow

counterparts. For example, at $\kappa_{\text{filler}} = 2000 \text{ Wm}^{-1}\cdot\text{K}^{-1}$ and $V_f = 50\%$, the κ_{eff} can be enhanced to $\sim 103 \text{ Wm}^{-1}\cdot\text{K}^{-1}$ by the solid nanoparticles.

However, in order to achieve a specific thermal conductivity by filling different types of nanoparticles into the PE polymer, the nanocomposites filled with hollow nanoparticles are shown to require much less filler materials and hence show much lower mass density. For example, as shown in **Figure 3a**, for a PE nanocomposite with an effective thermal conductivity of $\sim 1 \text{ Wm}^{-1}\cdot\text{K}^{-1}$, the mass density is $\sim 3,566 \text{ kg/m}^3$, $\sim 1,506 \text{ kg/m}^3$, $\sim 3,206 \text{ kg/m}^3$, and $\sim 1,614 \text{ kg/m}^3$ when the nanocomposite is filled with solid Ag, solid Al, solid Cu, and solid AlN nanoparticles, respectively. However, their counterparts only show a mass density of $\sim 1,271 \text{ kg/m}^3$, $\sim 774 \text{ kg/m}^3$, $\sim 1,156 \text{ kg/m}^3$, and $\sim 805 \text{ kg/m}^3$ when filled with the corresponding hollow nanoparticles.

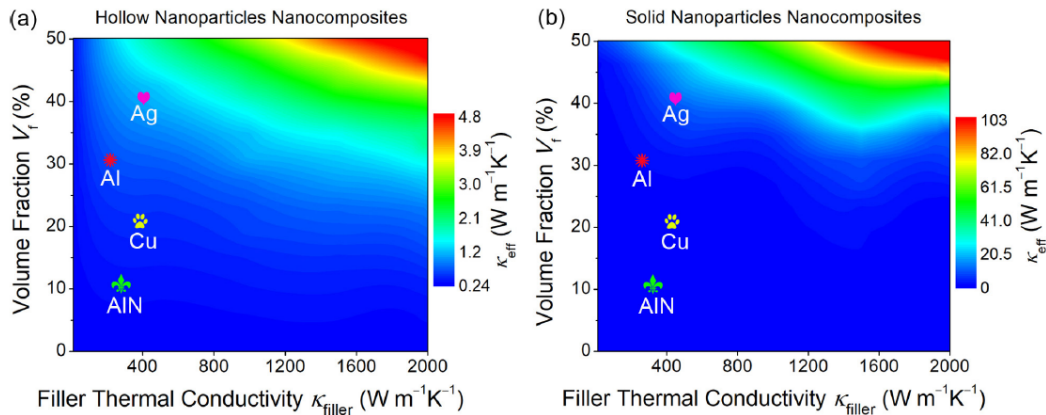


Figure 2. The effective thermal conductivity as function of the volume fraction and the filler thermal conductivity for polymer nanocomposites filled with (a) hollow nanoparticles and (b) solid nanoparticles.

Furthermore, the materials cost in the nanocomposites filled with the hollow nanoparticles will also be much less. As shown in **Figure 3b**, the unit costs of the polymer nanocomposites filled with hollow Ag, hollow Al, hollow Cu, and hollow AlN nanoparticles are ~ 0.839 $\$/\text{cm}^3$, ~ 0.001 $\$/\text{cm}^3$, ~ 0.0069 $\$/\text{cm}^3$, and ~ 0.161 $\$/\text{cm}^3$, while the unit costs of their counterparts filled with solid nanoparticles are ~ 2.35 $\$/\text{cm}^3$, ~ 0.0019 $\$/\text{cm}^3$, ~ 0.019 $\$/\text{cm}^3$, and ~ 0.322 $\$/\text{cm}^3$, respectively. Therefore, the usage of hollow nanoparticles reduces the weight of the nanocomposite and the materials cost of the nanocomposite. However, the hollow nanoparticles might not yield sufficient enhancement of the effective thermal conductivity. For instance, by filling hollow nanoparticles such as Fe, Al_2O_3 , and BN into the PE polymer, a target κ_{eff} of $1 \text{ Wm}^{-1}\cdot\text{K}^{-1}$ may not be achieved unless denser PE polymer with higher thermal conductivity is used as the matrix.

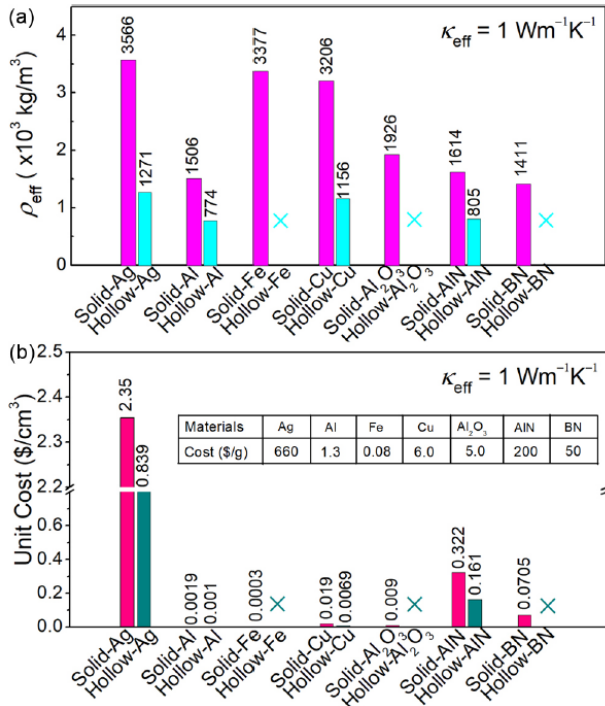


Figure 3. For a PE nanocomposite with a targeted effective thermal conductivity of $1 \text{ Wm}^{-1}\cdot\text{K}^{-1}$, (a) the mass density and (b) the unit cost of materials it has when it is filled with various solid and hollow nanoparticles. The inset Table of (b) lists the rough costs of different filler materials, which might change depending on the market.

In the light of the mapping result for the κ_{eff} as function of the κ_{filler} and the V_f shown in **Figure 2a**, we propose a hierarchical architecture for

the hollow nanoparticles. As shown in **Figure 4**, we suggest wrapping one graphene layer onto the shell of the hollow nanoparticle. This design is rationalized by the super-high thermal conductivity ($\sim 4,000 \text{ Wm}^{-1}\cdot\text{K}^{-1}$) of the graphene^[41,42], which can be employed to possibly wrap the shell of a hollow nanoparticle^[43-45]. The technique of wrapping a graphene layer onto the shell of a nanoparticle has been used to improve the performances of batteries^[43-45], and here we predict that it can be used to improve the effective thermal conductivity of the polymer nanocomposites.

It can be seen from **Figure 5a** that the effective thermal conductivity of the nanocomposite filled with graphene-wrapped hollow nanoparticles increases much faster with the volume fraction of the filler nanoparticles. At a V_f of 50%, the effective thermal conductivity of the nanocomposite can be enhanced to $\sim 11 \text{ Wm}^{-1}\cdot\text{K}^{-1}$, which is about 10 times of their counterparts filled with hollow nanoparticles without a graphene layer. Meanwhile, this hierarchical architecture does not increase the effective mass density much. As shown in **Figure 5b**, the effective mass density of the nanocomposite at a V_f of 50% is $\sim 1,290 \text{ kg/m}^3$, $\sim 817 \text{ kg/m}^3$, $\sim 1,153 \text{ kg/m}^3$, $\sim 1,196 \text{ kg/m}^3$, $\sim 877 \text{ kg/m}^3$, $\sim 847 \text{ kg/m}^3$, and $\sim 789 \text{ kg/m}^3$ when filled with graphene-wrapped hollow Ag, Al, Fe, Cu, Al_2O_3 , AlN, and BN nanoparticles, respectively (see **Table 2**). These values are about $\sim 3.5\%$, $\sim 20.0\%$, $\sim 3.9\%$, $\sim 5.3\%$, $\sim 16.0\%$, $\sim 15.8\%$, and $\sim 19.0\%$ higher than their counterparts filled with corresponding hollow nanoparticles without wrapping graphene.

Figure 6a shows the comparison of the effective mass density between the nanocomposites filled with solid nanoparticles and graphene-wrapped hollow nanoparticles. It can be seen that a target κ_{eff} of $1 \text{ Wm}^{-1}\cdot\text{K}^{-1}$ now can be achieved by all listed filler materials. The effective mass densities of the nanocomposites filled with graphene-wrapped hollow nanoparticles are much lower than their counterparts filled with solid nanoparticles. For nanocomposites filled with heavy fillers such as Ag, Fe, and Cu, the effective mass density can be reduced by $\sim 70\%$ by using graphene-wrapped hollow nanoparticles rather than solid nanoparticles, while still preserving the

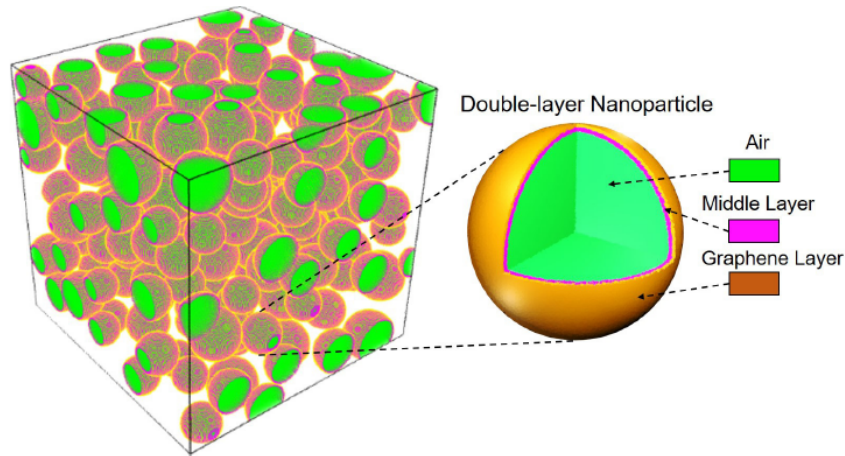


Figure 4. The microstructure of a polymer nanocomposite filled with a double-layer nanoparticle where the outer layer is graphene.

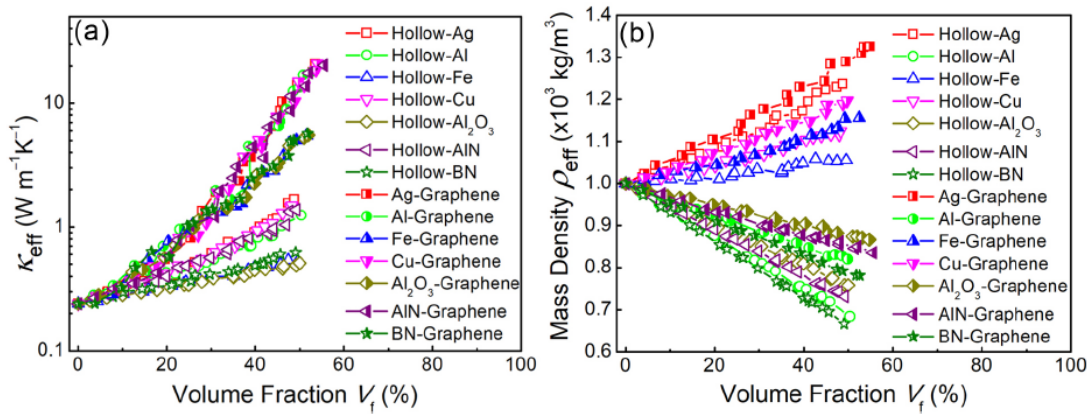


Figure 5. (a) The effective thermal conductivity and (b) mass density as function of filler volume fraction for polymer nanocomposites filled with graphene-wrapped hollow nanoparticles, compared with their counterparts without graphene layer.

same κ_{eff} of $1 \text{ W m}^{-1} \cdot \text{K}^{-1}$. This is not only beneficial to the reduction of the weight and materials costs, but also beneficial to the preservation of the flexibility performances of the polymers which can easily be damaged by a high loading level^[46–50]. As shown in **Figure 6b**, the V_f of the nanocomposites filled with graphene-wrapped hollow nanoparticles is universally reduced, compared with the counterpart in the nanocomposites filled with solid nanoparticles.

Now turn to the underlying mechanisms of the advantages of using hollow nanoparticles and graphene-wrapped nanoparticles over the solid nanoparticles. We consider three nanocomposites, which are filled with solid nanoparticles, hollow nanoparticles, and graphene-wrapped hollow nanoparticles, respectively. The filler materials are same, e.g., Cu metal, and the sizes of the filler nanoparticles are assumed to be similar. The volume fraction of Cu metal in the three nanocomposites

are set to be at the same value of 6%. While in the nanocomposite filled with solid nanoparticles the thermally conductive Cu metal concentrates at each solid particle, the Cu metal in the nanocomposite filled with hollow nanoparticles distributes on the surface of each hollow particle. Since the surface layer volume of the hollow particle is much lower than the whole volume of the solid particle, there must be more hollow particles in the same polymer. As a result, the probability of forming thermally conductive channels through surfaces connection of the hollow particles is increased, leading to the enhancement of the effective thermal conductivity. This can be understood from the comparison of the thermal energy flux distributions shown in **Figures 7a-b**. By wrapping a more thermally conductive graphene layer on the surfaces of the hollow nanoparticles, the formation probability of heat conductive channels and hence the effective thermal conductivity will be

further increased, as revealed in **Figure 7c**.

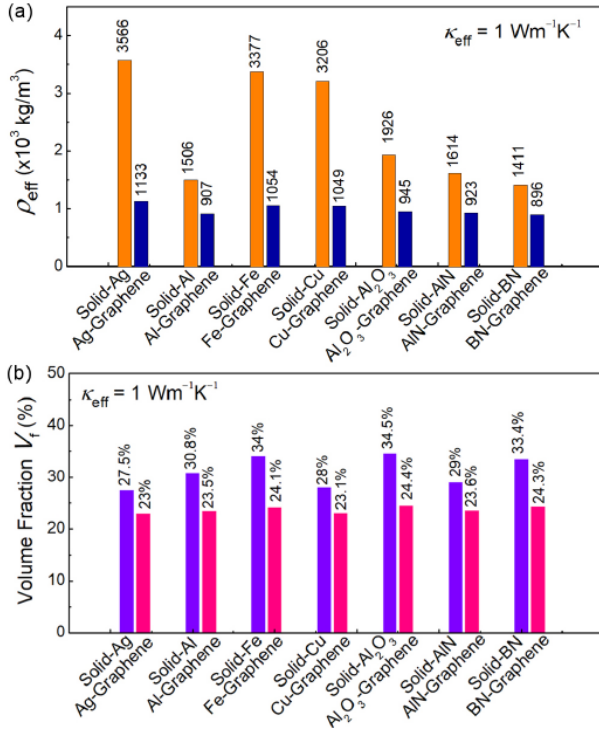


Figure 6. For a PE nanocomposite with a targeted effective thermal conductivity of 1 WK1m1, **(a)** the mass density and **(b)** the filler volume fraction it has when it is filled with various solid and graphene-wrapped hollow nanoparticles.

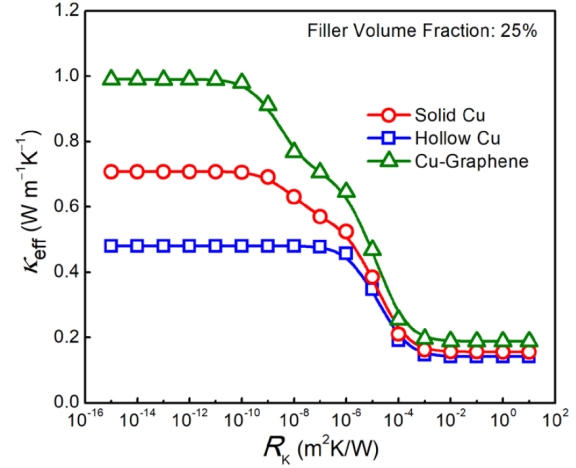


Figure 8. Effect of the interfacial thermal resistance on the effective thermal conductivity for PE nanocomposites filled with 25 vol.% solid Cu nanoparticles, hollow Cu nanoparticles, and graphene-wrapped hollow Cu nanoparticles.

In above simulations, the strategy of adding hollow and graphene-wrapped hollow nanoparticles into the polymer to enhance the thermal conductivity and reduce the mass density is illustrated without considering the interfacial thermal resistance (R_k). **Figure 8a** shows the parameterized study of R_k effects on the effective thermal conductivity for polymer nano-

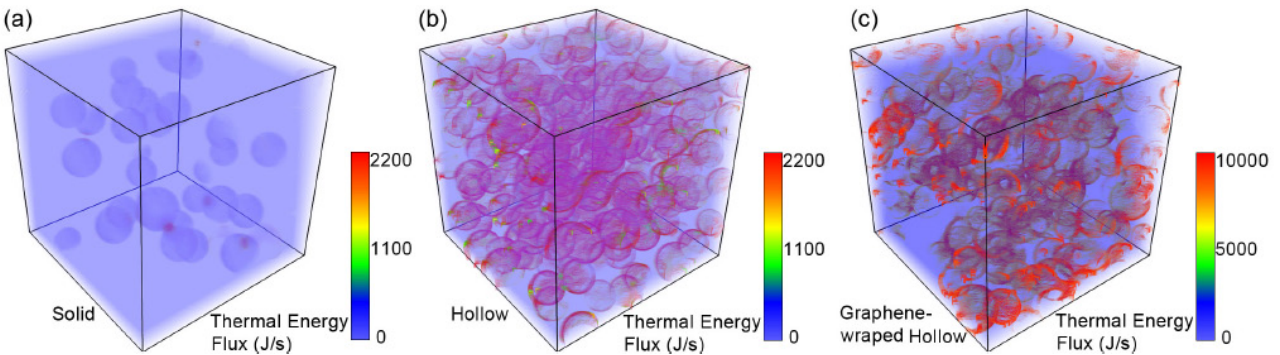


Figure 7. Thermal energy flux distributions for polymer nanocomposites filled with **(a)** solid Cu nanoparticles, **(b)** hollow Cu nanoparticles, and **(c)** graphene-wrapped hollow Cu nanoparticles. The volume fractions of Cu metal for these three polymer nanocomposites are at the same value of 6%. Due to the introduction of the hollow structure, the volume fractions of the hollow nanoparticles are 30%.

composites filled with solid, hollow, and graphene-wrapped Cu hollow nanoparticles. For polymer nanocomposites filled with solid Cu and graphene-wrapped hollow Cu nanoparticles, R_k is important when it is greater than $10^{-10} \text{ m}^2\cdot\text{K/W}$, whereas it is important when $R_k > 10^{-6} \text{ m}^2\cdot\text{K/W}$ for the polymer nanocomposite filled with hollow Cu nanoparticles. Specifically, the effective thermal conductivity can be

decreased by the interfacial thermal resistance from $1.0 \text{ Wm}^{-1}\cdot\text{K}^{-1}$ to $0.19 \text{ Wm}^{-1}\cdot\text{K}^{-1}$, from $0.71 \text{ Wm}^{-1}\cdot\text{K}^{-1}$ to $0.16 \text{ Wm}^{-1}\cdot\text{K}^{-1}$, and from $0.48 \text{ Wm}^{-1}\cdot\text{K}^{-1}$ to $0.14 \text{ Wm}^{-1}\cdot\text{K}^{-1}$ for polymer nanocomposite filled with 25 vol.% graphene-wrapped hollow Cu nanoparticles, solid Cu nanoparticles, and hollow Cu nanoparticles, respectively. Therefore, the effective thermal conductivity predicted in this work should be lower

when the interfacial thermal resistance is considered. In order to accurately predict the effective thermal conductivity as function of the microstructure, the knowledge of the interfacial thermal resistance is necessary. While it is challenging to measure the interfacial thermal resistance experimentally, it may be obtained via molecular dynamic simulations^[51–53].

3. Conclusions

The effective thermal conductivity and effective mass density of the polymer nanocomposites filled with solid nanoparticles and hollow nanoparticles are computed. It is predicted that the usage of hollow nanoparticles rather than the solid nanoparticles as fillers can enhance the thermal conductivity but preserve the low mass density of the polymer nanocomposites. By wrapping a graphene layer onto the surface of the hollow nanoparticles, the effective thermal conductivity can be further significantly enhanced while still preserving a low mass density of the polymer nanocomposite. The underlying mechanism of this microstructure design and the quantitative effect of the interfacial thermal resistance are presented. The present work is expected to stimulate future experimental and theoretical efforts to design light-weight thermally conductive polymer nanocomposites.

Conflict of interest

No conflict of interest was reported by the authors.

Acknowledgements

J. J. Wang and L. Q. Chen are partially supported by the US Air Force Office of Scientific Research through tasks (FA9550-17-1-0318) and by the Hamer Professorship. W Y Zhou gratefully acknowledge the financial supports from the National Natural Science Foundation of China (No.51577154), the Key Laboratory of Engineering Dielectrics and Its Application, Ministry of Education, Harbin University of Science and Technology (No. JZK201301, KF20151111).

References

1. Gurrum SP, Suman SK, Joshi YK, *et al.* Thermal issues in next-generation integrated circuits. *IEEE Transactions on Device and Materials Reliability* 2004; 4 (4): 709–714.
2. Ghosh S, Calizo I, Teweldebrhan D, *et al.* Extremely high thermal conductivity of graphene: Prospects for thermal management applications in nanoelectronic circuits. *Applied Physics Letters* 2008; 92 (15): 151911.
3. Otiaba KC, Ekere NN, Bhatti R, *et al.* Thermal interface materials for automotive electronic control unit: trends, technology and R&D challenges. *Microelectronics Reliability* 2011; 51(12): 2031–2043.
4. Moore AL, Shi L. Emerging challenges and materials for thermal management of electronics. *Materials Today* 2014; 17(4): 163–174.
5. Chen H, Ginzburg VV, Yang J, *et al.* Thermal conductivity of polymer-based composites: Fundamentals and applications. *Progress in Polymer Science* 2016; 59: 41–85.
6. Tong X. *Advanced materials for thermal management of electronic packaging*. New York: Springer Science & Business Media; 2011.
7. Han Z, Fina A. Thermal conductivity of carbon nanotubes and their polymer nanocomposites: A review. *Progress in polymer science* 2011; 36(7): 914–944.
8. T’Joen C, Park Y, Wang Q, *et al.* A review on polymer heat exchangers for HVAC&R applications. *International Journal of Refrigeration* 2009; 32(5): 763–779.
9. Gojny FH, Wichmann MH, Fiedler B, *et al.* Evaluation and identification of electrical and thermal conduction mechanisms in carbon nanotube/epoxy composites. *Polymer* 2006; 47(6): 2036–2045.
10. Marconnet AM, Yamamoto N, Panzer MA, *et al.* Thermal conduction in aligned carbon nanotube—Polymer nanocomposites with high packing density. *ACS Nano* 2011; 5(6): 4818–4825.
11. Rahmat M, Hubert P. Carbon nanotube—Polymer interactions in nanocomposites: A preview. *Composites Science and Technology* 2011; 72(1): 72–84.
12. Du Y, Shen SZ, Cai K, *et al.* Research progress on

- polymer–inorganic thermoelectric nanocomposite materials. *Progress in Polymer Science* 2012; 37(6): 820–841.
13. Liu Y, Kumar S. Polymer/carbon nanotube nano composite fibers—A review. *ACS Applied Materials & Interfaces* 2014; 6(9): 6069–6087.
 14. Das TK, Prusty S. Graphene-based polymer composites and their applications. *Polymer-Plastics Technology and Engineering* 2013; 52(4): 319–331.
 15. Potts JR, Dreyer DR, Bielawski CW, *et al.* Graphene-based polymer nanocomposites. *Polymer* 2011; 52(1): 5–25.
 16. Shahil KM, Balandin AA. Graphene–multilayer graphene nanocomposites as highly efficient thermal interface materials. *Nano Letters* 2012; 12(2): 861–867.
 17. Li B, Zhong WH. Review on polymer/graphite nanoplatelet nanocomposites. *Journal of materials science* 2011; 46(17): 5595–5614.
 18. Wang M, Hu N, Zhou L, *et al.* Enhanced interfacial thermal transport across graphene–polymer interfaces by grafting polymer chains. *Carbon* 2015; 85: 414–421.
 19. Zhou W, Qi S, Tu C, *et al.* Effect of the particle size of Al₂O₃ on the properties of filled heat-conductive silicone rubber. *Journal of Applied Polymer Science* 2007; 104(2): 1312–1318.
 20. Moreira D, Sphaier L, Reis J, *et al.* Experimental investigation of heat conduction in polyester–Al₂O₃ and polyester–CuO nanocomposites. *Experimental Thermal and Fluid Science* 2011; 35(7): 1458–1462.
 21. Zhang S, Cao X, Ma Y, *et al.* The effects of particle size and content on the thermal conductivity and mechanical properties of Al₂O₃/high density polyethylene (HDPE) composites. *Express Polymer Letters* 2011; 5(7): 581–590.
 22. Zhi C, Bando Y, Tang C, *et al.* Large-scale fabrication of boron nitride nanosheets and their utilization in polymeric composites with improved thermal and mechanical properties. *Advanced Materials* 2009; 21(28): 2889–2893.
 23. Huang X, Zhi C, Jiang P, *et al.* Polyhedral oligosilsesquioxane-modified boron nitride nanotube based epoxy nanocomposites: an ideal dielectric material with high thermal conductivity. *Advanced Functional Materials* 2013; 23(14): 1824–1831.
 24. Song WL, Wang P, Cao L, *et al.* Polymer/boron nitride nanocomposite materials for superior thermal transport performance. *Angewandte Chemie International Edition* 2012; 51(26): 6498–6501.
 25. Li TL, Hsu SLC. Preparation and properties of thermally conductive photosensitive polyimide/boron nitride nanocomposites. *Journal of Applied Polymer Science* 2011; 121(2): 916–922.
 26. Li Q, Chen L, Gadinski MR, *et al.* Flexible high-temperature dielectric materials from polymer nanocomposites. *Nature* 2015; 523(7562): 576.
 27. Mamunya YP, Davydenko V, Pissis P, *et al.* Electrical and thermal conductivity of polymers filled with metal powders. *European Polymer Journal* 2002; 38(9): 1887–1897.
 28. Chung D. Materials for thermal conduction. *Applied Thermal Engineering* 2001; 21(16): 1593–1605.
 29. Wang S, Cheng Y, Wang R, *et al.* Highly thermal conductive copper nanowire composites with ultralow loading: toward applications as thermal interface materials. *ACS Applied Materials & Interfaces* 2014; 6(9): 6481–6486.
 30. Bjornekleit A, Halbo L, Kristiansen H. Thermal conductivity of epoxy adhesives filled with silver particles. *International Journal of Adhesion and Adhesives* 1992; 12(2): 99–104.
 31. Pashayi K, Fard HR, Lai F, *et al.* High thermal conductivity epoxy-silver composites based on self-constructed nanostructured metallic networks. *Journal of Applied Physics* 2012; 111(10): 104310.
 32. Burger N, Laachachi A, Ferriol M, *et al.* Review of thermal conductivity in composites: Mechanisms, parameters and theory. *Progress in Polymer Science* 2016; 61: 1–28.
 33. King JA, Tucker KW, Vogt BD, *et al.* Electrically and thermally conductive nylon 6, 6. *Polymer Composites* 1999; 20(5): 643–654.
 34. Fan L, Khodadadi JM. Thermal conductivity enhancement of phase change materials for thermal energy storage: A review. *Renewable and Sustainable Energy Reviews* 2011; 15(1): 24–46.
 35. Wang JJ, Wang Y, Ihlefeld JF, *et al.* Tunable thermal conductivity via domain structure engineering in ferroelectric thin films: A phase-field simulation. *Acta*

- Materialia 2016; 111: 220–231.
36. Wang, J, Ma X, Li Q, *et al.* Phase transitions and domain structures of ferroelectric nanoparticles: Phase field model incorporating strong elastic and dielectric inhomogeneity. *Acta Materialia* 2013; 61(20): 7591–7603.
 37. Wang J, Song Y, Ma X, *et al.* Static magnetic solution in magnetic composites with arbitrary susceptibility inhomogeneity and anisotropy. *Journal of Applied Physics* 2015; 117(4): 043907.
 38. Parker W, Jenkins R, Butler C, *et al.* Flash method of determining thermal diffusivity, heat capacity, and thermal conductivity. *Journal of Applied Physics* 1961; 32(9): 1679–1684.
 39. Lee W, Han I, Yu J, *et al.* Thermal characterization of thermally conductive underfill for a flip-chip package using novel temperature sensing technique. *Thermo-chimica Acta* 2007; 455(1-2): 148–155.
 40. Zhou W, Qi S, An Q, *et al.* Thermal conductivity of boron nitride reinforced polyethylene composites. *Materials Research Bulletin* 2007; 42(10): 1863–1873.
 41. Stankovich S, Dikin DA, Dommett GHA, *et al.* Graphene-based composite materials. *Nature* 2006; 442(7100): 282.
 42. Kim SY, Noh YJ, Yu J. Thermal conductivity of graphene nanoplatelets filled composites fabricated by solvent-free processing for the excellent filler dispersion and a theoretical approach for the composites containing the geometrized fillers. *Composites Part A: Applied Science and Manufacturing* 2015; 69: 219–225.
 43. Tu W, Zhou Y, Liu Q, *et al.* Robust hollow spheres consisting of alternating titania nanosheets and graphene nanosheets with high photocatalytic activity for CO₂ conversion into renewable fuels. *Advanced Functional Materials* 2012; 22(6): 1215–1221.
 44. Wang H, Yang Y, Liang Y, *et al.* Graphene-wrapped sulfur particles as a rechargeable lithium–sulfur battery cathode material with high capacity and cycling stability. *Nano Letters* 2011; 11(7): 2644–2647.
 45. Wu P, Wang H, Tang Y, *et al.* Three-dimensional interconnected network of graphene-wrapped porous silicon spheres: In situ magnesiothermic-reduction synthesis and enhanced lithium-storage capabilities. *ACS Applied Materials & Interfaces* 2014; 6(5): 3546–3552.
 46. Dasari A, Yu ZZ, Mai YW. Fundamental aspects and recent progress on wear/scratch damage in polymer nanocomposites. *Materials Science and Engineering: R: Reports* 2009; 63(2): 31–80.
 47. Li F, Hu K, Li J, *et al.* The friction and wear characteristics of nanometer ZnO filled polytetrafluoroethylene. *Wear* 2001; 249(10–11): 877–882.
 48. Ding H, Guo Y, Leung SN. Development of thermally conductive polymer matrix composites by foaming-assisted networking of micron-and submicron-scale hexagonal boron nitride. *Journal of Applied Polymer Science* 2016; 133(4): 42910.
 49. Woltornist SJ, Varghese D, Massucci D, *et al.* Controlled 3D assembly of graphene sheets to build conductive, chemically selective and shape-responsive materials. *Advanced Materials* 2017; 29(18): 1604947.
 50. Okamoto M, Nam PH, Maiti P, *et al.* Biaxial flow-induced alignment of silicate layers in polypropylene/clay nanocomposite foam. *Nano Letters* 2001; 1(9): 503–505.
 51. Zhong H, Lukes JR. Interfacial thermal resistance between carbon nanotubes: Molecular dynamics simulations and analytical thermal modeling. *Physical Review B* 2006; 74(12): 125403.
 52. Diao J, Srivastava D, Menon M. Molecular dynamics simulations of carbon nanotube/silicon interfacial thermal conductance. *The Journal of Chemical Physics* 2008; 128(16): 164708.
 53. Stevens RJ, Zhigilei LV, Norris PM. Effects of temperature and disorder on thermal boundary conductance at solid–solid interfaces: Nonequilibrium molecular dynamics simulations. *International Journal of Heat and Mass Transfer* 2007; 50(19, 20): 3977–3989.

ORIGINAL RESEARCH ARTICLE

Liquid deposition modification of nano-ZSM-5 zeolite and catalytic performance in aromatization of Hexene-1

Yujun Fang^{1,2,3}, Xiaofang Su^{1,2,3}, Wei Wang^{1,2,3}, Wei Wu^{1,2,3*}

¹ National Center for International Research on Catalytic Technology, Heilongjiang University, Harbin 150080, China.
E-mail: wuwei@hlju.edu.cn

² Functional Inorganic Materials Chemistry Ministry of Education, Heilongjiang University, Harbin 150080, China

³ School of Chemical and Materials Science, Heilongjiang University, Harbin 150080, China

ABSTRACT

The Olefin aromatization is an important method for the upgrade of catalytic cracking (FCC) gasoline and production of fuel oil with high octane number. The nano-ZSM-5 zeolite was synthesized via a seed-induced method, a series of modified nano-ZSM-5 zeolite samples with different Ga deposition amount were prepared by Ga liquid deposition method. The XRD, N₂ physical adsorption, SEM, TEM, XPS, H₂-TPR and Py-IR measurements were used to characterize the morphology, textural properties and acidity of the modified ZSM-5 zeolites. The catalytic performance of the Hexene-1 aromatization was evaluated on a fixed-bed microreactor. The effects of Ga modification on the physicochemical and catalytic performance of nano-ZSM-5 zeolites were investigated. The Ga species in the modified nano-ZSM-5 zeolites mainly exist as the form of Ga₂O₃ and GaO⁺, which provide strong Lewis acid sites. The aromatics selectivity over Ga modified nano-ZSM-5 zeolite in the Hexene-1 aromatization was significantly increased, which could be attributed to the improvement of the dehydrogenation activity. The selectivity for aromatics over the Ga4.2/NZ5 catalyst with suitable Ga deposition amount reached 55.4%.

Keywords: Nanosized ZSM-5 Zeolite; Ga Modification; Liquid Deposition; Hexene-1; Aromatization

ARTICLE INFO

Received: 10 February 2021
Accepted: 29 March 2021
Available online: 7 April 2021

COPYRIGHT

Copyright © 2021 Yujun Fang, *et al.*
EnPress Publisher LLC. This work is licensed under the Creative Commons Attribution-NonCommercial 4.0 International License (CC BY-NC 4.0).
<https://creativecommons.org/licenses/by-nc/4.0/>

1. Introduction

With the rapid development of China's automobile industry, the demand for fuel oil such as gasoline is increasing day by day. At present, catalytic cracking (FCC) gasoline is still the main vehicle fuel oil used all over the world, especially in China, the proportion of FCC gasoline is as high as about 80%. Due to the high olefin content in FCC gasoline, insufficient combustion will lead to a series of environmental pollution problems such as high PM2.5 content in automobile exhaust and photochemical smoke^[1]. Therefore, reducing the olefin content in FCC gasoline to improve fuel quality has become an urgent problem to be solved. Aromatics are not only gasoline blending components with high octane number, but also important basic chemical raw materials. Therefore, converting olefins in FCC gasoline into high value-added aromatics through aromatization reaction can not only reduce the olefin content in gasoline and maintain or improve the octane number of gasoline, but also provide an effective channel for the production of aromatics. The research and development of high-efficiency catalyst is the technical core of this process.

ZSM-5 zeolite is widely used in petrochemical and other fields as an efficient catalyst because of its unique three-dimensional cross pore structure, rich active centers and good hydrothermal stability^[2,3]. However, ZSM-5 zeolite with micron scale and single micro-porous structure will limit the formation and diffusion of transition intermediates and products in the pores in the acid catalytic reaction, resulting in the rapid deactivation of the zeolite due to coking and carbon deposition. The strong Brønsted acid center of aluminosilicate zeolite is easy to lead to side reactions such as cracking of long-chain olefin intermediates generated in the process of olefin aromatization, so as to reduce the selectivity of aromatics. The pore characteristics and acidity of ZSM-5 zeolite can be adjusted by reducing the particle size of zeolite and adopting the modification method of secondary synthesis^[4-6]. The existing template method for synthesizing nano ZSM-5 still has many environmental problems such as large amount of organic template, high cost and large amount of nitrogen-containing wastewater. Therefore, it is necessary to establish a new green and efficient method for the synthesis of nano ZSM-5 zeolite. Methods for adjusting the acidity of zeolite include ion exchange method, isomorphic replacement method and liquid deposition method^[7-11]. Although acid dealumination modification will remove some skeleton aluminum atoms of zeolite and reduce strong acid sites, it will destroy the skeleton stability of zeolite and produce a large amount of acid wastewater. The introduction of metal species by ion exchange method is limited, and the acid regulation of the catalyst and the improvement of catalytic reaction performance are small. The isomorphic substitution modification reduces the acid strength of zeolite by introducing heteroatoms into the zeolite skeleton, and forms skeleton defect sites to a certain extent.

Introducing Ga species into zeolite by liquid phase deposition is the simplest and effective modification method to adjust its acid strength, Brønsted and Lewis acid site density and the ratio of two active sites^[12]. In the process of liquid phase deposition, Ga species will cover some strong acid sites of zeolite, and form active Ga species providing strong L acid,

promote the dehydrogenation rate control step in the aromatization reaction process, and effectively improve its catalytic aromatization performance.

In this paper, nano ZSM-5 zeolite synthesized by prefabricated seed method was modified by Ga liquid deposition, and the effects of Ga modification on the pore characteristics, acidity and catalytic aromatization of Hexene-1 of nano ZSM-5 zeolite were studied.

2. Experiment

2.1 Synthesis of nano ZSM-5 zeolite

The mixture of four propyl ammonium hydroxide, aluminum isopropyl alcohol, tetraethyl orthosilicate and deionized water were mixed according to the ratio of 35.7 TPAOH:100 SiO₂:Al₂O₃:1,083 H₂O (mole ratio). After mixing at room temperature, the mixed gel was prepared and then transferred into the crystallization reactor to heat the 30 min by microwave radiation. Obtain the preformed crystal seed for use. A uniform gel was prepared by mixing sodium aluminate, silica sol, sodium hydroxide and two deionized water, adding the preformed seed and then crystallizing 6 h at 180 °C. The crystallization product is centrifuged, dried, roasted, ion exchanged with NH₄NO₃ solution, dried and roasted to obtain H-type ZSM-5 zeolite, which is recorded as NZ5.

2.2 Preparation of Ga modified nano ZSM-5 zeolite

A certain amount of H-type nano ZSM-5 zeolite sample (NZ5) prepared according to the method described in 2.1 is added to a certain concentration of Ga(NO₃)₃ solution, stirred at room temperature for 2 h, dried overnight, and calcined at 550 degrees Celsius for 3 h. The prepared Ga modified nano ZSM-5 zeolite is recorded as Ga_x/NZ5, x is the mass percentage of Ga in the modified zeolite.

2.3 Evaluation of catalytic reaction performance

A fixed bed micro reactor was used to evaluate the catalytic performance of zeolite before and after modification for the aromatization of Hexene-1.

Weigh 1.0 g of 20–40 mesh catalyst, place it in the constant temperature zone of the reactor, and fill both ends with quartz sand. The reaction temperature was 480 degrees Celsius, the pressure was 0.5 MPa, the mass space velocity was 2.0 h^{-1} , and the flow rate of carrier gas (nitrogen) was $75 \text{ mL}\cdot\text{min}^{-1}$. The reaction product was cooled in a low-temperature constant temperature bath, and the time when the first drop of liquid phase product appeared was recorded as zero time, and then the product was collected every 2 h. The composition of the reaction product was analyzed by GC-7900 installed with FID detector and PONA capillary column ($50.0 \text{ m} \times 200 \mu\text{m} \times 0.5 \mu\text{m}$).

3. Experimental results and discus-

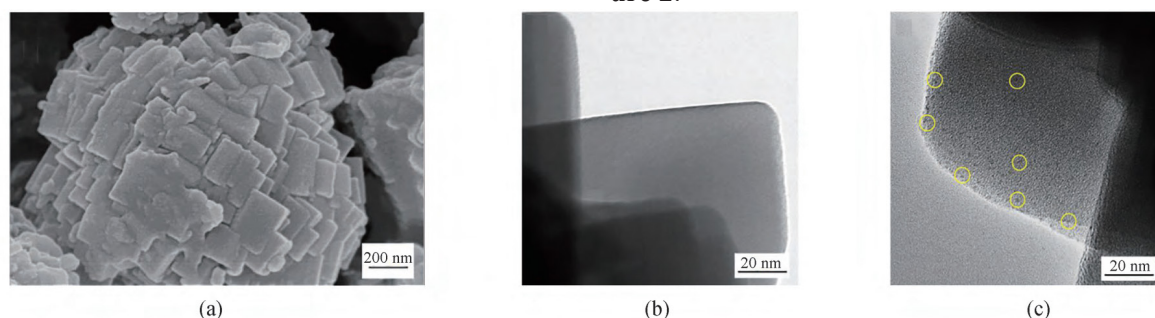


Figure 1. SEM and TEN images of nanosized ZSM-5 zeolite (a, b) and TEM image of Ga4.2-NZ5 sample modified by Ga-impregnation (c).

Table 1. Relative crystallinity, textural properties and chemical composition of ZSM-5 zeolite samples modified by Ga-impregnation

Sample	Relative crystallinity ^a /%	Chemical composition			Ga / (wt%)	Surface area / (m ² ·g ⁻¹)	
		Si/Al ^b	Si/Ga ^c	Si(Me) ^d		BET ^f	Micropore ^g
HNZ5	100	48	—	48	0	386	74
Ga1.5/NZ5	96	48	77	30	2.5	358	70
Ga2.1/NZ5	96	48	58	26	3.3	352	69
Ga4.2/NZ5	96	48	27	17	5.1	336	55

Note: ^aRelative crystallinity (RC) calculated from XRD patterns; ^bobtained by XRF method; ^cdetermined from ICP; ^dMe corresponds to the Al and Ga; ^emass percent content of Ga on the surface determined from XPS; ^fBET method; ^ggt-plot method.

It can be seen from **Figure 2** that the XRD spectrum of the modified zeolite still has only the characteristic diffraction peak of MFI topology, and there is no spectral peak of Ga_2O_3 , indicating that Ga species are highly dispersed in ZSM-5 zeolite. It can be seen from **Table 1** that the relative crystallinity of ZSM-5 zeolite modified by Ga decreases slightly, and its specific surface area decreases with the increase of Ga deposition, because gallium species block some pores of the zeolite. In addition, the Ga

sion

3.1 Structural characterization and analysis of Ga modified nano ZSM-5 zeolite

Nano ZSM-5 zeolite (sample NZ5) and Ga4.2-NZ5 (Ga content of 4.2 wt.%) modified by Ga liquid deposition were characterized by SEM and TEM, as shown in **Figure 1**. Gallium oxide nano-clusters with a uniform size of about 2 nm can be observed on the surface of the modified sample Ga4.2-NZ5.

The nano ZSM-5 zeolite before and after liquid deposition modification with different Ga content were characterized by XRD. The XRD spectrum and relative crystallinity are shown in **Table 1** and **Figure 2**.

content on the outer surface of Ga modified zeolite was analyzed by X-ray photoelectron spectroscopy (XPS), and compared with the Ga content of zeolite measured by ICP method, it was found that the Ga content on the outer surface of zeolite was higher, indicating that Ga species were mainly distributed on the outer surface of zeolite.

Ga modification can not only form Ga_2O_3 nano clusters on the surface of zeolite, but also form Ga^+ species with dehydrogenation activity^[13]. In order to

prove the existence of GaO^+ active species in the zeolite modified by Ga liquid phase deposition, the samples were characterized by H_2 -TPR and XPS. The results are shown in **Figure 3**, **Figure 4** and **Table 2** respectively.

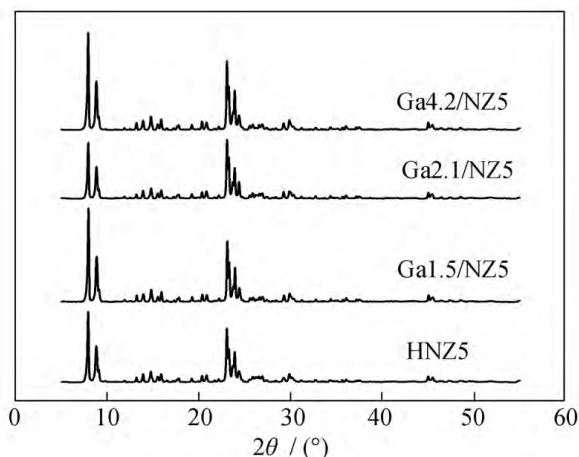


Figure 2. XRD patterns of nanosized ZSM-5 zeolite samples modified by Ga-impregnation.

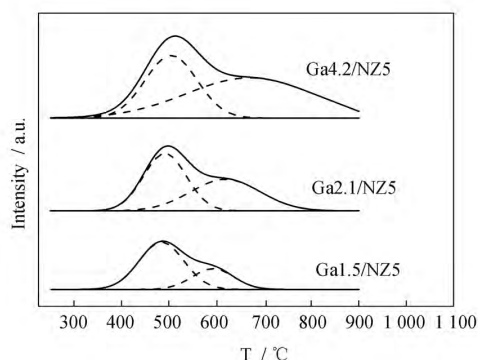


Figure 3. H_2 -TPR profiles of nanosized ZSM-5 zeolite samples modified by Ga-impregnation.

Table 2. H_2 -TPR data of nanosized ZSM-5 zeolite samples modified by Ga-impregnation

Sample	Temperature/°C		Consumption of $\text{H}_2/(\times 10^{-5} \text{ mol}\cdot\text{g}^{-1})$		
	L.T.	H.T.	$\text{Ga}_2\text{O}_3 \rightarrow \text{Ga}_2\text{O}$	$\text{GaO}^+ \rightarrow \text{Ga}^+$	Total
Ga1.5/NZ5	486	602	8.71	3.29	12.00
Ga2.1/NZ5	489	636	12.11	7.89	20.00
Ga4.2/NZ5	501	693	15.82	15.52	31.34

eton^[14].

It can be seen from **Figure 4** that with the increase of Ga deposition in the sample, the electron binding energy of $\text{Ga}_x/\text{NZ5}$ series modified samples increases from 1117.5 eV to 1117.8 eV, which can

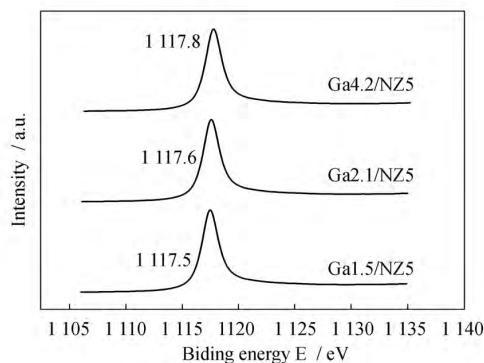


Figure 4. $\text{Ga } 2p^{3/2}$ XPS spectra of nanosized ZSM-5 zeolite samples modified by Ga-impregnation.

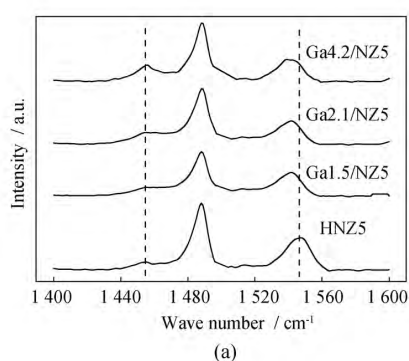
It can be seen from **Figure 3** and **Table 2** that in the H_2 -TPR curve of modified $\text{Ga}_x/\text{NZ5}$ series samples, there are reduction peaks corresponding to Ga_2O_3 and active GaO^+ species with strong interaction with the negative charge of zeolite skeleton at 350–600 °C and 500–800 °C respectively. With the increase of Ga deposition, the amount of hydrogen consumed when Ga_2O_3 and GaO^+ species are restored increases. The reduction temperature of Ga_2O_3 increases slightly with the increase of Ga deposition amount, from 486 °C to 501 °C, which may be due to the increase of the size of Ga_2O_3 nano clusters formed when the deposition amount of Ga increases, and thus it may be more difficult to be restored. When the deposition amount of Ga increases from 1.5% to 4.2%, the reduction temperature of corresponding GaO^+ species in $\text{Ga}_x/\text{NZ5}$ series modified samples increases significantly from 602 °C to 693 °C, which is due to the enhanced interaction between GaO^+ species and the negative charge of zeolite skeleton.

be attributed to the strong interaction between more GaO^+ species and the negative charge of zeolite skeleton. It is consistent with the characterization results of H_2 -TPR.

3.2 Characterization and analysis of acidity of Ga modified nano ZSM-5 zeolite

In order to study the effect of Ga liquid deposition modification on the acidity of nano ZSM-5 zeolite, the samples before and after modification were characterized by pyridine adsorption infrared spectroscopy (Py-IR). The results are shown in Figure 5.

It can be seen from **Figure 5(a)** that the Py-IR spectrum of the modified series of samples $Ga_x/NZ5$ corresponds to the absorption peaks of acid sites of Brønsted near $1,545\text{ cm}^{-1}$ move towards low wave



number, indicating that the acid intensity decreases. As can be seen from **Figure 5(b)**, the acid content of Brønsted of Ga modified zeolite decreased significantly. Due to partial Brønsted acid site is covered by the deposited Ga species, or the acid site of Brønsted in the pore cannot be detected due to blocking part of the pore of zeolite. The acid content of Brønsted of Ga modified $Ga_x/NZ5$ series modified samples did not change significantly. However, with the increase of Ga deposition, the Lewis acid content and total acid content of the modified samples increased due to the formation of more Ga_2O_3 and active Ga^{+} species.

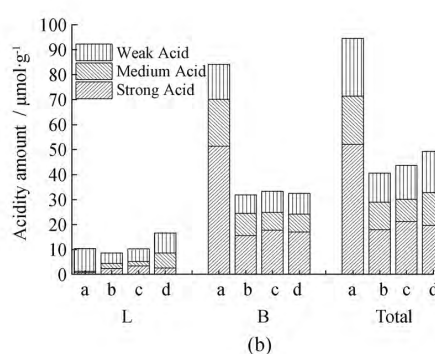


Figure 5. Py-IR spectra (a) and acid amount (b) of the nano-sized ZSM-5 zeolite samples modified by a. HNZ5, b. Ga1.5/NZ5, c. Ga2.1/NZ5, d. Ga4.2/NZ5.

3.3 Catalytic performance of Ga modified nano ZSM-5 zeolite for aromatization of Hexene-1

In order to explore the corresponding relationship between the structure and acidity of Ga modified nano ZSM-5 zeolite and its catalytic aromatization reaction performance, the catalytic performance of Ga liquid-phase deposition modified nano ZSM-5 was studied with Hexene-1 as a model compound.

The results are shown in **Figure 6**.

It can be seen from **Figure 6(a)** that the modified zeolite Ga4.2/NZ5 catalyst has better catalytic stability than the unmodified ZSM-5 zeolite (HNZ5), and the conversion of Hexene-1 is still close to 100% at 35 h, which is due to the reduction of strong acid content and milder acidity of Ga modified molecular sieve, the deactivation of molecular sieve due to carbon deposition is inhibited.

It can be seen from **Figure 6(b)** that when $Ga_x/$

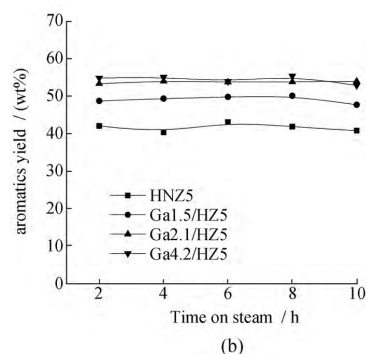
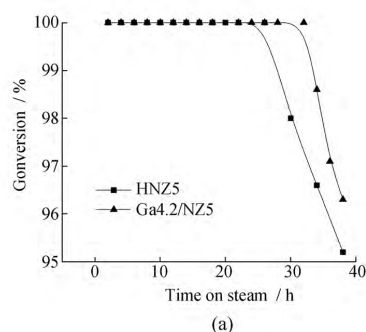


Figure 6. Catalytic performance in Hexene-1 aromatization over the nanosized ZSM-5 zeolite samples modified by Ga-impregnated.

NZ5 series modified zeolite are used as catalysts, the total aromatics selectivity of Hexene-1 aromatization reaction is improved to varying degrees. When the deposition amount of Ga on ZSM-5 zeolite is 1.5% and 2.1% respectively, the corresponding catalysts Ga1.5/NZ5 and Ga2.1/NZ5 can greatly improve the selectivity of aromatics in the reaction products. When the deposition amount of Ga increases to 4.2%, the selectivity of Ga4.2/NZ5 catalyst for aromatics reached the maximum, up to 55.4%, which is that the active GaO⁺ species with more strong L acid sites in Ga4.2/NZ5 catalyst promoted the dehydrogenation reaction.

4. Conclusion

The preformed seed method can not only greatly reduce the amount of organic template, but also synthesize nano ZSM-5 zeolite with regular morphology and high crystallinity. Liquid deposition modification is a simple and easy method to adjust the acidity of molecules. Because the liquid deposition modified GaZSM-5 not only weakens the strength of the acid site of Brønsted and inhibits the cracking reaction, but also forms an active GaO⁺ species with strong Lewis acid site, improves the dehydrogenation activity of the zeolite catalyst, and therefore significantly improves the aromatics selectivity of the aromatization reaction of Hexene-1. This research work provides a useful idea for the improvement of acidity regulation and catalytic performance of zeolites.

Conflict of interest

The authors declare that they have no conflict of interest.

Acknowledgements

This article was supported by the General Program of National Natural Science Foundation of China (21276067, 21676074).

References

1. Long H, Jin F, Xiong G, *et al.* Effect of lanthanum and phosphorus on the aromatization activity of Zn/ZSM-5 in FCC gasoline upgrading. *Microporous and Mesoporous Materials* 2014; 198(1): 29–34.
2. Chevella D, Macharla AK, Banothu R, *et al.* Synthesis of non-symmetrical alkyl carbonates from alcohols and DMC over nanocrystalline ZSM-5 zeolite. *Green Chemistry* 2019; 21(11): 2938–2945.
3. Lok CM, Van Doorn J, Almansa GA. Promoted ZSM-5 catalysts for the production of bio-aromatics, a review. *Renewable and Sustainable Energy Reviews* 2019; 113: 109248.
4. Peng P, Stosic D, Liu XM, *et al.* Strategy towards enhanced performance of zeolite catalysts: Raising effective diffusion coefficient versus reducing diffusion length. *Chemical Engineering Journal* 2020; 385: 123800.
5. Milina M, Mitchell S, Crivelli P, *et al.* Mesopore quality determines the lifetime of hierarchically structured zeolite catalysts. *Nature Communications* 2014; 5: 1–10.
6. Zhang Y, Wu S, Xu X, *et al.* Ethane aromatization and evolution of carbon deposits over nanosized and microsized Zn/ZSM-5 catalysts. *Catalysis Science & Technology* 2020; 10(3): 835–845.
7. Raad M, Astafan A, Hamieh S, *et al.* Catalytic properties of Ga-containing MFI-type zeolite in cyclohexane dehydrogenation and propane aromatization. *Journal of Catalysis* 2018; 365: 376–390.
8. Su X, Fang Y, Bai X, *et al.* Synergic effect of GaO⁺/Brønsted acid in hierarchical Ga/Al-ZSM-5 bifunctional catalysts for 1-hexene aromatization. *Industrial & Engineering Chemistry Research* 2019; 58(45): 20543–20552.
9. Zhang P, Guo X, Guo H, *et al.* Study of the performance of modified nano-scale ZSM-5 zeolite on olefins reduction in FCC gasoline. *Journal of Molecular Catalysis A: Chemical* 2007; 261(2): 139–146.
10. Su X, Fang Y, Gao P, *et al.* In-situ microwave synthesis of nano-GaZSM-5 bifunctional catalysts with controllable location of active GaO⁺ species for olefins aromatization. *Microporous and Mesoporous Materials* 2020; 306: 110388.
11. Jiang YC, Du YY, He ZF, *et al.* Preparation of mesoporous carbon nanospheres from resorcinol/melamine resins and performances of supercapacitors. *Journal of Engineering of Heilongjiang University* 2021; 12(1): 31–36.

12. Ausavasukhi A, Sooknoi T. Tunable activity of [Ga] HZSM-5 with H₂ treatment: Ethane dehydrogenation. *Catalysis Communications* 2014; 45: 63–68.
13. Fang Y, Su X, Bai X, *et al.* Aromatization over nanosized Ga-containing ZSM-5 zeolites prepared by different methods: Effect of acidity of active Ga species on the catalytic performance. *Journal of Energy Chemistry* 2017; 26 (4): 768–775.
14. Varela-Gandía FJ, Berenguer-Murcia Á, Lozano-Castelló D, *et al.* Total oxidation of naphthalene using palladium nanoparticles supported on BETA, ZSM-5, SAPO-5 and alumina powders. *Applied Catalysis B: Environmental* 2013; 129: 98–105.

ORIGINAL RESEARCH ARTICLE

Synthesis of titania fibers by electrospinning and its photocatalytic degradation properties

Yan Lv¹, Feng Chen¹, Yuanzheng Tang¹, Zhigang Chen^{1,2*}

¹School of Chemistry, Biology and Materials Engineering, SUST, Suzhou 215009, China

²Jiangsu Key Laboratory of Environmental Functional Materials, Suzhou 215009, China. E-mail: czg@ujs.edu.cn

Abstract

The electrospinning precursor solution was prepared by dissolving polyvinyl pyrrolidone as template, tetrabutyl titanate as titanium source, and acetic acid as inhibitor. The TiO₂ nanofibers were prepared by precursor solution electrospinning and subsequent calcination. Thermal gravimetric analysis (TG), scanning electron microscopy (SEM), X-ray powder diffraction (XRD), and transmission electron microscopy (TEM) were used to characterize and analyze the samples. The influence of technological parameters on spinning fiber morphology was also studied. The results indicate that the TiO₂ nanofibers morphology is good when the parameters are as follows: voltage 1.4×10^4 V, spinning distance 0.2 m, translational velocity $2.5 \times 10^{-3} \text{ m}\cdot\text{s}^{-1}$, flow rate $3 \times 10^{-4} \text{ m}\cdot\text{s}^{-1}$, and needle diameter $3 \times 10^{-4} \text{ m}$. The diameter of the fibers is about 150 nm. With the $1 \times 10^{-4} \text{ mol}\cdot\text{L}^{-1}$ methylene blue solution used as simulated degradation target, the degradation rate is 95.8% after 180 minutes.

Keywords: Titania; Electrospinning; Morphology; Structure; Photocatalytic Degradation

ARTICLE INFO

Received: 17 February 2021

Accepted: 8 April 2021

Available online: 15 April 2021

COPYRIGHT

Copyright © 2021 Yan Lv, *et al.*

EnPress Publisher LLC. This work is licensed under the Creative Commons Attribution-NonCommercial 4.0 International License (CC BY-NC 4.0).

<https://creativecommons.org/licenses/by-nc/4.0/>

1. Introduction

In recent years, the environmental problems caused by the rapid development of industrialization have become increasingly serious. Dyes are widely used in many industries, but they are not fully discarded. The water and soil pollution caused by waste dyes has caused serious harm to human health and ecosystem^[1]. At present, there are many methods to treat dye wastewater, the more common ones are adsorption method, membrane separation method, microbial degradation^[2], electrochemical method, etc.^[3] Among them, photocatalytic degradation technology has the characteristics of low cost, high efficiency, low energy consumption and environment-friendly, so it has developed rapidly^[4].

Among many semiconductor photocatalysts, titanium dioxide is favored for its stable chemical performance, strong oxidation ability, low price, easy availability, non-toxic and harmless and no secondary pollution in the process of organic degradation^[5]. At present, the degradation of organic pollutants by using titanium dioxide as photocatalyst has gradually shifted from experimental research to the development of practical products^[6]. The photocatalytic degradation process is divided into two steps: adsorption and photochemical reaction. Only when organic matter is adsorbed to the material surface can photocatalytic degradation be carried out. Therefore, the photocatalytic degradation

efficiency is closely related to the adsorption performance of materials to organic molecules and their photocatalytic ability. Nowadays, nano titanium dioxide photocatalytic materials include nano powder and nano film^[7]. For nano powder, although the particles are fine and easy to combine with organic matter in solution, agglomeration will occur, which will make the catalyst inactive, thus reducing the photocatalytic efficiency. Moreover, the nano particles are difficult to separate and recover, which is not conducive to the regeneration and reuse of the catalyst. Although nano films are easy to recover and recycle, their practical application is limited because of their small specific surface area and low photocatalytic efficiency. The film composed of one-dimensional titanium dioxide nanofibers can not only be recycled, but also improve the photocatalytic performance by increasing the specific surface area of the nano film. Wu Mingchung, Andra Sapi *et al.* synthesized palladium modified titanium dioxide composite nanofibers through cellulose/catalyst composite system, which greatly improved the photocatalytic performance of the materials^[8]. Electrospinning technology is the only one method that can directly and continuously prepare nanofibers^[9,10]. This is a spinning method to obtain nano fibers by spray stretching of polymer solution or melt under electrostatic action. It has the advantages of simple equipment, strong operability and high efficiency and has played an important role in many fields such as nano fiber preparation^[11]. The process parameters affecting the spinning were studied by electrospinning, and anatase titanium dioxide films mainly composed of fibers with a diameter of about 150 nm were synthesized^[12]. The fibers are disorderly and cross arranged, and have certain toughness. The crystal structure and micro morphology were studied by XRD, SEM and TEM. The material has high photocatalytic activity and is not easy to inactivate. The advantages of morphology and structure make it reusable and easy to separate and recover. The photocatalytic performance of methylene blue solution was studied by degrading it under ultraviolet light.

2. Experiment

2.1 Raw material

Tetra-n-butyl titanate ($C_{16}H_{36}O_4Ti$, chemically pure), absolute ethanol (analytically pure), glacial acetic acid (analytically pure), all of which are produced by Sinopharm Chemical Reagent Co., Ltd. Polyvinylpyrrolidone (PVP, analytical purity, $M_w = 1,300,000$, Aladdin Reagent Co., Ltd.), self-made deionized water, P25 powder (nano titanium oxide, Degussa, Germany, with an average diameter of about 20 nm).

2.2 Preparation

Weigh 2 g of polyvinylpyrrolidone (PVP) with molecular weight of 1.3 million, fully dissolve it in 40 ml of absolute ethanol, drop 2 ml of glacial acetic acid to keep the solution acidic, and stir at room temperature for 3 h. Transfer 3.7 ml of tetra-n-butyl titanate with a pipette gun and add it slowly, and then stir at room temperature for 6 h to prepare a slightly viscous light yellow transparent spinning solution. Use a 5 ml disposable medical syringe to suck a certain amount of spinning solution and install it on the SS electrospinning machine. First set the injection speed, injection distance, left-right translation speed of the nozzle and the distance between the nozzle and the plane receiving steel plate, turn on the LED observation lamp, apply high voltage at the nozzle through the high-voltage DC power supply, and adjust the voltage through the knob. Make the spinning fiber form Taylor cone pattern. In the spinning process, the nozzle is required to have neither spinning liquid accumulation nor spinning splash. After spinning, the obtained nanocomposite fiber material was placed in a vacuum drying oven for 6 hours, the temperature is set at 40 °C to remove the residual solvent. Then, the fiber was calcined to 600 °C in muffle furnace at 5 °C·min⁻¹ for 1 h to prepare nano-TiO₂ fiber film material.

2.3 Characterization and testing

It was characterized by thermogravimetric analysis (TG) and differential scanning calorimetry (DSC). The test conditions are: heating rate

20 °C·min⁻¹, air flow 2 × 10⁻³ L·s⁻¹, the injection amount is about 2 mg, and the temperature range is 25–800 °C. S-4800 field emission scanning electron microscope (FESEM) of Hitachi was used to observe the morphology of the samples. The powder was identified by D8 X-ray diffraction (XRD) produced by Bruker company. The prepared nano materials were analyzed by X-ray diffraction (XRD). The XRD measurement parameters were: CuK α radiation line, filtered by curved graphite crystal monochromator, working voltage 40 kV, working current 40 mA, scanning speed 5°·min⁻¹. The particles were observed by JEM-2100 transmission electron microscope (TEM) made in Japan, and the working voltage was 200 kV. The preparation concentration is 300 ml of 1 × 10⁻⁴ mol·L⁻¹ methylene blue solution, add 0.1 g of sample, stir magnetically in the dark for 60 min to establish the adsorption balance between dye and catalyst, and put it into the photocatalytic reaction device for reaction. The light source is four 15 W UV lamps. The constant temperature is 30 °C, and in the same proportion, P25 is also placed in the photocatalytic reaction device for reaction. Take samples at every certain time, centrifuge and take the supernatant. Measure the concentration after degradation with a spectrophotometer to obtain the degradation rate of dyes. Degradation rate = [(initial concentration – post-degradation concentration)/initial concentration] × 100%.

3. Results and discussion

3.1 Thermogravimetric analysis

Figure 1 is the TG-DSC diagram of the composite obtained after electrospinning. From **Figure 1**, it can be observed that there is an obvious weight loss process of the sample before 100 °C accompanied by the endothermic of the system, which is the desorption of H₂O physically adsorbed on the sample surface and the volatilization of residual solvent. There are two obvious exothermic peaks at about 380 °C and 516 °C, and the exothermic peak near 380 °C is due to the oxidation and decomposition of n-tetrabutyl titanate to form titanium dioxide in air. PVP began to decompose at 400 °C, and there was

a significant exothermic peak at 516 °C, and PVP completely decomposed near 550 °C. After 600 °C, the weight and heat flow curve of the sample will not decrease. In order to obtain pure titanium dioxide, the calcination temperature of the material can be set to 600 °C.

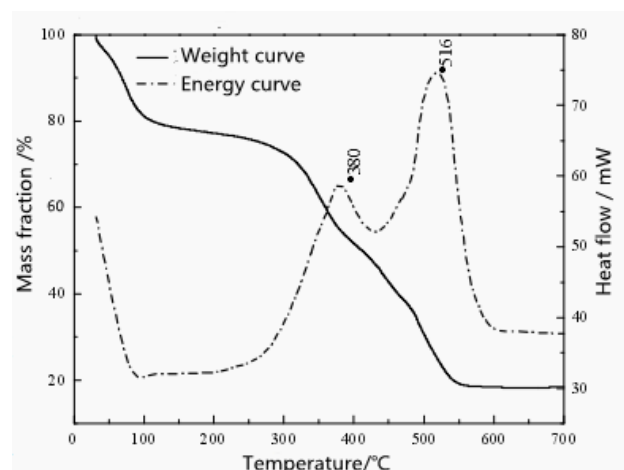


Figure 1. TG-DSC diagram of PVP/tetra-n-butyl titanate spinning film.

3.2 Exploration on the best spinning process

The titanium dioxide nanofiber film prepared by electrospinning has snow white, slightly ductile, flake and no cracks. The micro fiber morphology is affected by the spinning process, including voltage, spinning distance, nozzle translation speed, jet speed, needle inner diameter and so on. Through the control variable method, the five variables are regulated, and the micro morphology of the sample is analyzed by scanning electron microscope. The more uniform the fiber distribution, the smaller the diameter, the better the material morphology. And there is no fracture and adhesion, so as to obtain the best spinning process.

3.2.1 Voltage effect

Take the voltage as the variable, and the other variables remain unchanged. At 8 × 10³ V, 1.4 × 10⁴ V, 2.5 × 10⁴ V, the samples were spun to obtain SEM photos (**Figure 2**). **Figure 2(a)** shows voltage at 8 × 10³ V, the fiber thickness is uneven and beads appear. **Figure 2(b)** shows voltage at 1.4 × 10⁴ V, the fiber thickness is uniform, and the fiber surface is smooth and continuous. **Figure 2(c)** shows voltage at 2.5 ×

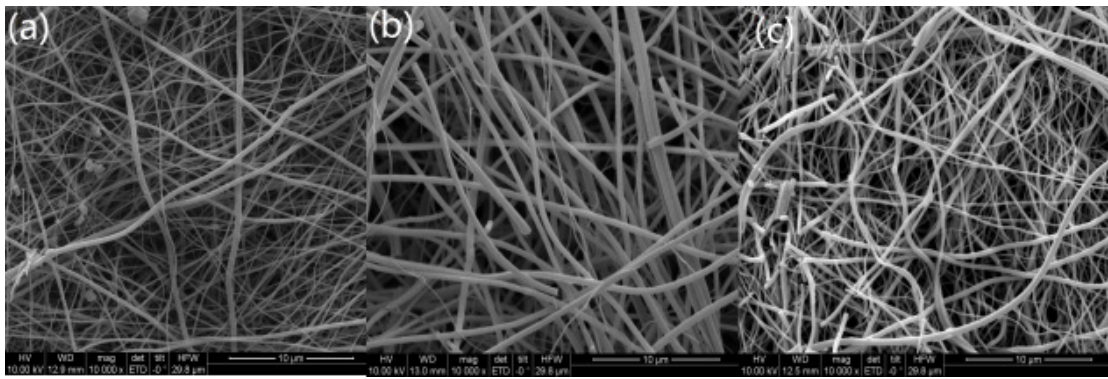


Figure 2. SEM of titanium dioxide film at positive voltage of 8×10^3 V (a), 1.4×10^4 V (b), 2.5×10^4 V (c).

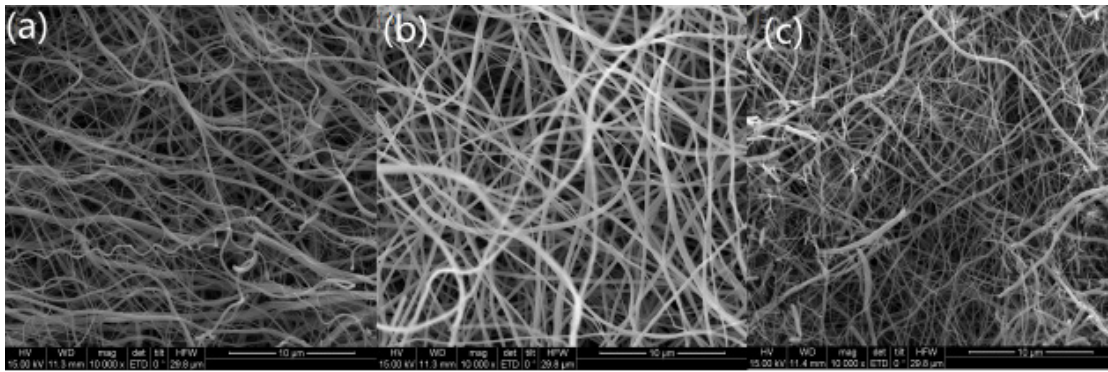


Figure 3. SEM of titanium dioxide film at spinning distance of 0.15 m (a), 0.2 m (b) and 0.25 m (c).

10^4 V, the fiber is fine, messy, and a large number of fractures occur. From this analysis, in **Figure 2(a)**, when the spinning voltage is too low, the formed electric field force is small, but to overcome the surface tension of the solution, the electrostatic field force is insufficient, resulting in that the spinning solution cannot be stretched into silk in time, so beads are formed. In **Figure 2(c)**, when the voltage is too high, during jet operation, the electric field is strong, so that the fibers are pulled very thin and disorderly, and even some fibers are pulled off. Therefore, it is necessary to select an appropriate voltage so that the electrostatic field force can overcome the surface tension of the solution without being too large to break the fiber. In **Figure 2(b)**, when the positive voltage is 1.4×10^4 V, the spinning is not only uniform in thickness, but also free of beads and fracture, and the morphology is intact. To sum up, when the voltage is 1.4×10^4 V, the spinning effect is the best.

3.2.2 Influence of spinning distance

The spinning distance is the distance between the spinning needle and the receiving plate. Take the spinning distance as the variable, keep the rest unchanged, and set the receiving distance as 0.15 m, 0.2 m and 0.25 m, then the samples were spun, and the SEM photos of the samples were obtained (**Figure 3**). It can be analyzed that the spinning distance has an obvious effect on the uniformity of fiber thickness. The change of curing distance mainly affects the electric field strength and whether the solvent in the fiber can volatilize completely. In **Figure 3(a)**, when the spinning distance is 0.15 m, the spinning distance is short, so that the fiber cannot be fully stretched, the thickness of the spinning fiber is uneven, and some filaments are thicker, so as to form a large number of curls. The solvent cannot be fully volatilized, so that the fiber can be partially bonded. In **Figure 3(b)**, when the spinning distance is 0.2 m, the distance is moderate; the fiber thickness is uniform; the arrangement is relatively orderly, and the spinning morphology is intact. In **Figure 3(c)**, when the spinning distance is 0.25 m, the spinning distance

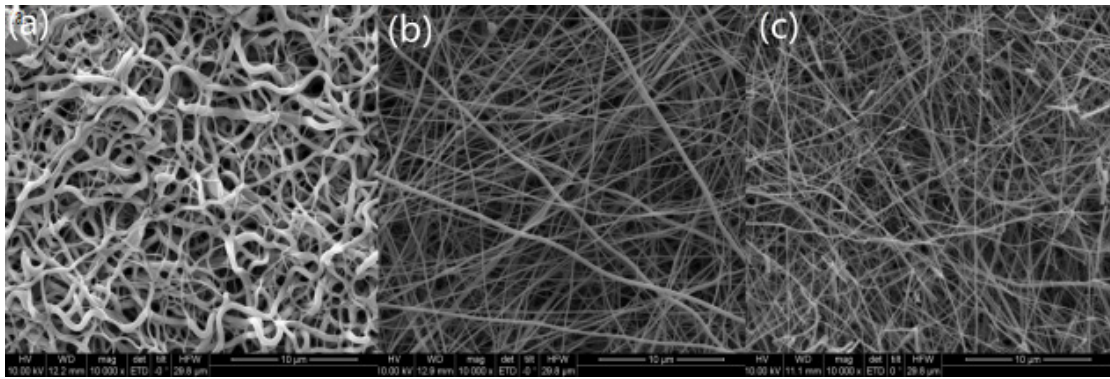


Figure 4. SEM of titanium dioxide film at nozzle translation speed of $0 \text{ m}\cdot\text{s}^{-1}$ (a), $2.5 \times 10^{-3} \text{ m}\cdot\text{s}^{-1}$ (b), $5 \times 10^{-3} \text{ m}\cdot\text{s}^{-1}$ (c).

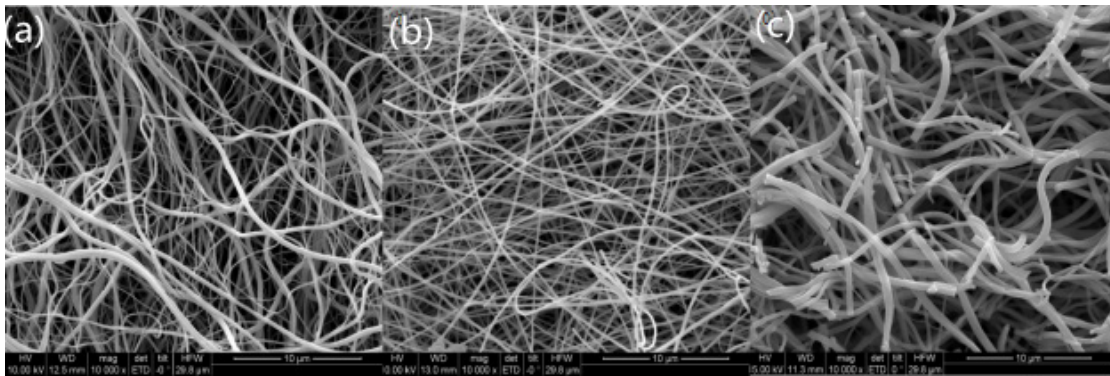


Figure 5. SEM of titanium dioxide film of pinning speed at $3 \times 10^{-4} \text{ m}\cdot\text{s}^{-1}$ (a), $5 \times 10^{-4} \text{ m}\cdot\text{s}^{-1}$ (b), $7 \times 10^{-4} \text{ m}\cdot\text{s}^{-1}$ (c).

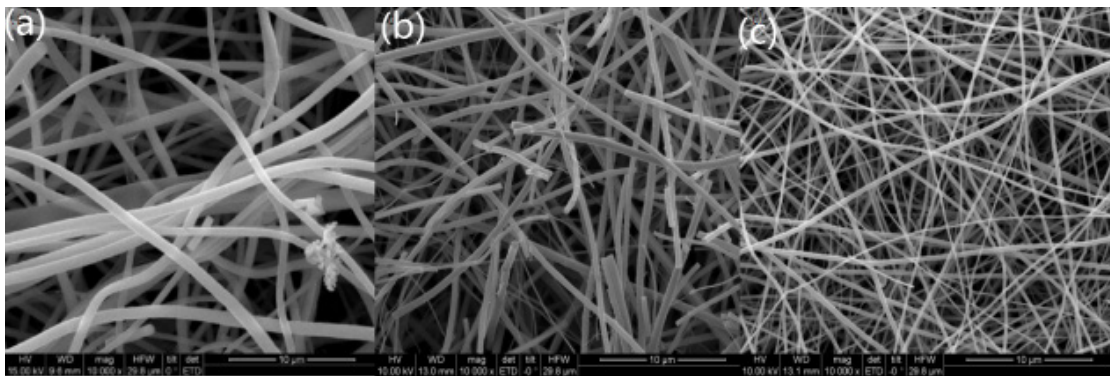


Figure 6. SEM of titanium dioxide film at the inner diameter of $7 \times 10^{-4} \text{ m}$ (a), $5 \times 10^{-4} \text{ m}$ (b), $3 \times 10^{-4} \text{ m}$ (c).

is long. Although the solvent is fully volatilized, the spun fiber cannot be received in time, and the electric field strength is relatively reduced, resulting in turbulence, and a large number of fiber fractures, more disorder and uneven fiber thickness. To sum up, the spinning distance, that is, the curing distance, is 0.2 m, the spinning effect was the best.

3.2.3 Translation speed

Taking the translational velocity of the needle as the variable, the other quantities remain unchanged. At the speed of $0 \text{ m}\cdot\text{s}^{-1}$, $2.5 \times 10^{-3} \text{ m}\cdot\text{s}^{-1}$, 5×10^{-3}

$\text{m}\cdot\text{s}^{-1}$ respectively, the spinning was carried out, and the scanning electron microscope photos of the samples were obtained (**Figure 4**). As can be seen from **Figure 4**, in **Figure 4(a)**, when the needle does not move, for no longitudinal traction, the fibers accumulate was in a fixed position, so the fibers are curled and the diameter is too large. In **Figure 4(b)**, when the needle translation speed is $2.5 \times 10^{-3} \text{ m}\cdot\text{s}^{-1}$, the spinning is smooth, fiber is uniform thickness and intact morphology. In **Figure 4(c)**, when the translation speed is $5 \times 10^{-3} \text{ m}\cdot\text{s}^{-1}$, the needle moves rapidly left and right, causing partial fracture of the

fiber. It can be analyzed that the translation speed has a significant impact on the fiber morphology. In order to control the phenomenon of fiber curling and fracture, it is necessary to select the appropriate translation speed. To sum up, the translation speed is set to $2.5 \times 10^{-3} \text{ m}\cdot\text{s}^{-1}$, the spinning effect was the best.

3.2.4 Jet speed

Taking the injection speed as the variable, the other quantities remain unchanged. At the speed of $3 \times 10^{-4} \text{ m}\cdot\text{s}^{-1}$, $5 \times 10^{-4} \text{ m}\cdot\text{s}^{-1}$, $7 \times 10^{-4} \text{ m}\cdot\text{s}^{-1}$, the samples were spun to obtain SEM photos (**Figure 5**). In **Figure 5(a)**, when the injection speed is $3 \times 10^{-4} \text{ m}\cdot\text{s}^{-1}$, the spinning is continuous, smooth, uniform, without fracture, and the fiber is fine. In **Figure 5(b)**, when the injection speed is $5 \times 10^{-4} \text{ m}\cdot\text{s}^{-1}$, the spinning is relatively uniform and partial fracture occurs. In **Figure 5(c)**, when the injection speed is $7 \times 10^{-4} \text{ m}\cdot\text{s}^{-1}$, the spinning fiber is thicker and has accumulation. It can be analyzed that the spinning speed has a significant impact on the diameter of the fiber. From **Figure 5(a)** to **Figure (c)**, the diameter of the fiber is gradually increasing with the increase of the jet speed, because the jet amount per unit time is increased with the increase of the jet speed, and the Taylor cone receiving surface formed by spinning is relatively fixed, so the tensile degree of the electrostatic field on the spinning solution must be reduced. Moreover, in the spinning process, the spinning liquid will accumulate in the needle due to the large injection volume and failure to spin in time. Of course, the smaller the jet speed, the better. If the amount is too small, there will be spinning discontinuity and fiber disconnection. To sum up, the injection speed is set to $3 \times 10^{-4} \text{ m}\cdot\text{s}^{-1}$, then the spinning effect was the best.

3.2.5 Needle size

The needle size is variable, and the other quantities remain unchanged. Under the inner diameter of $7 \times 10^{-4} \text{ m}$, $5 \times 10^{-4} \text{ m}$, $3 \times 10^{-4} \text{ m}$, the samples were spun to obtain SEM photos (**Figure 6**). In **Figure 6(a)**, when the needle of inner diameter $7 \times 10^{-4} \text{ m}$ is selected, the prepared fiber is thicker and the fiber is

not straight. Select the needle of inner diameter $5 \times 10^{-4} \text{ m}$ in **Figure 6(b)**, the prepared fiber is uniform in thickness, but slightly broken. Select the needle of inner diameter $3 \times 10^{-4} \text{ m}$ in **Figure 6(c)**, the prepared fibers are evenly distributed and the fiber diameter is much thinner. It can be analyzed that the thickness of the needle will also affect the diameter of the spinning fiber, because the thickness of the inner diameter of the needle directly affects the amount of spinning jet. From **Figure 6(a)** to **Figure 6(c)**, as the needle becomes thinner, the prepared fibers not only have small diameter, uniform distribution, but also have intact morphology. Therefore, the fiber prepared by selecting the needle with an internal diameter of $3 \times 10^{-4} \text{ m}$ is better.

Based on the above scanning morphology of fiber film under different voltage, spinning distance, jet speed and needle inner diameter, it can be concluded that the voltage is set to $1.4 \times 10^4 \text{ V}$ for electrospinning parameters, spinning distance 0.2 m, translation speed $2.5 \times 10^{-3} \text{ m}\cdot\text{s}^{-1}$, injection speed $3 \times 10^{-4} \text{ m}\cdot\text{s}^{-1}$, needle inner diameter $3 \times 10^{-4} \text{ m}$, the titanium dioxide fiber film with the smallest fiber diameter and the best uniformity and no fracture agglomeration can be obtained. The titanium dioxide film with this morphology is the best morphology.

3.3 Structure and morphology analysis

Figure 7 is at a voltage of $1.4 \times 10^4 \text{ V}$, spinning distance 0.2 m, translation speed $2.5 \times 10^{-3} \text{ m}\cdot\text{s}^{-1}$, injection speed $3 \times 10^{-4} \text{ m}\cdot\text{s}^{-1}$ and needle inner diameter $3 \times 10^{-4} \text{ m}$ XRD pattern of titanium dioxide fiber film with the best spinning morphology prepared. Wide diffraction peaks appeared at $2\theta = 25.4^\circ$, 37.5° , 48.1° , 54.0° , 55.1° , 62.7° , 68.8° , 70.3° and 75.0° . Corresponding to the characteristic peaks of (101), (004), (200), (105), (211), (204), (116), (220) and (215) crystal planes of anatase TiO_2 , narrow diffraction peaks also appeared at $2\theta = 27.4^\circ$, 36.1° , 41.2° and 56.6° . Corresponding to the characteristic peaks of (110), (101), (111) and (220) crystal planes of rutile TiO_2 , it can be seen that the titanium dioxide synthesized by electrospinning is mainly anatase phase (JCPDS21-1272), and there is also a small amount of more stable rutile phase (JCPDS21-1276). According

to Scherrer formula, the average grain size of TiO₂ nanofibers is about 14.3 nm.

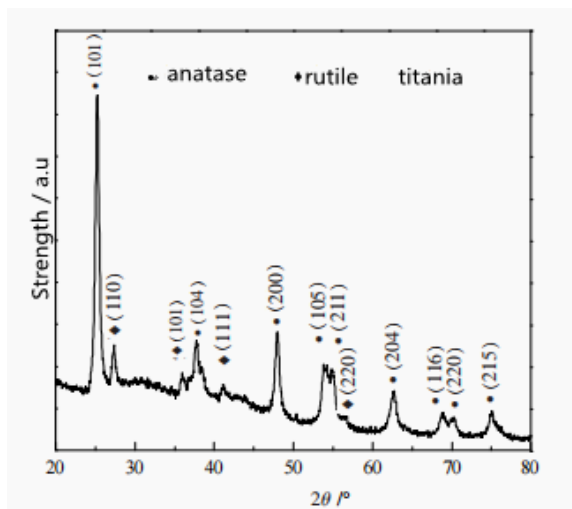


Figure 7. XRD diffraction pattern of titanium dioxide fiber film.

Figure 8 is a TEM photograph of nano titanium dioxide fiber film material at different resolutions. It can be observed from **Figure 8(a)** that titanium dioxide is fibrous, the fiber morphology is well preserved, and has a large aspect ratio. It can be seen in **Figure 8(b)** that the fiber is actually assembled from nano-sized titanium oxide particles. At the same time, it can be seen that the diameter of the fiber is about 150 nm. Under the high-power observation shown in the HRTEM photo (**Figure 8(c)**), it can be seen that there are a large number of lattice lines of titanium dioxide crystal. The measured spacing of lattice lines is 0.35 nm, which corresponds to the crystal plane of anatase phase (101), and the rutile phase is not observed due to the small amount.

3.4 Photocatalytic performance

In order to investigate the photodegradation effect of titanium dioxide fiber membrane material on common dye methylene blue solution, compare

it with P25, and the degradation rate is shown in **Figure 9**. Under the same experimental conditions, the degradation rate of methylene blue solution by titanium dioxide film was 95.8%, while the degradation rate of P25 was 66.9%. Therefore, titanium dioxide fiber membrane material has better photocatalytic activity. This is because the fluffy fiber structure of the sample makes the material have strong adsorption capacity, which makes methylene blue molecules easier to adsorb on the active sites of the material. The photogenerated hole transmission rate of titanium oxide is fast, which reduces the recombination probability of photogenerated electrons and holes, thus avoiding the rapid deactivation of the catalyst. Moreover, titanium fiber oxide surface is rich in hydroxyl group and has strong adsorption water capacity. Water and hydroxyl groups can react with surface holes to form strong oxidative hydroxy radicals, which can decompose the methyl blue solution in a short time.

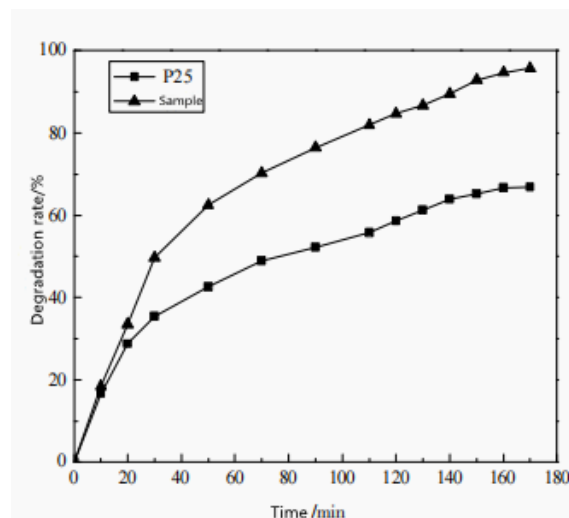


Figure 9. Degrade rate of titanium dioxide fiber membrane samples and P25 on methylene blue solution.

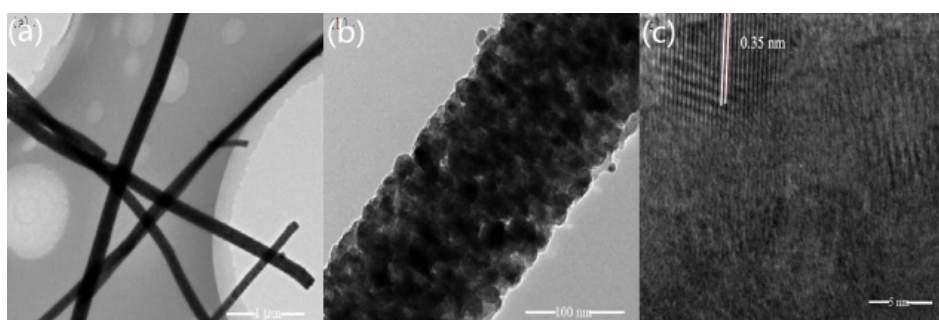


Figure 8. TEM photos of nano titanium dioxide fiber membrane material at different magnification.

4. Conclusion

PVP/tetra-n-butyl titanate composite nanofibers were prepared by electrospinning and calcined in a muffle furnace at 600 °C. By exploring the influencing factors of electrospinning, the optimum spinning conditions were obtained: the voltage was 1.4×10^4 V, spinning distance 0.2 m, translation speed $2.5 \times 10^{-3} \text{ m}\cdot\text{s}^{-1}$, injection speed $3 \times 10^{-4} \text{ m}\cdot\text{s}^{-1}$, needle inner diameter $3 \times 10^{-4} \text{ m}$. XRD and TEM characterization showed that the products obtained under the optimum conditions were mainly composed of anatase titanium oxide long fibers, with uniform fiber distribution and good morphological structure. The diameter of the fibers was about 150 nm. Titanium oxide grains of about 14 nm are deposited. The degradation ability of this material to methylene blue dye is much higher than that of commercial P25 titanium dioxide material, and the membrane structure of the material is more conducive to the recovery and reuse of the material, so it has great application potential.

Conflict of interest

The authors declare that they have no conflict of interest.

Acknowledgements

This work was supported by the National Natural Science Foundation of China (51478285), Natural Science Foundation of Jiangsu Province—Youth Fund (BK2014, 280) and Natural Science Foundation of colleges and universities of Jiangsu Province (16KJA430008).

References

1. Zhou Q, Zhao Y. Health impacts of typical dyes and pigments. *Journal of Environment and Health* 2005; 22(3): 229–231.
2. Lu J, Yu Z, Zhang H. Research progress in the microbial degradation of dye. *Industrial Water Treatment* 2014; 34(1): 1–4.
3. Morsi MS, Al-Sarawy AA, El-Dein WAS. Electrochemical degradation of some organic dyes by electrochemical oxidation on a Pb/PbO₂ electrode. *Desalination & Water Treatment* 2011; 26(1-3): 301–308.
4. Gumus D, Akbal F. Photocatalytic degradation of textile dye and wastewater. *Water, Air & Soil Pollution* 2011; 216(1): 117–124.
5. Ye M, Chen Z, Liu X, *et al.* Ozone enhanced activity of aqueous titanium dioxide suspensions for photodegradation of 4-chloronitrobenzene. *Journal of Hazardous Materials* 2009; 167(1-3): 1021–1027.
6. Wang L, Chen Z, Guo F, *et al.* Study on photocatalytic degradation of phenol wastewater solution by TiO₂ suspension. *Applied Chemical Industry* 2011; 40(1): 13–15, 22.
7. Chen J. Home advances in study on preparing nanosized titanium dioxide. *Guangdong Chemical Industry* 2012; 39(14): 93–95.
8. Wu M, Sapi A, Avila A. Enhanced photocatalytic activity of TiO₂ nanofibers and their flexible composite films: Decomposition of organic dyes and efficient H₂ generation from ethanol-water mixtures. *Nano Research* 2011; 4(4): 360–369.
9. Greiner A, Wendroff JH. Electrospinning: A fascinating method for the preparation of ultrathin fibers. *Angewandte Chemie International Edition* 2007; 46(30): 5670–5703.
10. Wu H, Hu L, Rowell MW, *et al.* Electrospun metal nanofiber webs as high-performance transparent electrode. *Nano Letters* 2010; 10(10): 4242–4248.
11. An B, Wang J. Electrostatic spinning research and application progress of zein fiber. *Shandong Textile Science & technology* 2016; (2): 50–52.
12. Xiao W, Zeng Y. Effects of parameters on fiber diameter in electrospinning: Experiment and numerical simulation. *Journal of Donghua University (Natural Science Edition)* 2009; 35(6): 632–638.



Characterization and Application of Nanomaterials

Focus and Scope

Characterization and Application of Nanomaterials (CAN) is an open access peer-reviewed journal allowing maximum visibility of articles published in it as they are available to a wide, global audience. We are interested in the scientific topics from all fields of nano. CAN provides a forum to share scholarly practice to advance the use of nanomaterials in the context of scientific application.

CAN publishes original research articles, review articles, editorials, case reports, letters, brief commentaries, perspectives, methods, etc.

Examples of relevant topics include but are not limited to:

1. Nanoparticle composites
2. Nanoscale quantum physics
3. Modeling
4. Simulation
5. Nanotechnology and its application
6. Nanochemistry
7. Nanoscience, nano-medicine and bio-nanotechnology
8. Nanomaterials and energy applications
9. Micro-nano scale
10. Fabrication of thin film
11. Nanomaterial synthesis, characterization, and application
12. Nanotechnology and environmental protection
13. Photocatalytic degradation properties
14. Preparation of nanostructured materials

EnPress Publisher, LLC

EnPress Publisher, LLC, is a scholastic conduit for an assembly of professionals in the domains of science, technology, medicine, engineering, education, social sciences and many more, as a roundtable for their intellectual discourse and presentation, and as an instrument to galvanize research designs, policy implementation and commercial interests, to facilitate the prevailing over their challenges and to encourage to the full advantage of their resources and true potential.

We are the intellectual and academic home for academic, educators, scholars, clinicians, corporate researchers, who all play important roles in a wide range of national and international research organisations, and whose interests, expertise, research approaches and industry objectives from around the world coalesce together to advance significant contributions in their research and professional fields.

As an instrument of information purveyor, we seek to combine academic rigor and originality with the nuanced development of policy and practice. Via our journals, client database, online campaigns and social media presence, we offer a platform for industry professionals to interconnect, as well as opening doors towards cost-effective solutions for them to succeed, and we confidently hope to inspire a new generation of multidisciplinary researchers, think-tank experts, policymakers and business entities to innovate and advance their knowledge across fields.



EnPress Publisher, LLC

Add: 14701 Myford Road, Suite B-1, Tustin, CA 92780, United States

Tel: +1 (949) 299 0192

Email: contact@enpress-publisher.com

Web: <https://enpress-publisher.com>